Femtochemistry and Laser Control of Photochemical Reactions

Thomas, Esben Folger

Publication date:
2019

Document Version
Publisher's PDF, also known as Version of record

Femtochemistry and Laser Control of Photochemical Reactions

Esben Folger Thomas

Kongens Lyngby 2018

Technical University of Denmark
Department of Chemistry
Kemitorvet, building 206,
2800 Kongens Lyngby, Denmark
Phone +45 61 71 00 49
Esbenfthomas@gmail.com

Abstract

Since the advent of the laser in the 1960's, the possibility of using coherent light sources to control molecules and molecular reactions has been a hot topic in photochemistry. The ability to generate laser pulses on ever shorter time scales, down to femto- and even atto-second durations, as well as the development of optical techniques for actively controlling the time-dependent features of these pulses, has driven the field forward into new lines of theoretical and experimental inquiry.

At higher field strengths, polarization forces, i.e., the distortion of electronic states leading to induced dipole moments related to the polarizability, can play an important role. The application and control of these polarization forces (via ultrashort optimized laser pulses) has previously been exploited experimentally in order to control, e.g., the rotational, vibrational, and dissociation dynamics of molecules through the so-called dynamic Stark effect.

This doctoral thesis contains a series of theoretical works where the concept of exploiting the dynamic Stark effect to control quantum molecular wave packets through dynamic Stark control (DSC) is introduced and explored through a variety of different applications.

In the second chapter, a clarifying interpretation is presented of how the dynamic Stark effect operates by shifting the energy levels of the potential surfaces present in a molecule using a simplified 1D harmonic model. Using this model, general properties and relationships are derived that paint an intuitive picture of this type of second order excitation process from a temporal, as well as a spectral, perspective.

In the third chapter, the concept of DSC is extended to include diatomic molecular rotations as well as vibrations, and it is shown that the spectral interpretation of the second order excitation process associated with DSC can be exploited to exert state selective control over ro-vibrational transitions.

Inspired and verified by impulsive alignment experiments performed on gas phase I_2 molecules, the aforementioned rotational model is then further ex-

tended to include the coupling between the quadrupole moments of the atomic nuclei and the molecular rotational states. It is demonstrated that this so-called quadrupole coupling will significantly perturb the time dependent alignment traces in molecules with large quadrupole coupling constants when they are prepared in superpositions of rotational states by ultrashort laser pulses.

In the fourth chapter, the concept of vibrational DSC is revisited and extended, and it is demonstrated that this approach can be used to control the delicate process of laser induced enantiomeric conversion (deracemization) in a racemic mixture of biaryl molecules. This is achieved using a simulated closed loop experimental setup to optimize the phases of a pair of nonresonant, linearly polarized Gaussian laser pulses. By carefully modelling the optimization process to accurately reflect current experimental techniques and capabilities, this work represents an advance towards a first-ever experimental implementation of laser-induced enantiomeric conversion.

This result is then extended by outlining a simplified approach to the deracemization task that does not require appreciable optimization of the laser pulse shape. While less effective than the full closed-loop approach, this method has the advantage of being significantly less challenging to implement experimentally.

In the fifth chapter, a different approach to experimental DSC is outlined. This method is based on the application of a trained neural network to generate a control field based on dynamic experimental feedback from the molecular system.

Resume

Siden udviklingen af laseren i 1960erne har muligheden for at kontrollere molekyler og molekylær reaktioner med kohærente lyskilder været et varmt emne inden for fotokemi. Muligheden for at generere laserpulser helt ned på femto- og endda atto- sekund tidsskalaer, koblet med udviklingen af optiske teknikker for at aktivt kontrollere de tids-afhængige karakteristika af disse pulser, har drevet feltet fremad imod nye retninger af teoretisk og eksperimentel udforskning.

Ved højere feltstyrker kan polariserings-kræfter, d.v.s. perturberede elektroniske tilstande som fører til inducerede dipolmomenter relaterede til den molekylær polarisibilitet, spille en vigtig rolle. Anvendelsen og kontrollen af disse polariseringskræfter (ved brug af optimerede ultrakorte laserpulser) har tidligere været udnyttet eksperimentelt til at, f.eks., kontrollere den rotationelle, vibrationelle, og dissociative dynamik i molekyler igennem den såkaldte dynamiske Stark effekt.

Denne PhD afhandling indholder en række teoretiske resultater hvori ideén om at udnytte den dynamiske Stark effekt til at kontrollere kvantemekanisk molekylær bølgepakker igennem dynamiske Stark control (DSC) er introduceret og udforsket igennem en række forskellige tilfælde.

I kapitel to beskrives en sammenfattende fortolkning vedrørende måden den dynamiske Stark effekt fører til forskudte energi-niveauer i potentielle energi flader af et molekyle ved brug af en forenklet 1D harmonisk model. Denne model bruges endvidere til at udlede nogle generelle egenskaber og sammenhænge som er med til at danne et intuitivt billede af denne type anden-ordens excitationsproces, både i tids- og frekvens- domænet.

I kapitel tre bliver DSC konceptet udviklet til at inkludere toatomige molekylære rotationer såvel som vibrationer, og det påvises at frekvens-fortolkingen af den anden-ordens excitationssprocess associeret med DSC kan udnyttes til at opnå tilstands-specifik kontrol over ro-vibrationelle overgange.

Inspireret og verificeret af impulsive orienterings eksperimenter på gas-fase I_2 molekyler bliver den førnævnte rotations-model videreudviklet til at inkludere koblingen imellem atom-kernernes kvadrupol-moment og de rotationelle til-

stande i molekylerne. Det demonstreres, at denne såkaldte kvadrupol-kobling markant vil ændre den tidsafhængige orientering af molekyler med store kvadrupol-koblings-konstanter, når de exciteres til superpositioner af rotationelle tilstande med ultrakorte laserpulser.

I kapitel fire bliver konceptet bag vibrationel DSC genbesøgt og udvidet, og det demonstreres at denne metode kan anvendes til at kontrollere en delikat proces: laser-induceret enantiomerisk transformation (deracemization) i en racemisk blanding af biaryl molekyler. Dette opnås ved at simulere en "closed-loop" eksperimentel opsætning og optimere et par ikke-resonante, lineært polariserede Gaussiske laserpulser. Ved at modellere optimerings-processen så den afspejler nuværende eksperimentelle teknikker og kapaciteter, repræsenterer dette arbejde et skridt fremad imod opnåelsen af laser-induceret enantiomerisk transformation i et laboratorie for første gang nogensinde.

Dette resultat udvides ydeligere ved fremlæggelsen af en forenklet tilgang til laser deracemization som ikke kræver synderlig optimering af laser-puls formen. Selvom den er mindre effektiv end et closed-loop approach, har denne metode fordelen af at være væsentligt nemmere at implementere i et eksperiment.

I kapitel fem beskrives en ny metode til implementering af eksperimentel DSC. Denne metode er baseret på anvendelsen af et trænet neuralt netværk til at generere et kontrol felt baseret på dynamisk eksperimentel feedback fra det molekylær system.

List of Publications

This thesis contains summaries of the following publications:

1. *Non-Resonant Dynamic Stark Control of Vibrational Motion with Optimized Laser Pulses*
   Esben F. Thomas and Niels E. Henriksen
   The Journal of Chemical Physics **144**, 244307 (2016)

2. *Femtochemistry in the Electronic Ground State: Dynamic Stark Control of Vibrational Dynamics*
   Chuan-Cun Shu, **Esben F. Thomas**, and Niels E. Henriksen
   Chemical Physics Letters **683**, 234-239 (2017)

3. *Phase-Modulated Nonresonant Laser Pulses Can Selectively Convert Enantiomers in a Racemic Mixture*
   Esben F. Thomas and Niels E. Henriksen
   The Journal of Physical Chemistry Letters **8**, 2212-2219 (2017)

4. *Hyperfine-Structure-Induced Depolarization of Impulsively Aligned* I_2 *Molecules*
   Esben F. Thomas, Anders A. Søndergaard, Benjamin Shepperson, Niels E. Henriksen, and Henrik Stapelfeldt
   Physical Review Letters **120**, 163202 (2018)

5. *Breaking Dynamic Inversion Symmetry in a Racemic Mixture Using Simple Trains of Laser Pulses*
   Esben F. Thomas and Niels E. Henriksen
   Submitted to The Journal of Chemical Physics (2018)

6. *A Novel Pulse Optimization Scheme for use in Coherent Control Experiments*
   Esben F. Thomas and Niels E. Henriksen
   To be submitted (2018)

Preface

This thesis was prepared at the department of Chemistry at Technical University of Denmark in fulfilment of the requirements for acquiring a PhD in theoretical femtochemistry and quantum coherent control. The work presented herein was carried out by me at the Department of Chemistry at the Technical University of Denmark from September 2015 to October 2018 under supervision of Niels E. Henriksen. I acknowledge the financial support I have received from the Department of Chemistry at the Technical University of Denmark.

Lyngby, 15-October-2018

Esben Folger Thomas

Acknowledgements

A common complaint amongst PhD students is that their supervisors treat them like slaves, forcing them to take on uninteresting projects and tasks that no one else in the department wants to do, and later taking credit for the results.

My supervisor, Niels Engholm Henriksen has completely shattered this misconception by consistently granting me the freedom to pursue my own ideas. Consequently, I am extremely grateful that the successes (and inevitable failures) associated with my research have always felt like they have been on my own terms.

This should not in any way be misconstrued with a lackadaisical attitude or lack of guidance from Niels's side; on the contrary, I have rarely encountered a situation where he was not ready to drop whatever he was working on and give me his undivided attention any time I spontaneously showed up at his office to discuss something. It is no exaggeration to say that I could never have achieved any of the results in this thesis without his expert guidance, ideas, and insight.

So Niels, thank you for living up to exactly zero of the negative stereotypes associated with PhD supervisors, the last three years have been an absolute blast!

Thank you Henrik Stapelfeldt and the rest of the Femtolab group at Aarhus university. I am grateful for the time you took to show me around your laboratory and the fruitful discussions we had during my external stay. Your impressive work with, and knowledge of, experimental femtochemistry has been an enormous source inspiration.

In particular, thank you Henrik Stapelfeldt, Anders Søndergaard, and Benjamin Shepperson for the opportunity to collaborate with you on your work with impulsively aligned I_2 molecules.

Thank you to Chuancun Shu for productive and inspiring discussions.

Thank you to my current (and former) officemates Gianluca Levi, Asmus O.

Dohn, Mostafa Abedi, Mats Simmermacher, and Mátyas I. Pápai for being a pleasure to work alongside.

Thank you to Klaus Braagaard Møller and the rest of the faculty at DTU Chemistry for creating a highly enjoyable working environment.

Last, but very far from least, a huge thank you to my wife Ditte and our daughter Hollie. You two are my whole world, and everything I do is dedicated to you.

Contents

Chapter 1

Introduction

1.1 A Brief History of Ultrafast Chemistry

The motion of atoms at the molecular scale is on the order of ~ 1 kilometer per second [1], and the characteristic length scale over which this motion occurs on is the order of a few Angströms, or ten-billions of a meter. Therefore, the timescales at which molecular reactions occur are on the order of a few to a few thousand million-billionths of a second, or *femtoseconds*. To underline how remarkably brief this time scale is, note that travelling to the moon and back (a distance roughly equivalent to travelling around the world 18 times) at light speed will only take about 2.5 seconds. Despite moving at such an astonishing speed, it still takes light about 100 femtoseconds to traverse the distance equivalent to the diameter of a single human hair. The burgeoning field of *femtochemistry* is the study of reactions on this timescale.

Over the past century, the time resolution at which chemical reactions can be studied has increased dramatically:

- The study of reaction rates led to the Arrhenius equation [2] in 1889, which relates temperature to chemical reaction rate.
- In 1923, the first direct sub-second resolution measurements of chemical reaction velocities were made possible when H. Hartridge *et al* designed an experiment in which reactants were mixed in high velocity flow tubes, and the reaction was observed at various spatial intervals along a flow channel [3], achieving time resolution on a scale of tens of milliseconds.
- Around 1950, time resolution at the microsecond timescale was achieved when R. G. W. Norrish and George Porter developed the method of flash photolysis, in which a brief intense flash of light is used to disturb the

equilibrium of a sample, after which a series of secondary light pulses probe the system and record the spectra of the intermediate states.

- Around 1954, Manfred Eigen was able to achieve micro- and even nanosecond time resolutions through development of the relaxation method [2, 4] which involves disturbing the equilibrium of a system via sudden change in temperature, pressure, or electric field, and following the kinetics as the system equilibrates.

At the time, it was widely thought that the last two techniques on this list represented the absolute lower limit of achievable time resolution. This quickly changed after the first laser was developed by Theodore Maiman in 1960. By 1966, lasers were able to generate short bursts of coherent light that were only a few picoseconds long, and a few decades later, it became possible to create light pulses of just a few femtoseconds [5].

In 1985 Ahmed Zewail *et al.* started working on an experiment at Caltech where the goal was to monitor the bond breakage ($\mathrm{ICN}^* \rightarrow \mathrm{I} + \mathrm{CN}$) [1]. Here, a "pump" pulse was used to dissociate the molecule, after which the reaction kinetics of the system were probed using a series of femtosecond pulses at varying time intervals. Two years later, a time resolution of about 40 fs was achieved, leading to the first ever time-resolved measurements of the transition states in a chemical bond. Lasers opened the door to monitoring chemical reactions with ever increasing time resolution, and today it is possible to generate pulses all the way down to the attosecond time scale [6], allowing us to even probe the sub-femtosecond dynamics of molecular electrons.

Now, imagine being able to also assume direct *control* of a chemical reaction, deciding exactly which bonds to break and which bonds to make, enabling the construction of molecular configurations never seen before in nature. In 1980, Zewail published a paper titled "Laser Selective Chemistry - is it Possible?" [7], in which he explored the feasibility of using tuned laser pulses to drive molecular systems into specific user-defined states. This helped spawn the femtochemistry subfield known as *coherent control*, which is essentially based around the idea of being able to "steer" dynamic molecular processes on femtosecond time scales using shaped laser pulses that couple to the molecular dipole moment.

Presently, a large body of theoretical (see, e.g., refs. [8–12]) and experimental (see, e.g., refs. [13–19]) work has been produced in which the feasibility of applying custom-tailored laser pulses to drive various systems into specific target states has been explored/demonstrated. On the theoretical side, the development of, e.g., optimal control theory [20] and its application to numerical simulations of light-matter interaction has provided a powerful tool for understanding the dynamics of coherently controlled molecular systems. Experimentally, the

implementation of so-called "closed-loop" pulse optimization schemes [5, 8] have proven to be particularly successful (a detailed explanation of this concept can be found chapter 4 of this thesis).

1.2 Methodology Overview

One of the primary topics in my PhD work is related to how light interacts with matter, or more specifically, how intense coherent laser light interacts with molecules in the gas phase. Because the intensity, and therefore the number of photons, associated with the laser pulses I am working with are relatively large, the semiclassical approximation will be used throughout (i.e. the electric field will be described as a classical wave, and the molecular dynamics will be described quantum-mechanically).

As I will discuss in chapter 2, in the semiclassical limit a laser pulse can, under certain conditions, be described by an electric field that varies as a function of time:

$$\varepsilon(t), \tag{1.1}$$

where $\varepsilon(t)$ is a real function. It is often convenient to describe $\varepsilon(t)$ as the real part of a complex function $E(t)$:

$$\varepsilon(t) = \mathrm{Re}\{E(t)\}. \tag{1.2}$$

Now, $E(t)$ can be represented in the spectral domain using the Fourier transform [21]:

$$\tilde{E}(\omega) = \frac{1}{\sqrt{2\pi}} \int_{-\infty}^{\infty} E(t) \exp(i\omega t) dt. \tag{1.3}$$

This means that a laser pulse can be described either by its complex frequency distribution $\tilde{E}(\omega)$, the complex temporal function $E(t)$, or the real temporal function $\varepsilon(t)$. The spectral distribution $\tilde{E}(\omega)$ can be separated into real and complex parts:

$$A(\omega) \exp[i\phi(\omega)], \tag{1.4}$$

Where $A(\omega)$ is the spectral *amplitude* and $\phi(\omega)$ is the spectral *phase*. It is common to approximate the shape of an ultrashort laser pulse as the product of an oscillating function and a Gaussian envelope:

$$E(t) = \exp(i\omega_c t + i\theta_c) \exp\left(-\frac{t^2}{2\sigma^2}\right), \tag{1.5}$$

or, in the spectral domain:

$$\tilde{E}(\omega) = \sigma \exp(i\theta_c) \exp\left(-\frac{\sigma^2(\omega_c + \omega)^2}{2}\right), \tag{1.6}$$

where ω_c is the *carrier frequency* and θ_c is its associated phase, and where σ characterizes the second moment temporal width of the pulse envelope. As the relationships between equations 1.5 and 1.6 indicate, the Fourier transform of a Gaussian temporal pulse with a constant carrier frequency will be a Gaussian spectral distribution with a flat phase, i.e. all of the oscillating components of the spectral distribution have the same phase angle at $t = 0$. Dividing the spectral distribution into a number of discrete components with frequency dependent amplitude A_n helps illustrate this concept:

$$E(t) = A_1 \exp(i\omega_1 t) + A_2 \exp(i\omega_2 t) + \ldots + A_n \exp(i\omega_n t). \tag{1.7}$$

A phase shift in the spectral domain means that a phase angle is added to one or more of these oscillators:

$$E(t) = A_1 \exp(i\omega_1 t + i\phi_1) + A_2 \exp(i\omega_2 t + i\phi_2) + \ldots + A_n \exp(i\omega_n t + i\phi_n). \tag{1.8}$$

In this thesis, changing the phase of a spectral distribution will henceforth be referred to as a *spectral chirp* (this is not to be confused with a temporal pulse frequency that varies over time, which can be referred to as a temporal chirp). In general, changing the phase (and/or amplitude) of the spectral pulse components will result in a change in the temporal pulse shape when the spectral distribution is transformed back into the temporal domain. As I will explain in chapter 4, this principle can be used in experiments to generate shaped laser pulses that can be used to control the ultrafast dynamics of molecular systems.

The quantum mechanical behaviour of a molecular system interacting with a laser pulse is determined by solving the time-dependent Schrödinger equation (TDSE):

$$i\hbar \frac{d}{dt} |\Psi(t)\rangle = \hat{H}(t) |\Psi(t)\rangle \tag{1.9}$$

where $\Psi(t)$ is the system wave function and $\hat{H}$ is the Hamiltonian operator that characterizes the total energy $\mathcal{E}$ of the system, i.e.

$$\hat{H}(t) |\Psi(t)\rangle = \mathcal{E} |\Psi(t)\rangle , \tag{1.10}$$

where I state the time-dependence of $\hat{H}(t)$ to underline that the system is interacting with the time-dependent external field $\varepsilon(t)$. In chapter 2, I will demonstrate that in some simple cases it is possible to obtain analytical solutions to equation 1.9, but in general numerical approaches such as split operator propagation [22] or Runge-Kutta methods [23] are required. As these types of numerical methods are generally well-known to anyone who has experience performing quantum dynamics simulations, I do not discuss them in this thesis or the accompanying publications, save for stating when a particular method has been used.

1.3 Narrowing the Gap Between Theory and Experiment

As in many areas of science and engineering, the fields of femtochemistry and coherent control have received intense scrutiny from theoreticians and experimentalists alike. As a theoretician, I have found the most stimulating work to be found in the overlap between the theoretical and experimental domains; the development of new theoretical tools generates insights into the physical processes observed in the laboratory, guiding the experimental work towards avenues of inquiry are likely to lead to interesting breakthroughs; conversely, the unavoidable limitations associated with working in a real experimental situation provide a never-ending source of interesting technical challenges that require creative problem solving to overcome.

My work over the course of the last three years has resulted in the submission and/or publication of a total of six papers, five of which I am the primary author on. These papers are included in appendices A-F, and represent the main "meat" of my accomplishments. My first paper (appendix A) deals with deriving and applying simple analytical models that are related to the second order excitation phenomenon known as dynamic Stark control (DSC). The reason for doing this is not simply academic; the unique dynamics that apply in the regime of pure DSC are attractive from a standpoint of experimental implementation due to the fact that the dynamic Stark effect dominates under non-resonant conditions, making this approach particularly interesting with respect to e.g. heavy molecules, as their lower vibrational frequencies will typically lie outside the operational bandwidths of conventional laser and pulse shaping technologies.

The second and third papers (appendices B and C) discussed in this thesis are also related to second order excitation processes; specifically the role they play in impulsive alignment via the generation of rotational wave packets. In particular, the third paper, written in collaboration with the experimental Femtolab group at Aarhus university, demonstrates that the coupling between molecular rotational states and the nuclear spin needs to be taken into account to accurately describe the rotational dynamics of impulsively aligned molecules containing atoms with large quadrupole coupling constants. Again, this is a result that is not just interesting from a theoretical perspective as it has potentially important practical implications for any experimentalists working with impulsively aligned molecular systems.

The fourth and fifth papers (appendices D and E) are also inspired by experimental work done by the Femtolab group in Aarhus. In the fourth paper, I describe and numerically verify an experimental approach to controlling the

very delicate process of selective purification of a 50/50% mixture of left and right handed molecular isomers (enantiomers). Unlike similar previous theoretical studies of this problem, my work again remains focused on experimental implementability by once more exploiting the flexibility of a nonresonant DSC approach, as well as carefully modelling the optimization process to accurately reflect current experimental techniques and capabilities. The fifth paper can be considered a follow-up to the fourth paper; here I suggest a simplified setup and show that a laboratory implementation will still lead to a potentially significant and important step on the road towards fully achieving laser induced deracemization.

The sixth and final paper (appendix F) outlined in this thesis is of a more speculative nature than the others; however the main motivation behind the work is to come up with a more efficient method of optimal control that can be implemented in a laboratory; i.e. it is once again a body of theoretical work that has been created specifically with the experimentalist in mind.

1.4 This Thesis

As the reader may know, academic and/or technical writing can be an extremely time-consuming process, where much effort is spent trying to explain things in a manner that is both succinct and informative. Having already attempted to achieve this goal to the best of my abilities throughout my publications, the tone of the writing in this thesis will be somewhat less formal. I will (as much as possible) avoid simply rehashing my published results, instead I will try to use this opportunity to paint an overall picture of my journey as a PhD student, as well as provide a few key background details that I have found relevant and/or interesting. To summarize, this thesis is primarily written with the following goals in mind:

- To provide a coherent "road map" guiding the reader through the topics that I have covered over the course of my PhD studies
- To provide derivations and background information for a few key relevant concepts
- To include original work that I found interesting, even though it was not necessarily "impactful" enough to warrant publication (i.e., negative or incomplete results)

Chapter 2

Quantum Control and the Dynamic Stark Effect

2.1 Deriving a Model of Light-Matter Interaction

The general Hamiltonian of a molecule can be written as $\hat{H} = \hat{T}_{\text{nuc}} + \hat{H}_e$, where $\hat{T}_{\text{nuc}}$ is the nuclear kinetic energy and $\hat{H}_e$ is the electronic Hamiltonian. Invoking the adiabatic approximation, and confining the dynamics to the electronic ground state ψ_0, the electronic energy as a function of the nuclear position $\mathbf{R}$ can be calculated by solving the equation

$$\hat{H}_e \psi_0 (\mathbf{R}; \mathbf{r}) = E_0 (\mathbf{R}) \psi_0 (\mathbf{R}; \mathbf{r}) , \tag{2.1}$$

where $\mathbf{R}$ and $\mathbf{r}$ denote the respective nuclear and electronic position vectors, $\mathbf{R}; \mathbf{r}$ denotes fixed $\mathbf{R}$ coordinates, and $E_0(\mathbf{R})$ is the electronic energy. Within the Born-Oppenheimer approximation, the time-dependent Schrödinger equation (TDSE) for the nuclear wave function $\chi_0 (\mathbf{R}, t)$ will take the form [24]

$$i\hbar \frac{\partial}{\partial t} \chi_0 (\mathbf{R}, t) = \left[\hat{T}_{\text{nuc}} + E_0 (\mathbf{R}) \right] \chi_0 (\mathbf{R}, t) . \tag{2.2}$$

When interacting with a molecule, a coherent laser pulse can be approximated as a spatially homogenous, time-dependent electric field $\boldsymbol{\varepsilon} (t)$, provided the carrier wavelength is large compared to the molecular dimensions. In this limit and using the semiclassical approximation, the interaction of the field with the electrons and nuclei within the electric-dipole approximation can be written as the following time-dependent contribution to the molecular Hamiltonian

$$\hat{H}_{\text{int}}(t) = -\boldsymbol{\mu} \cdot \boldsymbol{\varepsilon} (t) , \tag{2.3}$$

where $\boldsymbol{\mu}$ is the electric dipole moment:

$$\boldsymbol{\mu} = \sum_{j=1}^{N} q_i \mathbf{r}_i, \tag{2.4}$$

and where q_i and $\mathbf{r}_i$ denote the charge and position of the i^{th} particle in the system. When $\hat{H}_{\text{int}}$ is introduced into equation 2.1, the field-free potential energy surface $E_0(\mathbf{R})$ will become modified due to the interaction with $\boldsymbol{\varepsilon}(t)$. This modified energy surface, which will be called E_{int} (the notation will be simplified in the following steps by omitting functional dependencies on $\mathbf{R}$ and $\mathbf{r}$), can be expressed as

$$E_{\text{int}} = \langle \psi_0^{\varepsilon} | \hat{H}_e - \boldsymbol{\mu} \varepsilon(t) | \psi_0^{\varepsilon} \rangle, \tag{2.5}$$

where the $^{\varepsilon}$ superscript on ψ_0^{ε} indicates that the electronic wave function has been modified by the external field, and the integration is over the electronic coordinates $\mathbf{r}$. The subsequent analysis will be simplified by aligning the polarization direction of the external field with the molecular frame z axis, i.e. $\boldsymbol{\varepsilon}(t) = \varepsilon(t)\hat{z}$, and $\boldsymbol{\mu} = \mu_z$. Assuming that $\varepsilon(t)$ is sufficiently small, the modified potential energy surface $E_{\text{int}}(\mathbf{R})$ can be expressed as a second-order Taylor expansion around the unperturbed potential function $E_0(\mathbf{R})$

$$E_{\text{int}} \approx E_0 + \left.\frac{dE_{\text{int}}}{d\varepsilon(t)}\right|_{\varepsilon(t)=0} \times \varepsilon(t) + \frac{1}{2}\left.\frac{d^2 E_{\text{int}}}{d\varepsilon^2(t)}\right|_{\varepsilon(t)=0} \times \varepsilon^2(t). \tag{2.6}$$

To continue, the Hellmann-Feynman theorem [25] is invoked, which states that the derivative of the system energy with respect to some parameter λ is equivalent to the derivative of the Hamiltonian with respect to λ, i.e.

$$\frac{dE_\lambda}{d\lambda} = \int \Psi_\lambda^* \frac{d\hat{H}_\lambda}{d\lambda} \Psi_\lambda dV \tag{2.7}$$

Where V denotes a volume integral. Combining equations 2.7 and 2.5, it can be shown that differentiation of E_{int} with respect to $\varepsilon(t)$ yields

$$\frac{dE_{\text{int}}}{d\varepsilon(t)} = -\langle \mu_z \rangle. \tag{2.8}$$

Combining equations 2.6 and 2.8 leads to the relation

$$\langle \mu_z \rangle = -\left.\frac{dE_{\text{int}}}{d\varepsilon(t)}\right|_{\varepsilon(t)=0} - \left.\frac{d^2 E_{\text{int}}}{d\varepsilon^2(t)}\right|_{\varepsilon(t)=0} \times \varepsilon(t). \tag{2.9}$$

I will now show how to calculate $\left.\frac{dE_{\text{int}}}{d\varepsilon(t)}\right|_{\varepsilon(t)=0}$ and $\left.\frac{d^2 E_{\text{int}}}{d\varepsilon^2(t)}\right|_{\varepsilon(t)=0}$ using perturbation theory. First, note that $\langle \mu_z \rangle$ can be written as

$$\langle \mu_z \rangle = \langle \psi(t) | \mu_z | \psi(t) \rangle \tag{2.10}$$

where I have set $\psi(t) = \psi_0^{\mathcal{E}}$ to simplify the notation. Using the variation of constants method, the perturbed wavefunction $\psi(t)$ is expanded onto the unperturbed basis:

$$\begin{aligned}\psi(t) &= \psi_0^{(0)} + \sum_{n\neq 0} a_n(t)\,\psi_n^{(0)} \\ &= |0\rangle \exp\left(-i\frac{E_0^{(0)}t}{\hbar}\right) + \sum_{n\neq 0} a_n(t)\,|n\rangle \exp\left(-i\frac{E_n^{(0)}}{\hbar}t\right),\end{aligned} \tag{2.11}$$

where the $^{(0)}$ superscript denotes unperturbed wavefunctions/energies, and where it is assumed that $a_n(t) \ll 1$ and $a_0(t) \approx 1$. Combining equations 2.11 and 2.10:

$$\begin{aligned}\langle\mu_z\rangle = \langle 0|\mu_z|0\rangle &+ \sum_{n\neq 0} a_n^*(t)\,\langle n|\,\mu_z\,|0\rangle \exp(i\omega_{n0}t) \\ &+ \sum_{n\neq 0} a_n(t)\,\langle 0|\,\mu_z\,|n\rangle \exp(-i\omega_{n0}t) \\ &+ \sum_{n\neq 0}\sum_{m\neq 0} a_m^*(t)\,a_n(t)\,\langle m|\,\mu_z\,|n\rangle \exp(-i\omega_{nm}t),\end{aligned} \tag{2.12}$$

where $\omega_{nm} = \left(E_m^{(0)} - E_n^{(0)}\right)/\hbar$. The fourth term in equation 2.12 can be neglected since it contains a product of two very small coefficients, so we get

$$\begin{aligned}\langle\mu_z\rangle = \langle 0|\,\mu_z\,|0\rangle &+ \sum_{n\neq 0} a_n^*(t)\,\langle n|\,\mu_z\,|0\rangle \exp(i\omega_{n0}t) \\ &+ \sum_{n\neq 0} a_n(t)\,\langle 0|\,\mu_z\,|n\rangle \exp(-i\omega_{n0}t).\end{aligned} \tag{2.13}$$

The task at hand is now to determine the $a_n(t)$ coefficients. This can be accomplished using first order time-dependent perturbation theory. Start by again expanding $\psi(t)$ onto the unperturbed basis:

$$\begin{aligned}\psi(t) &= \sum_n a_n(t)\,|n\rangle \exp\left(-i\frac{E_n^{(0)}}{\hbar}t\right) \\ &= \sum_n a_n(t)\,\psi_n^{(0)}.\end{aligned} \tag{2.14}$$

Now consider the TDSE with a time-dependent Hamiltonian:

$$\hat{H}(t)\psi(t) = i\hbar\frac{\partial}{\partial t}\psi(t), \tag{2.15}$$

where $\hat{H}(t)$ can be split up into time-dependent and time-independent parts:

$$\hat{H}(t) = \hat{H}^{(0)} + \hat{H}^{(1)}(t). \tag{2.16}$$

Inserting the expanded form of $\psi(t)$ into the left and right sides of the TDSE yields:

$$\hat{H}(t)\psi = \sum_n a_n(t)\,\hat{H}^{(0)}\psi_n^{(0)}(t) + \sum_n a_n(t)\,\hat{H}^{(1)}(t)\,\psi_n^{(0)} \tag{2.17}$$

and

$$i\hbar\frac{\partial}{\partial t}\psi = \sum_n a_n(t)\,i\hbar\frac{\partial}{\partial t}\psi_n^{(0)}(t) + i\hbar\sum \dot{a}_n(t)\,\hat{H}^{(1)}(t)\,\psi_n^{(0)}. \tag{2.18}$$

The first terms on the right hand sides of the above expressions are equivalent, i.e.

$$\hat{H}^{(0)}\psi_n^{(0)}(t) = i\hbar\frac{\partial}{\partial t}\psi_n^{(0)}(t). \tag{2.19}$$

It is therefore easy to see that

$$\sum_n a_n(t)\,\hat{H}^{(1)}(t)\,\psi_n^{(0)} = i\hbar\sum \dot{a}_n(t)\,\psi_n^{(0)}, \tag{2.20}$$

or, using bra ket notation:

$$\sum_n a_n(t)\,\hat{H}^{(1)}(t)\,|n\rangle \exp\left(-i\frac{E_n^{(0)}}{\hbar}t\right) = i\hbar\sum \dot{a}_n(t)\,|n\rangle \exp\left(-i\frac{E_n^{(0)}}{\hbar}t\right). \tag{2.21}$$

Now, multiply through by $\langle k|$ from the left and note that $\langle n|\,m\rangle = \delta_{n,m}$:

$$\sum_n a_n(t)\,\langle k|\,\hat{H}^{(1)}(t)\,|n\rangle \exp\left(-i\frac{E_n^{(0)}}{\hbar}t\right) = i\hbar\dot{a}_k(t)\exp\left(-i\frac{E_k^{(0)}}{\hbar}t\right). \tag{2.22}$$

Rearranging the expression to isolate $\dot{a}_k(t)$ and integrating on both sides yields

$$a_k(t) - a_k(0) = -\frac{i}{\hbar}\sum_n \int_0^t a_n(t')\,\hat{H}_{kn}^{(1)}(t)\exp(i\omega_{kn}t')\,dt', \tag{2.23}$$

where the notation has been changed so t' is a dependent variable and t is the integration limit, and where $\hat{H}_{kn}^{(1)}(t') = \langle k|\,\hat{H}^{(1)}(t')\,|n\rangle$ and $\omega_{kn} = \left(E_k^{(0)} - E_n^{(0)}\right)/\hbar$. Solving this coupled system of linear equations is simplified by assuming that the perturbation is small, and therefore $a_0(t') \approx 1$ and $a_{n\neq 0}(t') \approx 0$. This results in the following:

$$a_n(t) = -\frac{i}{\hbar}\int_0^t \hat{H}_{n0}^{(1)}(t')\exp(i\omega_{kn}t')\,dt'. \tag{2.24}$$

Now, let $\varepsilon(t')$ be an oscillating function with amplitude ε_0 and carrier frequency ω_c, and an envelope function that is slowly turned on:

$$\begin{aligned}\varepsilon(t') &= 2\varepsilon_0\left[1 - \exp\left(-\frac{t'}{\tau}\right)\right]\cos(\omega_c t') \\ &= \varepsilon_0\left[1 - \exp\left(-\frac{t'}{\tau}\right)\right]\left[\exp(i\omega_c t') + \exp(-i\omega_c t')\right].\end{aligned} \tag{2.25}$$

The time-dependent part of the Hamiltonian in equation 2.24 becomes

$$\hat{H}_{n0}^{(1)}(t') = -\varepsilon_0 \langle n|\,\mu_z\,|0\rangle \left[1 - \exp\left(-\frac{t'}{\tau}\right)\right] \left[\exp\left(i\omega_c t'\right) + \exp\left(-i\omega_c t'\right)\right]. \quad (2.26)$$

Inserting this into equation 2.24 yields

$$\begin{aligned} a_n(t) &= \varepsilon_0 \frac{i}{\hbar} \langle n|\,\mu_z\,|0\rangle \int_0^t \left[1 - \exp\left(-\frac{t'}{\tau}\right)\right] \left[\exp\left(i\omega_c t'\right) + \exp\left(-i\omega_c t'\right)\right] \\ &\quad \times \exp\left(i\omega_{kn} t'\right) dt' \\ &= \frac{\varepsilon_0 \langle n|\,\mu\,|0\rangle}{\hbar} \left[\frac{\exp\left(i\left[\omega_{n0} + \omega_c\right]t\right) - 1}{\left[\omega_{n0} + \omega_c\right]} + \frac{\exp\left(i\left[\omega_{n0} - \omega_c\right]t\right) - 1}{\left[\omega_{n0} - \omega_c\right]}\right. \\ &\quad - \frac{\tau\left[\exp\left(i\left[\omega_{n0} + \omega_c\right]t\right)\exp\left(-\frac{t}{\tau}\right) - 1\right]}{\tau\left[\omega_{n0} + \omega_c\right] - 1} \\ &\quad \left. - \frac{\tau\left[\exp\left(i\left[\omega_{n0} - \omega_c\right]t\right)\exp\left(-\frac{t}{\tau}\right) - 1\right]}{\tau\left[\omega_{n0} - \omega_c\right] - 1}\right]. \end{aligned} \quad (2.27)$$

Inserting this expression into equation 2.13 and simplifying yields:

$$\begin{aligned} \langle \mu_z \rangle = \langle 0|\,\mu_z\,|0\rangle &+ \frac{2}{\hbar} \sum_{n\neq 0} \frac{\omega_{n0} \left|\langle n|\,\mu_z\,|0\rangle\right|^2}{\omega_{n0}^2 - \omega_c^2} 2\varepsilon_0 \left[1 - \frac{\Omega_\tau}{\Omega} \exp\left(-\frac{t}{\tau}\right)\right] \cos(\omega_c t) \\ &+ \frac{4\varepsilon_0}{\hbar} \sum_{n\neq 0} \frac{\omega_{n0} \left|\langle n|\,\mu_z\,|0\rangle\right|^2}{\omega_{n0}^2 - \omega_c^2} \left[\frac{\Omega_\tau}{\Omega} - 1\right] \cos(\omega_{n0} t), \end{aligned} \quad (2.28)$$

where

$$\Omega = \frac{\omega_{n0}}{\omega_{n0}^2 - \omega_c^2} \quad (2.29)$$

and

$$\Omega_\tau = \frac{\left(\omega_{n0} - \frac{1}{\tau}\right)}{\left(\omega_{n0} - \frac{1}{\tau}\right)^2 - \omega_c^2}. \quad (2.30)$$

Now, if $1/\tau \ll \omega_{n0}$, then the $1/\tau$ terms in the numerator and denominators of Ω_τ can be neglected (i.e. $\Omega_\tau/\Omega = 1$), and equation 2.28 will immediately reduce to

$$\langle \mu_z \rangle = \langle 0|\,\mu_z\,|0\rangle + \frac{2}{\hbar} \sum_{n\neq 0} \left|\langle n|\,\mu_z\,|0\rangle\right|^2 \frac{\omega_{n0}}{\omega_{n0}^2 - \omega_c^2} 2\varepsilon_0 \left[1 - \exp\left(-\frac{t}{\tau}\right)\right] \cos\left(\omega_c t\right), \quad (2.31)$$

or, since $\varepsilon(t) = 2\varepsilon_0\left[1 - \exp\left(-\frac{t}{\tau}\right)\right]\cos\left(\omega_c t\right)$:

$$\langle \mu_z \rangle = \langle 0|\,\mu_z\,|0\rangle + \frac{2}{\hbar} \sum_{n\neq 0} \frac{\omega_{n0} \left|\langle n|\,\mu\,|0\rangle\right|^2}{\omega_{n0}^2 - \omega_c^2} \varepsilon(t). \quad (2.32)$$

Assuming that $\omega_c \ll \omega_{n0}$, i.e. the field carrier frequency is much lower than the electronic state transition frequencies of the molecule, which is generally true as long as the nuclear motion is confined to the electronic ground state, equation 2.32 simplifies to

$$\langle \mu_z \rangle = \langle 0 | \mu_z | 0 \rangle + \frac{2}{\hbar} \sum_{n \neq 0} \frac{|\langle n | \mu_z | 0 \rangle|^2}{\omega_{n0}} \varepsilon(t) . \tag{2.33}$$

The first and second terms on the right hand side of equation 2.33 are the permanent electric dipole (PED) and static molecular polarizability (SMP) terms, respectively. The PED term is merely the charge distribution of the field-free molecule. If the field is relatively weak the molecular electrons will not be significantly perturbed and the PED term is sufficient to accurately describe the dynamics of the system. If the molecule is subjected to more intense fields, the ψ_0 electronic wave functions will be significantly modified, leading to a shift in the molecular charge distribution that the PED will not be able to account for. The SMP term is the first order correction to this field induced charge shift, and is therefore linearly proportional to the field amplitude $\varepsilon(t)$.

While equation 2.33 demonstrates how the PED and SMP terms may be calculated provided the electronic eigenfunctions are known, I will now disregard the exact form of these functions and instead focus on their relation to $\varepsilon(t)$. Equation 2.33 can thus be recast in a simplified form:

$$\langle \mu_z \rangle = \mu + \alpha \varepsilon(t) . \tag{2.34}$$

Comparing Eqs. 2.34, 2.9 and 2.6, it can be seen that

$$E_{\text{int}} = E_0 - \mu \varepsilon(t) - \frac{1}{2} \alpha \varepsilon^2(t) . \tag{2.35}$$

At this point, lets rewind a bit and look at the third term in equation 2.28 again:

$$\frac{4\varepsilon_0}{\hbar} \sum_{n \neq 0} \frac{\omega_{n0} |\langle n | \mu_z | 0 \rangle|^2}{\omega_{n0}^2 - \omega_c^2} \left[\frac{\Omega_\tau}{\Omega} - 1 \right] \cos(\omega_{n0} t) \tag{2.36}$$

Remember that τ can be interpreted as the timescale at which the field $\varepsilon(t)$ is switched on, i.e. if τ is very small it means that the field is switched on very quickly. In a situation where $1/\tau \sim \omega_{n0}$ it will hold that $\Omega_\tau/\Omega > 1$. In this regime equation 2.36 will be nonzero, meaning the second term in equation 2.28 will now contain one or more time-dependent terms oscillating at a frequency of ω_{n0}. Now, in terms of equation 2.35 this will manifest itself as the addition of a time-dependent term to the PED term μ. Physically, this can be interpreted

as the very sudden application of the field causing oscillations in the electronic density that will persist even after the field has been shut off. This is contrasted by the regime that we normally consider where $1/\tau \ll \omega_{n0}$. Here the application of the field still causes the electronic density to move around in the molecule (i.e. induce polarization as represented by the α term in equation 2.6), but the process happens adiabatically and therefore does not cause lasting electronic oscillations. Note that while an in-depth analysis of this phenomenon will not be forthcoming in this thesis, I found it an interesting enough detail to include in the hope that it may inspire future investigations.

Within the Born-Oppenheimer approximation, μ and α will be functions of $\mathbf{R}$ as they contain the electronic eigenfunctions $\psi_n(\mathbf{R};\mathbf{r})$, where the electronic coordinates have been integrated out in the matrix elements of equation 2.33. Returning to equation 2.2, the expression can now be updated to include the second order correction to the energy that arises due to coupling with the external field, reinstating the functional dependencies on $\mathbf{R}$ for completeness

$$i\hbar\frac{\partial}{\partial t}\chi_0(\mathbf{R},t) = \left[\hat{T}_{\text{nuc}} + E_0(\mathbf{R}) - \hat{C}_{\text{int}}(\mathbf{R},t)\right]\chi_0(\mathbf{R},t), \tag{2.37}$$

where

$$\hat{C}_{\text{int}}(\mathbf{R},t) = \mu(\mathbf{R})\,\varepsilon(t) + \frac{1}{2}\alpha(\mathbf{R})\,\varepsilon^2(t). \tag{2.38}$$

Equations 2.37 and 2.38 represent the general form of the molecular models that I will be making use of many places in this thesis. I leave the calculation of $E_0(\mathbf{R})$, $\mu(\mathbf{R})$, and $\alpha(\mathbf{R})$ to the computational chemists. My interests lay instead with understanding how to control the dynamics of a given system through its interaction with the $\varepsilon(t)$ term. A natural first approach to this task is to simplify the model as much as possible and see what we can learn. In this spirit, I will now show how equations 2.37 and 2.38 can be applied to derive analytical solutions to the dynamic response of a diatomic system to a perturbing field.

2.2 The Forced Harmonic Potential

In general, the expectation value of a given operator A is given by

$$\langle A\rangle = \int \Psi^* A \Psi d\tau, \tag{2.39}$$

assuming Ψ is normalized. The time derivative of $\langle A\rangle$ is then given by

$$\frac{d\langle A\rangle}{dt} = \left\langle \frac{d\Psi}{dt}\middle| A\Psi\right\rangle + \left\langle \Psi\middle|\frac{dA}{dt}\Psi\right\rangle + \left\langle \Psi\middle| A\frac{d\Psi}{dt}\right\rangle. \tag{2.40}$$

Using the the relations:

$$i\hbar\frac{d\Psi}{dt} = \hat{H}\Psi \tag{2.41}$$

$$i\hbar\frac{d\Psi^*}{dt} = -\hat{H}\Psi, \tag{2.42}$$

it is possible to write equation 2.40 as

$$\begin{aligned}\frac{d\langle A\rangle}{dt} &= \frac{1}{i\hbar}\left\langle -\hat{H}\Psi\middle|A\Psi\right\rangle + \frac{1}{i\hbar}\left\langle \Psi A\middle|\hat{H}\Psi\right\rangle + \left\langle \Psi\middle|\frac{dA}{dt}\Psi\right\rangle \\ &= \frac{1}{i\hbar}\left\langle \Psi\middle|\left[A,\hat{H}\right]\middle|\Psi\right\rangle + \left\langle \Psi\middle|\frac{dA}{dt}\Psi\right\rangle. \end{aligned} \tag{2.43}$$

If the A operator has no explicit time dependence, the above expression can be written as

$$\frac{d\langle A\rangle}{dt} = \frac{1}{i\hbar}\left\langle \Psi\middle|\left[A,\hat{H}\right]\middle|\Psi\right\rangle. \tag{2.44}$$

The above expression can be extended to the p (impulse) and x (spatial) operators for Hamiltonians of the form $\hat{H} = \frac{p^2}{2m} + V(x)$:

$$\begin{aligned}\frac{d\langle x\rangle}{dt} &= \frac{1}{i\hbar}\left\langle \Psi\middle|\left[x,\hat{H}\right]\middle|\Psi\right\rangle \\ &= \frac{\langle p\rangle}{m} \end{aligned} \tag{2.45}$$

$$\begin{aligned}\frac{d\langle p\rangle}{dt} &= \frac{1}{i\hbar}\left\langle \Psi\middle|\left[p,\hat{H}\right]\middle|\Psi\right\rangle \\ &= \left\langle -\frac{dV(x)}{dx}\right\rangle. \end{aligned} \tag{2.46}$$

Equations 2.45 and 2.46 are a formulation of Erhenfest's theorem [26]. Note that while these expressions may superficially resemble the classical equations of motion for a point particle, they are quantitatively different. This is due to the appearance of $\left\langle -\frac{dV(x)}{dx}\right\rangle$ in equation 2.46; to calculate this quantity we need to know what the wave function looks like, which means that in general the time evolution of quantum mechanical observables will not obey classical mechanics. However, by expanding $\frac{dV(x)}{dx}$ around $\langle x\rangle$, it can be shown that the time evolution of $\langle x\rangle$ and $\langle p\rangle$ will behave in a classical manner when the order of $V(x)$ is quadratic or less:

$$\left.\frac{dV(x)}{dx}\right|_{x=\langle x\rangle} \approx \frac{dV(\langle x\rangle)}{d\langle x\rangle} + \frac{d^2V(\langle x\rangle)}{d\langle x\rangle^2}\left(x-\langle x\rangle\right) + \frac{1}{2}\frac{d^3V(\langle x\rangle)}{d\langle x\rangle^3}\left(x-\langle x\rangle\right)^2. \tag{2.47}$$

Now, note that

$$\langle 1\rangle = 1, \tag{2.48}$$

and

$$\langle x - \langle x \rangle \rangle = \langle x \rangle - \langle x \rangle = 0, \tag{2.49}$$

and

$$\langle (x - \langle x \rangle)^2 \rangle = \sigma_x^2, \tag{2.50}$$

i.e. equation 2.48 states that the mean of a scalar is just the same scalar, equation 2.49 states that the mean of a distribution minus the distribution mean is equal to zero, and equation 2.50 is simply the definition of the distribution variance. Inserting equation 2.47 into equation 2.46 and applying these relations, we get

$$\frac{d\langle p \rangle}{dt} = -\frac{dV(\langle x \rangle)}{d\langle x \rangle} - \frac{\sigma_x^2}{2}\frac{d^3V(\langle x \rangle)}{d\langle x \rangle^3}. \tag{2.51}$$

Now, note that the second term in equation 2.51 will evaluate to 0 whenever the order of $V(x)$ is quadratic or less. When this is the case, the coupled differential equations governing the time evolution of $\langle p \rangle$ and $\langle x \rangle$ become

$$\frac{d\langle x \rangle}{dt} = \frac{\langle p \rangle}{m} \tag{2.52}$$

$$\frac{d\langle p \rangle}{dt} = -\frac{dV(\langle x \rangle)}{d\langle x \rangle}, \tag{2.53}$$

which are identical to the classical equations of motion for a point particle with momentum p and position x. Now, consider a case where the potential function $V(x)$ is a linearly forced harmonic oscillator being driven by a time-dependent function $f(t)$, i.e.

$$V(x,t) = \frac{1}{2}m\omega^2 x^2 - \beta x f(t), \tag{2.54}$$

where β is a constant and the t in $V(x,t)$ indicates that the potential function is now time-dependent. Using Ehrenfest's theorem and noting that the order of equation 2.54 is quadratic, the equations of motion governing the time-evolution of the expected position $\langle x \rangle$ and momentum $\langle p \rangle$ of a quantum wave packet propagating in $V(x,t)$ are given by

$$\frac{d\langle x \rangle_t}{dt} = \frac{\langle p \rangle_t}{m} \tag{2.55}$$

$$\frac{d\langle p \rangle_t}{dt} = -m\omega\langle x \rangle_t + \beta f(t), \tag{2.56}$$

where the $_t$ subscript has been added to remind us that these quantities are time-dependent. These equations can combined and rewritten into a second order linear non-homogeneous differential equation:

$$\frac{d^2\langle x \rangle_t}{dt^2} + \omega^2 \langle x \rangle_t = \frac{\beta}{m} f(t). \tag{2.57}$$

First, we find the solution to the homogenous version of equation 2.57,

$$\frac{d^2 \langle x \rangle_t}{dt^2} + \omega^2 \langle x \rangle_t = 0, \tag{2.58}$$

is given by

$$\begin{aligned} \langle x \rangle_t &= c_1 \exp(i\omega t) + c_2 \exp(-i\omega t) \\ &= y_1 + y_2. \end{aligned} \tag{2.59}$$

Using the variation of parameters method, it can be shown that the solution to the non-homogenous case is given by

$$\langle x \rangle_t = -y_1 \int_{t_1}^{t_2} \frac{y_2}{\dot{y}_1 y_2 - \dot{y}_2 y_1} dt + y_2 \int_{t_1}^{t_2} \frac{y_1}{\dot{y}_1 y_2 - \dot{y}_2 y_1} dt. \tag{2.60}$$

Inserting the homogeneous solutions from equation 2.59 into equation 2.60 and simplifying yields

$$\langle x \rangle_t = \frac{\beta}{\omega m} \left[\sin(\omega t) \int_{t_1}^{t_2} \cos(\omega t) f(t) dt - \cos(\omega t) \int_{t_1}^{t_2} \sin(\omega t) f(t) dt \right]. \tag{2.61}$$

Equation 2.61 can be used to obtain analytical solutions to the dynamic behaviour of a quantum mechanical wave packet. In the next section, I will describe how I used this as a jumping-off point for the results obtained in my first publication.

2.3 Summary: *Non-Resonant Dynamic Stark Control of Vibrational Motion with Optimized Laser Pulses*

As stated, my published paper in appendix A uses the equations derived in sections 2.1 and 2.2 of this thesis to calculate analytical expressions for the vibrational dynamics of a diatomic molecule that is aligned with the polarization axis of a time-dependent laser field $\varepsilon(t)$. Specifically, I combined equations 2.37 and 2.38 with equation 2.61 by approximating the unperturbed ground state energy surface of the molecule $E_0(R)$ as a harmonic expansion around the equilibrium bond distance R_{eq}:

$$E_0(R)|_{R=R_{\text{eq}}} \approx \frac{1}{2} m \omega_0^2 R^2. \tag{2.62}$$

Where I define $R_{\mathrm{eq}} \coloneqq 0$ for simplicity. Likewise, $\mu(R)$ and $\alpha(R)$ are approximated as linear expansions around R_{eq}, i.e.

$$\begin{aligned}\hat{C}_{\mathrm{int}}(R,t)\Big|_{R=R_{\mathrm{eq}}} &\approx \left[\left.\frac{d\mu(R)}{dR}\right|_{R=R_{\mathrm{eq}}} \times \varepsilon(t) + \frac{1}{2}\left.\frac{d\alpha(R)}{dR}\right|_{R=R_{\mathrm{eq}}} \times \varepsilon^2(t)\right] R \\ &= \left[\mu'\varepsilon(t) + \frac{1}{2}\alpha'\varepsilon^2(t)\right] R. \end{aligned} \tag{2.63}$$

Using these approximations, and noting that the total order of the potential is quadratic and therefore the time-evolution of wave packet position will follow classical dynamics (i.e. $\langle R \rangle(t) \equiv R(t)$), the expectation value of the bond length as a function of time is given by

$$\begin{aligned} R(t) = \frac{\mu'}{\omega_0 m}&\left[\sin(\omega_0 t)\int_{t_1}^{t_2}\cos(\omega_0 t)\varepsilon(t)dt - \cos(\omega_0 t)\int_{t_1}^{t_2}\sin(\omega_0 t)\varepsilon(t)dt\right] \\ + \frac{\alpha'}{2\omega_0 m}&\left[\sin(\omega_0 t)\int_{t_1}^{t_2}\cos(\omega_0 t)\varepsilon^2(t)dt - \cos(\omega_0 t)\int_{t_1}^{t_2}\sin(\omega_0 t)\varepsilon^2(t)dt\right]. \end{aligned} \tag{2.64}$$

This key result is then used to derive a number of properties. In particular, I show that when the carrier frequency of a pulse ω_c is much higher than the system eigenfrequency ω_0, the amplitude of the vibrational response will be entirely related to the shape of pulse envelope and completely independent of the carrier frequency of the laser pulse (see, e.g., equations 21, 22, and 23, as well as figure 1 in appendix A). This is the behavior that characterizes a central concept in my PhD work; namely the nonresonant dynamic Stark effect. In the dynamic Stark regime, the contribution from the permanent electric dipole term in equation 2.38 is completely neglected and the interaction term becomes

$$\hat{C}_{\mathrm{int}}\left(\mathbf{R},t\right) = -R\frac{1}{4}\alpha' E_{\mathrm{env}}^2(t), \tag{2.65}$$

where $E_{\mathrm{env}}(t)$ denotes the pulse envelope. I use the analytical results in the dynamic Stark regime to show that when the pulse envelope shape is a variable width Gaussian with a constant peak intensity, the optimal pulse width (i.e. the pulse width that will maximize the amplitude of the wave packet oscillations) is related to the oscillation period of the system $T = 2\pi/\omega_0$ by

$$\sigma_{\mathrm{optimum}} = \frac{T}{\pi\sqrt{2}}, \tag{2.66}$$

Equation 2.64 is also solved for the case where the molecule is driven by a nonresonant train of N Gaussian pulses with spacing τ. Note that it has come to my attention that there is a minor error in the general solution to this problem given by equation 30 in appendix A, due to the fact that the overlap between adjacent pulses will lead to cross terms in the expression for $E_{\mathrm{env}}^2(t)$. For this

reason, it should be understood that the given solution will only hold when the edges of the pulses do not significantly overlap with each other. Minor errors notwithstanding, the results here demonstrate that dynamic Stark control may be accomplished using "pseudo-frequencies" generated via pulse trains with spacings tuned to the vibrational period of specific molecular modes.

In the next part of the paper, I show how the expression in equation 2.64 can be expressed in the spectral domain when E_{env} is a square integrable function, i.e.

$$\int_{-\infty}^{\infty} \left|E_{\text{env}}(t)\right|^2 dt < \infty. \tag{2.67}$$

I will now show the derivation of this expression. As stated in the paper, assuming conditions where the dynamic Stark effect dominates and the system response is independent of the pulse carrier frequency, and given a generalized, square-integrable pulse envelope function $E_{\text{env}}(t)$, the amplitude Γ of the wave packet when $t \to \infty$ can be written as

$$\Gamma = \frac{\alpha'}{4\omega_0 m}\left(\left[\int_{-\infty}^{\infty}\cos(\omega_0 t)E_{\text{env}}^2(t)dt\right]^2 + \left[\int_{-\infty}^{\infty}\sin(\omega_0 t)E_{\text{env}}^2(t)dt\right]^2\right)^{1/2}. \tag{2.68}$$

Now, rewrite the first integrand:

$$\begin{aligned}\int_{-\infty}^{\infty}\cos(\omega_0 t)E_{\text{env}}^2(t)dt &= \frac{1}{2}\int_{-\infty}^{\infty}\exp(i\omega_0 t)E_{\text{env}}^2\,(t)\,dt \\ &\quad + \frac{1}{2}\int_{-\infty}^{\infty}\exp(-i\omega_0 t)E_{\text{env}}^2\,(t)\,dt \\ &= \frac{1}{2}\int_{-\infty}^{\infty}\left[E_{\text{env}}(t)\right]\left[E_{\text{env}}^*(t)\exp(-i\omega_0 t)\right]^* dt \\ &\quad + \frac{1}{2}\int_{-\infty}^{\infty}\left[E_{\text{env}}(t)\right]\left[E_{\text{env}}^*(t)\exp(i\omega_0 t)\right]^* dt. \end{aligned}\tag{2.69}$$

Next, make use of Parseval's theorem [27], which states that for any set of square integrable functions $F(t)$ and $G(t)$, it holds that

$$\int_{-\infty}^{\infty}F(t)\left[G(t)\right]^* dt = \frac{1}{2\pi}\int_{-\infty}^{\infty}\tilde{F}(\omega)\left[\tilde{G}(\omega)\right]^* d\omega. \tag{2.70}$$

Using this relation, equation 2.69 can be rewritten as

$$\frac{1}{4\pi}\int_{-\infty}^{\infty}\tilde{E}_{\text{env}}(\omega)\tilde{E}_{\text{env}}^*(\omega-\omega_0)d\omega + \frac{1}{4\pi}\int_{-\infty}^{\infty}\tilde{E}_{\text{env}}(\omega)\tilde{E}_{\text{env}}^*(\omega+\omega_0)d\omega, \tag{2.71}$$

and likewise performing the same procedure on the second integrand in equation 2.69 yields

$$\frac{i}{4\pi}\int_{-\infty}^{\infty}\tilde{E}_{\text{env}}(\omega)\tilde{E}_{\text{env}}^*(\omega+\omega_0)d\omega - \frac{i}{4\pi}\int_{-\infty}^{\infty}\tilde{E}_{\text{env}}(\omega)\tilde{E}_{\text{env}}^*(\omega-\omega_0)d\omega. \tag{2.72}$$

Finally, inserting equations 2.71 and 2.72 into equation 2.69 and simplifying leaves us with equation 34 from the paper:

$$\frac{\alpha'}{8\omega_0 m\pi}\left(\left[\int_{-\infty}^{\infty}\tilde{E}_{\mathrm{env}}(\omega)\tilde{E}^*_{\mathrm{env}}(\omega+\omega_0)d\omega\right]\left[\int_{-\infty}^{\infty}\tilde{E}_{\mathrm{env}}(\omega)\tilde{E}^*_{\mathrm{env}}(\omega-\omega_0)d\omega\right]\right)^{1/2}. \tag{2.73}$$

In the next part of the paper, equation 2.73 is used to generate insight into how the underlying excitation mechanism associated with the dynamic Stark effect can be interpreted as a two step Stokes-Raman scattering event to and from a higher lying virtual state. Furthermore, we show how the intuition generated by this spectral interpretation can be exploited to manipulate the spectral pulse phase and generate so-called "dark pulses", i.e. pulses with envelope shapes designed to make Raman transitions impossible within our model system of the linearly forced harmonic oscillator. In the next section of this chapter we will use this result to further investigate the characteristics of optimal nonresonant pulse spectra, and in chapter 3 we will make use of this result again to demonstrate how to design a spectral phase chirp function that allows us to selectively control ro-vibrational excitations.

2.4 Optimizing A Pulse Spectrum

In this section I will go over a result I obtained that was not deemed significant or relevant enough to warrant publication. This includes a relatively long derivation, so any reader that is not inclined to wade through such an analysis is welcome to skip ahead to the next chapter; doing so will not impact the overall continuity of the thesis presentation.

As stated in the previous section, in my paper in appendix A I perform an analysis where the optimal width of a Gaussian pulse envelope interacting with the harmonic system in the non-resonant limit is calculated, assuming that the intensity of the pulse is kept constant. Here, I attempt to take this analysis a step further by investigating what the optimal (i.e. greatest induced amplitude per pulse energy unit) pulse will look like if I allow it to assume *any* shape, given a constrained bandwidth (it is trivial to show that the optimal shape given *no* bandwidth constraints will be a delta function). In the subsequent analysis I will first prove some general statements about these types of optimal pulse envelopes, after which I will use a combination of variational calculus and numerical methods to derive expressions for the optimal pulse spectra.

2.4.1 Optimal pulse symmetry requirements

Let $E_{\text{env}}(t)$ be a square-integrable function representing a pulse envelope with finite energy. Now, let $E_{\text{env}}(t+\delta)$ represent the same pulse envelope, where the shape has been time-shifted forwards or backwards in time by δ. Using equation (18) from appendix A (and ignoring the constant prefactor to simplify the notation), the dynamic response of the wave packet position to a non resonant pulse with $E_{\text{env}}(t+\delta)$ is given by

$$\begin{aligned} R(t,\delta) &= \sin(\omega_0 t)\int_{-\infty}^{t}\cos(\omega_0 t')\,E_{\text{env}}^2(t'+\delta)\,dt' \\ &\quad + \cos(\omega_0 t)\int_{-\infty}^{t}\sin(\omega_0 t')\,E_{\text{env}}^2(t'+\delta)\,dt' \\ &= \sin(\omega_0 t)\,I_1(t,\delta) + \cos(\omega_0 t)\,I_2(t,\delta). \end{aligned} \tag{2.74}$$

In the $t \gg 1$ limit, where it is assumed that $E_{\text{env}}(t+\delta)$ has died out completely, the trajectory $R(t,\delta)$ corresponds to simple harmonic motion since the two integrands in equation 2.74 will be constant as a function of t:

$$R(t,\delta)\,|_{t\gg 1} = \Gamma\cos(\omega_0 t+\theta), \tag{2.75}$$

where the amplitude of the oscillations Γ is given by

$$\Gamma = \sqrt{I_1^2(\infty,\delta) + I_2^2(\infty,\delta)}, \tag{2.76}$$

and the phase θ is given by

$$\theta = \arctan\left(-\frac{I_1(\infty,\delta)}{I_2(\infty,\delta)}\right). \tag{2.77}$$

Note that varying δ and translating the location of $E_{\text{env}}(t+\delta)$ forwards or backwards in time will not have any impact on Γ as long as we look at the wave packet in the $t \gg 1$ limit, i.e.

$$\sqrt{I_1^2(\infty,\delta_1) + I_2^2(\infty,\delta_1)} = \sqrt{I_1^2(\infty,\delta_2) + I_2^2(\infty,\delta_2)}, \tag{2.78}$$

when $\delta_1 \neq \delta_2$. However, varying δ can clearly cause the value of θ to change, since this will also translate the trajectory representing the harmonic motion of the wave packet in the $t \gg 1$ limit forwards or backwards in time. Furthermore, it is easy to see how this means that we can get θ to assume *any* value between 0 and 2π by simply varying δ. This is important because it means that for *any* given pulse shape $E_{\text{env}}(t+\delta)$ it is always possible to choose a δ that leads to one of the integrals in equation 2.74 becoming 0 in the $t \gg 1$ limit (for example, if $E_{\text{env}}(t+\delta)$ is a symmetrical function, setting $\delta = 0$ will lead to the second

integrand I_2 becoming 0 in the $t \gg 1$ limit since $\sin(\omega_0 t)$ is an odd function). Using this information, the wave packet ampltitude at $t = \infty$ can be expressed in a slightly simpler way:

$$\Gamma = \int_{-\infty}^{\infty} \cos(\omega_0 t') E_{\text{env}}^2(t' + \delta)\, dt', \tag{2.79}$$

where it is assumed that the temporal shift δ of the (arbitrary) pulse envelope shape $E_{\text{env}}(t + \delta)$ has been chosen in a way that cancels the second integrand in equation 2.74. Note that in our following analysis we generally won't need to know what value of δ will satisfy this condition; I am simply stating that *some* δ always exists that allows us to use equation 2.79 to calculate the wave packet amplitude in the $t \gg 1$ limit.

Now, let $E_{\text{env}}^{\text{opt}}(t)$ be an optimal pulse envelope shape designed to maximize non-resonant transitions, given some sort of constraints. The fact that we can always calculate the wave packet amplitude using equation 2.79 can be used to argue that a necessary, but not sufficient, condition of pulse optimality is that $E_{\text{env}}^{\text{opt}}(t)$ should be symmetrical in time (assuming, of course, that the constraints allow this to be possible). The argument is as follows: The symmetry of the $\cos(\omega_0 t)$ function in equation 2.79 means that if $E_{\text{env}}^{\text{opt}}(t)$ is optimal in the interval between 0 and ∞, then it must hold that

$$E_{\text{env}}^{\text{opt}}(-t) = E_{\text{env}}^{\text{opt}}(t), \tag{2.80}$$

Note that I have not said anything about the carrier frequency of the pulse, as in the non-resonant limit this parameter does not play a roll in system excitations. This proves that the optimal pulse shape for nonresonant transitions $E_{\text{env}}^{\text{opt}}(t)$ is a real, even function around $t = 0$. It can be shown that the Fourier transform of a real and even function will also be a real and even function, which means that the spectral distribution of $E_{\text{env}}^{\text{opt}}(t)$ will be real and even as well, i.e.

$$\begin{aligned} \tilde{E}_{\text{env}}^{\text{opt}}(\omega) &= \tilde{E}_{\text{env}}^{\text{opt}}(-\omega) \\ \tilde{E}_{\text{env}}^{\text{opt}}(\omega) &= \text{Re}\left\{\tilde{E}_{\text{env}}^{\text{opt}}(\omega)\right\}. \end{aligned} \tag{2.81}$$

For this reason, the wave packet amplitude given by equation 2.79 can be rewritten in the spectral domain for $\tilde{E}_{\text{env}}^{\text{opt}}(\omega)$ using equation (34) from ref. [28] as:

$$\Gamma = \int_{-\infty}^{\infty} \tilde{E}_{\text{env}}^{\text{opt}}\left(\omega + \frac{\omega_0}{2}\right) \tilde{E}_{\text{env}}^{\text{opt}}\left(\omega - \frac{\omega_0}{2}\right) d\omega, \tag{2.82}$$

where I have once again omitted the constant prefactor for simplicity. Now, let's assume that $\tilde{E}_{\text{env}}^{\text{opt}}(\omega)$ contains a finite amount of energy, and a bandwidth that lies between ω_a and ω_b. I will now attempt to answer the question of how to distribute the energy in $\tilde{E}_{\text{env}}^{\text{opt}}(\omega)$ within the interval running from ω_a to ω_b in a way that maximizes the non-resonant excitations in a system with transition frequency ω_0.

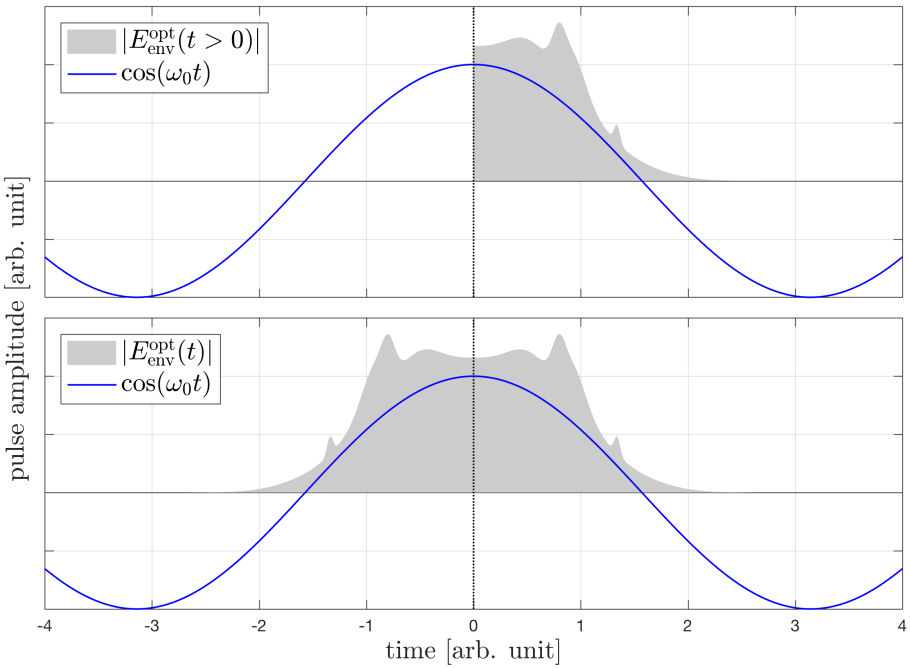

Figure 2.1: Visual representation of the argument that when $E_{\mathrm{env}}^{\mathrm{opt}}(t)$ is optimal in the region from 0 to ∞, it is necessarily so that the shape of $E_{\mathrm{env}}^{\mathrm{opt}}(t)$ from $-\infty$ to 0 will be a reflection of the shape in the positive domain because the integral in equation 2.79 contains a multiplication of $\cos(\omega_0 t)$ times $E_{\mathrm{env}}^{\mathrm{opt}}(t)$, and $\cos(\omega_0 t)$ is an even function.

2.4.2 Applying the calculus of variations

I will show how this question can be partially answered using the calculus of variations and functional optimization. For clarity of notation, the following substitutions will be used in the subsequent derivations:

$$\omega = x, \qquad \tilde{E}_{\text{env}}^{\text{opt}}(\omega) = f(x), \qquad \omega_0 = \Delta, \qquad \omega_a = a, \qquad \omega_b = b, \tag{2.83}$$

i.e. equation 2.82 becomes

$$\Gamma = \int_{-\infty}^{\infty} f\left(x + \frac{\Delta}{2}\right) f\left(x - \frac{\Delta}{2}\right) dx \tag{2.84}$$

To proceed, note that the bandwidth constaints mean that $f(x)$ is zero everywhere except between a and b. This means that the limits in equation 2.84 can be rewritten as

$$\Gamma = \int_{a+\Delta/2}^{b-\Delta/2} f\left(x + \frac{\Delta}{2}\right) f\left(x - \frac{\Delta}{2}\right) dx. \tag{2.85}$$

The energy constraints mean that we would like to determine the form of $f(x)$ that will maximize the integral in equation 2.85 while keeping the total energy, defined by $\int_a^b f(x)^2\, dx$, constant. For this reason, the functional $J(f)$ to be optimized can be written as

$$J(f) = \frac{\int_{a+\Delta/2}^{b-\Delta/2} f\left(x + \frac{\Delta}{2}\right) f\left(x - \frac{\Delta}{2}\right) dx}{\int_a^b f(x)^2\, dx}, \tag{2.86}$$

where dividing by the energy in the denominator effectively normalizes the expression (otherwise the optimal $f(x)$ would clearly be infinity everywhere between a and b) The question is now how to determine the form of $f(x)$ that will maximize the functional given by equation 2.86. I start by assuming $f(x)$ is a smooth, differentiable function and that Δ is small compared to the interval between a and b. This allows us to expand $f\left(x + \frac{\Delta}{2}\right) f\left(x - \frac{\Delta}{2}\right)$ to second order in Δ:

$$f\left(x + \frac{\Delta}{2}\right) f\left(x - \frac{\Delta}{2}\right) \approx f(x)^2 - \frac{1}{4}\Delta^2 \dot{f}(x)^2 + \frac{1}{4}\Delta^2 f(x)\, \ddot{f}(x). \tag{2.87}$$

Combining equations 2.87 and 2.86, we get

$$J\left(f, \dot{f}, \ddot{f}\right) = \frac{\int_{a+\Delta/2}^{b-\Delta/2} F(x)\, dx}{\int_a^b f(x)^2\, dx}, \tag{2.88}$$

where $F(x) = f(x)^2 - \frac{1}{4}\Delta^2 \dot{f}(x)^2 + \frac{1}{4}\Delta^2 f(x)\,\ddot{f}(x)$. To proceed, we need to rework the limits in the numerator so they are the same as the denominator. Start by rearranging the expression as follows:

$$\int_{a+\Delta/2}^{b-\Delta/2} F(x)\,dx = \int_a^b F(x)\,dx - \int_a^{a+\Delta/2} F(x)\,dx - \int_{b-\Delta/2}^b F(x)\,dx. \quad (2.89)$$

Now, note that $F(x)$ can be expanded around an arbitrary point at $x = \gamma$ to second order:

$$F(t)\,|_{x=\gamma} \approx F(\gamma) + (x-\gamma)\,\dot{F}(\gamma) + (x-\gamma)^2\,\frac{1}{2}\ddot{F}(\gamma), \quad (2.90)$$

where

$$F(\gamma) = f(\gamma)^2 + \frac{1}{4}\Delta^2\left[f(\gamma)\,\ddot{f}(\gamma) - \dot{f}(\gamma)^2\right] \quad (2.91)$$

$$\dot{F}(\gamma) = 2f(\gamma)\,\dot{f}(\gamma) + \frac{1}{4}\Delta^2\left[f(\gamma)\,f^{(3)}(\gamma) - \dot{f}(\gamma)\,\ddot{f}(\gamma)\right] \quad (2.92)$$

$$\ddot{F}(\gamma) = 2\left[f(\gamma)\,\ddot{f}(\gamma) + \dot{f}(\gamma)^2\right] + \frac{1}{2}\Delta^2\left[\frac{1}{2}f(\gamma)\,f^{(4)}(\gamma) - \frac{1}{2}\ddot{f}(\gamma)^2\right]. \quad (2.93)$$

We can use this approach to evaluate the last two integrals in equation 2.89 by expanding $F(x)$ around $x = a$ and $x = b$, i.e.

$$\begin{aligned}\int_a^{a+\Delta/2} F(x)\,dx &\approx \int_a^{a+\Delta/2}\left[F(a) + (x-a)\,\dot{F}(a) + (x-a)^2\,\frac{1}{2}\ddot{F}(a)\right]dx \\ &= \frac{\Delta}{2}F(a) + \frac{\Delta^2}{8}\dot{F}(a) + \frac{\Delta^3}{48}\ddot{F}(a) \end{aligned} \quad (2.94)$$

and

$$\begin{aligned}\int_{b-\Delta/2}^b F(x)\,dx &\approx \int_{b-\Delta/2}^b\left[F(b) + (x-b)\,\dot{F}(b) + (x-b)^2\,\frac{1}{2}\ddot{F}(b)\right]dx \\ &= \frac{\Delta}{2}F(b) - \frac{\Delta^2}{8}\dot{F}(b) + \frac{\Delta^3}{48}\ddot{F}(b). \end{aligned} \quad (2.95)$$

Now, inserting equations 2.91, 2.92, and 2.93, and removing all terms involving Δ^k when $k > 2$ yields

$$\frac{\Delta}{2}F(a) + \frac{\Delta^2}{8}\dot{F}(a) + \frac{\Delta^3}{48}\ddot{F}(a) \approx \frac{\Delta}{2}f(a)^2 + \frac{\Delta^2}{4}f(a)\,\dot{f}(a) \quad (2.96)$$

and

$$\frac{\Delta}{2}F(b) - \frac{\Delta^2}{8}\dot{F}(b) + \frac{\Delta^3}{48}\ddot{F}(b) \approx \frac{\Delta}{2}f(b)^2 - \frac{\Delta^2}{4}f(b)\,\dot{f}(b). \quad (2.97)$$

These quantities can be expressed inside the $\int_a^b$ integral limits using Dirac delta functions:

$$\frac{\Delta}{2} f(a)^2 + \frac{\Delta^2}{4} f(a)\,\dot{f}(a) = \int_a^b \left[\frac{1}{2}\Delta f(x)^2 + \frac{1}{4}\Delta^2 f(x)\,\dot{f}(x)\right]\delta(x-a)\,dx$$
$$= \int_a^b I_a(x)\,dx \tag{2.98}$$

$$\frac{\Delta}{2} f(b)^2 - \frac{\Delta^2}{4} f(b)\,\dot{f}(b) = \int_a^b \left[\frac{1}{2}\Delta f(x)^2 - \frac{1}{4}\Delta^2 f(x)\,\dot{f}(x)\right]\delta(x-b)\,dx$$
$$= \int_a^b I_b(x)\,dx. \tag{2.99}$$

Now, combining equations 2.98, 2.99, 2.94, 2.95 and 2.89, we have

$$\int_{a+\Delta/2}^{b-\Delta/2} F(x)\,dx = \int_a^b F(x)\,dx - \int_a^b I_a(x)\,dx - \int_a^b I_b(x)\,dx$$
$$= \int_a^b \left[F(x) - I_a(x) - I_b(x)\right]dx, \tag{2.100}$$

and the functional in equation 2.88 can be written as

$$J\left(f,\dot{f},\ddot{f},x\right) = \frac{\int_a^b \left[F(x) - I_a(x) - I_b(x)\right]dx}{\int_a^b f(x)^2\,dx}, \tag{2.101}$$

or, inserting the explicit forms of $F(x)$, $I_a(x)$ and $I_b(x)$:

$$J\left(f,\dot{f},\ddot{f},x\right) = 1 + \frac{\Delta^2}{4\int_a^b f(x)^2\,dx}\int_a^b \Bigg(f(x)\,\ddot{f}(x) - \dot{f}(x)^2$$
$$- \left[\frac{2}{\Delta} f(x)^2 + f(x)\,\dot{f}(x)\right]\delta(x-a)$$
$$- \left[\frac{2}{\Delta} f(x)^2 - f(x)\,\dot{f}(x)\right]\delta(x-b)\Bigg)dx. \tag{2.102}$$

Now that we have reworked the limits so they are the same in the numerator and denominator of the functional, we can apply the calculus of variations to find the form of $f(x)$ that maximizes $J\left(f,\dot{f},\ddot{f},x\right)$. Start by replacing $f(x)$ with $g_\varepsilon(x) = f(x) + \varepsilon\eta(x)$, where ε is small and $\eta(x)$ is an arbitrary differentiable function satisfying $\eta(a) = \eta(b) = 0$. We get

$$J_\varepsilon\left(f,\dot{f},\ddot{f},x,\varepsilon\right) = 1 + \frac{\Delta^2}{4}\frac{A_\varepsilon}{B_\varepsilon}, \tag{2.103}$$

where

$$B_\varepsilon = \int_a^b g_\varepsilon(x)^2\, dx \tag{2.104}$$

and

$$A_\varepsilon = \int_a^b \Bigg(\left[g_\varepsilon(x)\, \ddot{g}_\varepsilon(x) - \dot{g}_\varepsilon(x)^2 \right] - \left[\frac{2}{\Delta} g_\varepsilon(x)^2 + g_\varepsilon(x)\, \dot{g}_\varepsilon(x) \right] \delta(x-a) - \left[\frac{2}{\Delta} g_\varepsilon(x)^2 - g_\varepsilon(x)\, \dot{g}_\varepsilon(x) \right] \delta(x-b) \Bigg) dx. \tag{2.105}$$

Differentiating J_ε with respect to ε yields

$$\frac{dJ_\varepsilon}{d\varepsilon} = \frac{\Delta^2}{4B_\varepsilon^2} \left(B_\varepsilon \frac{dA_\varepsilon}{d\varepsilon} - A_\varepsilon \frac{dB_\varepsilon}{d\varepsilon} \right), \tag{2.106}$$

so at a stationary point in the functional it must hold that

$$B_\varepsilon \frac{dA_\varepsilon}{d\varepsilon} - A_\varepsilon \frac{dB_\varepsilon}{d\varepsilon} = 0. \tag{2.107}$$

The task is now to find an explicit form of the function in equation 2.107. Applying the chain rule to $\frac{d}{d\varepsilon}$ yields

$$\begin{aligned} \frac{d}{d\varepsilon} &= \frac{dt}{d\varepsilon}\frac{\partial}{\partial t} + \frac{dg_\varepsilon}{d\varepsilon}\frac{\partial}{\partial g_\varepsilon} + \frac{d\dot{g}_\varepsilon}{d\varepsilon}\frac{\partial}{\partial \dot{g}_\varepsilon} + \frac{d\ddot{g}_\varepsilon}{d\varepsilon}\frac{\partial}{\partial \ddot{g}_\varepsilon} \\ &= 0 + \eta(x)\frac{\partial}{\partial g_\varepsilon} + \dot{\eta}(x)\frac{\partial}{\partial \dot{g}_\varepsilon} + \ddot{\eta}(x)\frac{\partial}{\partial \ddot{g}_\varepsilon}. \end{aligned} \tag{2.108}$$

Now, applying equation 2.108 to equations 2.104 and 2.105 yields

$$\frac{dB_\varepsilon}{d\varepsilon} = 2\int_a^b g_\varepsilon(x)\, \eta(x)\, dx \tag{2.109}$$

and

$$\begin{aligned} \frac{dA_\varepsilon}{d\varepsilon} = \int_a^b \Bigg[\Bigg(& \ddot{g}_\varepsilon(x) - \delta(x-a)\left[\frac{4}{\Delta} g_\varepsilon(x) + \dot{g}_\varepsilon(x) \right] \\ & - \delta(x-b)\left[\frac{4}{\Delta} g_\varepsilon(x) - \dot{g}_\varepsilon(x) \right] \Bigg) \eta(x) \\ & + \left[g_\varepsilon(x)\, \delta(x-b) - 2\dot{g}_\varepsilon(x) - g_\varepsilon(x)\, \delta(x-a) \right] \dot{\eta}(x) + g_\varepsilon(x)\, \ddot{\eta}(x) \Bigg] dx. \end{aligned} \tag{2.110}$$

Now that we have an expression for $\frac{d}{d\varepsilon}A_\varepsilon$, and $\frac{d}{d\varepsilon}B_\varepsilon$, proceed by setting $\varepsilon = 0$ and combining equations 2.104, 2.105, 2.109, 2.110, and 2.107. We get

$$B_\varepsilon \frac{dA_\varepsilon}{d\varepsilon} - A_\varepsilon \frac{dB_\varepsilon}{d\varepsilon} = \int_a^b \left[F_0(x)\eta(x) + F_1(x)\dot{\eta}(x) + F_2(x)\ddot{\eta}(x)\right] dx, \quad (2.111)$$

where

$$F_0(x) = 2\left(C_a + C_b - C_2\right) f(x) + C_1 \ddot{f}(x) - \frac{4}{\Delta} C_1 f(x)\,\delta(x-a) - C_1 \dot{f}(x)\,\delta(x-a) - \frac{4}{\Delta} C_1 f(x)\,\delta(x-b) + C_1 \dot{f}(x)\,\delta(x-b) \quad (2.112)$$

$$F_1(x) = -2C_1 \dot{f}(x) - C_1 f(x)\,\delta(x-a) + C_1 f(x)\,\delta(x-b) \quad (2.113)$$

$$F_2(x) = C_1 f(x) \quad (2.114)$$

and

$$C_1 = \int_a^b f(x)^2\, dt \quad (2.115)$$

$$C_2 = \int_a^b \left[f(x)\,\ddot{f}(x) - \dot{f}(x)^2\right] dx \quad (2.116)$$

$$C_a = \int_a^b \left[\frac{2}{\Delta} f(x)^2 + f(x)\,\dot{f}(x)\right] \delta(x-a)\, dx \quad (2.117)$$

$$C_b = \int_a^b \left[\frac{2}{\Delta} f(x)^2 - f(x)\,\dot{f}(x)\right] \delta(x-b)\, dx. \quad (2.118)$$

The fundamental theorem of the calculus of variations states that for the integrated expression in 2.111 to be equal to zero, it must hold that

$$F_0(x) - \left[F_1(x) - F_2'(x)\right]' = 0. \quad (2.119)$$

Inserting equations 2.112, 2.113, and 2.114 into equation 2.119 yields

$$F_0(x) - \left[F_1(x) - F_2'(x)\right]' = \left[2\left(C_a + C_b - C_2\right)\right] f(x) + 4C_1 \ddot{f}(x) - \frac{4}{\Delta} C_1 f(x)\,\delta(x-a) - \frac{4}{\Delta} C_1 f(x)\,\delta(x-b) + C_1 f(x)\,\dot{\delta}(x-a) - C_1 f(x)\,\dot{\delta}(x-b). \quad (2.120)$$

The differential equation we must solve to find $f(x)$ is therefore

$$\ddot{f}(x) + \kappa^2 f(x) - \frac{1}{\Delta} f(x)\,\delta(x-a) - \frac{1}{\Delta} f(x)\,\delta(x-b) + \frac{1}{4} f(x)\,\dot{\delta}(x-a) - \frac{1}{4} f(x)\,\dot{\delta}(x-b) = 0, \quad (2.121)$$

where

$$\kappa^2 = \frac{(C_a + C_b - C_2)}{2C_1}. \tag{2.122}$$

Now, take a closer look at κ^2. For the DE in equation 2.121 to hold, κ^2 must a constant that is independent of $f(x)$ and/or x. With this in mind, we write the explicit expression for κ^2 by inserting equations 2.115, 2.116, 2.117, and 2.118:

$$\kappa^2 = \frac{\frac{2}{\Delta} f(a)^2 + f(a)\,\dot{f}(a)}{2\int_a^b f(x)^2\,dx} + \frac{\frac{2}{\Delta} f(b)^2 - f(b)\,\dot{f}(b)}{2\int_a^b f(x)^2\,dx} - \frac{\int_a^b \left[f(x)\,\ddot{f}(x) - \dot{f}(x)^2\right] dx}{2\int_a^b f(x)^2\,dx}. \tag{2.123}$$

We can rewrite the numerator of the last term using integration by parts:

$$\int_a^b \left[f(x)\,\ddot{f}(x) - \dot{f}(x)^2\right] dx = \int_a^b f(x)\,\ddot{f}(x)\,dx - \left[f(x)\,\dot{f}(x)\right]_a^b + \int_a^b f(x)\,\ddot{f}(x)\,dx \tag{2.124}$$

$$= 2\int_a^b f(x)\,\ddot{f}(x)\,dx - f(b)\,\dot{f}(b) + f(a)\,\dot{f}(a). \tag{2.125}$$

Inserting this reformulated expression into equation 2.123 and simplifying yields

$$\kappa^2 = \frac{\frac{1}{\Delta} f(a)^2 + \frac{1}{\Delta} f(b)^2}{\int_a^b f(x)^2\,dx} - \frac{\int_a^b f(x)\,\ddot{f}(x)\,dx}{\int_a^b f(x)^2\,dx}. \tag{2.126}$$

Now, take a closer look at the $\int_a^b f(x)\,\ddot{f}(x)\,dx$ term in the above expression. By directly inserting the expression for $\ddot{f}(x)$ as it appears in equation 2.121, this term can be rewritten as

$$\int_a^b f(x)\,\ddot{f}(x)\,dx = -\kappa^2 \int_a^b f(x)^2\,dx + \frac{1}{\Delta}\int_a^b f(x)^2\,\delta(x-a)\,dx + \frac{1}{\Delta}\int_a^b f(x)^2\,\delta(x-b)\,dx - \frac{1}{4}\int_a^b f(x)^2\,\dot{\delta}(x-a)\,dx + \frac{1}{4}\int_a^b f(x)^2\,\dot{\delta}(x-b)\,dx. \tag{2.127}$$

By the sifting property of $\delta(x)$, equation 2.127 becomes

$$\int_a^b f(x)\,\ddot{f}(x)\,dt = -\kappa^2 \int_a^b f(x)^2\,dx + \frac{1}{\Delta} f(a)^2 + \frac{1}{\Delta} f(b)^2 - \frac{1}{4}\int_a^b f(x)^2\,\dot{\delta}(x-a)\,dx + \frac{1}{4}\int_a^b f(x)^2\,\dot{\delta}(x-b)\,dx. \tag{2.128}$$

Furthermore, it can be shown that the distributional derivative of $\delta(x)$ is given by $\left\langle \dot{\delta}(x-a), \phi(x) \right\rangle = -\dot{\phi}(a)$, so equation 2.128 can be rewritten as

$$\int_a^b f(x)\,\ddot{f}(x)\,dx = -\kappa^2 \int_a^b f(x)^2\,dx + \frac{1}{\Delta} f(a)^2 + \frac{1}{\Delta} f(b)^2 + \frac{1}{2} f(a)\,\dot{f}(a) - \frac{1}{2} f(b)\,\dot{f}(b). \quad (2.129)$$

Inserting equation 2.129 into the expression for κ^2 in equation 2.126 and simplifying, we get

$$\kappa^2 = \frac{f(b)\,\dot{f}(b) - f(a)\,\dot{f}(a)}{2\int_a^b f(x)^2\,dx} + \kappa^2. \quad (2.130)$$

The first term on the right side of equation 2.130 must be equal to 0, so it must hold that

$$f(a)\,\dot{f}(a) = f(b)\,\dot{f}(b) \quad (2.131)$$

Now, based on our previous analysis (see equation 2.81), we know that $f(x)$ has to be an even function on the interval between a and b. It must therefore hold that $\dot{f}(a) = -\dot{f}(b)$. This means that the only way to ensure that equation 2.131 holds is if $f(a) = f(b) = 0$. We will be making use of this information shortly when we solve the DE in equation 2.121 using the Fourier transform. Below are a few identities that will be needed to accomplish this:

$$\mathcal{F}\{f(x)\} = \frac{1}{\sqrt{2\pi}} \int_{-\infty}^{\infty} f(x) \exp(i\xi t)\,dx \quad (2.132)$$

$$\mathcal{F}^{-1}\left\{\tilde{f}(\xi)\right\} = \frac{1}{\sqrt{2\pi}} \int_{-\infty}^{\infty} \tilde{f}(\xi) \exp(-i\xi t)\,d\xi \quad (2.133)$$

$$\mathcal{F}\left\{\ddot{f}(x)\right\} = -\xi^2 \tilde{f}(\xi) \quad (2.134)$$

$$\mathcal{F}\{f(x)\,\delta(x-\gamma)\} = \frac{1}{\sqrt{2\pi}} f(\gamma) \exp(i\xi\gamma) \quad (2.135)$$

$$\mathcal{F}\left\{f(x)\,\dot{\delta}(x-\gamma)\right\} = \frac{1}{\sqrt{2\pi}} \left[\dot{f}(\gamma) + i\xi f(\gamma)\right] \exp(i\xi\gamma) \quad (2.136)$$

$$\mathcal{F}^{-1}\left\{\frac{\exp(i\xi\gamma)}{\kappa^2 - \xi^2}\right\} = \frac{1}{\kappa}\sqrt{\frac{\pi}{2}} \operatorname{sgn}(\gamma - x) \sin(\kappa[\gamma - x]), \quad (2.137)$$

where $\mathcal{F}$ and $\mathcal{F}^{-1}$ denote the forward and reverse Fourier transform, respectively, the relationship in equation 2.136 is based on the assumption that $f(\pm\infty)$ and $\dot{f}(\pm\infty)$ are equal to 0, and sgn is the sign function, defined by

$$\operatorname{sgn}(x) = \begin{cases} -1 & \text{if } x < 0 \\ 0 & \text{if } x = 0 \\ 1 & \text{if } x > 0 \end{cases}$$

Using these identities, we now apply the Fourier transform to the DE in equation 2.121, yielding

$$\tilde{f}(\xi)\left[\kappa^2-\xi^2\right]-\frac{f(a)\exp(i\xi a)}{\Delta\sqrt{2\pi}}-\frac{f(b)\exp(i\xi b)}{\Delta\sqrt{2\pi}} + \frac{\left[\dot{f}(a)+i\xi f(a)\right]\exp(i\xi a)}{4\sqrt{2\pi}}-\frac{\left[\dot{f}(b)+i\xi f(b)\right]\exp(i\xi b)}{4\sqrt{2\pi}}=0. \quad (2.138)$$

Now remember that equation 2.131 tells us that $f(a) = f(b) = 0$, and the required symmetry of the function means that $\dot{f}(a) = -\dot{f}(b)$. This means that equation 2.138 simplifies to

$$\tilde{f}(\xi)=\frac{\dot{f}(b)}{4\sqrt{2\pi}}\frac{\exp(i\xi a)+\exp(i\xi b)}{\kappa^2-\xi^2}. \quad (2.139)$$

Performing the reverse Fourier transform and using the relation in equation 2.137, the solution to the DE is given by

$$f(x)=\frac{\dot{f}(b)}{8\kappa}\left[\operatorname{sgn}(a-x)\sin(\kappa[a-x])+\operatorname{sgn}(b-x)\sin(\kappa[b-x])\right]. \quad (2.140)$$

Note that the constant pre-factor $\frac{\dot{f}(b)}{8\kappa}$ will cancel in the functional in equation 2.86 since it appears in the numerator and denominator. It is therefore sufficient to write

$$f(x)=\operatorname{sgn}(a-x)\sin(\kappa[a-x])+\operatorname{sgn}(b-x)\sin(\kappa[b-x]). \quad (2.141)$$

This is nice because it means we don't have to worry about the fact that $f(x)$ isn't technically differentiable at a or b due to the appearance of the sgn function. The task is now to determine the optimal value of κ for a given a, b, and Δ. The first thing to do is simplify things a bit by setting $a = -1/2$ and $b = 1/2$:

$$f(x)=\operatorname{sgn}\left(x+\frac{1}{2}\right)\sin\left(\kappa\left[x+\frac{1}{2}\right]\right)+\operatorname{sgn}\left(x-\frac{1}{2}\right)\sin\left(\kappa\left[x-\frac{1}{2}\right]\right). \quad (2.142)$$

Which we can do because the choice of a and b is arbitrary. Confining ourselves to the interval between $-1/2$ and $1/2$, $f(x)$ is given by

$$\begin{aligned} f(x) &= \sin\left(\kappa\left[x+\frac{1}{2}\right]\right)-\sin\left(\kappa\left[x-\frac{1}{2}\right]\right) \\ &= 2\sin\left(\frac{\kappa}{2}\right)\cos(\kappa x) \\ &= \cos(\kappa x), \end{aligned} \quad (2.143)$$

where the removal of $2\sin(\kappa/2)$ in the last line is once again due to the fact that it is a constant pre-factor that will cancel when $f(x)$ is inserted into the

functional in equation 2.86. We can now determine the value of $J(f)$ as a function of κ and Δ by inserting $f(x)$ into equation 2.86 and evaluating the integrals at the appropriate limits:

$$\begin{aligned} J(\kappa,\Delta) &= \frac{\int_{-0.5+\Delta/2}^{0.5-\Delta/2} \cos\left(\kappa\left[x+\frac{\Delta}{2}\right]\right)\cos\left(\kappa\left[x-\frac{\Delta}{2}\right]\right)dx}{\int_{-0.5}^{0.5}\cos(\kappa x)\,dx} \\ &= \frac{\sin(\kappa[1-\Delta])}{\sin(\kappa)+\kappa} + \frac{\kappa(1-\Delta)\cos(\kappa\Delta)}{\sin(\kappa)+\kappa} \end{aligned} \tag{2.144}$$

We can numerically evaluate the maxima of the transcendental expression given by equation 2.144 to determine the optimal κ for any given Δ. Note that when $\kappa \gg 1$ the expression in equation 2.144 will reduce to

$$J(\kappa,\Delta)\,|_{\kappa\gg 1} = (1-\Delta)\cos(\kappa\Delta), \tag{2.145}$$

a plot of equation 2.144 when $\Delta = 0.05$ is shown in figure 2.2. Here it is clear to see that the first peak corresponds to the optimal value of κ. Panels (b) and (c) in figure 2.2 shows respective plots of $\tilde{E}_{\text{env}}^{\text{opt}}(\omega)$ and $E_{\text{env}}^{\text{opt}}(t)$ as they will look when κ is optimal.

2.4.3 A numerical approach

Combining my results from section 2.4.2 with the original notation used in section 2.4, I have shown that if the transition frequency ω_0 of the system is much smaller than the bandwidth of the pulse, the optimal spectral envelope will be given by a simple trigonometric function that is centered around the middle of the pulse bandwidth (see panel (b) in figure 2.2).

Now, it is clear that the expansions performed to obtain this solution mean that the results will probably not hold for larger transition frequencies. Of course, I could go back and repeat the work done in section 2.4.2 and expand to higher orders, however this is likely to be quite tedious, so at this point I chose to search for solutions using a numerical approach instead. A benefit of doing this is that it will allows me to verify whether or not my preliminary analytical results are accurate.

I now restate the functional that I would like to optimize:

$$J(f) = \frac{\int_{a+\Delta/2}^{b-\Delta/2} f\left(x+\frac{\Delta}{2}\right) f\left(x-\frac{\Delta}{2}\right) dx}{\int_a^b f(x)^2\,dx} \tag{2.146}$$

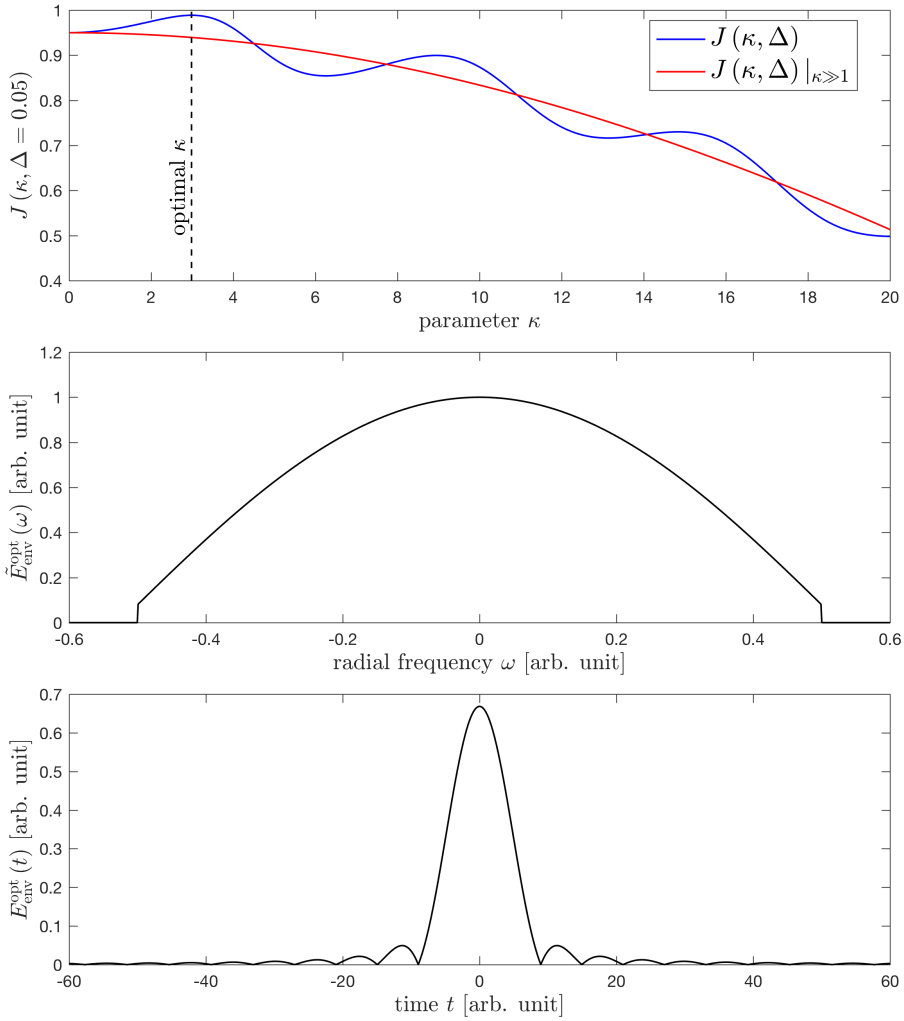

Figure 2.2: The top panel shows a plot of equation 2.144 as a function of κ when $\Delta = 0.05$, i.e. when the transition frequency is equal to 5% of the total pulse bandwidth. The middle panel shows the spectral distribution that will maximize equation 2.144 under the given circumstances, and the bottom panel shows the corresponding optimal temporal pulse envelope.

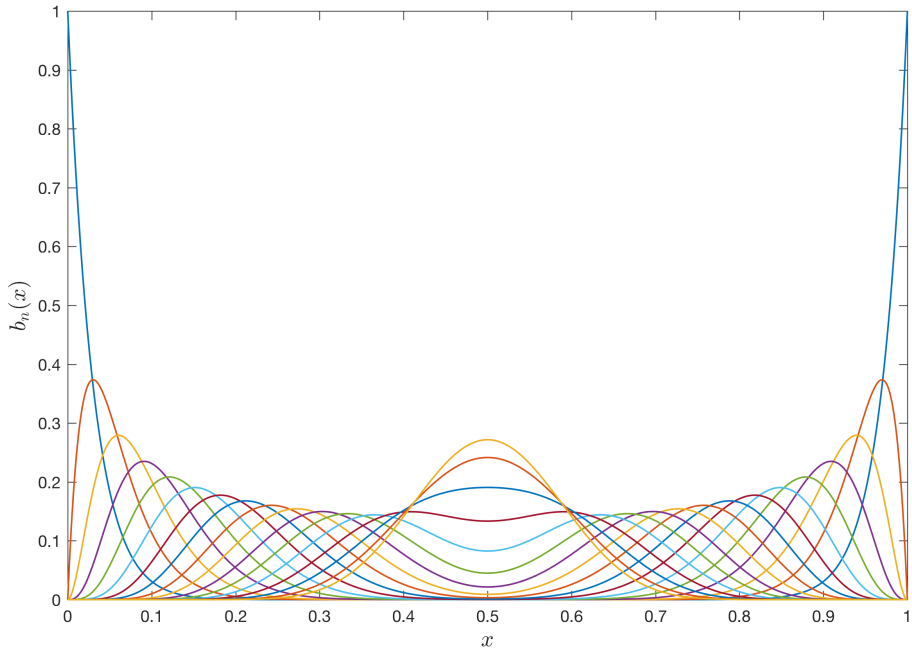

Figure 2.3: plot of the symmetrical basis functions described in equation 2.147 when $N = 17$. As stated in the main text, the numerical optimization task is to find the coefficients for each of the pictured curves that will maximize the functional in 2.148 when they are added together in a linear combination.

My approach is now to represent $f(x)$ using a linear combination of symmetrical Bernstein polynomials [29]:

$$\begin{aligned} f(x) &= \sum_{n=1}^{N} \beta_n \binom{2N-1}{n-1} \left[x^{n-1} (1-x)^{2N-1-n+1} + x^{2N-1-n+1} (1-x)^{n-1} \right] \\ &= \sum_{n=1}^{N} \beta_n b_n(x), \end{aligned} \tag{2.147}$$

where $\binom{2N-1}{n-1}$ is the binomial coefficent and β_n are the expansion coefficients. Combining equations 2.146 and 2.147 yields

$$J(\boldsymbol{\beta}, \Delta) = \frac{\int_{\Delta/2}^{1-\Delta/2} \left[\sum_{n=1}^{N} \beta_n b_n \left(x + \frac{\Delta}{2} \right) \right] \left[\sum_{n=1}^{N} \beta_n b_n \left(x - \frac{\Delta}{2} \right) \right] dx}{\int_0^1 \left[\sum_{n=1}^{N} \beta_n b_n (x) \right]^2 dx}, \tag{2.148}$$

where $\boldsymbol{\beta} = \{\beta_1, \beta_2, \ldots, \beta_N\}$ is a vector of expansion coefficients and the integral limits between 0 and 1 reflect that the Bernstein basis polynomials are defined on the interval $[0, 1]$. Note that these integration limits mean that the size of the bandwidth in question is equal to 1, exactly as is the case in the expression found in equation 2.144, i.e. in both cases, the size of Δ can be interpreted as fraction of the total bandwidth since $0 \leq \Delta \leq 1$. The advantage of the approach outlined by equation 2.148 is that integrated numerator and denominator will evaluate to polynomials. This makes it (relatively) easy to compute analytical gradients of $J(\boldsymbol{\beta})$ with respect to the coeffiecients β_{1-N}. These gradients can be used to iteratively optimize the coeffiecients in $\boldsymbol{\beta}$, i.e. at each iteration step i the expansion coefficients are updated as follows:

$$\boldsymbol{\beta}_{i+1} = \boldsymbol{\beta}_i + \gamma \nabla J(\boldsymbol{\beta}_i) \tag{2.149}$$

where the operator ∇ generates a vector of partial derivatives of the functional $J(\boldsymbol{\beta}_i)$ with respect to each expansion coefficient, and γ is a scaling coefficient that determines the size of the steps taken at each iteration. Initializing the first "guess" $\boldsymbol{\beta}_0$ with random values, I iterate the computation shown in equation 2.149 until the functional value of $J(\boldsymbol{\beta})$ converges to a constant value.

I performed the aforementioned numerical optimization procedure on a range of Δ values between 0 to 0.6 (note that $\Delta = 0$ cannot be optimized since in such a case the functional will simply evaluate to 1). The optimal value of the functional $J(\boldsymbol{\beta}, \Delta)$ (equation 2.146) for numerically optimized spectral functions is shown in blue in figure 2.4. For comparison, the optimal value when $\tilde{E}_{\text{env}}(\omega)$ is given by the expanded/analytical solution in equation 2.141, $J(\kappa, \Delta)$, is represented by the dashed black line. Note that we can also easily evaluate the functional for a flat spectral distribution (e.g. $\tilde{E}_{\text{env}}(\omega) = 1$):

$$J(1, \Delta) = \frac{\int_{\Delta/2}^{1-\Delta/2}(1)dx}{\int_0^1(1)dx} = 1 - \Delta \tag{2.150}$$

This result is plotted in grey in figure 2.4. Finally, we can also make the assumption that $f(x)$ is given by a Gaussian function that is centered around the middle of the pulse bandwidth limits i.e.:

$$f(x) = \exp\left(-\frac{x^2}{2\sigma^2}\right) \tag{2.151}$$

In this case the functional to optimize becomes

$$\begin{aligned} J(\sigma, \Delta) &= \frac{\int_{-0.5+\Delta/2}^{0.5-\Delta/2} \exp\left(-\frac{[x-\Delta/2]^2}{2\sigma^2}\right) \exp\left(-\frac{[x+\Delta/2]^2}{2\sigma^2}\right) dx}{\int_{-0.5}^{0.5} \exp\left(-\frac{x^2}{\sigma^2}\right) dx} \\ &= -\frac{\exp\left(-\frac{\Delta^2}{4\sigma^2}\right) \operatorname{erf}\left(\frac{\Delta-1}{2\sigma}\right)}{\operatorname{erf}\left(\frac{1}{2\sigma}\right)}, \end{aligned} \tag{2.152}$$

where I numerically determine the value of σ that optimizes $J(\sigma, \Delta)$ for each Δ. This result is shown in figure 2.4 in red. Note that the expressions given by equations 2.150 and 2.152 are evaluated where the total bandwidth is set to 1 just as before, so once again Δ can be interpreted as a number that represents the fraction of the total bandwidth.

2.4.4 Analysis and future perspectives

At this point it is important to note that in the top panel of figure 2.4 there does not appear to be any significant difference between the numerical, analytical and Gaussian solutions when $\Delta < 0.18$. However, if we "zoom in" by subtracting the Gaussian solution from all curves as done in the bottom panel of figure 2.4, we see that the numerical and analytical solutions are indeed marginally better than the Gaussian solution when Δ is between 0 and 0.14. We can also see here that the numerical and analytical curves are virtually identical when Δ is small, which is exactly what we would expect since the analytical solution and numerical solutions are both expected to be exactly equal to the optimal solution in this domain (i.e. it appears that the derivation in section 2.4.2 is correct, assuming the numerical approach is also working correctly), and as Δ gets larger the numerical solution begins to outperform both the Gaussian and analytical solutions, which is also what we would expect assuming that the numerical optimization method is moderately successful at determining the optimal spectral for larger Δ. At this point it is worthwhile to note that both the expanded analytical and the numerical approaches to determining the optimal spectrum both assume that it will be a smooth, differentiable function, however this may not actually be the case.

Now I am going to talk about why this work was not published. First of all, the relatively minor discrepancies between the four curves in the top panel of figure 2.4 mean that even if we work very hard to optimize the shape of the pulse spectrum we can only hope to achieve very small improvements in pulse efficiency compared to simply using a Gaussian shape or similar. The second, and perhaps most important reason why I chose not to publish this work in its present form is that that optimizing the pulse efficiency (i.e. the vibrational amplitude as a function of pulse energy) is actually not that relevant a problem when it comes to second order processes. Aside from the pulse bandwidth, the most important limiting factor in this regime is generally the pulse *intensity*. This is because we often have to drive the molecules using nonresonant pulses that are at, or near, the ionization limit of the molecular system to be effective when working in the dynamic Stark regime. For this reason, it would be more useful if I had succeeded in optimizing the pulse given constraints on both bandwidth *and* peak intensity. This was part of my original plan when I started

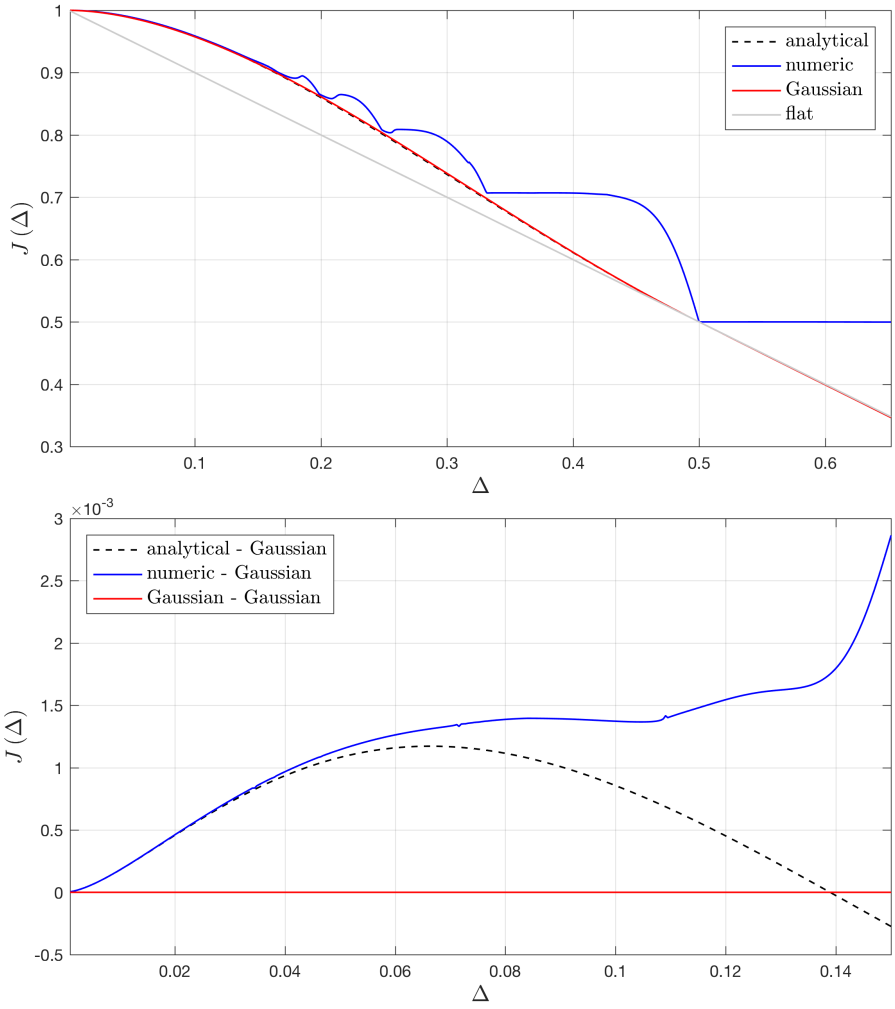

Figure 2.4: The top panel shows the maximized functional values when the pulse spectrum is given by the expanded analytical solution from equation 2.144 (dashed black curve), the optimized numerical result represented by equation 2.148 (blue curve), the Gaussian curve given by equation 2.152 (red curve), and a uniformly flat distribution given by equation 2.150 (grey curve). The bottom panel shows a "zoomed in" view of the curve in the region from $\Delta = 0$ to $\Delta = 0.15$, where I have subtracted the curve corresponding to the Gaussian spectrum from the analytical and numerical results to better illustrate the minute differences between these three results.

this work, however at present time I have not been able to come up with a tractable analytical approach to solving this problem.

All in all, while I am satisfied with the fact that I was able to at least partly solve an interesting functional optimization problem, the results presented in this section are at present time not something that I am confident will have an appeal to a broader audience and for this reason they will remain unpublished, perhaps until someone with a better idea picks up where I left off.

Chapter 3

Nonadiabatic Alignment of Diatomic Molecules

3.1 Introduction to Nonadiabatic Alignment

Until this point, I have only considered the vibrational dynamics of simple diatomic molecules that are aligned with the field polarization axis (i.e. along the molecular-frame z axis). In this chapter, this diatomic model is expanded to include molecular rotations. The background literature covering this topic is already quite extensive, so I will now only provide a very brief overview of a few key relevant elements.

Allowing for rotations, the field-free Hamiltonian can be described (in atomic units) by

$$\hat{H}_0 = \frac{1}{2m}\left(\frac{\partial^2}{\partial R^2} + \frac{2}{R}\frac{\partial}{\partial R}\right) + \frac{\hat{J}^2}{2mR^2} + V(R), \tag{3.1}$$

where R is the internuclear distance, $\hat{J}^2$ is the angular momentum operator of the nuclear rotation, and $V(R)$ is the potential energy curve of the electronic ground state. The stationary eigenstates of this diatomic system can be expressed using three quantum numbers:

$$\hat{H}_0 \left|\nu JM\right\rangle = E_{\nu JM} \left|\nu JM\right\rangle, \tag{3.2}$$

where ν is the vibrational quantum number, J is the angular momentum quantum number, and M is the quanta of the projection of the angular momentum onto the lab-frame Z axis

As outlined in the previous chapter, the interaction Hamiltonian of the molecule with an external field contains a term describing the interaction with the permanent electric dipole and a term arising from the field-induced polarization of

the electronic density (PED/SMP terms). If the carrier frequency of the electric field is much higher than the characteristic time-scales of the vibrational and rotational motion (or if the molecule is homonuclear), we can assume that the impact of the permanent electric dipole on the interaction Hamiltonian will be negligible, and only polarization forces will play a role (i.e. we are once again operating in the non-resonant dynamic Stark regime). In such a case, the Hamiltonian of a diatomic molecule interacting with a field $\varepsilon(t)$ that is linearly polarized along the lab-frame Z axis can be described by [30]

$$\hat{H}_{\text{int}} = -\frac{\varepsilon^2(t)}{2}\left(\left[\boldsymbol{\alpha}_{\parallel}(R) - \boldsymbol{\alpha}_{\perp}(R)\right]\cos^2(\theta) + \boldsymbol{\alpha}_{\perp}(R)\right), \tag{3.3}$$

where $\boldsymbol{\alpha}_{\parallel}(R)$ and $\boldsymbol{\alpha}_{\perp}(R)$ refer to the respective parallel and perpendicular components of the polarizability tensor, and θ is the orientation angle with respect to Z (i.e. when $\theta = 0$ the molecular axis is aligned with Z). Note that when $\theta = 0$ equation 3.4 will reduce to

$$\hat{H}_{\text{int}} = -\frac{1}{2}\varepsilon^2(t)\boldsymbol{\alpha}_{\parallel}(R), \tag{3.4}$$

Which is functionally equivalent to equation 2.65 from chapter 2. Now, given a molecule starting out in the $|000\rangle$ ground state or similar, the interaction with a field $\varepsilon(t)$ can be simulated by numerically solving the time-dependent Schrödinger equation using, e.g., split operator propagation [22] or Runge-Kutta methods [23], as outlined in chapter 1. (note that in all the work discussed in this chapter it is assumed that $\varepsilon(t)$ is a linearly polarized field, and subsequently there will be no changes in the M quantum number). This will generally lead to transitions to higher lying ν and J states. In the so called "impulsive limit", where the time evolution of $\varepsilon(t)$ is much shorter than the molecular rotational period, the molecule will be left in a superposition of rotational and vibrational eigenstates:

$$\Psi(t) = \sum_{\nu,J} a_{\nu,J}\left|\nu J M_i\right\rangle, \tag{3.5}$$

where the $_i$ subscript on M_i indicates that this value is the same as that of the initial state at $t = 0$, and $a_{\nu,J}$ are expansion coefficients.

3.2 Summary: *Femtochemistry in the Electronic Ground State: Dynamic Stark Control of Vibrational Dynamics*

In this article, numerical simulations are performed in which a series of Gaussian pulses with various widths and constant intensity are simulated interacting with

homonuclear H_2 and Cl_2 molecules starting in their $|000\rangle$ ro-vibrational states. It is shown that the H_2 molecule will generally experience excitations into a superposition of the initial $|000\rangle$ state and one or more of the $|100\rangle$, $|120\rangle$, and $|020\rangle$ states (see figure 1 in appendix B). The results for the Cl_2 molecule are similar, although the transition rate to higher rotational states is generally stronger due to the larger anisotropy of the polarizability terms.

It is demonstrated that the analytically estimated optimal pulse width given by equation 2.66 in chapter 2 (or equation 24 in appendix A) will indeed maximize the transition probabilities for lower pulse intensities, however this approximation begins to break down when excitations beyond first order begin to take place at higher intensities. Another notable result here is that in general it is not possible to achieve vibrational transitions without also producing rotational transitions when applying a single flat-phase Gaussian pulse to the system, i.e. when the H_2 molecule is driven with a 10 TW/cm^2 pulse where the width has been optimized for vibrational transitions (i.e. $\sigma = 1.9$ fs), the population of the $|100\rangle$ state becomes 1.79×10^{-5} and the population of the $|020\rangle$ state is comparable at 3.23×10^{-5}. This is because the large bandwidth of the pulses optimized for vibrational excitation will generally also cause substantial rotational excitations to take place.

My principle contribution to this paper was inventing a method of manipulating the phase of a transform limited Gaussian pulse in a manner that (in principle) eliminates the rotational transitions while leaving the vibrational transitions unaltered, provided we confine ourselves to a regime where the harmonic approximation described in the previous chapter is valid. To do this, I exploit the physical insight generated by equation 2.73. In my first article in appendix A, I show that when the spectral distribution is real [i.e. $\mathrm{Re}\{\tilde{A}(\omega)\} = \tilde{A}(\omega)$], then the transition probability P_{ab} between any two states a and b is proportional to the continuous cross-correlation integral of $\tilde{A}(\omega)$ with itself at lag $\omega_{ab} = (E_a - E_b)/\hbar$, i.e.

$$P_{ab} \propto \int_{-\infty}^{\infty} \tilde{A}(\omega)\tilde{A}(\omega - \omega_{ab})d\omega \tag{3.6}$$

Using this relation, I devised a spectral chirp function $\Phi(\omega)$ that, when applied to a flat-phase Gaussian pulse as shown in figure 5 of appendix B, can lead to a modified temporal pulse where the rotational transitions from $|000\rangle$ to $|020\rangle$ are almost completely eliminated, while the vibrational transitions from $|000\rangle$ to $|100\rangle$ remain roughly the same as they where for the un-chirped pulse. To demonstrate, such a chirp function was calculated and applied to the Gaussian pulse with a width optimized for vibrational transitions in H_2. A comparison of the resulting excitation levels for H_2 is shown in table 3.1.

Here it can be seen that the transitions to $|020\rangle$ are reduced by nearly three

Table 3.1: Final state populations after applying the chirped/un-chirped pulses to H_2

state	no chirp	chirped
$\|100\rangle$	1.79×10^{-5}	1.61×10^{-5}
$\|020\rangle$	3.23×10^{-5}	4.37×10^{-8}

orders of magnitude when the chirped pulse is used, while the population of $|100\rangle$ is nearly unaltered. This shows that the chirped pulse has largely worked as intended for the H_2 molecule. We also performed the same analysis using a 10 TW/cm^2 pulse with a width optimized to induce vibrational transitions on the Cl_2 molecule, the results of which are shown in table 3.2

Table 3.2: Final state populations after applying the chirped/un-chirped pulses to Cl_2

state	no chirp	chirped
$\|100\rangle$	5×10^{-4}	1.14×10^{-4}
$\|120\rangle$	2.5×10^{-4}	6.35×10^{-5}
$\|020\rangle$	1.2×10^{-1}	1.4×10^{-3}
$\|040\rangle$	0.35×10^{-2}	2.4×10^{-5}

Here it can be seen that the $|020\rangle$ transitions are reduced by a factor of about 100, while the purely vibrational $|100\rangle$ transitions have been reduced by roughly a factor of 4. Quantitatively this is not as good as in the H_2 example, but it's still not a bad result since the magnitude of the pure rotational transitions are reduced by a significant amount compared to the reduction in the vibrational transitions. The discrepancies are likely due to the fact that the simple harmonic (i.e. perturbative) model begins to break down for the Cl_2 system at this intensity, and due to the fact that the temporal width of the numerical chirped pulse data we used was truncated to contain 90% of the energy of the original un-chirped pulse in order to reduce the simulation time.

If I had more time to pursue this project, there are a number of other things I would have liked to investigate. For example, it would be worthwhile to compare the numerical and analytical models in a more systematic way to gain an understanding of exactly where and how the analytical approximation I derived in my first article breaks down. Furthermore, while it is not an entirely new concept (see, e.g., refs [31, 32]), it would be interesting to further explore the idea of controlling second order transitions via pure spectral phase chirping; e.g. is it possible to devise simple analytic phase functions that are capable of selectively controlling three or more transitions instead of just two, or can explicit limits

be defined on what can be achieved by using phase shaping alone to control second order processes within the perturbative/harmonic regime? Such a study would be in a similar vein to an analysis performed by Paul Brumer and Moshe Shapiro regarding the limitations of pulse shaping in the perturbative weak field limit [33, 34].

3.3 Summary: *Hyperfine-Structure-Induced Depolarization of Impulsively Aligned I_2 Molecules*

This work began after a meeting with Anders Søndergaard, a former PhD student at Aarhus university who worked on impulsive molecular alignment experiments as part of the Femtolab experimental group. In Anders's thesis [35], he describes an experiment where he measured the time-dependent alignment of isolated I_2 molecules that had been excited into a superposition of rotational eigenstates using a 1.06 TW/cm^2, 450 fs FWHM laser pulse. It is well known that such a superposition is expected to lead to periodically recurring alignment trace structures called revivals (see, e.g., figures 2(b) and 2(d) in my previous article in appendix B), however, when the alignment trace of the I_2 molecules was measured for an extended period of about 3.2 ns (equivalent to about 7 revival periods) it was found that the trace was not periodic; the permanent (average) level of alignment and the amplitude of the revival structures appeared to be decreasing and changing shape with time, as can be seen in figure 5.9 in Anders's thesis.

Anders suspected that this apparent loss of alignment was due to interaction between the quadrupole moment of the nuclear charge distribution and the molecular electrons, i.e. the so-called quadrupole coupling effect. This phenomena is well known to cause hyperfine splitting in frequency-resolved high-resolution rotational spectroscopy experiments, but this was potentially the first time that its effects had been directly observed in an impulsive alignment experiment.

I was tasked with developing a quantum-mechanical model of the aligned I_2 system that included the effects of quadrupole coupling, as this would help verify if this was indeed the cause of the observed deviations from the expected behaviour. The first step was to understand the nature of the quadrupole coupling and how it could be described quantum mechanically. There is a large body of literature devoted to this subject; in the following subsection I will briefly go over a derivation of the matrix coupling elements given by equation 2 in the published article in appendix C.

3.3.1 Deriving the quadrupole coupling terms

The classical expression for the electrostatic interaction between a nuclear charge distribution $\rho_n(\mathbf{r}_n)$ and electronic charge distribution $\rho_e(\mathbf{r}_e)$ is given by [36]

$$\mathcal{H}_Q = -\int_n \rho_n(\mathbf{r}_n)\left[\int_e \frac{\rho_e(\mathbf{r}_e)}{|\mathbf{r}_n - \mathbf{r}_e|} d^3 r_e\right] d^3 r_n. \tag{3.7}$$

Now, the denominator in the second integrand in equation 3.7 can be written as a multipole expansion:

$$\frac{1}{|\mathbf{r}_n - \mathbf{r}_e|} = \sum_{k=0}^{\infty} \frac{4\pi}{2k+1} \frac{r_n^k}{r_e^{k+1}} \sum_{q=-k}^{k} (-1)^q Y_q^{(k)}(\theta_e, \phi_e) Y_{-q}^{(k)}(\theta_n, \phi_n), \tag{3.8}$$

where Y_a^b are spherical harmonic functions. Equation 3.7 can therefore be rewritten as

$$\mathcal{H}_Q = \sum_{k=0}^{\infty} \frac{4\pi}{2k+1} \sum_{q=-k}^{k} (-1)^q \int_n \rho_n(\mathbf{r}_n) r_n^k Y_{-q}^{(k)}(\theta_n, \phi_n) d^3 r_n \int_e \frac{\rho_e(\mathbf{r}_e)}{r_e^{k+1}} Y_q^{(k)}(\theta_e, \phi_e) d^3 r_e. \tag{3.9}$$

It can be shown that the parity of the integrands in equation 3.9 will lead to only even k terms being nonzero. Futhermore, it can also be shown that the $k = 2$ (quadrupole) term is by far the largest and will therefore dominate the interaction, so equation 3.9 can be simplified to

$$\mathcal{H}_Q = \frac{4\pi}{5} \sum_{q=-2}^{2} (-1)^q \int_n \rho_n(\mathbf{r}_n) r_n^2 Y_{-q}^{(2)}(\theta_n, \phi_n) d^3 r_n \int_e \frac{\rho_e(\mathbf{r}_e)}{r_e^3} Y_q^{(2)}(\theta_e, \phi_e) d^3 r_e. \tag{3.10}$$

Now in general, a list of quantities

$$\mathbf{T}^{(k)} = \left\{T_{-k}^{(k)}, T_{-k+1}^{(k)} \dots T_{k-1}^{(k)}, T_k^{(k)}\right\} \tag{3.11}$$

that transforms like the spherical harmonics $Y_q^{(k)}$ is, by definition, an irreducible tensor of rank k. Moreover, the scalar product of two irreducible tensors $\mathbf{T}^{(k)}$ and $\mathbf{U}^{(k)}$ is given by

$$\mathbf{T}^{(k)} \cdot \mathbf{U}^{(k)} = \sum_{q=-k}^{k} (-1)^q T_q^{(k)} U_{-q}^{(k)}. \tag{3.12}$$

Comparing equations 3.10, 3.11, and 3.12, we see that the quadrupole interaction term can be rewritten as

$$\mathcal{H}_Q = \mathbf{V}^{(2)} \cdot \mathbf{Q}^{(2)}, \tag{3.13}$$

where the elements of the electric field gradient tensor $\mathbf{V}^{(2)}$ are given by

$$V_q^{(2)} = \sqrt{\frac{4\pi}{5}} \int_e \frac{\rho_e(\mathbf{r}_e)}{r_e^3} Y_q^{(2)}(\theta_e, \phi_e) d^3 r_e, \tag{3.14}$$

and the elements of the nuclear quadrupole tensor are given by

$$Q_q^{(2)} = \sqrt{\frac{4\pi}{5}} \int_n \rho_n(\mathbf{r}_n) r_n^2 Y_q^{(2)}(\theta_n, \phi_n) d^3 r_n. \tag{3.15}$$

Now, the $q = 0$ component of equation 3.15 is

$$\begin{aligned} Q_0^{(2)} &= \sqrt{\frac{4\pi}{5}} \int_n \rho_n(\mathbf{r}_n) r_n^2 Y_0^{(2)}(\theta_n, \phi_n) d^3 r_n \\ &= \frac{1}{2} \int_n \rho_n(\mathbf{r}_n) r_n^2 \left(3\cos\theta_n - 1\right) d^3 r_n. \end{aligned} \tag{3.16}$$

Conveniently, the nuclear quadrupole moment operator is defined by

$$\hat{Q} \equiv \frac{1}{e} \int_n \rho_n(\mathbf{r}_n) r_n^2 \left(3\cos\theta_n - 1\right) d^3 r_n, \tag{3.17}$$

and the quantum mechanical observable Q is defined by

$$Q = \left\langle I_*, M_{I_*} = I_* \left| \hat{Q} \right| I_*, M_{I_*} = I_* \right\rangle, \tag{3.18}$$

where $|I_*, M_{I_*}\rangle$ are nuclear spin basis functions of a single atom. Combining equations 3.16, 3.17, and 3.18 leads to the following relation:

$$\left\langle I_*, M_{I_*} = I_* \left| Q_0^{(2)} \right| I_*, M_{I_*} = I_* \right\rangle = \frac{1}{2} eQ. \tag{3.19}$$

Applying the Wigner-Eckhart theorem [37] to equation 3.19 yields an expression for a reduced matrix element that is independent of the projection number M_{I_*}

$$\begin{aligned} \left\langle I_* \left\| Q^{(2)} \right\| I_* \right\rangle &= \frac{1}{2} eQ \begin{pmatrix} I_* & 2 & I_* \\ -I_* & 0 & I_* \end{pmatrix}^{-1} \\ &= eQ \left[\frac{(2I_*+1)(2I_*+2)(2I_*+3)}{8I_*(2I_*-1)} \right]^{1/2}. \end{aligned} \tag{3.20}$$

By a similar, slightly more involved derivation it can be shown (see, e.g., ref. [38]) that the reduced matrix element coupling rotational states J^a and J^b is given by

$$\left\langle J^a \left\| V^{(2)} \right\| J^b \right\rangle = q\left(-1\right)^{J^b} \left[\left(2J^a+1\right)\left(2J^b+1\right)\right]^{1/2} \begin{pmatrix} J^b & 2 & J^a \\ 0 & 0 & 0 \end{pmatrix}, \tag{3.21}$$

where q is the second derivative of the electric field potential V with respect to the principle inertial axis of the molecular frame z axis:

$$q \equiv \frac{\partial^2 V}{\partial z^2}. \tag{3.22}$$

Now, we consider a diatomic molecule (linear rotor) containing two coupled nuclei with spin I_1 and I_2. The coupling scheme is

$$\mathbf{I} = \mathbf{I}_1 + \mathbf{I}_2 \tag{3.23}$$

$$\mathbf{F} = \mathbf{I} + \mathbf{J}. \tag{3.24}$$

Note that a more detailed explanation of this scheme can be found in the published article in appendix C. The basis functions in the coupled representation are given by

$$|I\,(I_1 I_2)\,JFM_F\rangle\,, \tag{3.25}$$

where the parenthesis around I_1 and I_2 indicate that these quantities are constant since they represent the nuclear spin of each iodine atom (i.e. $I_1 = I_2 = 5/2$). The quadrupole coupling element of the Hamiltonian for this system is given by

$$\mathcal{H}_Q = \mathbf{V}^{(2)}(1) \cdot \mathbf{Q}^{(2)}(1) + \mathbf{V}^{(2)}(2) \cdot \mathbf{Q}^{(2)}(2)\,, \tag{3.26}$$

where the two terms on the right side of equation 3.26 represent the coupling of nuclei 1 and 2 to the electric field. Now, we would like to calculate the coupling matrix elements, given by

$$\left\langle I^a\,(I_1 I_2)\,J^a F^a M_F^a \left|\mathcal{H}_Q\right| I^b\,(I_1 I_2)\,J^b F^b M_F^b \right\rangle. \tag{3.27}$$

It can be shown [39] that

$$\begin{aligned}\left\langle I^a\,(I_1 I_2)\,J^a F^a M_F^a \left|\mathbf{V}^{(2)}(1) \cdot \mathbf{Q}^{(2)}(1)\right| I^b\,(I_1 I_2)\,J^b F^b M_F^b \right\rangle = \\ \delta_{F^a F^b}\delta_{M_F^a M_F^b}\,(-1)^{I^a+F^b+I_1+I_2}\left[\left(2I^b+1\right)\left(2I^a+1\right)\right]^{1/2} \\ \times \begin{Bmatrix} F^b & I^a & J^a \\ 2 & J^b & I^a \end{Bmatrix} \begin{Bmatrix} I_1 & I^a & I_2 \\ I^b & I_1 & 2 \end{Bmatrix} \left\langle I_1 \left\| Q^{(2)}(1) \right\| I_1 \right\rangle \left\langle J^a \left\| V^{(2)}(1) \right\| J^b \right\rangle,\end{aligned} \tag{3.28}$$

which can be rewritten using equations 3.20 and 3.21 and noting that $I_1 = 5/2$:

$$\begin{aligned}\left\langle I^a\,(I_1 I_2)\,J^a F^a M_F^a \left|\mathbf{V}^{(2)}(1) \cdot \mathbf{Q}^{(2)}(1)\right| I^b\,(I_1 I_2)\,J^b F^b M_F^b \right\rangle = \\ -\,\delta_{F^a F^b}\delta_{M_F^a M_F^b}\,eqQ\,(-1)^{I^a+I^b+F^b} \\ \times \left[\frac{21}{5}\left(2I^b+1\right)\left(2I^a+1\right)\left(2J^a+1\right)\left(2J^b+1\right)\right]^{1/2} \\ \times \begin{pmatrix} J^b & 2 & J^a \\ 0 & 0 & 0 \end{pmatrix} \begin{Bmatrix} F^b & I^a & J^a \\ 2 & J^b & I^a \end{Bmatrix} \begin{Bmatrix} \frac{5}{2} & I^a & \frac{5}{2} \\ I^b & \frac{5}{2} & 2 \end{Bmatrix}.\end{aligned} \tag{3.29}$$

Performing the same calculation for $\mathbf{V}^{(2)}(2)\cdot\mathbf{Q}^{(2)}(2)$ yields

$$\begin{aligned}\left\langle I^a\left(I_1I_2\right)J^aF^aM_F^a\left|\mathbf{V}^{(2)}(2)\cdot\mathbf{Q}^{(2)}(2)\right|I^b\left(I_1I_2\right)J^bF^bM_F^b\right\rangle = \\ -\delta_{F^aF^b}\delta_{M_F^aM_F^b}eqQ\left(-1\right)^{2I^a+F^b} \\ \times\left[\frac{21}{5}\left(2I^b+1\right)\left(2I^a+1\right)\left(2J^a+1\right)\left(2J^b+1\right)\right]^{1/2} \\ \times\begin{pmatrix}J^b & 2 & J^a\\ 0 & 0 & 0\end{pmatrix}\begin{Bmatrix}F^b & I^a & J^a\\ 2 & J^b & I^a\end{Bmatrix}\begin{Bmatrix}\frac{5}{2} & I^a & \frac{5}{2}\\ I^b & \frac{5}{2} & 2\end{Bmatrix}.\end{aligned} \tag{3.30}$$

Finally, adding equations 3.29 and 3.30 leaves us with the expression for the quadrupole coupling matrix element as it appears in equation 2 in appendix C.

$$\begin{aligned}\left\langle I^a\left(I_1I_2\right)J^aF^aM_F^a\left|\mathcal{H}_Q\right|I^b\left(I_1I_2\right)J^bF^bM_F^b\right\rangle = \\ -(eqQ)\delta_{F^aF^b}\delta_{M_F^aM_F^b}\left[(-1)^{I_a}+(-1)^{I_b}\right](-1)^{F^a+I^a} \\ \times\left[\frac{21}{20}\left(2I^b+1\right)\left(2I^a+1\right)\left(2J^a+1\right)\left(2J^b+1\right)\right]^{1/2} \\ \times\begin{pmatrix}J^b & 2 & J^a\\ 0 & 0 & 0\end{pmatrix}\begin{Bmatrix}F^b & I^a & J^a\\ 2 & J^b & I^a\end{Bmatrix}\begin{Bmatrix}\frac{5}{2} & I^a & \frac{5}{2}\\ I^b & \frac{5}{2} & 2\end{Bmatrix}.\end{aligned} \tag{3.31}$$

3.3.2 Interpreting the results

As outlined in appendix C, equation 3.31 can be used to generate a coupling matrix that an initial superposition of impulsively aligned J states, $\sum_J a_J\left|JM_i\right\rangle$, can be projected onto (this initial superposition is determined by numerically simulating the interaction of the pulse with the system *sans* quadrupole coupling, which is safe to do since the time scale of the aligning pulse is much shorter than the time scale where the quadrupole coupling will begin to have a significant effect on the alignment trace). Diagonalizing this matrix yields a list of complex coefficients that describe the time dependent evolution of the population of coupled states (as represented by equation 3.25).

Transforming our coupled state solution back into the uncoupled state representation (see equation 3 in appendix C) allows us to calculate the theoretical alignment trace shown in figure 1 in appendix C. As the plot shows, the agreement between the experimental and theoretical traces is quite good. This strongly indicates that we are observing and verifying the existence of quadrupole coupling in an impulsive alignment experiment for the first time ever. This was an exciting result, and the decision was made to write a paper about it and submit it to Physical Review Letters.

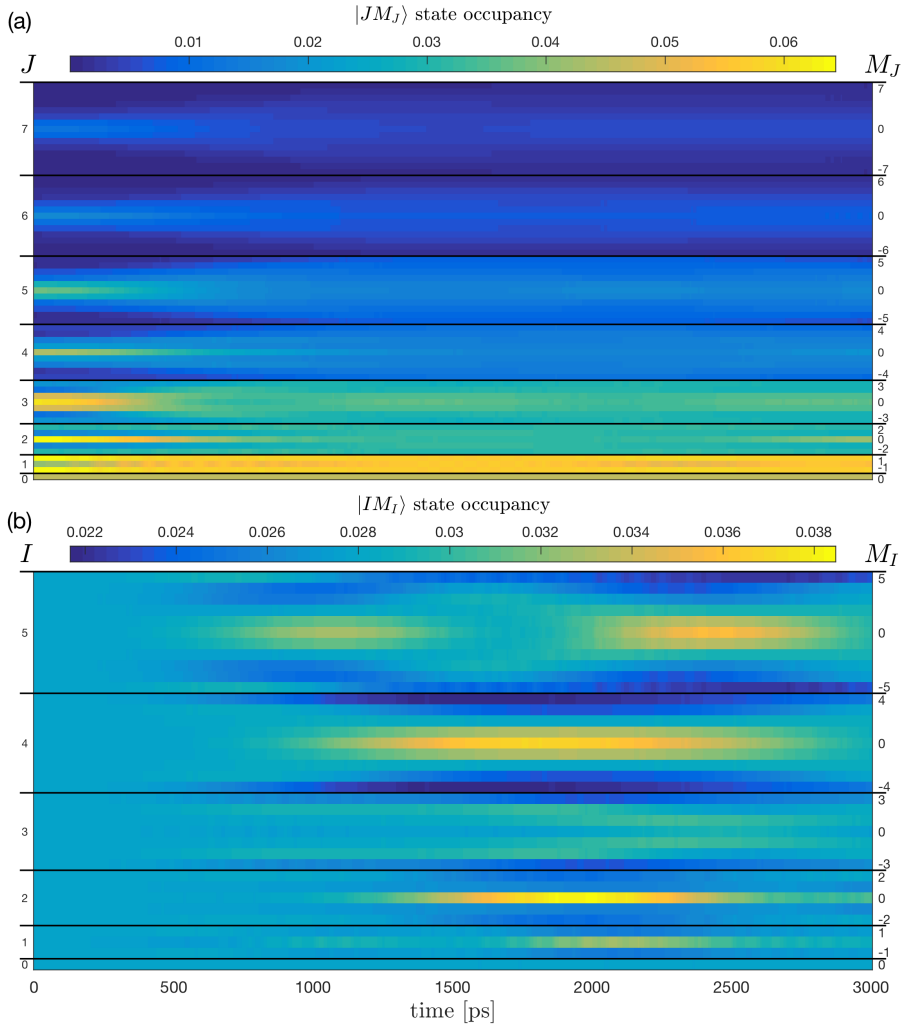

Figure 3.1: The simulated alignment trace in figure 1 of the published article is naturally associated with a number of quantum states, and this figure shows the total occupation levels of these states in the uncoupled representation and how they evolve as a function of time. I have separated the representation into the $|JM_J\rangle$ rotational states and $|IM_I\rangle$ nuclear spin states (i.e. the total occupation of all states in the top panel will sum to 1, as will the total occupation of states in the bottom panel). Here it can be seen how the initial rotational state distributions spread out over time, leading on average to larger average values of $|M_J|$, which is associated with the well understood decrease in permanent alignment (i.e. "precession type" depolarization).

After overcoming the technical efforts associated with developing a functioning model that included the effects of quadrupole coupling, it was time to do the "real science", i.e. to try and understand exactly what the quadrupole coupling was doing to the alignment trace and why. In general the quadrupole coupling causes each $|JM_i\rangle$ from an initial $\sum_J a_J |JM_i\rangle$ superposition to spread out across a "J-manifold" of coupled states (see figure 3 in appendix C). As stated in the article text, the complete alignment trace is the weighted incoherent sum of traces from all the different initial $\sum_J a_J |JM_i\rangle$ superpositions that exist because of thermal and focal volume averaging, as described in refs. [35, 40]. The total $|JM_J\rangle$ and $|IM_I\rangle$ state occupation for the complete set of systems is visualized in figure 3.1. Here we see that the occupation levels in the $|JM_J\rangle$ state distributions for each J evolve in a way that is initially qualitatively similar to the process of diffusion as the average value of $|M_J|$ increases, which also leads to a general decrease in the permanent alignment. We can also see that this decrease in anisotropy in the $|JM_J\rangle$ states is countered by an apparent *increase* in anisotropy in the $|IM_I\rangle$ states, as they go from their initial uniform distributions at $t = 0$ to being concentrated around lower values of $|M_I|$ at around 1 ns. This apparent "conservation of anisotropy" is directly attributed to the fact that the angular projection numbers are a conserved quantity, i.e. all $|JM_J\rangle$ and $|IM_I\rangle$ associated with a given J manifold must have projection numbers that add up to the M_i of the initial occupied state at $t = 0$, so as each initial distribution spreads out across its corresponding J-manifold to states with larger values of $|M_J|$ there is an equal and opposite change in the associated average value of $|M_I|$.

The nice thing about having an accurate working model is that it allowed me to perform numerical experiments by modifying and/or removing certain model components and analyzing the effects on the resulting simulated trace. This allowed me to draw a few notable conclusions. As stated in the paper, I found that the quadrupole coupling affects the off diagonal contributions to the revival structures in a different way compared to the well-understood impact on the "permanent" alignment of a molecule in a single rotational state. The most important qualitative difference here is that while the effect on the permanent alignment is known to be negligible in the limit where the rotational angular momentum is much larger than the angular momentum of the total nuclear spin, the hyperfine coupling will always significantly perturb the off diagonal component of the revival structures over time (see figure 4 in appendix C).

The other main conclusion that I draw is that the perturbations in the off-diagonal ($J \neq J'$) component of the revival structures can be traced to two intertwined, but fundamentally different, physical process; the most significant one is related to the fact that the energy splitting of in each J state (see figure 3(b) in appendix C) introduces small frequency shifts in the off diagonal components of the alignment trace, and the resulting frequency beating causes attenuation of the revival peaks as well as modifications of the substructures (see

figure 2 in appendix C). The second effect, which I have chosen to call "asynchronous distributional dynamics", is due to the fact that each $|IM_I\rangle \otimes |JM_J\rangle$ state in a given J-manifold will combine with at most one state in any other J-manifold to yield a nonzero addition to the overall alignment trace. This bijective/injective manner of combining different off diagonal states leads to a net loss of amplitude when the state distributions in two different J-manifolds are dissimilar. While the truth of this latter statement may seem intuitive, I found that it was an interesting exercise to prove it using Lagrange multipliers:

3.3.3 Analyzing the effect of asymmetrical distributional dynamics

Let $\Psi(t)$ represent the wave function of a quadrupole coupled system containing 2 different J-manifolds;

$$\Psi(t) = \sqrt{\alpha}\chi_a(t) + \sqrt{\alpha - 1}\chi_b(t), \tag{3.32}$$

where $\chi_a(t)$ and $\chi_b(t)$ each contain N coupled states, and where we assume that there is no inter-J coupling and α is a normalization constant (i.e. $0 \leq \alpha \leq 1$). Now, let $a_n(t)$ $[b_n(t)]$ be the complex time dependent coefficient representing the occupation of the n^{th} coupled state in manifold $\chi_a(t)$ $[\chi_b(t)]$ (see, e.g., figure 3 in the article). Based on equation 3.32, it is easy to see that for proper normalization of $\Psi(t)$, it must hold at all times that

$$\sum_{n=1}^{N} |a_n(t)|^2 = 1 \tag{3.33}$$

$$\sum_{n=1}^{N} |b_n(t)|^2 = 1. \tag{3.34}$$

We now separate $a_n(t)$ and $b_n(t)$ into their real and imaginary components, i.e.

$$a_n(t) = a_{n,r} + ia_{n,i} \tag{3.35}$$

$$b_n(t) = b_{n,r} + ib_{n,i}, \tag{3.36}$$

where I have omitted including the time-dependence in the terms on the right side for notational clarity. Using these relations, equations 3.33 and 3.34 can be

rewritten as

$$\sum_{n=1}^{N} \left(a_{n,r}^2 + a_{n,i}^2\right) = 1 \tag{3.37}$$

$$\sum_{n=1}^{N} \left(b_{n,r}^2 + b_{n,i}^2\right) = 1. \tag{3.38}$$

If we assume that all of the components in $\left\langle \cos^2 \theta_{2\mathrm{D}} \right\rangle_{\mathrm{coh}}$ are oscillating at the same frequency and phase (see, e.g., panel (b) in figure 2 of the article), it can be shown that the total amplitude of these oscillations $A\,(t)$ will be proportional to

$$A\,(t) \propto \sum_{n=1}^{N} a_{n,r} b_{n,r} + a_{n,i} b_{n,i}, \tag{3.39}$$

Now, we want to prove that the asynchronous distributional dynamics in different J-manifolds cause a net loss of amplitude in $\left\langle \cos^2 \theta_{2\mathrm{D}} \right\rangle_{\mathrm{coh}}$ due to the bijective or injective (one to at most one) way of combining different sets of states associated with different manifolds when calculating nonzero contributions to the trace. This can be accomplished by using Lagrange multipliers to show that the value of $A(t)$ is maximized (i.e. at a stationary point) whenever $|a_n(t)|^2 = |b_n(t)|^2$ for all N coupled states in $\chi_a(t)$ and $\chi_b(t)$, as this means that $A(t)$ will necessarily decrease any time $|a_n(t)|^2 \neq |b_n(t)|^2$ for any n. Formally put, the objective functional we wish to maximize is given by equation 3.39, and the constraints are defined by the normalization conditions in equations 3.37 and 3.38. The Lagrangian is therefore given by

$$\mathcal{L} = \sum_{n=1}^{N} \left(a_{n,r} b_{n,r} + a_{n,i} b_{n,i}\right) - \lambda_1 \left[\sum_{n=1}^{N} \left(a_{n,r}^2 + a_{n,i}^2\right) - 1\right] - \lambda_2 \left[\sum_{n=1}^{N} \left(b_{n,r}^2 + b_{n,i}^2\right) - 1\right]. \tag{3.40}$$

We now find the stationary point(s) by differentiating $\mathcal{L}$ with respect to $a_{n,r}$, $a_{n,i}$, $b_{n,r}$, and $b_{n,i}$

$$\frac{\partial \mathcal{L}}{\partial a_{n,i}} = b_{n,i} - 2\lambda_1 a_{n,i} \tag{3.41}$$

$$\frac{\partial \mathcal{L}}{\partial a_{n,r}} = b_{n,r} - 2\lambda_1 a_{n,r} \tag{3.42}$$

$$\frac{\partial \mathcal{L}}{\partial b_{n,i}} = a_{n,i} - 2\lambda_2 b_{n,i} \tag{3.43}$$

$$\frac{\partial \mathcal{L}}{\partial b_{n,r}} = a_{n,r} - 2\lambda_2 b_{n,r}. \tag{3.44}$$

At a stationary point, these derivatives should all be equal to 0, which yields the following relations:

$$b_{n,i} = 2\lambda_1 a_{n,i} \tag{3.45}$$
$$b_{n,r} = 2\lambda_1 a_{n,r} \tag{3.46}$$
$$a_{n,i} = 2\lambda_2 b_{n,i} \tag{3.47}$$
$$a_{n,r} = 2\lambda_2 b_{n,r}. \tag{3.48}$$

Inserting equations 3.47 and 3.48 into equation 3.37, we get

$$\sum_{n=1}^{N} \left([2\lambda_2 b_{n,r}]^2 + [2\lambda_2 b_{n,i}]^2 \right) = 1, \tag{3.49}$$

which can be rewritten as

$$4\lambda_2^2 \sum_{n=1}^{N} \left(b_{n,r}^2 + b_{n,i}^2 \right) = 1 \tag{3.50}$$

and finally, using equation 3.38, we get

$$4\lambda_2^2 = 1 \tag{3.51}$$

i.e.

$$\lambda_2 = \pm\frac{1}{2}. \tag{3.52}$$

Performing the same procedure with equations 3.45, 3.46, and 3.38 yields

$$\lambda_1 = \pm\frac{1}{2}, \tag{3.53}$$

which means that equations 3.45, 3.46, 3.47, and 3.48 can now be rewritten as

$$b_{n,i}^2 = a_{n,i}^2 \tag{3.54}$$
$$b_{n,r}^2 = a_{n,r}^2 \tag{3.55}$$
$$a_{n,i}^2 = b_{n,i}^2 \tag{3.56}$$
$$a_{n,r}^2 = b_{n,r}^2, \tag{3.57}$$

which means that

$$a_{n,r}^2 + a_{n,i}^2 = b_{n,r}^2 + b_{n,i}^2, \tag{3.58}$$

or, using the relationship defined in equations 3.35 and 3.36:

$$|a_n(t)|^2 = |b_n(t)|^2. \tag{3.59}$$

The fact that the result in equation 3.59 this will hold for all n states means that the magnitude of $A(t)$ is only maximized when the state distributions in $\chi_a(t)$ and $\chi_b(t)$ are identical. The fact that this implies a stationary point in the Lagrangian in equation 3.40 means that whenever equation 3.59 does not hold, $A(t)$ will decrease, as evidenced by the attenuated peak amplitudes in the trace shown in panel (b) of figure 2.

Chapter 4

Deracemization of Biphenyl Molecules

4.1 Introduction to the Closed-Loop method of Coherent Control

The energy required to drive chemical reactions is normally supplied in the form of heat or incoherent light. These methods are statistical in nature; they influence global parameters of the system, and the focus is on the end products of the reaction. As stated in chapter 1, coherent control differs in this respect as it involves coherently manipulating the evolution of a system "in real time".

In order for this to be achieved in a laboratory, it has been necessary to develop tools and techniques that are capable operating on femtosecond timescales. The introduction of the 4f-line spectral pulse shaper by C. Froehly *et al.* in 1983 [41], coupled with the development of controllable liquid crystal phase masks, led to the ability to create and tailor complex femtosecond laser pulses with features that evolve on the same characteristic time scales as the molecular systems.

For simple molecules, where it is possible to make theoretical predictions, a so called "open-loop" [5] experimental coherent control scheme may be employed, where the pulse shapes are designed based on a priori knowledge of the molecular system in question. However, many systems are far too complicated for theoretical approximations to be of much help. In these cases, a so called "closed loop" scheme may be used, in which a series of test pulses are applied to the system, and the resulting experimental feedback is fed into a gradient-free optimization algorithm that attempts to determine the set of pulse shaping parameters that will drive the system into the desired target state.

In the first part of this section, I will describe the 4f-line pulse shaper, and how it

can be implemented as part of a closed loop approach to experimental coherent control. In the second part, I will outline a published work in appendix D where I implement a numerical model of such an experiment and demonstrated that it can in principle be used to deracemize a racemic mixture of biphenyl molecules, an accomplishment that has yet to be achieved in a laboratory. Finally in the third part I will summarize a follow-up publication to this work that is included in appendix E.

4.1.1 Spectral pulse shaping

Speaking in very general of terms, pulse shaping is about transforming an incoming laser pulse into a desired shape. For ultrashort pulses on the femtosecond time scale, this shaping is generally accomplished in the spectral domain. The method of spectral pulse shaping introduced by Colombeau C. Froehly et al in 1983 known as the zero dispersion line or 4f line [5] is a simple and versatile approach that operates in the following way:

1. An ultrashort pulse is angularly dispersed into its spectral components via a diffraction grating
2. The angularly diffracted spectral components are focused via a lens or mirror into equally spaced diffraction spots in the Fourier plane.
3. The phase, intensity and/or polarization of each spatially separated spectral component is manipulated in the Fourier plane using a spatial light modulator (SLM) or "mask".
4. After manipulation, the spatially distributed spectral components are focused back down to a single point by another lens or mirror
5. The focused spectral elements are "recombined" back into a temporal pulse by means of another diffraction grating

A sketch of this process is shown in figure 4.1. The spectral manipulations caused by the SLM will impact the shape of the recombined temporal pulse. It is therefore possible to actively control the shape of the temporal pulse using an adjustable SLM where the phase, intensity and/or polarization of the spectral distribution can be modified. The liquid crystal spatial light modulator (LC-SLM) is one an example of such an adjustable SLM. This device independently modifies the optical path of each spectral component using an array of nematic liquid crystals that change their orientation when voltage is applied. A representative sketch of such an array with typical component sizes is shown in

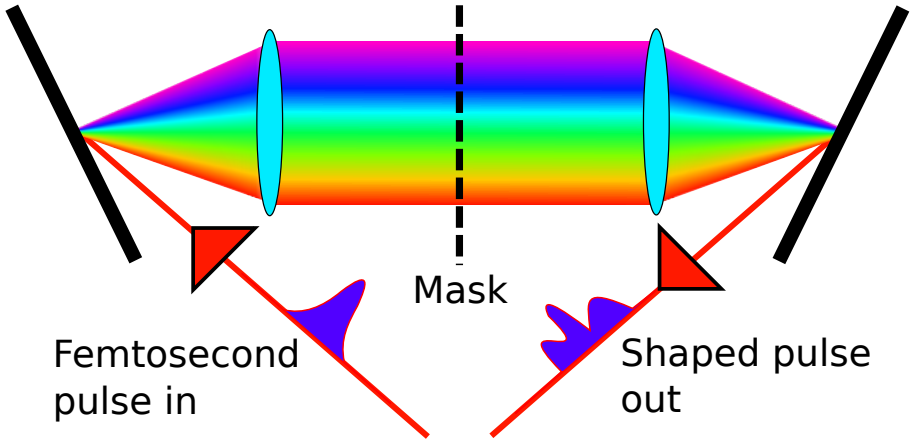

Figure 4.1: Schematic sketch of the 4f-line pulse shaper. The incoming unshaped pulse is diffracted off the grating on the left side, and the spectral elements are focused by the first lens. After passing through the mask in the Fourier plane, the spectral components are transformed back into a shaped spectral pulse by the second lens and grating.

figure 4.2, and figure 4.3 shows examples of two actual devices. By assuming direct control over the spectral modification generated by each pixel, it becomes possible to produce tailored frequency dependent modifications in the spectral domain.

As alluded to in the introduction to this chapter, combining a 4f-line setup with an adjustable spectral mask gives experimentalists the ability to generate nearly arbitrary pulse shapes. In terms of coherent control, the next question becomes which type of pulse shape is required to achieve a given control objective, i.e. drive a molecular system into a desired terminal state? A compelling method of answering this question was first posited by Richard S. Judson and Herschel Rabitz in their 1992 PRL article entitled "Teaching Lasers to Control Molecules", in which they theoretically demonstrated that a genetic algorithm [42] (GA) could be used to optimize the spectral mask of a pulse shaper in a way that leads to selective excitation of rotational states in KCl.

A sketch of this scheme is shown in figure 4.4. The first experimental implementation of this idea was achieved by Christopher Bardeen *et al.* in 1997 [43], where it was demonstrated that this so-called "closed-loop" approach could be used to optimize the population transfer from ground to first excited state in fluorescence dye molecules in solution. In the following years this method has

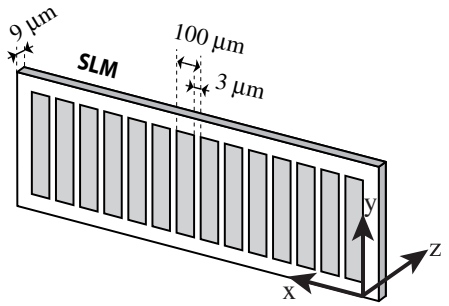

Figure 4.2: Typical dimensions and geometry of part of a LC-SLM pixel array. The light gray areas contain the nematic liquid crystals. (Figure borrowed from ref. [5])

Figure 4.3: Example of a 128×1 (left) and 640×1 (right) pixel resolution LC-SLM (Meadowlark Optics)

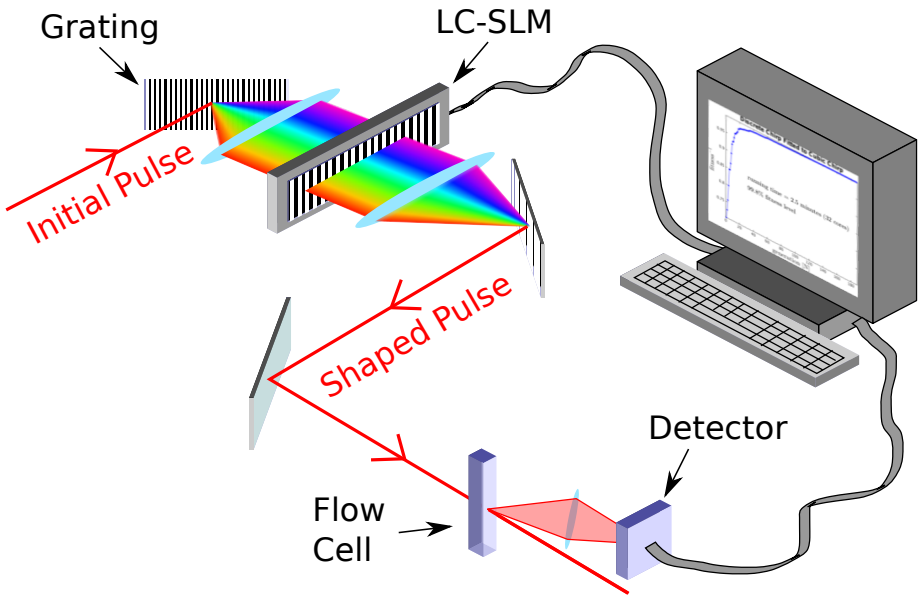

Figure 4.4: Sketch of a closed-loop control system. A series of test pulses are applied to the system, and the performance of each pulse configuration is analyzed by measuring the products of the reaction in the reaction chamber. The results are fed into a computer which updates the LC-SLM based on the performance using an optimization algorithm until the best configuration is found.

found a number of other experimental applications, including ionization of gas phase diatomic sodium [16], photoisomerization of organic molecules [17], probing of chemical mechanisms via optimized pulse analysis [18], and manipulation of biological proteins [19].

4.1.2 The genetic algorithm

As stated in the previous subsection, the closed-loop approach requires a genetic algorithm (or some other variant of a gradient-free optimization algorithm) to determine the optimal configuration of the spectral mask that will produce a pulse that drives a molecular system into a user defined target state or configuration.

In this subsection I will briefly describe how genetic algorithms work. The description will be general, and I refer readers that are interested in specific

implementation details to the supplementary material sections in my included papers. GA's and other types of evolutionary algorithms have the potential to offer robust solutions to optimization problems with:

- a large number of parameters (i.e. high dimensionality)
- little or no a priori knowledge about the relationship between problem inputs and outputs
- objective functions that are highly nonlinear, stochastic, non differentiable, or contain many local minima

The only requirement is that there be a way to evaluate the performance of a trial solution. In a broad sense, genetic algorithms attempt to mimic the natural selection process when searching for an optimal solution. The basic procedure a genetic algorithm uses to find optimal inputs to a given problem is as follows:

1. Create an initial list of trial solutions with randomly selected parameters. Henceforth, each trial solution will be known as an "individual" and the sum total of all the individuals on the list will be known as the "population". The set of parameters that describe each individual in the population is referred to as a "genome", much in the sense that an actual genetic sequence encodes all the information to required to produce a real life organism.
2. Determine the "fitness" of each individual in the population by using their parameters as an input to the optimization problem, and evaluate the performance in relation to the goal output. An important point is that the fitness criteria are user defined, i.e. there must be some way of delineating "good" solutions from "bad" ones.
3. Create a new list, or "generation" of individuals from the current population. There are a number of ways to do this, but the two most important factors are that individuals in the present generation with higher fitness levels should be more likely to pass on traits to the new generation (selection), and there should be some element of randomness introduced to the genomes of the new generation (mutation)
4. Repeat steps $2-3$ until the best fitness level in the population converges, or until a specified number of generations or time steps have passed.

In this way, the fitness of each subsequent generation will ideally be higher than the previous generation, just as the forces of natural selection and mutation will

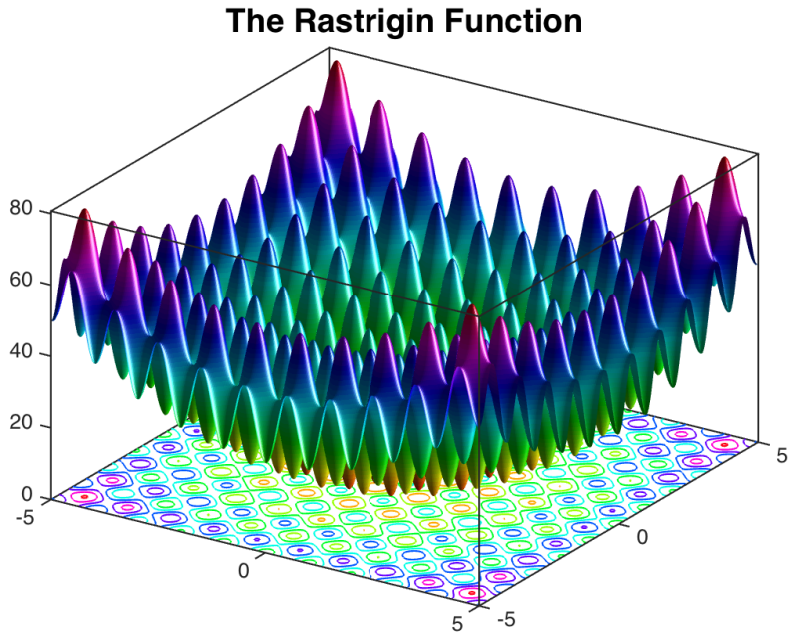

Figure 4.5: The non-convex Rastrigin function is a typical benchmark test for optimization algorithms, as it contains one global minimum and a large number of local minima.

induce a population of animals to evolve traits that increase their fitness and ensure their survival.

A simple example of a genetic algorithm in action can be demonstrated by attempting to minimize the Rastrigin function, which has the form:

$$\mathrm{Ras}\,(x, y) = 20 + x^2 + y^2 - 10\,[\cos\,(2\pi x) + \cos\,(2\pi y)] \tag{4.1}$$

This function has a global minimum at $x = y = 0$, surrounded by a large number of local minima, as the sketch in figure 4.5 indicates. minimizing the Rastrigin function means finding the value of x and y that will yield the lowest value when plugged into equation 4.1. In terms of a genetic optimization, this means that each individual will have a genome of length 2, corresponding to the x and y values of a given trial solution. Since the goal is minimization, individuals with x and y inputs that yield the lowest values will be scored the highest. Using these rules, an initial population of 60 individuals was created, where each individual was assigned a uniformly distributed random initial x and y value between -5 and 5. The MATLAB [44] genetic algorithm was

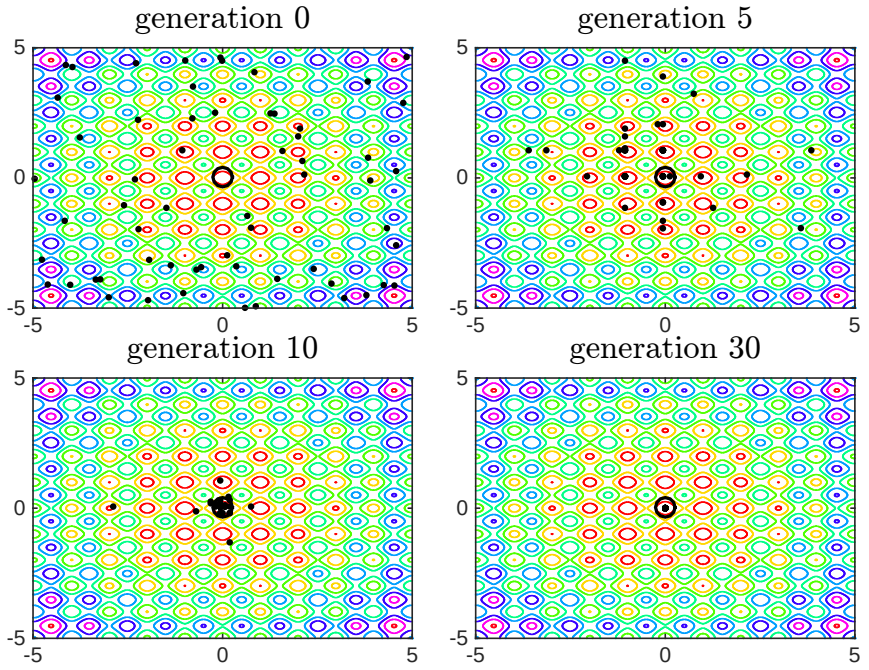

Figure 4.6: Evolving an initial random population of 60 uniformly distributed individuals using a genetic algorithm to find the global minimum of Rastrigin's function (figure 4.5). The global minimum is indicated by the black circle in the center of each plot.

then used to evolve the population of solutions using the procedure outlined in steps $1-4$. The distributions of the individuals at generations 0, 5, 10, and 30 are shown in figure 4.6. The first panel at generation 0 shows a random distribution of individuals within the initial parameter boundaries. Note that none of the individuals are very close to the center. Already at generation 5 a few of the individuals can be found in the global minimum, and many are in nearby local minima. At generation 10 the population distribution has become even more concentrated towards the center, and finally at generation 30 every single individual has assumed the optimal value. In practice, the optimized output of the algorithm is determined by the individual from each generation with the highest fitness. Going by this rule, the optimization in 4.6 could in principle already have been halted at generation 5, since the best performing individuals here have already found values that are very close to the optimal value. It is not necessary for the starting population to be distributed near or around the global minimum as it was in this example, however as a general rule, the further the initial population distribution is from the optimal point,

the larger the population must be in order to adequately explore the parameter space.

4.2 Summary: *Phase-Modulated Nonresonant Laser Pulses Can Selectively Convert Enantiomers in a Racemic Mixture*

This paper was once again inspired by work performed by the Femtolab experimental group in Aarhus. Henrik Stapelfeldt happened to be the external censor at my masters thesis defence, which also was about pulse shaping and its applications to coherent control. In part of my thesis, I demonstrate that an optimized laser field can induce wave packet transfer between minima in a 1D double well potential model. Henrik's group had published a series of papers where they had worked with 3,5-difluoro-3′,5′-dibromobiphenyl ($F_2H_3C_6 - C_6H_3Br_2$, see, e.g., charts 1 and 2 in appendix D), a molecule consisting of an F-substituted phenyl ring connected to a Br substituted ring by a $C-C$ bond. The potential energy landscape of this system as a function of the torsional angle between the phenyl rings can be described by a symmetrical double well potential, and it was for this reason that Henrik suggested that I look into his groups results.

At high temperatures, the two substituted phenyl rings of the $F_2H_3C_6-C_6H_3Br_2$ molecule rotate freely around the axial $C-C$ bond that connects them; however, in work performed by researchers at Aarhus it was demonstrated that cooling a gas-phase population to a few Kelvin will hinder this internal rotation, and the dihedral angle between the rings will become fixed at either $39°$ or $-39°$. these angular configurations correspond to two different stable structures that are each other's mirror image, that is, an enantiomeric pair. Using Coulomb explosion imaging, they had been able to demonstrate that they could induce torsional vibrations between the phenyl rings by subjecting a gas-phase population of the molecules to one or two moderately intense nonresonant laser pulses.

4.2.1 On enantiomers and deracamization

A molecule with a *chiral* structure cannot be superposed onto its own mirror image. As the article introduction in appendix D states, the inherent symmetry of the physical laws means that the energies of a given chiral molecule and its corresponding mirror image will be identical. Effectively, this means that synthesizing molecules with chiralic structures will lead to a $50\% : 50\%$ mixture

of left- and right-handed versions of the molecule (unless a chiralic precursor is applied at some point to target one of the structures). Such a mixture of left- and right-handed forms (or *enantiomers*) is known as a *racemic* mixture. The process of *deracemization* refers to the separation or transformation of a racemic mixture into one containing an excess of a single type of enantiomer.

In the work published by the Femtolab group [45–47], it was speculated that it may be possible to use a laser pulse or series of laser pulses to deracemize the system of gas-phase molecules by inducing wave packet transfer between potential well minima in the left handed versions of the molecule, while simultaneously suppressing this behaviour in the mirrored right-handed versions. In general, demonstrating laser-induced deracemization in a laboratory has been a long-standing goal for many scientists who work with coherent control, and a number of theoretical studies have demonstrated the basic feasibility of this idea using a variety of different approaches (see, e.g., refs [48–58]). Many of these theoretical investigations have been based around the use of optimal control theory to determine the shape of a deracemizing laser pulse. In spite of these predictions, laboratory implementations of laser-induced deracemization schemes have remained largely out of reach for experimentalists.

For this reason, I decided to attempt to narrow the gap between theory and experiment by suggesting a new and robust method of generating deracemization via enantiomeric conversion based on a simulated closed-loop optimization scheme by carefully modelling the optimization process to accurately reflect current experimental techniques and capabilities. Furthermore, I decided to follow the same approach as Henrik's group and exploit the principle of dynamic Stark control (DSC) to achieve this objective. As already discussed in chapter 2, DSC is a phenomenon that dominates when the laser pulse frequencies are non-resonant with respect to the vibrational eigenfrequencies of the molecule. This further emphasized the flexibility of the methodology since a successful experimental implementation would not be contingent on the frequencies contained in the applied laser pulse. The published paper containing this work, as well as extensive supplementary information, can be found in appendix D.

As the results in the publication show, it is in principle possible to achieve deracemization, with a final enantiomeric purity of 98%, with the suggested setup. Moreover, the pulse parameters are reasonable (e.g. the peak intensity of roughly 14 TW/cm^2 is not expected to ionize the molecules). However, as discussed in the article conclusion, there is possibly an issue with the way the fitness of each trial pulse is evaluated; in particular it requires that we have a good idea of what the quantum probability distribution representing the dihedral angle between the rings looks like when the system is in its terminal state. While the experiments performed in Aarhus show that this type of information can be obtained using Coulomb explosion imaging, it may be very time consuming to

gather the number of measurements required to optimize the pulse. This issue will be revisited in chapter 5.

4.3 Summary: *Breaking Dynamic Inversion Symmetry in a Racemic Mixture Using Simple Trains of Laser Pulses*

After publishing our initial work on deracemization, Niels and I felt that the next logical step was to advertize our results to experimental groups that might be interested in, or capable of, implementing our idea in a laboratory. As a part of this campaign, I presented a poster at the Femto 13 conference in Cancún Mexico. Here I spoke with a number of people and learned some interesting things about how experimentalists approach a problem. First of all, experiments (especially challenging ones that require complicated setups) are very resource-intensive to set up and perform. This, coupled with the fact that the human and financial resources available to a department are generally finite, means that decisions about which experimental endeavours to attempt are generally based on careful risk-reward analyses.

From this perspective, our suggested deracemization experiment would be considered a "high-risk/high-reward" endeavour; no one has ever achieved laser-induced deracemization in a laboratory, so any successful attempt will likely be an immediate boon to the scientific careers and notoriety of those involved; on the other hand, the practical difficulties associated with this task means that it would require investing significant resources, with no prior guarantee that anything will work as predicted.

Based on these considerations, I was asked if it would be possible to come up with a more modest proposal that could function as a “stepping stone” on the path towards the end goal of fully achieving laser induced enantiomeric conversion (i.e., let’s try to land on the moon before we try to land on mars!). After presenting my work to the Femtolab group in Aarhus and a few fruitful discussions, I identified such an intermediate step which became the basis for the publication in appendix E, which I will now briefly paraphrase.

In my first article concerned with deracemization, I identify the general mechanism exploited by the optimized laser pulse; namely that the polarization axis of the driving field must “hit” each enantiomer from slightly different angles while simultaneously pumping the amplitude of the torsional oscillations, and that this can be achieved by alternating the polarization axis of the driving field over

time.

In my follow-up paper in appendix E, I devised a simplified experimental setup that does not require a closed-loop optimization scheme. Here, I show that a simple train of pulses with alternating polarization axes is sufficient to significantly break the symmetry of the internal structures in the enantiomers. Furthermore, I demonstrate that these differences should be easy to detect using Coulomb explosion imaging.

Chapter 5

New Experimental Approaches to Coherent Control

5.1 Summary: *A Novel Pulse Optimization Scheme for use in Coherent Control Experiments*

The final paper I will discuss in this thesis is also partially inspired by my previous work with deracemization. As stated in chapter 4, one possible issue with the general approach outlined in my article in appendix D is that performing the required number of measurements to optimize the field may take an extremely long time. For example, the time series data in the I_2 alignment experiment described in our PRL article in appendix C, which was also performed using Coulomb explosion imaging, contained 896 measurements and required running the experimental apparatus overnight. In comparison to this, the converged results shown in appendix D require evaluating the performance of 1.2 million different trial pulses, i.e. performing at least 1.2 million experimental measurements of the system in its terminal state. Assuming it takes roughly 12 hours to perform 1000 measurements, an experimental implementation of the same simulated optimization process would take more than a year to complete!

Clearly this is unfeasible. One possible solution is to find a more efficient optimization algorithm, i.e. one that requires a smaller number of experimental measurements to converge on an optimal pulse shape. Now, there is likely room for improvement regarding the specific choice of genetic/evolutionary algorithm; in my optimizations I simply made use of the standard MATLAB genetic algorithm implementation and tuned the parameters until I saw that the process was reliably converging on good solutions. Late in my PhD, Niels and I had a

conversation with professor Carsten Witt from DTU compute, who suggested that we might get better/faster convergence using a more modern "state-of-the-art" evolutionary algorithm known as covariance matrix adaptation evolution strategy (CMA-ES). While this is certainly a worthwhile idea that I would have liked to try out given more time, the basis for this final article was inspired by an idea I had for solving the problem using a more unorthodox approach.

To provide some background, part of what attracted me to working on coherent control problems was my fascination with the way a computer program can exhibit emergent complexity; for example a genetic algorithm is generally a relatively elementary program to write and implement, yet somehow by just following a few simple rules this search heuristic is able to generate extremely novel solutions that no human mind is likely to conceive of. The related fields of machine learning and artificial intelligence have also captured my general interest, and there is at present time a quickly growing body of work in which it is demonstrated that these techniques can be successfully implemented to solve a wide variety of problems.

In the paper in appendix F I put forth the idea that an artificial neural network (ANN) can be used to "learn" the general rules associated with achieving an objective in a coherent control experiment. This idea is tested and verified on a system consisting of a 1D torsional model of the $F_2H_3C_6 - C_6H_3Br_2$ molecule that has been used in my previous work. As stated in the article abstract, I demonstrate that the optimized ANN is able to achieve robust quantum control of nuclear wave packet transfer between the potential wells of the $F_2H_3C_6 - C_6H_3Br_2$ system despite the addition of random perturbations to the simulated molecular potential energy and polarizability surfaces. I then argue that this capability potentially allows the ANN to achieve the same control objective in an experimental situation. The main advantage of this is that the required number of measurements is equal to the number of parameters that describe the temporal shape of the field (i.e. the dimensionality of the optimization problem).

I want to make it very clear that this article is intended as a preliminary proof of concept for a general idea: that machine learning techniques can be used to increase the speed and efficiency of closed loop optimization schemes in coherent control experiments. I am not stating that the presented solutions are the best way to achieve this goal; the work is instead intended to demonstrate that this general approach may have potential.

This idea came along relatively late in my PhD, and there are many more things that I would have liked to try given more time. For example, transferring a wave packet between two wells is a relatively simple task; it would be interesting to see how well the general approach works for more challenging objectives like

deracemization. Furthermore, a linchpin of my work in its present form is the assumption that discrepancies between a simulated quantum model and the real experimental dynamics of a molecule can be rectified via the addition of one or more perturbing functions to the model Hamiltonian (see, e.g., equations (2) and (3) in appendix E). While it is very unlikely that this assumption is *always* true, it is likely that it is *sometimes* true. Short of a full experimental implementation, one could test when this assumption breaks down by increasing the number of degrees of freedom in the simulated model and seeing whether or not the ANN is able to effectively achieve the control objective. Finally, as stated in the article, there are countless other ways that an ANN could be implemented to interface with the measurement data and generate an optimized field, and it is therefore likely that a different setup could lead to increased robustness against larger perturbation amplitudes.

Chapter 6

Conclusion

In this thesis I have summarized the work contained in six different research papers that represent my main accomplishments as a PhD student, as well as some additional derivations and results that have not been published and/or submitted to journals. While each paper in this list covers a relatively unique topic, they are all tied together by the fundamental concept of the non-resonant dynamic Stark effect and the applications that this phenomenon has to coherent control.

The first paper I present is concerned with providing a clarifying interpretation of how the dynamic Stark effect operates to shift the energy levels of the potential surfaces present in a molecule using a simplified 1D harmonic model. By doing this I am able to uncover some general properties and relationships that help paint a more intuitive picture of how the dynamic Stark effect operates. In general, the fact that the dynamic Stark effect dominates under non-resonant conditions allows us to conclude that we can effectively disregard the carrier frequency of the laser in this regime, which is attractive from the standpoint of experimental implementation.

The second paper extends the concepts of DSC to include rotations and vibrations in diatomic molecules, and I show how a spectral interpretation of second order excitation processes can be exploited to exert state selective control over ro-vibrational transitions, provided that the interaction can be described within the perturbative/harmonic approximation outlined in the first paper. The exact nature by which the aforementioned approach breaks down at higher field strengths/excitation rates is an open question that requires further study.

The third paper extends the rotational model by demonstrating that the nuclear quadrupole moment will couple to the rotational states of impulsively aligned I_2 molecules. This theoretical work is inspired and verified by experiments performed by the Femtolab group at Aarhus university. It is concluded that

the quadrupole coupling affects the revival structures in qualitatively different ways compared to the well-understood impact on the "permanent" alignment of a molecule prepared in a single rotational state. Specifically, the effect on the permanent alignment is known to be negligible in the limit where the rotational angular momentum is much larger than the angular momentum of the total nuclear spin. By contrast, it is observed that the hyperfine coupling will always significantly perturb the revival structures over time.

The fourth paper revisits the concept of DSC by demonstrating that this approach can be used to control the delicate process of laser induced enantiomeric conversion in a racemic mixture of molecules. I show how this can be accomplished using a simulated closed loop coherent control approach. Unlike previous theoretical explorations of laser-induced deracemization, my work focuses on implementability by relying on experimentally verified methods and techniques. I am able to theoretically demonstrate that a racemic mixture consisting of a 50% : 50% mix of left and right handed enantiomers can be transformed into one where 98% of the molecules share the same structural parity. Finally, I identify a possible challenge associated with the outlined approach; namely that a prohibitively large number of experimental measurements may be required to obtain the optimized pulse parameters.

The fifth paper extends the conclusions drawn in the fourth paper by exploiting some of the general principles related to the process of deracemization that were uncovered in the previous work. In doing this, I am able to develop a simplified approach to deracemization/dynamic inversion symmetry breaking that does not require appreciable optimization of the laser pulse shape. Instead, I show how to significantly break the structural inversion symmetry of the enantiomers by properly alternating the polarization axes of the pulses in the driving field, and I use numerical simulations to demonstrate that this approach will lead to significant and experimentally measurable structural asymmetries between the enantiomers when detected by Coulomb explosion imaging. While less effective than the full closed-loop approach described in the fourth article, this new method has the important advantage of being significantly less challenging to implement experimentally.

In the sixth and final paper, I describe a novel approach to coherent control of my own design that is based on the application of a trained neural network to generate a control field based on dynamic experimental feedback from the molecular system. By training the network to generate a control field that can successfully achieve a desired control objective on a system being subject to arbitrary random perturbations, I argue that the network should in principle be able to achieve the same objective in a real life experimental situation. In general, this relates to my previous work in the sense that I once again exploit the flexibility that comes with a nonresonant DSC approach to manipulating

molecular dynamics. This final paper is fairly speculative in nature, and there are still a number of open questions that need resolving before the ideas put forth here can be considered fully mature.

Appendix A

Non-resonant dynamic stark control of vibrational motion with optimized laser pulses

Non-resonant dynamic stark control of vibrational motion with optimized laser pulses

Esben F. Thomas and Niels E. Henriksen

Citation: The Journal of Chemical Physics **144**, 244307 (2016); doi: 10.1063/1.4954663
View online: http://dx.doi.org/10.1063/1.4954663
View Table of Contents: http://scitation.aip.org/content/aip/journal/jcp/144/24?ver=pdfcov
Published by the AIP Publishing

Non-resonant dynamic stark control of vibrational motion with optimized laser pulses

Esben F. Thomas and Niels E. Henriksen
Department of Chemistry, Technical University of Denmark, Building 207, DK-2800 Kongens Lyngby, Denmark

(Received 2 May 2016; accepted 10 June 2016; published online 28 June 2016)

The term dynamic Stark control (DSC) has been used to describe methods of quantum control related to the dynamic Stark effect, i.e., a time-dependent distortion of energy levels. Here, we employ analytical models that present clear and concise interpretations of the principles behind DSC. Within a linearly forced harmonic oscillator model of vibrational excitation, we show how the vibrational amplitude is related to the pulse envelope, and independent of the carrier frequency of the laser pulse, in the DSC regime. Furthermore, we shed light on the DSC regarding the construction of optimal pulse envelopes — from a time-domain as well as a frequency-domain perspective. Finally, in a numerical study beyond the linearly forced harmonic oscillator model, we show that a pulse envelope can be constructed such that a vibrational excitation into a specific excited vibrational eigenstate is accomplished. The pulse envelope is constructed such that high intensities are avoided in order to eliminate the process of ionization. *Published by AIP Publishing.* [http://dx.doi.org/10.1063/1.4954663]

I. INTRODUCTION

Since the advent of the laser in the 1960's, the possibility of using coherent light sources to control molecules and molecular reactions has been a hot topic in photochemistry.[1–6] The ability to generate laser pulses on ever shorter time scales, down to femto- and even atto-second durations, as well as the development of optical techniques for actively controlling the time-dependent features of these pulses, has driven the field forward into new lines of theoretical and experimental inquiry. In general, the attainment of tools that are controllable on the same characteristic time scales as the molecular systems on which they act has led to a deeper understanding of a variety of time-dependent quantum phenomena.

Experimentally, capabilities have advanced in step with developments in laser, computer, and optical technology. In 1992 Judson and Rabitz[7] described a novel method of combining adjustable spectral pulse shapers[8,9] with evolutionary algorithms[10] in closed-loop schemes that could generate shaped laser pulses for driving molecular systems into desired states. While this technique has been demonstrated and employed successfully in a number of experimental applications,[5,11–16] the complexity of the systems, and of the pulses that are generated via this kind of "black box" optimization approach, makes it difficult to ascertain the mechanisms behind the interaction dynamics.

At higher field strengths, polarization forces, i.e., the distortion of electronic states leading to induced dipole moments related to the polarizability, can play an important role. The application and control of these polarization forces (via ultrashort optimized laser pulses) has been exploited experimentally in order to control the rotational, vibrational, and dissociation dynamics of molecules. The application of laser pulses with a temporal duration shorter than a rotational period leads to post-pulse time-dependent molecular alignment due to the sudden switch-on/-off of an angular-dependent interaction potential.[17] Similarly, time-dependent modifications of the interaction potential associated with vibrational/torsional motion in molecules have been reported.[18–20] For non-adiabatic motion in molecular photodissociation involving excited electronic states, similar effects have been used to modify the dissociation dynamics.[21–24] A key feature of the above phenomena involving polarization forces is that control can be exerted under non-resonant conditions.

The challenge for theorists is to develop models and techniques that describe the interaction between an electromagnetic field and a molecule that are accurate enough to be realistic, yet simple enough to be understood qualitatively. A few theoretical studies have discussed the systematic numerical treatment of polarization effects,[25,26] and some approaches have treated the interaction approximately;[27–30] however, the majority of theoretical studies in laser control of chemical dynamics have only included permanent dipole moments in the laser-molecule interaction.

The motivation behind this paper is to enhance our physical insight into time-dependent shifts in relevant electronic energy levels that can arise due to polarization forces. When a molecule interacts with a time-dependent electric field, the distortion of the electronic states leads to the so-called dynamic Stark effect,[22,31] which as the name suggests is the time-dependent counterpart to the static Stark effect.[32] The term dynamic Stark control (DSC) has been used to describe methods of quantum control related to the dynamic Stark effect (see, e.g., Refs. 18 and 21). At this point, it is also pertinent to mention the related phenomenon of Impulsive Stimulated Raman Scattering (ISRS).[33–37] One of our intentions here is to employ analytical models that present clear and concise interpretations of the principles behind DSC, so that we may develop our intuitive understanding of how these effects operate.

The structure and main results of this paper are summarized in the following. For completeness, we start with a derivation of the laser-molecule interaction within the Born-Oppenheimer approximation, including the polarization term described in a perturbative manner. Then, within a linearly forced harmonic oscillator model of vibrational excitation, we show analytically (in the non-resonant regime) how the vibrational amplitude is related to the pulse envelope and independent of the carrier frequency of the laser pulse. Furthermore, we shed light on the DSC regarding the construction of optimal pulse envelopes – from a time-domain as well as a frequency-domain perspective.

Finally, in a numerical study beyond the linearly forced harmonic oscillator model, we show that a pulse envelope can be constructed such that a vibrational excitation into a specific excited vibrational eigenstate is accomplished. The pulse envelope is constructed such that high intensities are avoided in order to eliminate the process of ionization. Since control can be exerted under non-resonant conditions, we show that ignoring the carrier frequency allows for a relaxation of the criteria that an optimized pulse must fulfill, which in turn may help facilitate experimental implementation of theoretical results.

II. MODELING THE FIELD/MOLECULE INTERACTION

The general Hamiltonian of a molecule can be written as $\hat{H} = \hat{T}_{\text{nuc}} + \hat{H}_e$, where $\hat{T}_{\text{nuc}}$ is the nuclear kinetic energy and $\hat{H}_e$ is the electronic Hamiltonian. Invoking the adiabatic approximation, and confining ourselves to the electronic ground state ψ_0, we can calculate the electronic energy as a function of the nuclear position $\mathbf{R}$ by solving the equation

$$\hat{H}_e \psi_0(\mathbf{R};\mathbf{r}) = E_0(\mathbf{R})\,\psi_0(\mathbf{R};\mathbf{r}), \tag{1}$$

where $\mathbf{R}$ and $\mathbf{r}$ denote the respective nuclear and electronic position vectors, $\mathbf{R};\mathbf{r}$ denotes fixed $\mathbf{R}$ coordinates, and $E_0(\mathbf{R})$ is the electronic energy. Within the Born-Oppenheimer approximation, the time-dependent Schrödinger equation for the nuclear wave function $\chi_0(\mathbf{R},t)$ will take the form

$$i\hbar\frac{\partial}{\partial t}\chi_0(\mathbf{R},t) = \left[\hat{T}_{\text{nuc}} + E_0(\mathbf{R})\right]\chi_0(\mathbf{R},t). \tag{2}$$

When interacting with a molecule, a coherent laser pulse can be approximated as a spatially homogenous, time-dependent electric field $\boldsymbol{\varepsilon}(t)$, provided the carrier wavelength is large compared to the molecular dimensions. In this limit, the interaction of the field with the electrons and nuclei within the electric-dipole approximation can be written as the following contribution to the molecular Hamiltonian,

$$\hat{H}_{\text{int}} = -\boldsymbol{\mu}\cdot\boldsymbol{\varepsilon}(t), \tag{3}$$

where $\boldsymbol{\mu}$ is the electric dipole moment. When this term is introduced into Eq. (1), the field-free potential energy surface $E_0(\mathbf{R})$ will become modified due to the interaction with $\boldsymbol{\varepsilon}(t)$. This modified energy surface, which we will call E_{int} (we will simplify the notation in the following steps by omitting functional dependencies on $\mathbf{R}$ and $\mathbf{r}$), can be expressed as

$$E_{\text{int}} = \left\langle \psi_0^{\varepsilon} \middle| \hat{H}_e - \boldsymbol{\mu}\cdot\boldsymbol{\varepsilon}(t) \middle| \psi_0^{\varepsilon} \right\rangle, \tag{4}$$

where the $^{\varepsilon}$ superscript on ψ_0^{ε} indicates that the electronic wave function has been modified by the external field, and the integration is over the electronic coordinates $\mathbf{r}$. As stated, some treatments correct for the shift in charge distribution by explicitly calculating the ψ_0^{ε} eigenfunctions in the presence of external fields of varying strengths.[25] While this yields a solution that is in principle exact, the complexity of the approach can obfuscate the dynamics behind the interaction. We will instead utilize a simpler approach that treats the influence of the field on the electronic wave functions as a perturbation. We simplify the subsequent analysis by aligning the polarization direction of the external field with the z axis, i.e., $\boldsymbol{\varepsilon}(t) = \varepsilon(t)\,\hat{z}$, and $\boldsymbol{\mu} = \mu_z$. Assuming that $\varepsilon(t)$ is sufficiently small, we can express the modified potential energy surface $E_{\text{int}}(\mathbf{R})$ as a second-order Taylor expansion around the unperturbed potential function $E_0(\mathbf{R})$,

$$E_{\text{int}} \approx E_0 + \left(\frac{dE_{\text{int}}}{d\varepsilon(t)}\right)_0 \varepsilon(t) + \frac{1}{2}\left(\frac{d^2E_{\text{int}}}{d\varepsilon^2(t)}\right)_0 \varepsilon^2(t), \tag{5}$$

where the $_0$ subscript indicates that the derivative is evaluated at $\varepsilon(t) = 0$. Applying the Hellmann-Feynman theorem[38] to Eq. (4), it can be shown that differentiation of E_{int} with respect to $\varepsilon(t)$ yields

$$\frac{dE_{\text{int}}}{d\varepsilon(t)} = -\langle\mu_z\rangle. \tag{6}$$

Combining Eqs. (5) and (6) leads to the relation

$$\langle\mu_z\rangle = -\left(\frac{dE_{\text{int}}}{d\varepsilon(t)}\right)_0 - \left(\frac{d^2E_{\text{int}}}{d\varepsilon^2(t)}\right)_0 \varepsilon(t). \tag{7}$$

We can derive explicit functions for these two terms by applying first-order perturbation theory to the electronic wave functions and assuming that the envelope of $\varepsilon(t)$ changes slowly relative to the characteristic time scales of the system, i.e., we disregard any transient oscillations in electronic density that may arise due to the sudden application of a perturbing field,[27]

$$\langle\mu_z\rangle = \langle\psi_0|\,\mu_z\,|\psi_0\rangle + \frac{2}{\hbar}\sum_{n\neq 0}\frac{\omega_{n0}|\langle\psi_n|\,\mu_z\,|\psi_0\rangle|^2}{\omega_{n0}^2 - \omega_c^2}\varepsilon(t), \tag{8}$$

where $\omega_{n0} = (E_n - E_0)/\hbar$ are the unperturbed electronic state transition frequencies, ω_c is the carrier frequency of $\varepsilon(t)$, and the $n \neq 0$ subscript indicates that the ground state is omitted from the sum. In our analysis, we assume that $\omega_c \ll \omega_{n0}$, i.e., the field carrier frequency is much lower than the electronic state transition frequencies of the molecule, which is generally true as long as the nuclear motion is confined to the electronic ground state. In this case Eq. (8) simplifies to

$$\langle\mu_z\rangle = \langle\psi_0|\,\mu_z\,|\psi_0\rangle + \frac{2}{\hbar}\sum_{n\neq 0}\frac{|\langle\psi_n|\,\mu_z\,|\psi_0\rangle|^2}{\omega_{n0}}\varepsilon(t). \tag{9}$$

The first and second terms on the right hand side of Eq. (9) are the permanent electric dipole (PED) and static molecular polarizability (SMP) terms, respectively. The PED term is merely the charge distribution of the field-free molecule. If the field is relatively weak, the molecular electrons will not be significantly perturbed and the PED term is sufficient to accurately describe the dynamics of the system. If the

molecule is subjected to more intense fields, the ψ_0 electronic wave functions will be significantly modified, leading to a shift in the molecular charge distribution that the PED will not be able to account for. The SMP term is the first order correction to this field induced charge shift and is therefore linearly proportional to the field amplitude $\varepsilon(t)$.

It is possible to extend the aforementioned principle of derivation to include higher orders of $\varepsilon(t)$. Nevertheless, in this paper it will be shown that even when only the PED and SMP terms are included, it is possible to qualitatively reproduce many of the behaviors observed in more complicated models, the strength of the approach being that we are afforded the clarity that comes from being able to derive relatively simple analytical solutions for the time-dependent dynamics.

While Eq. (9) demonstrates how the PED and SMP terms may be calculated provided the electronic eigenfunctions are known, we will now disregard the exact form of these functions and instead focus on their relation to $\varepsilon(t)$. Equation (9) can thus be recast in a simplified form

$$\langle \mu_z \rangle = \mu + \alpha \varepsilon(t). \tag{10}$$

Comparing Eqs. (10), (7), and (5), we see that

$$E_{\text{int}} = E_0 - \mu\varepsilon(t) - \frac{1}{2}\alpha\varepsilon^2(t). \tag{11}$$

Within the Born-Oppenheimer approximation, μ and α will be functions of $\mathbf{R}$ as they contain the electronic eigenfunctions $\psi_n(\mathbf{R};\mathbf{r})$, where the electronic coordinates have been integrated out in the matrix elements of Eq. (9). Returning to Eq. (2), we can now update the expression to include the second order correction to the energy that arises due to coupling with the external field, reinstating the functional dependencies on $\mathbf{R}$ for completeness,

$$i\hbar\frac{\partial}{\partial t}\chi_0(\mathbf{R},t) = \left[\hat{T}_{\text{nuc}} + E_0(\mathbf{R}) - \hat{C}_{\text{int}}(\mathbf{R},t)\right]\chi_0(\mathbf{R},t), \tag{12}$$

where

$$\hat{C}_{\text{int}}(\mathbf{R},t) = \mu(\mathbf{R})\varepsilon(t) + \frac{1}{2}\alpha(\mathbf{R})\varepsilon^2(t). \tag{13}$$

III. A LINEARLY FORCED HARMONIC OSCILLATOR MODEL OF DSC

In order to gain insight into the wave packet dynamics described by Eqs. (12) and (13), we consider a one-dimensional model of a simple diatomic molecule aligned with the field polarization direction, with interatomic distance coordinate R. If we assume that the variation in R is small, we can approximate $\mu(R)$ and $\alpha(R)$ as linear expansions around the molecular equilibrium distance R_{eq}. It can be shown that the zeroth order terms of these expansions will not impact the dynamics of the field/molecule interaction, and can therefore be disregarded.[39] Approximating the unperturbed ground state energy surface as a harmonic expansion around R_{eq}, the potential energy of the molecule takes the form of a linearly forced harmonic oscillator with eigenfrequency ω_0,

$$V(R,t) = \frac{1}{2}m\omega_0^2R^2 - \left[\left(\frac{d\mu(R)}{dR}\right)_{\text{eq}}\varepsilon(t) + \frac{1}{2}\left(\frac{d\alpha(R)}{dR}\right)_{\text{eq}}\varepsilon^2(t)\right]R, \tag{14}$$

where we have set $R_{\text{eq}} = 0$ to simplify the notation, and the $_{\text{eq}}$ subscript indicates that the derivative is taken at $R = R_{\text{eq}} = 0$. We denote the expectation value of the wave packet position at time t as $\langle R \rangle(t)$. Ehrenfest's theorem can be used to show that the expectation value in a harmonic potential will obey classical dynamics.[40] This allows us simplify the description of the wave packet by letting $\langle R \rangle(t) \equiv R(t)$, where $R(t)$ denotes the position of a classical point particle. Assuming $R(t_0) = 0$, the position expectation value of the wave packet at time t can be found by solving the integral,[41]

$$R(t) = \frac{1}{\omega_0 m}\left[\sin(\omega_0 t)\int_{t_0}^{t}\cos(\omega_0 t)F(t)\,dt - \cos(\omega_0 t)\int_{t_0}^{t}\sin(\omega_0 t)F(t)\,dt\right], \tag{15}$$

where $F(t)$ represents the time-dependent component of the differential equation, which in our case can be found from Eq. (14) to be

$$F(t) = \left[\mu'\varepsilon(t) + \frac{1}{2}\alpha'\varepsilon^2(t)\right], \tag{16}$$

where we recast $\alpha' = (d\alpha(R)/dR)_{\text{eq}}$ and $\mu' = (d\mu(R)/dR)_{\text{eq}}$ to simplify the notation. Inserting $F(t)$ into Equation (15), we can split the resulting expression into two components $R(t) = R_\mu(t) + R_\alpha(t)$, where

$$R_\mu(t) = \frac{\mu'}{\omega_0 m}\left[\sin(\omega_0 t)\int_{t_0}^{t}\cos(\omega_0 t)\varepsilon(t)\,dt - \cos(\omega_0 t)\int_{t_0}^{t}\sin(\omega_0 t)\varepsilon(t)\,dt\right] \tag{17}$$

and

$$R_\alpha(t) = \frac{\alpha'}{2\omega_0 m}\left[\sin(\omega_0 t)\int_{t_0}^{t}\cos(\omega_0 t)\varepsilon^2(t)\,dt - \cos(\omega_0 t)\int_{t_0}^{t}\sin(\omega_0 t)\varepsilon^2(t)\,dt\right]. \tag{18}$$

Now, let $\varepsilon(t)$ take the form of a transform limited Gaussian pulse with amplitude A_0, second moment pulse width σ and (positive) angular carrier frequency ω_c,

$$\varepsilon(t) = A_0\cos(\omega_c t)\exp\left(-\frac{t^2}{2\sigma^2}\right), \tag{19}$$

where it is assumed that $\omega_c\sigma \gg 1$, i.e., the pulse envelope is wide enough to allow for multiple oscillations. When this pulse interacts with the system, it may induce oscillations in the position of the wave packet which will continue after the pulse has died out. Combining Eqs. (17)–(19), and evaluating the integrals in the limit where $t_0 \to -\infty$ and $t \to \infty$, the parity of the integrand functions leads to the elimination of the second terms in the brackets of Eqs. (17) and (18). The amplitude of the wave packet oscillation in the $t \to \infty$ limit,

which will henceforth be denoted by Γ, can be written as

$$\Gamma\left(A_0,\omega_c,\sigma\right) = \left(I_\mu^2\left(A_0,\omega_c,\sigma\right) + I_\alpha^2\left(A_0,\omega_c,\sigma\right)\right)^{1/2}, \tag{20}$$

where

$$I_\mu\left(A_0,\omega_c,\sigma\right) = \frac{\mu' A_0 \sigma}{\omega_0 m}\sqrt{\frac{\pi}{2}}\left[\exp\left(-\frac{\sigma^2(\omega_0-\omega_c)^2}{2}\right) + \exp\left(-\frac{\sigma^2(\omega_0+\omega_c)^2}{2}\right)\right] \tag{21}$$

and

$$I_\alpha\left(A_0,\omega_c,\sigma\right) = \frac{\alpha' A_0^2 \sigma\sqrt{\pi}}{4\omega_0 m}\left[\exp\left(-\frac{\sigma^2\omega_0^2}{4}\right) + \frac{1}{2}\exp\left(-\frac{\sigma^2(\omega_0-2\omega_c)^2}{4}\right) + \frac{1}{2}\exp\left(-\frac{\sigma^2(\omega_0+2\omega_c)^2}{4}\right)\right], \tag{22}$$

where $\Gamma\left(A_0,\omega_c,\sigma\right)$ indicates that the wave packet amplitude is dependent on the pulse amplitude, carrier frequency, and width and $I_\mu\left(A_0,\omega_c,\sigma\right)$ and $I_\alpha\left(A_0,\omega_c,\sigma\right)$ are the contributions from the dipole and polarizability terms, respectively. Inspecting Eq. (21), it is clear that the contribution from the first bracketed term becomes large when the carrier frequency ω_c is close to the harmonic eigenfrequency ω_0. Likewise, the middle term in Eq. (22) will become large when $\omega_c \approx \frac{1}{2}\omega_0$. We note in passing that this result is similar to one obtained in a study in which the excitation of a homonuclear diatomic molecule was investigated using a complete quantum mechanical treatment.[25] The two aforementioned contributions to the wave packet amplitude can be interpreted as one and two photon absorption processes, respectively. These terms are dependent on the pulse carrier frequency, and their behavior differs qualitatively from the first term in the brackets on the right side of Eq. (22), which dominates in the $|\omega_c| \gg \omega_0$ limit, in which Eq. (20) is reduced to the following form:

$$\Gamma(A_0,\sigma)_{|\omega_c|\gg\omega_0} = \frac{\alpha' A_0^2 \sigma\sqrt{\pi}}{4\omega_0 m}\exp\left(-\frac{\sigma^2\omega_0^2}{4}\right). \tag{23}$$

In this limit, we see the behavior that characterizes the dynamic Stark effect, since the wave packet amplitude in this regime is no longer influenced by the pulse carrier frequency. To further illustrate this concept, a graphical representation of $\Gamma\left(A_0,\omega_c,\sigma\right)$ for parameters selected to approximate the HCl electronic ground state[42,43] is shown in Fig. 1. Here, the function is plotted for varying values of σ and ω_c, at a constant peak pulse intensity of 10 TW/cm^2. The two horizontal excitation "channels" visible in the top half of the figure arise due to the one and two photon absorption terms. The bottom half of the figure shows how the wave packet response becomes independent of carrier frequency as the system parameters move into the dynamic Stark regime.

Note also how the wave packet amplitude in Fig. 1 starts to primarily respond to changes in the pulse width when $|\omega_c| \gg \omega_0$, as Eq. (23) indicates. Fig. 2 shows a 1D plot of variations in Γ as a function of the pulse width in the region under the red line in Fig. 1.

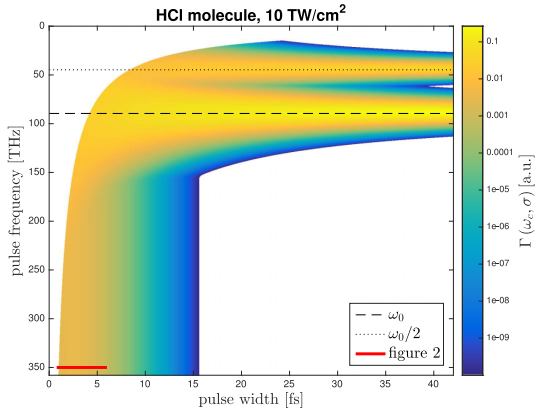

FIG. 1. The wave packet oscillation amplitude $\Gamma(\omega_c,\sigma)$ (Eq. (20)) as a function of pulse carrier frequency ω_c and pulse width σ. For comparison, the peak intensity is held constant at 10 TW/cm^2. White regions represent pulses that either produce negligible wave packet amplitude ($<1\times10^{-10}a_0$) or are comprised of envelopes that are too narrow to allow for one full field oscillation. The dashed black line shows the location of the harmonic eigenfrequency ω_0 of the system, and the dotted black line shows the location of $\omega_0/2$. Note how the peaks present at these frequencies become narrower as the pulse width increases. The red line shows the location of the 1D cross section plotted in Fig. 2.

The peak of this function indicates that there is a pulse width that will produce maximum excitation. The location of this peak can be found by differentiating Eq. (23) and can be shown to be proportional to the system oscillation period $T = 2\pi/\omega_0$,

$$\sigma_{\text{optimum}} = \frac{T}{\pi\sqrt{2}}. \tag{24}$$

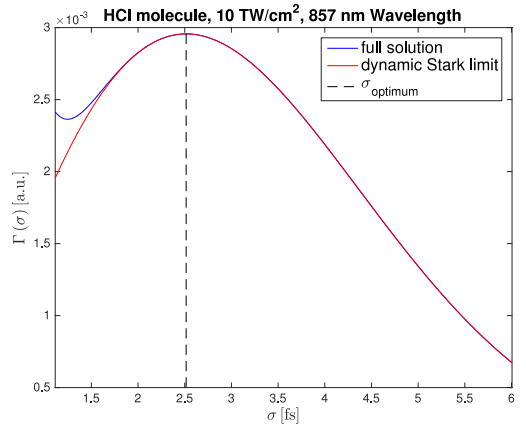

FIG. 2. The wave packet amplitude when the central frequency of the driving Gaussian pulse approaches the off-resonant Stark limit. As in Figure 1, the peak intensity is held fixed at 10 TW/cm^2. In this regime, the system ceases to respond to the pulse frequency and instead the excitation becomes primarily dependent on the shape of the pulse envelope. The blue curve indicates the full solution from Eq. (20), the red curve shows the predicted behavior when the dynamic Stark effect is the only contributing factor to wave packet amplitude as per Equation (23), and the dashed line shows the location of optimal pulse width given by the relation in Eq. (24).

Note that in Figs. 1 and 2, pulse fluence is not held constant since we vary the width and keep the peak intensity fixed. The motivation behind this choice is traced to the fact that at the frequencies we are considering, it can be shown that limiting the peak intensity is of critical importance when it comes to diminishing unwanted ionization effects, whereas changes in the pulse fluence have been shown to be less impactful in this respect.[44–47] If we choose to change the parameters of our analysis by instead keeping the pulse energy constant, it would not be possible to calculate a non-trivial optimal pulse width like the one in Eq. (24). The reason for this can easily be understood considering that in order to keep the fluence constant, the amplitude A_0 must be inversely proportional to the square root of the pulse width, i.e., $A_0 \propto 1/\sqrt{\sigma}$. Inserting this relation into Eq. (23), we see that the exponential prefactor will become independent of σ, resulting in a monotonic increase in the wave packet amplitude as $\sigma \to 0$.

We will now demonstrate the impact of applying a pure Gaussian envelope to our model in the dynamic Stark limit. Defining the envelope function as

$$E_{\text{env}}(t) = A_0 \exp\left(-\frac{t^2}{2\sigma^2}\right), \tag{25}$$

we see that setting $\omega_c = 0$ in Eq. (19) will result in the same expression. We can use this relation to immediately find the solutions to Eq. (15) when $F(T) = E_{\text{env}}(t)$ by simply setting $\omega_c = 0$ in the results we have already derived. The amplitude that arises due to coupling with the polarizability term can be calculated in this way using Eq. (22), and is found to be

$$I_\alpha(A_0, \omega_c, \sigma)_{\omega_c=0} = \frac{\alpha' A_0^2 \sigma\sqrt{\pi}}{2\omega_0 m} \exp\left(-\frac{\sigma^2\omega_0^2}{4}\right). \tag{26}$$

Note that setting $\omega_c = 0$ is just a mathematical trick, and for the purposes of this derivation, we can assume the system is still operating in the dynamic Stark regime. This allows us to disregard contributions from the permanent molecular dipole term, meaning Eq. (26) is an expression for the total wave packet amplitude in this limit, i.e.,

$$\Gamma(A_0, \sigma)_{\text{env}} = I_\alpha(A_0, \omega_c, \sigma)_{\omega_c=0}. \tag{27}$$

Comparing Eqs. (26), (27), and (23), we see that $\Gamma(A_0, \sigma)_{\text{env}} = 2 \times \Gamma(A_0, \sigma)_{|\omega_c| \gg \omega_0}$. This demonstrates how contributions to the wave packet amplitude from the molecular polarizability term will double when the carrier frequency is eliminated from the pulse envelope. The reason for this is obvious when one considers that as a potential surface is shifted by a field oscillating in the $|\omega_c| \gg \omega_0$ limit, the wave packet will only "feel" the period averaged displacement since it cannot react quickly enough to the rapidly changing field components. Since the contribution from the molecular polarizability term is proportional to the square of the driving pulse, this is equivalent to multiplying the squared envelope function by a factor of 1/2, the upshot of which is that in the dynamic Stark limit, Eq. (14) can be simplified into the familiar form:[31]

$$V(R,t) = \frac{1}{2} m\omega_0^2 R^2 - \frac{1}{4}\alpha' E_{\text{env}}^2(t)\, R, \tag{28}$$

where the last term is equivalent to a time-dependent shift of the potential following the squared pulse envelope.

A. Pulse trains

We now investigate the impact of splitting the Gaussian pulse described by Eq. (19) into a train of N identical copies of itself separated by time interval τ, making use of the linearly forced harmonic oscillator model to derive analytical solutions to the time-dependent dynamics. We assume the pulses interact with the molecule in the dynamic Stark limit, and all share the same phase (i.e., they constructively interfere). The envelope of the pulse train function can therefore be expressed as

$$E_{\text{env}}(t) = \frac{A_0}{\sqrt{N}} \sum_{n=0}^{N-1} \exp\left(-\frac{(t - n\tau)^2}{2\sigma^2}\right). \tag{29}$$

Note that the peak amplitude of each pulse in the series is set to $A_0/\sqrt{N}$, which ensures that the total fluence of the pulse train will be equivalent to that of the original pulse. Inserting (29) into Eq. (15) and solving in the dynamic Stark limit, the general solution for the wave packet amplitude is found to be

$$\Gamma(A_0, \sigma, \tau, N) = \frac{\alpha' A_0^2 \sigma\sqrt{\pi}}{4\omega_0 m} \exp\left(-\frac{\sigma^2\omega_0^2}{4}\right) \times \frac{1}{N}\left[N + \sum_{n\neq m}^{N-1} \cos\left(\omega_0 \tau\,[n-m]\right)\right]^{1/2}. \tag{30}$$

If $\tau = 2\pi k/\omega_0 = kT$, where $k \in \mathbb{N}$ and T is the length of one wave packet oscillation period, the sum in the brackets of Eq. (30) can be rewritten as

$$\sum_{n\neq m}^{N-1} \cos\left(2\pi k\,[n-m]\right) = N(N-1). \tag{31}$$

Combining relations (30) and (31), we see that the second line of Eq. (30) becomes unity and the functional dependency on N and τ drops out, leaving a result that is identical to Eq. (23). This means that when the pulse spacing τ is an integer multiple of the system oscillation period T, the wave packet amplitude induced by the pulse train is equivalent to the amplitude produced by a single pulse of equivalent energy. This indicates that when they are spaced in this manner, the effect of each sub-pulse on the total amplitude will be additive. It is interesting to note that these results will also hold when the pulses in the train significantly overlap.

If we instead consider a pulse train containing only two pulses, and let $\tau = T(k + 1/2)$, i.e., the spacing between the pulses is an integer number of wave packet oscillation periods plus 1/2, we find that the bracketed term in Eq. (30) disappears, since

$$\sum_{n\neq m}^{N-1} \cos\left(2\pi\,(k+1/2)\,[n-m]\right) = -2, \tag{32}$$

when $N = 2$ and $k \in \mathbb{N}$. This result demonstrates that spacing two pulses in this manner will lead to no net excitation of the system, since effectively the oscillations set in motion by the first pulse are exactly canceled by the second pulse. In this way, we can see that the effect of multiple pulses on the wave packet amplitude may also be subtractive, depending on how we time their arrival to the system. Here, one may consider the analogy of pushing a child on a swing, since it is clear that

the change in the swing amplitude depends largely on when we apply our push.

If $\tau \neq kT$ and N is very large, it can be shown that the sum term in Eq. (30) will be $\ll N$, since the negative and positive contributions to the sum will on average cancel each other out. In this limit, the resulting amplitude will be negligible since the solution given by Eq. (30) will be proportional to $1/\sqrt{N}$. In this way it is shown how the ability to control the spacing in a train of pulse envelopes can effectively be used to highlight certain system transitions by dampening others. Note, also, that using a pulse train in place of a single pulse allows us to limit the peak intensity while still exerting control over the molecule, an important factor when it comes to minimizing unwanted ionization.

In 1991, it was demonstrated how individual phonon modes in an α-perylene molecular crystal sample were excited by trains of pulses with non-resonant carrier frequencies when the inter-pulse spacing was equivalent to a modal oscillation period.[33] It was also found that applying a single pulse of equivalent energy to the same system resulted in the excitation of a large number of different modes, i.e., the ability to selectively excite an individual mode was lost. These experimental results are in accordance with our theoretical predictions that controlling the pulse train spacing leads to modal selectivity.

More recently, it has been shown that the amplitude of the induced dihedral oscillations in a molecule approximately doubled when the system was hit with two Gaussian kick pulses instead of one, provided the temporal separation between the pulses was equivalent to the system oscillation period. It was also shown that the dihedral oscillations became very small when the spacing between the pulses was reduced to roughly half a system oscillation period.[20] This backs up our result showing that the effect of multiple pulses on the wave packet oscillation amplitude can be additive or subtractive, depending on how we adjust the timing between each pulse.

B. Frequency-space interpretation

Assuming conditions where the dynamic Stark effect dominates and the system response is independent of the pulse frequency, and given a generalized pulse envelope function $E_{\text{env}}(t)$, we can use Eqs. (15), (18), and (20) to show that the wave packet amplitude when $t \to \infty$ can be written as

$$\Gamma(A_0,\sigma) = \frac{\alpha'}{4\omega_0 m}\left(\left[\int_{-\infty}^{\infty}\cos(\omega_0 t)\,E_{\text{env}}^2(t)\,dt\right]^2 + \left[\int_{-\infty}^{\infty}\sin(\omega_0 t)\,E_{\text{env}}^2(t)\,dt\right]^2\right)^{1/2}. \quad (33)$$

If $E_{\text{env}}(t)$ is a square integrable function, Parseval's theorem[48] allows us to recast Eq. (33) in the spectral domain

$$\Gamma(A_0,\sigma) = \frac{\alpha'}{8\pi\omega_0 m}\left(\left[\int_{-\infty}^{\infty}\tilde{E}_{\text{env}}(\omega)\,\tilde{E}^*_{\text{env}}(\omega-\omega_0)\,d\omega\right] \times \left[\int_{-\infty}^{\infty}\tilde{E}_{\text{env}}(\omega)\,\tilde{E}^*_{\text{env}}(\omega+\omega_0)\,d\omega\right]\right)^{1/2}, \quad (34)$$

where $\tilde{E}_{\text{env}}(\omega)$ is the Fourier transform of $E_{\text{env}}(t)$ and the * superscript denotes complex conjugation. Inspecting the two integrals on the right side of Eq. (34) shows that the width of the spectral distribution must be broader than ω_0 in order to lead to appreciable vibrational amplitude. Additionally, the form of Eq. (34) can generate insight as to how the underlying mechanism of the dynamic Stark effect can be interpreted as impulsive stimulated Raman scattering. To understand why this is, consider first the schematic shown in Fig. 3(a) of a Stokes-Raman scattering event, in which the ground state of a harmonic oscillator is excited up one level via a two step process consisting of transitions to and from a higher lying virtual state by two non-resonant frequencies.

This type of transition may occur provided that the spectral distribution of the laser pulse contains at least two frequencies where the difference between these frequencies is an eigenfrequency of the system. To further illustrate the

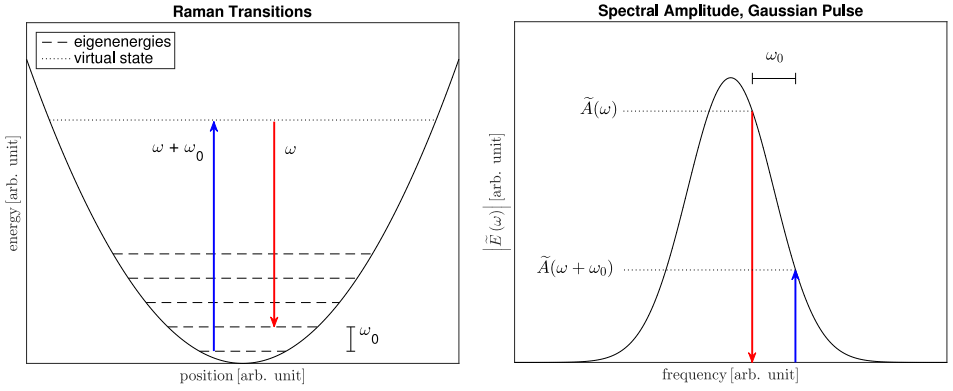

FIG. 3. (a) A pictorial representation of a Stokes-Raman scattering event in the quantum harmonic oscillator. Starting in the ground state, a photon with energy $\hbar(\omega+\omega_0)$ is absorbed, resulting in a transition to a higher virtual state. Strictly speaking, this is a forbidden transition; however, emission of a photon with energy $\hbar\omega$ directly afterwards results in a net absorption of $\hbar\omega_0$. (b) Spectral amplitude of a temporal Gaussian pulse. The arrows indicate the location of one possible Stokes-Raman scattering event. To find the total probability of a certain transition taking place, we must integrate the probability of all possible scattering events of a specific frequency, as indicated by Eq. (34).

point, assume that the transitions illustrated in Figure 3(a) are caused by a flat phase spectral distribution of a Gaussian pulse like the one from Eq. (19), as shown in Fig. 3(b). Here we see that if the pulse contains frequencies separated by the harmonic eigenfrequency ω_0, it may generate transitions to and from higher lying virtual states and thereby produce non-resonant transitions in our model system.

To show how this picture relates to Eq. (34), we put forth the naive argument that the probability of the transition in Fig. 3(b) taking place must somehow be proportional to the product of the spectral amplitudes of the two frequency components $\tilde{A}(\omega)$ and $\tilde{A}(\omega+\omega_0)$,

$$P_{\uparrow\omega\downarrow\omega+\omega_0} \propto \tilde{A}(\omega)\,\tilde{A}(\omega+\omega_0). \tag{35}$$

Building on this notion, the total probability of a Raman transition of a specific frequency taking place must be proportional to the sum of all possible two step transitions that the frequency content of the pulse will allow, which can be expressed in integral form as

$$P_{\text{tot}} \propto \int_{-\infty}^{\infty} \tilde{A}(\omega)\,\tilde{A}(\omega+\omega_0)\,d\omega. \tag{36}$$

Comparing Eqs. (36) and (34) we see that they are qualitatively similar. Indeed, for a flat phase spectral distribution, i.e., given $\tilde{E}_{\text{env}}(\omega) = \left|\tilde{E}_{\text{env}}(\omega)\right| \exp(i\phi(\omega))$ and $\phi(\omega) = const.$, it can easily be shown that $\int_{-\infty}^{\infty} \tilde{E}_{\text{env}}(\omega)\,\tilde{E}^{*}_{\text{env}}(\omega+\omega_0)\,d\omega = \int_{-\infty}^{\infty} \tilde{E}_{\text{env}}(\omega)\,\tilde{E}^{*}_{\text{env}}(\omega-\omega_0)\,d\omega$, in which case the two expressions are identical save for the fact that in the exact solution given by Eq. (34) we have been able to determine the pre-factor as well.

These results, particularly the form of Eq. (36), are quite similar to results obtained by Meshulach and Silberberg.[36] The key difference is that in our paper, Eq. (34) is in principle exact, although our model of vibrational excitation is a simplified one. Qualitatively, the work done by Meshulach and Silberberg takes the opposite approach by invoking an approximate solution to a fully described system, it is therefore noteworthy that they arrive at an expression similar to Eq. (36).

We can exploit our understanding of the mechanics behind the dynamic Stark effect to construct so-called dark pulses,[36] i.e., pulses with envelope shapes designed to make Raman transitions impossible within our model system of the linearly forced harmonic oscillator. We have already considered one example of a dark pulse envelope in this paper, namely, the case where a system with oscillation period T is driven by two sub-pulses with a temporal separation of $T(k+1/2), k \in \mathbb{N}$. While we demonstrated it analytically for completeness, from a temporal perspective it is perhaps fairly intuitive why this kind of pulse will produce no excitation.

A less trivial way we can construct a dark pulse is by using our knowledge of the relationship between the spectral distribution of the pulse envelope and the Raman transition rate. Equation (34) indicates that the integrand functions are effectively multiplied by -1 any time the phases of $\tilde{E}_{\text{env}}(\omega)$ and $\tilde{E}_{\text{env}}(\omega \pm \omega_0)$ differ by $n\pi$ (where $n \in \mathbb{Z}$). Therefore, phase-chirping $\tilde{E}_{\text{env}}(\omega)$ with a π step function over certain intervals can be shown to either limit or fully extinguish the rate of Raman transitions.

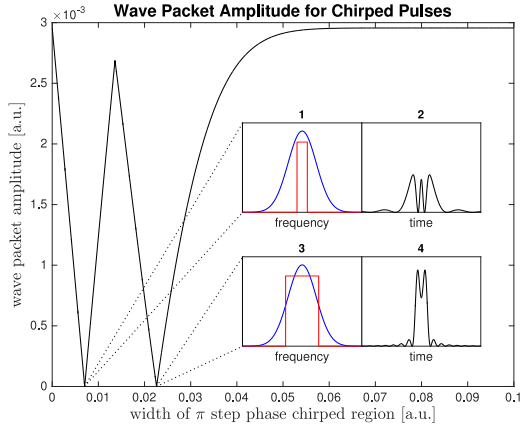

FIG. 4. This plot shows how the wave packet amplitude Γ changes as the width of the π step boxcar phase function increases. Insets 1 and 3 show sketches of the spectral pulse amplitude (blue) and the π step phase functions (red) when $\Gamma = 0$, while insets 2 and 4 show the corresponding temporal dark pulse envelope intensities $\propto |E_{\text{env}}(t)|^2$.

To exemplify this idea, we choose $\tilde{E}_{\text{env}}(\omega)$ to be the spectral distribution of a Gaussian pulse with $\sigma = \sigma_{\text{optimum}}$ as per Eq. (24). Figure 4 shows the analytic solution to Eq. (34) when $\tilde{E}_{\text{env}}(\omega)$ is phase chirped by a variable width π step "boxcar" function centered at the spectral intensity peak.

As we would expect, when the chirped region becomes very wide, Γ approaches the same value as that of the un-chirped pulse. The two minima where the wave packet amplitude becomes 0 occur when the width of the π chirped region is such that the positive and negative contributions to the integrals in Eq. (34) cancel each other out. The envelope intensities of these two dark pulses are sketched in insets 2 and 4 of Fig. 4, and their corresponding spectral amplitudes and phase functions are shown in insets 1 and 3. From a purely temporal perspective, it is not at all obvious that these envelope shapes should both be dark pulses, illustrating how knowledge of the spectral mechanism behind the dynamic Stark effect can be a useful tool when it comes to predicting and/or analyzing how a pulse will interact with a molecular system.

IV. STATE-TO-STATE VIBRATIONAL EXCITATION VIA DSC—A NUMERICAL EXAMPLE

While the analysis of simple pulse trains interacting with a harmonic potential allowed us to obtain analytic solutions to the time-dependent dynamics, so far we have only been able to affect the wave packet amplitude, due to the Ehrenfest (classical) dynamics of our simplified harmonic model.

We will now consider a more realistic system which will allow us to capture more complex behavior. The purpose of this investigation is twofold: One goal is to examine how well the principles discussed in Sec. III will generalize when we move beyond the harmonic approximation. Additionally, we feel it may be informative to demonstrate, as a proof of principle, that DSC can be employed to control dynamics that

are more sophisticated than simply increasing or decreasing the wave packet amplitude.

To this end, we expand the model of the HCl molecule to a Morse potential. As in the harmonic approximation, we retain the 1D description by once again assuming that the molecule is aligned with the field polarization direction along the z axis. The polarizability function will now be a semi-empirical function,[42] instead of the linear expansion we have been using thus far. Once again we assume the pulse carrier frequency is non-resonant and disregard any contributions to the molecular energy from the permanent electric dipole function. The pulse is simulated interacting with the HCl molecule using the split-operator method[49] to solve the time-dependent Schrödinger equation, where the time-dependent part of Eq. (12) is modeled by the simplified expression that holds in the dynamic Stark limit,

$$\hat{C}_{\text{int}}(R,t) = \frac{1}{4}\alpha(R)\,E^2_{\text{env}}(t)\,. \tag{37}$$

With respect to our stated intentions, the objective of achieving a state-to-state transition within this model was determined to be a suitable goal, as modifying the shape of the wave packet to overlap a target eigenstate calls for a more refined approach to the distribution of pulse energy over time than we have considered thus far. For this purpose, a genetic algorithm[10] was used to optimize the envelope shape of a 1 ps pulse, with the goal of maximizing the population transfer from the ground to the second vibrational state of the HCl molecule. The temporal pulse envelope is parameterized using a series of discrete, equally spaced regions or "bins." Each bin is assigned a constant value between 0 and some user-defined maximum that serves as the intensity cutoff limit. Construction of the actual pulse envelope for use in the simulation is accomplished by smoothing the entire series of bins using a Gaussian low pass filter, as shown in Fig. 5.

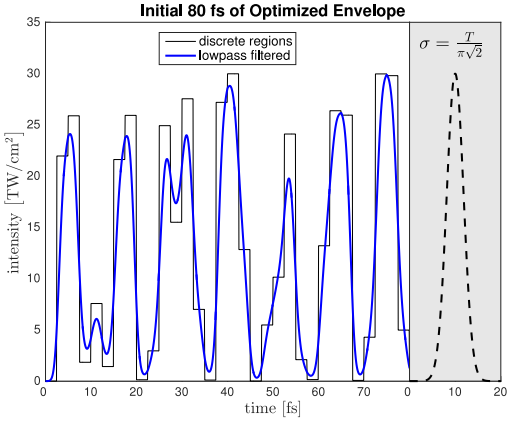

FIG. 5. The first 80 fs of the optimized pulse envelope shown in Fig. 6 (blue curve). The black line shows the pre-filtered distribution of the 2.5 fs discrete regions, where the genetic algorithm treats the height of each region as a free parameter. For comparison, the intensity-limited Gaussian pulse envelope calculated to maximize the wave packet amplitude within the harmonic approximation of the HCl model, in the dynamic Stark regime (as per Eq. (24)), is sketched on the same time scale in the gray box to the right.

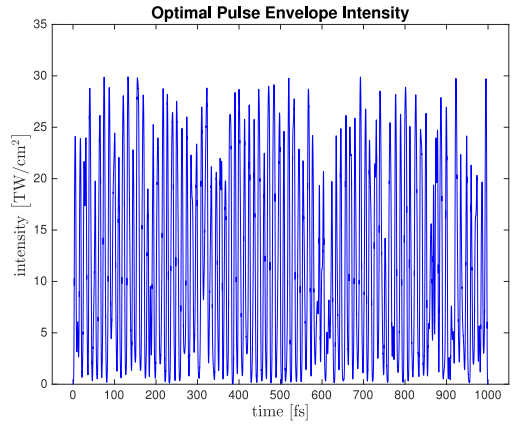

FIG. 6. The temporal intensity profile of the optimized pulse envelope. Note that the pulse carrier frequency (not pictured) is assumed to be oscillating much faster than the temporal evolution of the envelope shape.

The width of each bin was set to 2.5 fs, leading to a total of 400 free parameters distributed over the 1 ps time window. The temporal standard deviation of the Gaussian smoothing kernel was set to 1 fs, and the intensity limit of the pulse envelope was set to 30 TW/cm^2, which was estimated to be low enough as to not cause any appreciable system ionization using the FC-ADK tunneling ionization model.[47] Using these parameters, the genetic algorithm was able to achieve ~99% population transfer from the ground to second vibrational state of the HCl molecule after 346 generations with a population size of 2000 individuals. The full intensity profile of the optimized pulse envelope is shown in Fig. 6, and the occupancies of the first four vibrational states as a function of time are shown in Fig. 7.

The absolute value of the pulse envelope Fourier transform is shown in Fig. 8. For reference, we include the 0–1 and 1–2 transition frequencies here. The spectral interpretation of Stokes-Raman scattering events which we

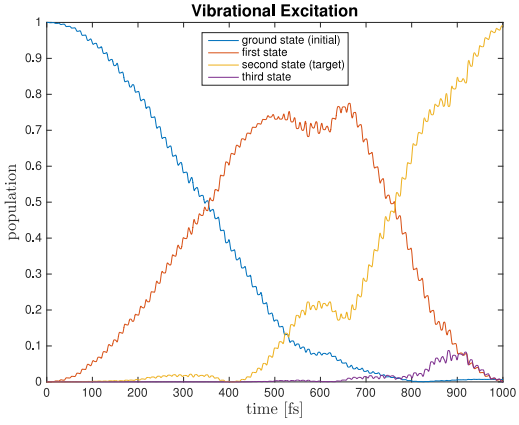

FIG. 7. Population of the ground, first, second, and third vibrational states of the HCl molecule when driven by the optimized pulse shown in Fig. 6, as a function of time. The final population of the second excited state is >99%.

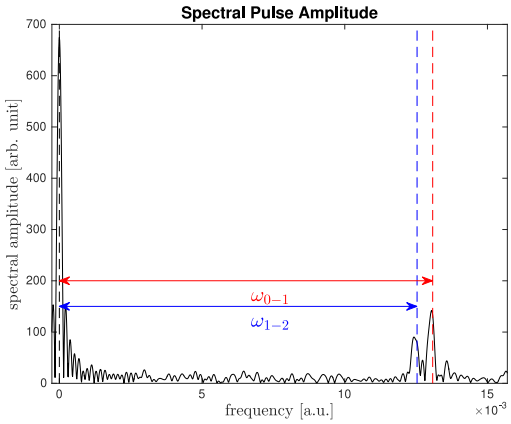

FIG. 8. Fourier transform of the optimized pulse envelope shown in Figure 6. Note that the pulse carrier frequency is disregarded here as well. Including the carrier frequency would merely shift the spectral distribution, but would not change its overall shape.

outlined in Eqs. (34) and (36) indicates that the optimized pulse should generate non-resonant transitions at the first two eigenfrequencies of the HCl molecule, since the spacing between the first and third peaks is very close to the 0–1 transition frequency, and likewise the spacing between the first and second peaks is close to the 1–2 transition.

As Figs. 5 and 6 indicate, the pulse envelope required to achieve the population transfer exhibits a complicated pulse-train structure, containing a large number of sub-pulses that evolve on ∼5–7 fs time scales. The sketch on the right side of Fig. 5 demonstrates how the sub-pulses present within the initial 80 fs of the optimized envelope evolve on comparable time scales to that of the optimal Gaussian pulse envelope calculated using the harmonic model of HCl as discussed in Section III, and in particular, as expressed by Eq. (24). While the comparison is rough, it does make sense from a controllability perspective that the numerically optimized pulse would generally contain subfeatures with shapes similar to the analytically calculated result from Eq. (24).

The narrow temporal widths of the sub-pulses, which are a reflection of the high vibrational frequency of the HCl molecule, may be challenging to implement experimentally. Heavier molecules are attractive in this respect, since they generally vibrate on slower time scales. The degree of influence each sub-pulse has on the system is related to the magnitude of the first derivative of the polarizability function $\alpha(\mathbf{R})$. This means that systems where the polarizability changes significantly as a function of the relative atomic displacement(s) are particularly well suited for the application of DSC.

Generally, the production of non-trivial shaped laser pulses on ultra-fast time scales is accomplished by manipulating the spectral components of an unshaped laser pulse using a spectral pulse shaper. Using such a device, the frequency components of the unshaped pulse may be acted on by attenuating their intensity and/or modifying their phase. The ability to change the phase and intensity distributions of the unshaped spectral pulse allows for a large degree of controllability with respect to achieving a desired target pulse, however the cost of this approach is often a significant loss of energy due to the attenuation of the spectral components.

Phase-only pulse shaping is an attractive alternative in this respect, as energy losses are kept to a minimum. The sacrifice of a phase-only approach is that it becomes much harder, and in many cases impossible, to achieve an arbitrary target pulse envelope and carrier frequency distribution. Working with pulses that interact with molecules in the dynamic Stark limit allows us to disregard the carrier frequency and focus only on the pulse envelope. This relaxes the requirements on the target pulse and might open up the possibilities of generating arbitrary envelope shapes using phase-only spectral manipulation. While the task of determining the spectral phase function that will produce a desired envelope shape is still not trivial, there are a variety of iterative optimization methods which have been shown to be well suited for this task.[50–52]

As stated in the article outset, applying tailored laser pulses to control molecular transitions has been the subject of numerous studies. In particular, analytical insights have been developed for generating pulse shapes tuned to produce specific state-to-state vibrational transitions via coupling to the permanent molecular dipole moment.[53,54] The observant reader may therefore wonder what the advantage of a pure DSC approach may be, when compared to these more established methods.

The answer comes down to the unique dynamics that apply in the regime of pure DSC. The fact that the dynamic Stark effect dominates under non-resonant conditions means that we can effectively disregard the carrier frequency of the laser, which is attractive from the standpoint of experimental implementation. Another obvious advantage of DSC compared to resonant approaches is that it can applied to molecules where there is no coupling to the permanent electric dipole moment.

DSC may be accomplished using "pseudo-frequencies," generated via pulse trains with spacings tuned to specific molecular modes. This approach is particularly interesting with respect to heavy molecules with long vibrational periods, as their low frequencies will typically lie outside the operational bandwidths of conventional laser and pulse shaping technologies.

One major drawback of a pure DSC approach is that the required intensities are typically much higher than those needed for resonant control. As discussed in this article, this problem may be mitigated by splitting high intensity pulses into trains of smaller sub-pulses; however this typically results in an increase of the overall temporal duration of the pulse envelope, which may in turn lead to issues with dissipation or other unwanted coupling effects.

V. CONCLUDING REMARKS

We have used the linearly forced harmonic oscillator to model the interaction of a laser pulse with a diatomic molecule which allows for analytic solutions to the time-dependent

evolution of the quantum wave packet. Using these solutions, we have been able to show how the dynamic Stark effect arises from the interaction with the electric field envelope of a laser pulse, and an optimal pulse width has been determined.

The impact of driving our model with multiple evenly spaced pulses demonstrates how modal selectivity can be achieved. Additionally, we show that the effect of multiple pulses can contribute both additively and subtractively to the wave packet amplitude in our harmonic model.

Using Parseval's theorem, we describe and predict how a pulse interacts with our model system in the DSC limit using the spectral phase and amplitude of the pulse envelope. The spectral interpretation of DSC can generate insight that would not be available from a purely temporal perspective, which we demonstrate via phase-only manipulation of a flat-phase Gaussian to generate non-trivial dark pulse envelopes that produce no net excitation.

Finally, we demonstrate how quantum control may be achieved via the dynamic Stark effect by shaping a parameterized pulse envelope function, allowing us to produce state-to-state vibrational excitation in an anharmonic oscillator. The fact that the carrier frequency of the optimized envelope can be disregarded opens the door for arbitrary waveform generation by optical pulse shapers. We expect that careful pulse optimization will allow for dynamic Stark control of various more complicated competing processes which are currently being studied.

[1]S. A. Rice and M. Zhao, *Optical Control of Molecular Dynamics* (Wiley, New York, 2000).
[2]C. Brif, R. Chakrabarti, and H. Rabitz, New J. Phys. **12**, 075008 (2010).
[3]M. Shapiro and P. Brumer, *Quantum Control of Molecular Processes* (Wiley, New York, 2012).
[4]A. H. Zewail, Phys. Today **33**(11), 27 (1980).
[5]T. C. Weinacht, J. Ahn, and P. H. Bucksbaum, Nature **397**, 233 (1999).
[6]I. Barth and J. Manz, Angew. Chem., Int. Ed. **45**, 2962 (2006).
[7]R. S. Judson and H. Rabitz, Phys. Rev. Lett. **68**, 1500 (1992).
[8]A. M. Weiner, Rev. Sci. Instrum. **98**, 1929 (2000).
[9]A. Monmayrany, S. Weber, and B. Chatel, J. Phys. B **43**, 103001 (2010).
[10]M. Mitchell, *An Introduction to Genetic Algorithms*, 5th ed. (MIT Press, 1999).
[11]A. Assion, T. Baumbert, M. Bergt, T. Brixner, B. Kiefer, V. Seyfried, M. Strehle, and G. Gerber, Science **282**, 919 (1998).
[12]R. J. Levis, G. M. Menkir, and H. Rabitz, Science **292**, 709 (2001).
[13]B. J. Pearson, J. L. White, T. C. Weinacht, and P. H. Bucksbaum, Phys. Rev. A **63**, 063412 (2001).
[14]G. Vogt, G. Krampert, P. Nikaus, P. Nuernberger, and G. Gerber, Phys. Rev. Lett. **94**, 068305 (2005).
[15]J. Savolainen, R. Fanciulli, N. Dijkhuizen, A. L. Moore, J. Hauer, T. Buckup, M. Motzkus, and J. L. Herek, Proc. Natl. Acad. Sci. U. S. A. **105**, 7641 (2008).
[16]A. C. Florean, D. Cardoza, J. L. White, J. K. Lanyi, R. J. Sension, and P. H. Bucksbaum, Proc. Natl. Acad. Sci. U. S. A. **106**, 10896 (2009).
[17]H. Stapelfeldt and T. Seideman, Rev. Mod. Phys. **75**, 543 (2003).
[18]H. Niikura, P. B. Corkum, and D. M. Villeneuve, Phys. Rev. Lett. **90**, 203601 (2003).
[19]C. B. Madsen, L. B. Madsen, S. S. Viftrup, M. P. Johansson, T. B. Poulsen, L. Holmegaard, V. Kumarappan, K. A. Jørgensen, and H. Stapelfeldt, J. Chem. Phys. **130**, 234310 (2009).
[20]L. Christensen, J. H. Nielsen, C. B. Brandt, C. B. Madsen, L. B. Madsen, C. S. Slater, A. Lauer, M. Brouard, M. P. Johansson, B. Shepperson, and H. Stapelfeldt, Phys. Rev. Lett. **113**, 073005 (2014).
[21]B. J. Sussman, D. Townsend, M. Y. Ivanov, and A. Stolow, Science **314**, 278 (2006).
[22]D. Townsend, B. J. Sussman, and A. Stolow, J. Phys. Chem. A **115**, 357 (2011).
[23]M. E. Corrales, J. González-Vázquez, G. Balerdi, I. R. Solá, R. de Nalda, and L. Bañares, Nat. Chem. **6**, 785 (2014).
[24]I. R. Solá, J. González-Vázquez, R. de Nalda, and L. Bañares, Phys. Chem. Chem. Phys. **17**, 13163 (2015).
[25]Q. Ren, G. G. Balint-Kurti, F. R. Manby, M. Artamonov, T.-S. Ho, and H. Rabitz, J. Chem. Phys. **124**, 014111 (2006).
[26]J. Haruyama, C. Hu, and K. Watanabe, Phys. Rev. A **85**, 062511 (2012).
[27]P. Atkins and R. Friedman, *Molecular Quantum Mechanics*, 4th ed. (Oxford University Press, 2005).
[28]S. Sharma, H. Singh, and G. G. Balint-Kurti, J. Chem. Phys. **132**, 064108 (2010).
[29]C. Sanz-Sanz, G. W. Richings, and G. A. Worth, Faraday Discuss. **153**, 275 (2011).
[30]Y. Korosaki, T.-S. Ho, and H. Rabitz, J. Chem. Phys. **140**, 084305 (2014).
[31]B. J. Sussman, Am. J. Phys. **79**, 477 (2011).
[32]D. J. Griffiths, *Introduction to Quantum Mechanics*, 2nd ed. (Pearson Education International, New Jersey, 2005).
[33]A. M. Wiener, D. E. Leaird, G. P. Wiederrecht, and K. A. Nelson, J. Opt. Soc. Am. B **8**, 1264 (1991).
[34]R. Kosloff and A. D. Hammerich, Phys. Rev. Lett. **69**, 2172 (1992).
[35]J. A. Cina and T. J. Smith, J. Chem. Phys. **98**, 9211 (1993).
[36]D. Meshulach and Y. Silberberg, Phys. Rev. A **60**, 1287 (1999).
[37]R. A. Bartels, S. Backus, M. M. Murnane, and H. C. Kapteyn, Chem. Phys. Lett. **374**, 326 (2003).
[38]R. P. Feynman, Phys. Rev. **56**, 340 (1939).
[39]N. E. Henriksen and F. Y. Hansen, *Theories of Molecular Reaction Dynamics* (Oxford University Press, 2008).
[40]D. J. Tannor, *Introduction to Quantum Mechanics: A Time-Dependent Perspective* (University Science Books, 2007).
[41]M. Machholm and N. E. Henriksen, J. Chem. Phys. **111**, 3051 (1999).
[42]M. A. Buldakov, V. N. Cherepanov, and N. S. Nagornova, J. Comput. Methods Sci. Eng. **6**, 153 (2006).
[43]J. F. Harrison, J. Chem. Phys. **128**, 114320 (2008).
[44]A. M. Perelomov, V. S. Popov, and M. V. Terent'ev, J. Exp. Theor. Phys. **50**, 1393 (1966).
[45]X. M. Tong, Z. X. Zhao, and C. D. Lin, Phys. Rev. A **66**, 033402 (2002).
[46]E. Räsänen and L. B. Madsen, Phys. Rev. A **86**, 033426 (2012).
[47]J. Förster, Y. V. Vanne, and A. Saenz, Phys. Rev. A **90**, 053424 (2014).
[48]W. Rudin, *Real and Complex Analysis*, 3rd ed. (McGraw-Hill, 1987).
[49]R. Kosloff, J. Phys. Chem. **92**, 2087 (1988).
[50]A. M. Weiner, S. Oudin, D. E. Leaird, and D. H. Reitze, J. Opt. Soc. Am. A **10**, 1112 (1993).
[51]D. Meshulach, D. Yelin, and Y. Silberberg, J. Opt. Soc. Am. B **15**, 1615 (1998).
[52]M. Hacker, G. Stobrawa, and T. Feurer, Opt. Express **9**, 191 (2001).
[53]M. V. Korolkov and G. K. Paramonov, Phys. Rev. A **57**, 4998 (1998).
[54]S. Chelkowski, A. D. Bandrauk, and P. B. Corkum, Phys. Rev. Lett. **65**, 2355 (1990).

Appendix B

Femtochemistry in the electronic ground state: Dynamic Stark control of vibrational dynamics

Chemical Physics Letters 683 (2017) 234–239

Contents lists available at ScienceDirect

Chemical Physics Letters

journal homepage: www.elsevier.com/locate/cplett

Research paper

Femtochemistry in the electronic ground state: Dynamic Stark control of vibrational dynamics

Chuan-Cun Shu [a,b], Esben F. Thomas [a], Niels E. Henriksen [a,*]

[a] Department of Chemistry, Technical University of Denmark, Building 207, DK-2800 Kongens Lyngby, Denmark
[b] School of Engineering and Information Technology, University of New South Wales, Canberra, ACT 2600, Australia

ARTICLE INFO

Article history:
Received 22 December 2016
In final form 4 March 2017
Available online 7 March 2017

Keywords:
Vibrational excitation
Dynamic Stark effect
Pulse shaping

ABSTRACT

We study the interplay of vibrational and rotational excitation in a diatomic molecule due to the non-resonant dynamic Stark effect. With a fixed peak intensity, optimal Gaussian pulse durations for maximizing vibrational or rotational transitions are obtained analytically and confirmed numerically for the H_2 and Cl_2 molecules. In general, pulse trains or more advanced pulse shaping techniques are required in order to obtain significant vibrational excitation. To that end, we demonstrate that a high degree of selectivity between vibrational and rotational excitation is possible with a suitably phase-modulated Gaussian pulse.

1. Introduction

The majority of the pioneering femtochemistry studies by Ahmed Zewail and coworkers have been conducted for electronically excited states of molecules [1–3]. In general, excited electronic states set the stage for photochemistry, whereas the electronic ground state is associated with the large class of thermally activated chemical reactions. Far fewer studies of femtosecond dynamics have addressed molecules in the electronic ground state (see, e.g. [4–6] and references therein) where, in general, it is more difficult to induce significant structural change via laser excitation.

Controlled femtosecond dynamics in the electronic ground state can be induced via the dynamic Stark effect, also known as impulsive Raman scattering [7–10]. One advantage of this approach compared to direct resonant excitation (e.g. of vibrational states in the infrared region) is that it operates under non-resonant conditions, giving more flexibility from an experimental point of view.

In this letter, we focus on vibrational excitation of (diatomic) molecules induced by the dynamic Stark effect. Whereas a large literature exists pertaining to rotational excitation and alignment via the dynamic Stark effect (see, e.g. [11–13] and references therein) the discussion of vibrational (or torsional) excitation is much more limited [7,14,15,10]. We have recently studied vibrational excitation within a one-dimensional framework corresponding to perfect alignment along the polarization direction of the laser field [10]. The main purpose of the present work is to investigate the interplay of vibrational with rotational excitation, i.e. alignment.

2. Theory

We focus on diatomic molecules, whose Hamiltonian under field-free conditions can be described by

$$\widehat{H}_0 = -\frac{\hbar^2}{2m}\left(\frac{\partial^2}{\partial R^2} + \frac{2}{R}\frac{\partial}{\partial R}\right) + \frac{\widehat{J}^2}{2mR^2} + V(R), \tag{1}$$

where R is the internuclear distance, $\widehat{J}^2$ is the angular momentum operator of the nuclear rotation, and $V(R)$ is the potential energy curve of the electronic ground state. The stationary states $|vJM\rangle$ with eigenvalues E_{vJM} can be expressed as a product of the nuclear radial wave function $R_{vJ}(R)$ and the associated-Legendre polynomial $P_J^M(\cos\theta)$, where v is the vibrational quantum number, J is the rotational quantum number, and θ is the angle between the molecular axis and the z direction.

The interaction with an external field contains a term describing the interaction with the permanent electric dipole and a term arising due to polarization of the electrons, the latter of which plays a role for strong fields. In the following we consider only homonuclear diatomic molecules, and the interaction Hamiltonian of the molecule interacting with a field $\mathcal{E}(t)$ linearly polarized along the z direction can be described by

$$\widehat{H}_{int}(t) = -\frac{\mathcal{E}^2(t)}{2}\left\{[\alpha_{\parallel}(R) - \alpha_{\perp}(R)]\cos^2\theta + \alpha_{\perp}(R)\right\} \tag{2}$$

* Corresponding author.
E-mail address: neh@kemi.dtu.dk (N.E. Henriksen).

http://dx.doi.org/10.1016/j.cplett.2017.03.006
0009-2614/

where $\alpha_{\parallel}(R)$ and $\alpha_{\perp}(R)$ refer to the parallel and perpendicular components, respectively, of the polarizability tensor. Initially, the molecule is assumed to be in the ground vibrational and rotational state of the electronic ground state, $|000\rangle$, and due to the linear polarization of the field, $M = 0$ is conserved in the following. The wave function $\Psi(R,\theta,t)$ of the molecule can be obtained by solving the time-dependent Schrödinger equation (TDSE) with the Hamiltonian $\widehat{H}_0 + \widehat{H}_{int}$. The TDSE is solved numerically, as described in Ref. [16]. The time-dependent vibrational amplitude, i.e., the expectation value of the internuclear distance R can be calculated by $\langle R\rangle = \langle\Psi(R,\theta,t)|R|\Psi(R,\theta,t)\rangle$, and the degree of alignment of the molecule is defined as $\langle\cos^2\theta\rangle = \langle\Psi(R,\theta,t)|\cos^2\theta|\Psi(R,\theta,t)\rangle$.

We first consider a molecule that is excited by a single Gaussian laser pulse $\mathcal{E}(t) = \mathcal{E}_0\exp(-t^2/(2\sigma^2))\cos(\omega_0 t)$, where σ is the pulse width (FWHM = $2\sigma\sqrt{2\ln 2} \sim 2.36\sigma$), $\mathcal{E}_0$ is the field strength, and ω_0 is the carrier frequency. In this work we choose $\hbar\omega_0$ corresponding to 12,500 cm^{-1} (equivalent to 800 nm), which is off-resonant with respect to the excited rovibrational or electronic states of our chosen molecules, and the peak intensity ($\propto \mathcal{E}_0^2$) is fixed at 1.0×10^{13} W/cm^2.

In order to analytically investigate the dynamics which can be induced, we consider the non-resonant dynamic Stark regime, where the carrier frequency can be neglected (e.g. $\omega_0 = 0$) [10]. To first order, the transition probability from a stationary state $|i\rangle = |v_0 J_0 M_0\rangle$ to an excited state $|f\rangle = |vJM\rangle$, can be written as

$$P_{if} = \left|\frac{1}{i\hbar}\int_{-\infty}^{\infty}\langle f|\widehat{H}_{int}(t)|i\rangle e^{i\omega_{if}t}dt\right|^2 \propto \sigma^2\exp\left(\frac{-\sigma^2\omega_{if}^2}{2}\right) \quad (3)$$

where $\omega_{if} = (E_{vJM} - E_{v_0J_0M_0})/\hbar$. A maximum in the transition probability P_{if} is obtained for

$$\sigma_{max} = \frac{T_{rov}}{\sqrt{2}\pi} \quad (4)$$

where $T_{rov} = 2\pi/\omega_{if}$. In the following we apply this expression to rovibrational excitations. Although the result above was derived within first-order perturbation theory, we note that for vibrational excitation of a harmonic oscillator, Eq. (4) is identical to the exact (to infinite order) result for maximizing the vibrational amplitude at a constant peak amplitude, with the polarizability described as a linear forcing [10].

Eq. (4) shows that there is an optimal ratio σ_{max}/T_{rov}, i.e. the ratio between the pulse duration and the timescale of the dynamics. Thus, vibrational or rotational excitation (alignment) at a given peak pulse intensity can be maximized by optimizing the pulse duration. Furthermore, it is noted that in the limit $\sigma \to 0$, there is no transition. That is, for a transient change in the Hamiltonian over a time that is very short compared to the timescale of the system, there is no change in the state (in agreement with the general "sudden theorem" of quantum mechanics). Note that the peak intensity of the Gaussian pulse is fixed, and the energy (fluence) will increase with the pulse width σ. Thus, the maximum excitation is obtained for $\sigma = \sigma_{max}$ although the energy of the pulse will increase when $\sigma > \sigma_{max}$. In addition to the duration of the (squared) pulse envelope, the ease of excitation depends on the polarizability. For rotational excitation it is determined by the anisotropy of the polarizability, i.e. $[\alpha_{\parallel}(R) - \alpha_{\perp}(R)]$ which, in general, increases with the number of electrons, and for vibrational excitation determined by the derivative of the polarizability with respect to the bond length.

The dynamic Stark effect can also be analyzed in the frequency domain, leading to the picture of impulsive Raman scattering. Thus, the frequency distribution of the pulse envelope must effectively cover several vibrational or rotational eigenstates, in order to lead to substantial excitation [10]. A further discussion of this point is given below.

We consider in the following the homonuclear diatomic molecules H_2 and Cl_2, with internuclear potentials and polarizabilities from Refs. [17–20]. For H_2, the vibrational period associated with the two lowest rovibrational states $|000\rangle$ and $|100\rangle$ is $T_{vib} = 2\pi/\omega_{vib} = 8.0$ fs and the rotational period associated with the states $|000\rangle$ and $|020\rangle$ is $T_{rot} = 2\pi/6B_0 = 95$ fs, within the rigid-rotor harmonic oscillator limit where B_0 is the rotational constant. For Cl_2, the corresponding values are $T_{vib} = 61$ fs and $T_{rot} = 22.8$ ps. Since we work with homonuclear diatomic molecules with half-integral nuclear spins, the symmetry requirement to the total wave function implies that each molecule consists of two types "ortho" or "para" where, respectively, only odd or even rotational states are accessible.

3. Results and discussion

Fig. 1 shows the final populations in the rovibrational states as a function of the pulse width σ. Both "para" H_2 and Cl_2 show similar population dynamics, i.e. the rotational excitations with $\Delta J = 2$ to the state $|020\rangle$ are dominant, and are stronger than the (pure) vibrational excitation with $\Delta J = 0$ to the state $|100\rangle$ and $\Delta J = 2$ to the state $|120\rangle$. In H_2, the maximum of the vibrational excitation to the state $|100\rangle$, and rotational excitation to $|020\rangle$, is reached for $\sigma = 1.9$ fs and $\sigma = 21$ fs, respectively, in full agreement with the analytical formula in Eq. (4). The anisotropy of the polarizability is more than 10 times larger for Cl_2 compared to H_2. For Cl_2, we obtain again full agreement with the analytical formula if the intensity is reduced to $I_0 = 10^{12}$ W/cm^2. At $I_0 = 10^{13}$ W/cm^2, the maximum of the rovibrational excitations in Cl_2 is reached in the neighborhood of 15 fs (see Fig. 1(c)) in fair agreement with the 13.7 fs from the analytical formula, Eq. (4). The rather strong rotational excitation implies that excitation beyond first order takes place, and the linearly forced harmonic oscillator description discussed in connection to Eq. (4) did not include the possibility of rotational transitions during the interaction with the Gaussian pulse. Nevertheless, there is overall quite good agreement with the analytical expression, in this case where substantial rotational transitions take place during the interaction with the pulse.

It is clear that application of a single Gaussian pulse optimized for vibrational excitation leads to some rotational excitation and alignment. The probability of rotational excitation to $|020\rangle$ in H_2 is very weak as compared with that in Cl_2. Besides the different polarizabilities, this can be understood in terms of Eq. (3) where the probability distribution is quite broad for rotational excitation in Cl_2 due to the relatively small rotational frequency.

For a Gaussian pulse at the optimal pulse width $\sigma = \sigma_{max}$ for vibrational excitation of, respectively, H_2 and Cl_2, Fig. 2 shows the time-dependent expectation values of the displacement of the internuclear distance relative to the uncertainty of the rovibrational ground state ($\Delta R = 0.1685$ a.u. for H_2 and $\Delta R = 0.0781$ a.u. for Cl_2). The vibrational amplitude in Cl_2 is about 5 times larger than in H_2 but it is clear that both vibrational amplitudes are quite small. The accompanying degree of alignment is shown in panels (b) and (d), with a full revival at $T_{rot} = 2\pi/6B_0$ corresponding to a coherent superposition of the $J = 0$ and $J = 2$ states. The alignment is much larger in Cl_2 due to the higher population in the $J = 2$ state (see Fig. 1(d)). The first maximum in the field-free time-dependent alignment is observed at ~ 25 fs for H_2 and at ~ 6 ps for Cl_2. With the expansion coefficients of the rotational wave packet established, essentially, instantaneously (at $t = 0$) on the rotational timescale, the time-dependent interference terms are proportional

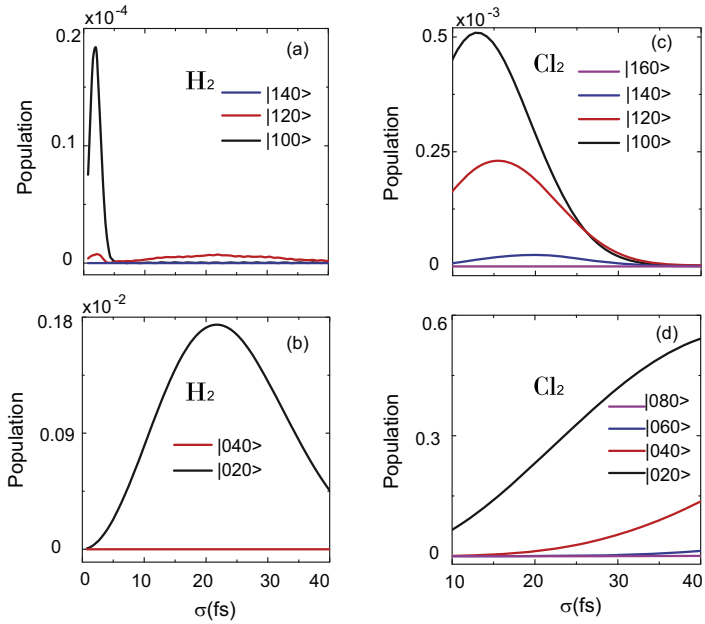

Fig. 1. The final populations in the rovibrational states $|vJM\rangle$ as a function of the pulse width σ of a Gaussian pulse with peak intensity fixed at 1.0×10^{13} W/cm^2, for the molecules H_2 (in (a) and (b)) and Cl_2 (in (c) and (d)). Note the different scales for the populations. For H_2, the maximum in the population of $|100\rangle$ is 1.79×10^{-5} and at the same pulse width the population in the rotational state $|020\rangle$ is 3.23×10^{-5}.

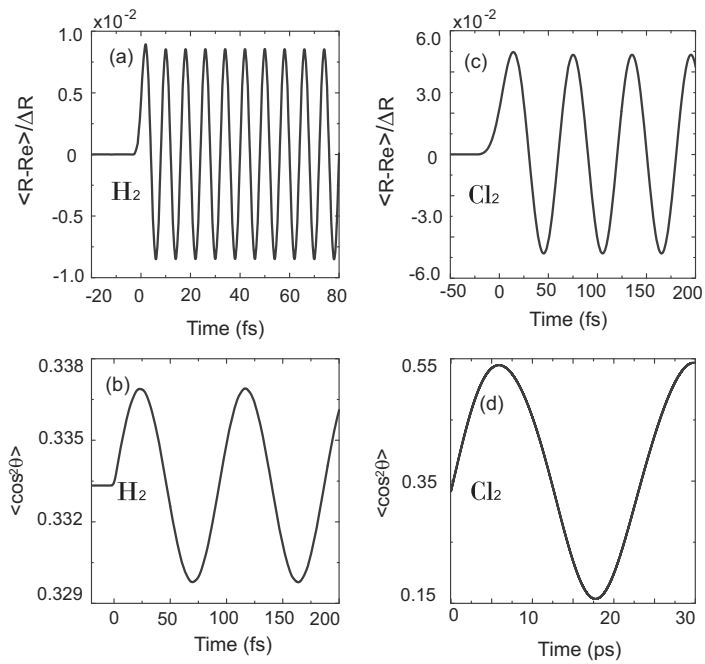

Fig. 2. The time-dependent expectation values of the displacement of the internuclear distance relative to the uncertainty of the vibrational ground state and the degree of alignment induced by a Gaussian pulse at the optimal pulse width $\sigma = \sigma_{max}$ for vibrational excitation. The peak intensity is fixed at 1.0×10^{13} W/cm^2. Panels (a)-(b) are for H_2 and panels (c)-(d) are for Cl_2.

to $\sin(6B_0t/\hbar)$. The first maximum of this function is obtained at $T_{rot}/4$ in agreement with the numerical results. The change in alignment after vibrational excitation is fast for H_2 and slower for Cl_2, i.e. some vibrational motion can take place before a significant change in alignment shows up.

Fig. 3 shows the same quantities as in Fig. 2, but now for a train of 6 identical pulses with $\sigma = \sigma_{max}$ for vibrational excitation and a time delay corresponding to the vibrational periods of, respectively, H_2 and Cl_2. The vibrational amplitude is now ~ 6 times larger in agreement with the analytical one-dimensional harmonic oscillator model [10]. The rotational revival structure for Cl_2 is more complicated than in Fig. 2 due to the involvement of higher ($J > 2$) rotational states, and the first maximum in the field-free time-dependent alignment shows up faster than in the one-pulse case due to the faster timescales associated with higher rotational states.

Fig. 4 shows higher vibrational amplitude when the molecule is prepared in the rotationally excited state $|010\rangle$. This result is readily understood because the (partial) alignment prior to the arrival of the pulse train leads to a higher average value of the term proportional to $\cos^2\theta$ in the interaction Hamiltonian in Eq. (2).

Based on these results, it is clear that *selective* vibrational excitation is a challenge and it cannot be obtained after the interaction with a Gaussian pulse or the simple trains of Gaussian pulses studied above. The large bandwidth of the pulses optimized for vibrational excitation implies that substantial rotational excitation takes place. We note in passing that selective rotational excitation and alignment can be obtained already with a single Gaussian pulse when the pulse duration is somewhat larger than the vibrational period. However, due to the rotation-vibration coupling in Eq. (1), a small smooth increase in the average bond length will accompany the rotational excitation [21].

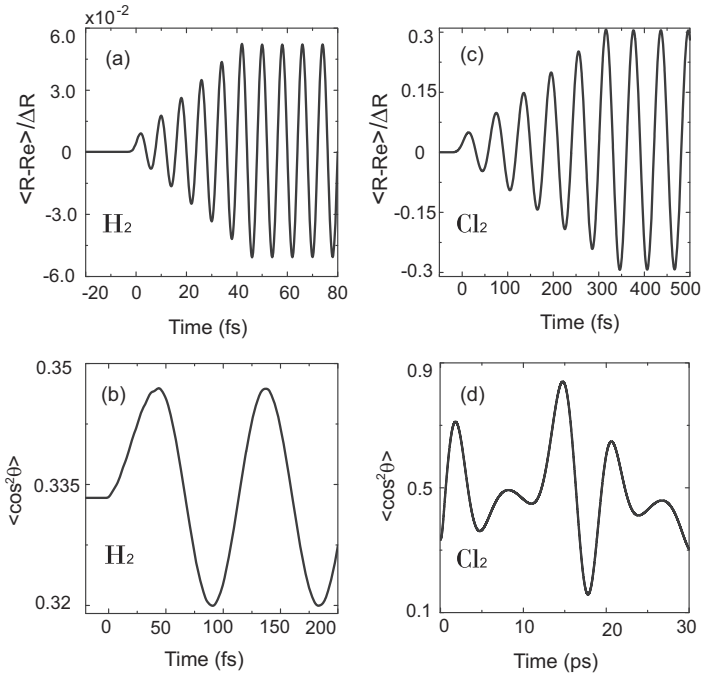

Fig. 3. Same as Fig. 2 but for a train of 6 Gaussian pulses with $\sigma = \sigma_{max}$ for vibrational excitation, and a time delay $\tau = T_{vib}$.

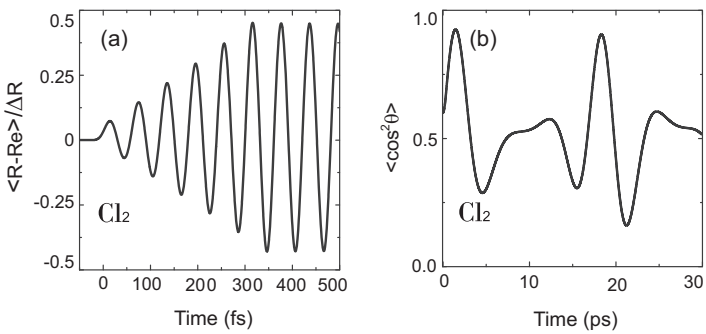

Fig. 4. Same as Fig. 3 but for the rotationally excited initial state $|010\rangle$ of Cl_2.

We will now demonstrate how more advanced pulse shaping may lead to enhanced selective vibrational excitation. Let ω_{rot} and ω_{vib} be the $|000\rangle - |020\rangle$ rotational and $|000\rangle - |100\rangle$ vibrational state transition frequencies of a diatomic molecule, respectively. In the spectral domain, as stated previously, these excitations can be interpreted as Stokes-Raman scattering events consisting of transitions to and from higher lying virtual states. Assuming the spectral distribution of a finite width laser pulse in the Fourier domain is given by $\widetilde{E}(\omega)$, it can be shown both within the analytical one-dimensional model of a linearly forced harmonic oscillator [10], and via second-order time-dependent perturbation theory [22], that the transition probability P_{ab} between any two states a and b is proportional to the continuous cross-correlation integral of $\widetilde{E}(\omega)$ with itself at lag $\omega_{ab} = (E_a - E_b)/\hbar$, i.e.

$$P_{ab} \propto \int_{-\infty}^{\infty} \widetilde{E}(\omega)\widetilde{E}^*(\omega - \omega_{ab})d\omega \tag{5}$$

From Eq. (5) it can be seen that the bandwidth of a transform limited Gaussian pulse optimized for vibrational excitation will generally lead to rotational excitation, since it generally holds that $\omega_{\text{rot}} \ll \omega_{\text{vib}}$. This corroborates the coupled rotation-vibration excitation effects we have observed thus far in our numerical simulations.

Using the insights gained from the aforementioned spectral interpretation of the system excitation, we can demonstrate how pure spectral phase modification of the vibrationally optimized Gaussian pulses can lead to decoupling of the vibrational and rotational excitations (i.e. we can fully eliminate the pure rotational transitions while keeping pure vibrational transitions unmodified). To show this, let $\widetilde{A}(\omega)$ represent the (flat phase) Fourier transform of a Gaussian pulse and let $\widetilde{E}(\omega)$ represent the spectral function when the phase of $\widetilde{A}(\omega)$ is shifted by the phase function $\Phi(\omega)$, i.e.

$$\widetilde{E}(\omega) = \widetilde{A}(\omega)\exp[i\Phi(\omega)] \tag{6}$$

Combining Eqs. (5) and (6), it can be shown that in order to decouple the excitations, the phase function must meet the following requirements:

$$\int_{-\infty}^{\infty} \widetilde{A}(\omega)\widetilde{A}^*(\omega - \omega_{\text{rot}})\exp[i(\Phi(\omega) - \Phi(\omega - \omega_{\text{rot}}))]d\omega = 0 \tag{7}$$

$$\Phi(\omega) = \Phi(\omega - \omega_{\text{vib}}) \tag{8}$$

Clearly, the condition set by Eq. (7) leads to the elimination of the $|000\rangle - |020\rangle$ rotational transitions. When Eq. (8) is fulfilled, the complex phase argument in Eq. (6) will disappear for all ω in the integration domain of Eq. (5), which means that the transition probabilities at ω_{vib} for the phase modulated and non-phase modulated pulses will be identical.

The $\Phi(\omega)$ function we use consists of an equally spaced sequence of repeating identical subsequences (see Fig. 5). The spacing between each subsequence is ω_{vib}, which ensures that the periodicity requirement given by Eq. (8) is satisfied. Every subsequence consists of a square wave function with periodicity $2\omega_{\text{rot}}$, alternating min/max values of 0 and π, and spectral width Ω. From Eq. (7), it can be seen that these subsequence phase structures will cause parts of the integral over $\widetilde{A}(\omega)\widetilde{A}^*(\omega - \omega_{\text{rot}})$ to assume negative values when the complex exponential function becomes $\exp(\pm i\pi)$. By adjusting Ω, we can vary the substructure widths until the overall negative and positive contributions to the integral cancel each other out, leading to a situation where Eq. (7) is satisfied, in principle eliminating the rotational excitation.

To test this principle, we calculated phase functions designed to eliminate rotational transitions in H_2 and Cl_2. The initial, unshaped Gaussian pulses were again assigned peak intensities of 1.0×10^{13} W/cm^2, and Eq. (4) was used to define the applied pulse

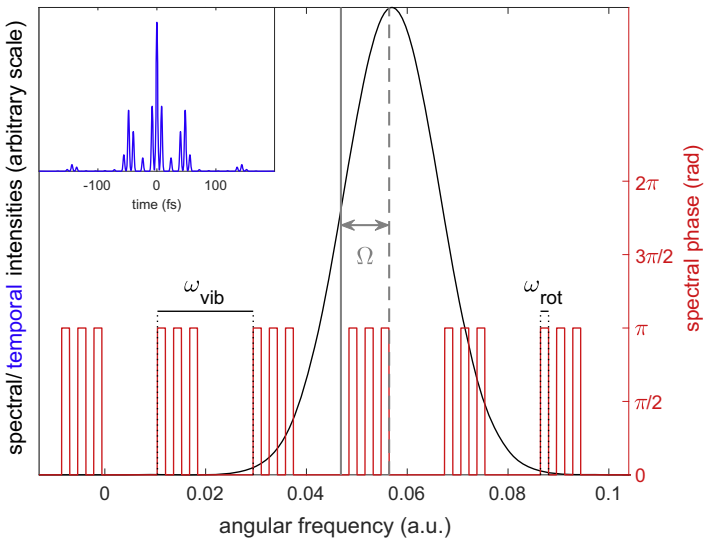

Fig. 5. In the main figure, the black curve indicates the spectral intensity of a Gaussian pulse when $\sigma = \sigma_{max}$, calculated for the H_2 molecular parameters. For reference, the spectral widths of the vibrational and rotational transition frequencies are also illustrated (ω_{vib} and ω_{rot}, respectively). The red line shows the spectral phase function $\Phi(\omega)$ that is predicted to eliminate all pure rotational transitions in H_2 while keeping the pure vibrational transition probability unaltered. The solid and dashed gray lines visually illustrate the location of the beginning and end of a given chirp subsequence, respectively. Determining the full chirp function $\Phi(\omega)$ that satisfies Eqs. (7) and (8) is accomplished by varying the parameter Ω, which effectively shifts the location of the dashed line(s), increasing or decreasing the length of all subsequences until positive and negative contributions to the integral in Eq. (7) cancel out. Note also how the spacing between each subsequence is equivalent to ω_{vib}, which ensures that the periodicity requirement from Eq. (8) is always met. In the left inset we include a sketch of the corresponding temporal pulse envelope intensity. (For interpretation of the references to color in this figure legend, the reader is referred to the web version of this article.)

width for each molecule in an attempt to maximize the vibrational excitation. As an example, Fig. 5 illustrates the spectral intensity and phase of the pulse determined to produce optimal vibrational excitation of H_2 while eliminating rotational transitions, with a sketch of the corresponding temporal pulse envelope intensity shown in the figure inset.

Using the phase modulated (chirped) and un-chirped pulses, we numerically simulated their interaction with the molecules starting in the ground state, and compared the resulting state excitation levels. For H_2, the $|100\rangle$ vibrational population created by the chirped pulse was $\sim 90\%$ as large as the population created by the un-chirped pulse, whereas rotational state transitions to $|020\rangle$ were decreased by nearly three orders of magnitude. The small discrepancy in the vibrational excitation levels can be traced to the fact that we truncated the width of the shaped pulse until it contained 95% of the original energy before simulating it, as the un-truncated temporal width was found to be quite large with small recurring structures of decreasing amplitude appearing at $|t| \gg 0$. Visual inspection of the inset in Fig. 5 indicates that the H_2 chirped pulse is made up of features that operate on two different timescales. The smaller, high frequency oscillations in the envelope are spaced according to the H_2 vibrational period (8 fs), and the spacings between the larger temporal features appear to be equal to 1 or 1/2 times the H_2 rotational period (95 fs). This is potentially interesting from a control perspective, as it indicates that in the regime of dynamic Stark control, the shortest useful pulse width may be limited by, or contingent on, the longest timescales present in the system dynamics.

While the numerical results for H_2 are very promising, for Cl_2 the case is less clear. As discussed previously, the interaction here appears to be too strong to be accurately described within the perturbative or harmonic approximation that Eq. (5) is based on. Nevertheless, we did find that the chirped pulse reduces the rotational excitations by a factor of ~ 100, while the vibrational excitation is only reduced by a factor of ~ 4. Note that in this case the chirped pulse was truncated to a width containing $\sim 90\%$ of the original energy, which may partly explain the larger discrepancy between the chirped and un-chirped vibrational excitations compared to results for H_2. As a final comment, the degree to which the aforementioned discrepancies may also be attributed to excitation of mixed rovibrational states or the breakdown of the perturbative/harmonic approximations is an open question that requires further study.

4. Concluding remarks

We identified optimal pulse durations for vibrational (or rotational) excitation via the non-resonant dynamic Stark effect. Optimal conditions for vibrational excitation leads to substantial accompanying rotational excitation and overall the excitations could be enhanced by application of pulse trains. Furthermore, we constructed a phase modulated shaped laser pulse which is capable of giving a high degree of selective vibrational excitation in the perturbative/rigid-rotor harmonic oscillator regime.

One can imagine several applications of the vibrational excitation described above. For example, excitation of torsional modes leading to isomerizations [14] and applications related to selective bond breaking in molecules, e.g. for UV-photofragmentation of HOD with vibrational pre-excitation in the electronic state [6,23].

References

[1] M. Dantos, M.J. Rosker, A.H. Zewail, J. Chem. Phys. 87 (1987) 2395.
[2] T.S. Rose, M.J. Rosker, A.H. Zewail, J. Chem. Phys. 88 (1988) 6672.
[3] A.H. Zewail, J. Phys. Chem. 104 (2000) 5660.
[4] T. Witte, T. Hornung, L. Windhorn, D. Proch, R. de Vivie-Riedle, M. Motzkus, K.L. Kompa, J. Chem. Phys. 118 (2003) 2021.
[5] R. Schanz, V. Botan, P. Hamm, J. Chem. Phys. 122 (2005) 044509.
[6] N.E. Henriksen, Chem. Phys. 442 (2014) 2.
[7] H. Niikura, P.B. Corkum, D.M. Villeneuve, Phys. Rev. Lett. 90 (2003) 203601.
[8] B.J. Sussman, D. Townsend, M.Y. Ivanow, A. Stolow, Science 314 (2006) 278.
[9] D. Townsend, B.J. Sussman, A. Stolow, J. Phys. Chem. A 115 (2011) 357.
[10] E.F. Thomas, N.E. Henriksen, J. Chem. Phys. 144 (2016) 244307.
[11] F. Rosca-Pruna, M.J.J. Vrakking, Phys. Rev. Lett. 87 (2001) 153902.
[12] C.Z. Bisgaard, T.B. Poulsen, E. Peronne, S.S. Viftrup, H. Stapelfeldt, Phys. Rev. Lett. 92 (2004) 173004.
[13] L. Holmegaard, J.H. Nielsen, I. Nevo, H. Stapelfeldt, F. Filsinger, J. Kupper, G. Meijer, Phys. Rev. Lett. 102 (2009) 023001.
[14] C.B. Madsen et al., J. Chem. Phys. 130 (2009) 234310.
[15] B.A. Ashwell, S. Ramakrishna, T. Seideman, J. Chem. Phys. 138 (2013) 044310.
[16] C.-C. Shu, J. Yu, K.-J. Yuan, W.H. Hu, J. Yang, S.L. Cong, Phys. Rev. A 79 (2009) 023418.
[17] S.A. Alexander, R.L. Coldwell, J. Chem. Phys. 121 (2004) 11557.
[18] R.L. Wilkins, H.S. Taylor, J. Chem. Phys. 48 (1968) 4934.
[19] L. Guilherme, M. de Macedo, W.A. de Jong, J. Chem. Phys. 128 (2008) 041101.
[20] B. Maroulis, Mol. Phys. 77 (1992) 1085.
[21] C.C. Shu, N.E. Henriksen, J. Chem. Phys. 142 (2015) 221101.
[22] D. Meshulach, Y. Silberberg, Phys. Rev. A 60 (1999) 1287.
[23] B. Amstrup, N.E. Henriksen, J. Chem. Phys. 97 (1992) 8285.

Appendix C

Hyperfine-Structure-Induced Depolarization of Impulsively Aligned I_2 Molecules

Hyperfine-Structure-Induced Depolarization of Impulsively Aligned I_2 Molecules

Esben F. Thomas,[1] Anders A. Søndergaard,[2] Benjamin Shepperson,[2] Niels E. Henriksen,[1] and Henrik Stapelfeldt[2]
[1]Department of Chemistry, Technical University of Denmark, Building 206, DK-2800 Kongens Lyngby, Denmark
[2]Department of Chemistry, Aarhus University, Langelandsgade 140, DK-8000 Aarhus C, Denmark

(Received 30 January 2018; published 19 April 2018)

A moderately intense 450 fs laser pulse is used to create rotational wave packets in gas phase I_2 molecules. The ensuing time-dependent alignment, measured by Coulomb explosion imaging with a delayed probe pulse, exhibits the characteristic revival structures expected for rotational wave packets but also a complex nonperiodic substructure and decreasing mean alignment not observed before. A quantum mechanical model attributes the phenomena to coupling between the rotational angular momenta and the nuclear spins through the electric quadrupole interaction. The calculated alignment trace agrees very well with the experimental results.

DOI: 10.1103/PhysRevLett.120.163202

The alignment of isolated molecules, i.e., confinement of their internal axes to directions fixed in space, by moderately intense laser pulses is considered a well-understood process resulting from the polarizability interaction [1–4]. In the impulsive limit, where a laser pulse much shorter than the molecular rotational period is used, each molecule is left in a superposition of rotational eigenstates. For the widely studied case of linear molecules and a linearly polarized femtosecond alignment pulse, this wave packet formation causes the molecules to align shortly after the laser pulse and in periodically occurring narrow time windows, termed revivals [5–9]. In the rigid rotor approximation, the revival pattern repeats itself [10], unless the rotational coherence is distorted by, e.g., a dissipative environment [11–16].

Decades of frequency-resolved high-resolution spectroscopy [17,18] and time-dependent depolarization experiments on molecules prepared in single rotational states (see Refs. [19–31] for previous examples) have, however, established that a rigid rotor model is insufficient and that a precise description of rotational spectra must include the coupling between rotational angular momentum and electronic or nuclear spin. It is, therefore, surprising that the influence of such effects, notably the hyperfine coupling between the electric quadrupole moment of the nuclei and the electric field of the electrons, has never been addressed in femtosecond-laser-induced molecular alignment studies. In the current work we measured the time-dependent degree of alignment, induced by a 450 fs pulse, for a sample of I_2 molecules covering the first seven rotational revivals. By contrast to the aforementioned depolarization studies, which do not involve coherent superpositions of rotational states, our experiment probes the impact of hyperfine coupling on the revival structures.

Using a quantum mechanical model in conjunction with the experimental results, we find that the hyperfine coupling affects the revival structures in qualitatively different ways compared to the well-understood impact on the "permanent" alignment of a molecule prepared in a single rotational state. Notably, the effect on the permanent alignment is known to be negligible in the limit where the rotational angular momentum is much larger than the angular momentum of the total nuclear spin [29]. By contrast, we find that the hyperfine coupling will always significantly perturb the revival structures over time.

The experimental setup and methods were described previously [32], so only a few details are pointed out here. A pulsed molecular beam, formed by expanding ~1 mbar iodine gas in 80 bar of He gas into a vacuum, enters a velocity map imaging spectrometer, where it is crossed at 90° by two pulsed collinear laser beams. The first pulse (kick pulse, $\lambda = 800$ nm, $\tau_{\mathrm{FWHM}} = 450$ fs, $I_0 = 1.1 \times 10^{12}$ W/cm^2) creates rotational wave packets in the I_2 molecules. The second pulse (probe pulse, 800 nm, 35 fs, 4.3×10^{14} W/cm^2) Coulomb explodes the molecules. This leads to I^+ ion fragments with recoil directions given by the angular distribution of the molecular axes at the instant of the probe pulse. The emission directions of the I^+ ions are recorded with a 2D imaging detector at different kick-probe delays, which allows us to determine the time-dependent degree of alignment $\langle \cos^2 \theta_{2D} \rangle$, θ_{2D} being the angle between the alignment pulse polarization and the projection of an I^+ ion velocity vector on the detector [33].

The time dependence of $\langle \cos^2 \theta_{2D} \rangle$ determined experimentally is shown in black in Fig. 1. The alignment trace is dominated by the pronounced half and full revivals, but their amplitude decreases with the revival order and their structure is changing. These observations are not caused by experimental factors such as collisions or limited temporal detection windows (see Supplemental Material [34], which includes Refs. [35–42]). For comparison, $\langle \cos^2 \theta_{2D} \rangle$ calculated by solving the time-dependent Schrödinger equation (TDSE) for a rigid rotor is also shown. It is clear that the

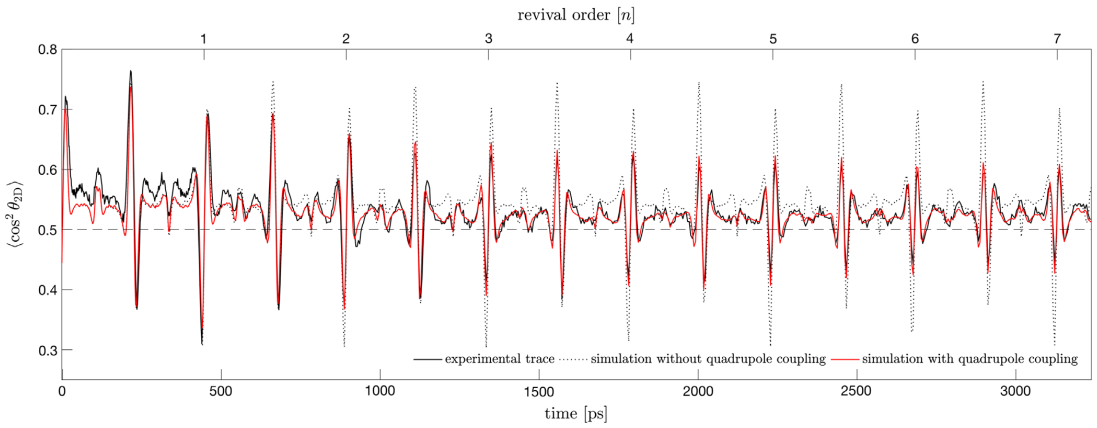

FIG. 1. Experimental results (black line) and the model calculations (red line) calculated at $T = 0.8$ K. An alignment trace calculated without quadrupole coupling is also shown (dotted black line).

decreasing amplitude and changing structure of the revivals observed experimentally are at odds with the calculations. In particular, significant experimental deviations from the calculated results are evident in the higher-order fractional revivals; for instance, at the $6 + (3/4)$ revival the experimental and calculated peaks point in opposite directions.

We now show that the numerical results match the experimental findings to a high degree of accuracy when hyperfine coupling is included in the theoretical model. For I_2 molecules, this mainly stems from the coupling between the electric quadrupole moment of the atomic nuclei and the gradient of the electric field created by the electrons. The coupling between the magnetic dipole moment of the nuclei and the B field from the electrons is much weaker and not included in our model [43]. The total nuclear spin $\mathbf{I}$ is the sum of the spins of the two atomic nuclei: $\mathbf{I} = \mathbf{I}_1 + \mathbf{I}_2$. As a result, there are 36 nuclear spin isomers $|IM_I\rangle$ with $0 \le I \le 5$ and $-I \le M_I \le I$, since the nuclear spin of ^{127}I is 5/2. We assume that the 36 nuclear spin isomers are initially equally abundant [44]. The rotational wave packet created by the alignment pulse from an initial rotational eigenstate $|J_i M_i\rangle$ is denoted $\sum_J a_J |JM_i\rangle$ (M_i is not changed due to the linear polarization of the alignment pulse). The symmetry requirements of the total molecular wave function entail that the parity of the I and J states must be the same in a given molecule [44]. Consequently, there are 15 (21) para (ortho) [even (odd) I and J] spin isomers. The coupled spin isomer–rotational wave packet is described as

$$|IM_I\rangle \otimes \sum_J a_J |JM_i\rangle = \sum_J a_J \sum_F C^{IJF}_{M_I M_i M_F} |IJFM_F\rangle, \quad (1)$$

where F is the total angular momentum, $\mathbf{F} = \mathbf{I} + \mathbf{J}$, $M_F = M_I + M_i$, and $C^{IJF}_{M_I M_i M_F}$ are the Clebsch-Gordan coefficients.

In preparation for solving the TDSE, we construct a square matrix $\mathbf{H}$ in the $|IJFM_F\rangle$ basis, with elements given by [45]

$$\begin{aligned} H_{a,b} &= \langle I^a J^a F^a M_F^a | \mathcal{H}_B + \mathcal{H}_Q | I^b J^b F^b M_F^b \rangle \\ &= \delta_{J^b J^a} B_0 J^a (J^a + 1) \\ &\quad - (eqQ) \delta_{F^b F^a} \delta_{M_F^b M_F^a} [(-1)^{I^a} + (-1)^{I^b}] (-1)^{F^a + I^a} \\ &\quad \times \left[\frac{21}{20} (2I^b + 1)(2I^a + 1)(2J^b + 1)(2J^a + 1) \right]^{1/2} \\ &\quad \times \begin{pmatrix} J^b & 2 & J^a \\ 0 & 0 & 0 \end{pmatrix} \begin{Bmatrix} F^a & I^a & J^a \\ 2 & J^b & I^b \end{Bmatrix} \begin{Bmatrix} \frac{5}{2} & I^a & \frac{5}{2} \\ I^b & \frac{5}{2} & 2 \end{Bmatrix} \end{aligned} \quad (2)$$

$\mathcal{H}_B$ describes the rigid rotor Hamiltonian, where $B_0 = 1.118\,63$ GHz [35] is the molecular rotational constant of I_2 in the vibrational ground state (centrifugal distortion was found to be negligible [34]), and $\mathcal{H}_Q$ is the electric quadrupole interaction component of the hyperfine structure Hamiltonian for a diatomic molecule, where $eqQ = -2.452\,58$ GHz [43] is the quadrupole coupling constant.

$\mathcal{H}_Q$ introduces shifts in the diagonal elements of $\mathbf{H}$ and off-diagonal couplings when $\Delta I = \pm 2$ and/or $\Delta J = \pm 2$. Generally, $\mathbf{H}$ must incorporate all initial states occupied at $t = 0$ [i.e., those given by the right side of Eq. (1)] as well as states that may become occupied over time as a result of the off-diagonal couplings. Specifically, it was found that any states that can be reached via inter-I coupling must be included to faithfully reproduce the experimental alignment trace; however, inter-J couplings were found to have a negligible impact on $\langle\cos^2\theta_{2D}\rangle$ (attributed to the relatively large energy differences between various J states). As such, the $|IJFM_F\rangle$ states incorporated in $\mathbf{H}$ need only contain J values that were already present in $\sum_J a_J |JM_i\rangle$.

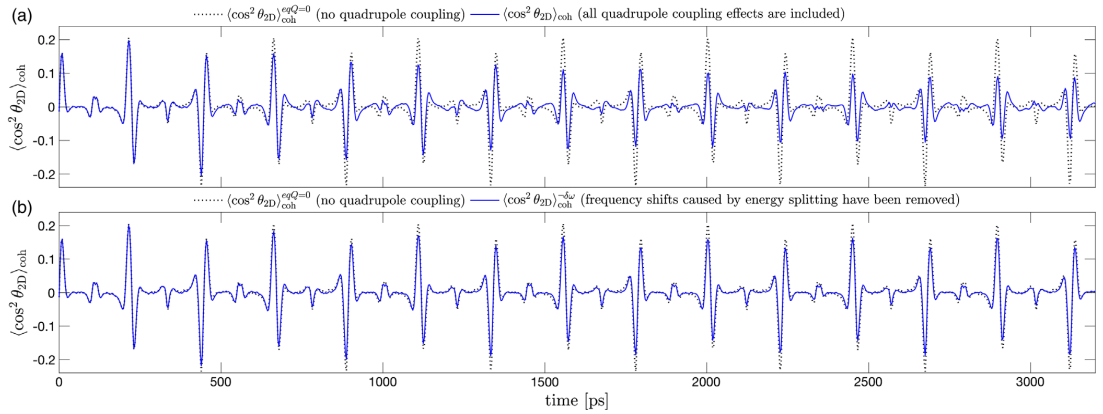

FIG. 2. In (a), the sum of $J \neq J'$ matrix elements comprising the theoretical quadrupole coupled alignment trace $\langle\cos^2\theta_{2D}\rangle_{coh}$ is shown in blue. The blue trace in (b) shows $\langle\cos^2\theta_{2D}\rangle_{coh}^{\neg\delta\omega}$, where the frequency and phase shifts caused by the hyperfine energy splitting have been suppressed. Both (a) and (b) are superposed with equivalent traces calculated without quadrupole coupling (dotted black lines).

The TDSE is solved by expanding the full wave function Ψ onto the coupled basis functions, i.e., $\Psi(t) = \sum_{k=1}^{N} c_k(t)|I^k J^k F^k M_F^k\rangle$, where N is the order of $\mathbf{H}$ and $\Psi(0)$ is given by Eq. (1). The $c_k(t)$ coefficients are found by diagonalizing $\mathbf{H}$ to solve the resulting system of coupled linear differential equations. $\Psi(t)$ is then transformed back into the uncoupled representation to calculate the alignment trace, i.e.,

$$\Psi(t) = \sum_{k=1}^{N} c_k(t) \sum_{M_I,M_J} C^{F^k I^k J^k}_{M_F^k M_I M_J} |I^k M_I\rangle \otimes |J^k M_J\rangle. \quad (3)$$

The efficient calculation of $\langle\cos^2\theta_{2D}\rangle$ is achieved by expanding $\cos^2\theta_{2D}$ onto a basis of Legendre polynomials as described in Ref. [33] and noting the orthonormality of the $|IM_I\rangle$ states in Eq. (3).

The alignment trace of any initial $\sum_J a_J|JM_i\rangle$ superposition is the equally weighted, incoherent sum of traces generated by coupling to all nuclear spin isomers that symmetry requirements will permit. The *complete* alignment trace is the weighted incoherent sum of traces from all the *different* initial $\sum_J a_J|JM_i\rangle$ superpositions that exist because of thermal and focal volume averaging, as per the methodology outlined in Refs. [46,47].

The simulated alignment trace with the effects of quadrupole coupling included is shown in red in Fig. 1. Based on previous work in our group, we estimate that the molecules are initially in thermal (Boltzmann) equilibrium at 0.8 K [32]. The minor discrepancy between the theoretical and experimental traces from 0 to 600 ps can essentially be eliminated by fitting the temperature [34]; however, this results in a fitted temperature of ~0.4 K, which we believe is unrealistically low.

Let $\sum_{J,J'}\langle JM_J|\cos^2\theta_{2D}|J'M_J\rangle$ represent the sum of matrix elements that generates the theoretical alignment trace, where we omit the nuclear spin states and time-dependent coefficients in Eq. (3) for clarity. The $J \neq J'$ terms are sinusoidal functions oscillating at frequencies proportional to the energy difference between the J and J' states. These terms represent the coherence of the wave packet and are responsible for the revivals. In analogy with previous work [11], we refer to their sum as $\langle\cos^2\theta_{2D}\rangle_{coh}$. Conversely, the terms where $J = J'$ represent the population of the rotational states and characterize the permanent alignment. Their sum is denoted $\langle\cos^2\theta_{2D}\rangle_{perm}$ [11]. Note that the mean alignment of the trace is well characterized by $\langle\cos^2\theta_{2D}\rangle_{perm}$, as this term provides the baseline value around which $\langle\cos^2\theta_{2D}\rangle_{coh}$ oscillates.

A visual inspection of Fig. 1 indicates that the mean alignment is slightly decreasing from 0 to 1000 ps. This behavior is attributed to the well-understood fact that quadrupole coupling leads to changes in the M_J projection of a single J state due to the angular "precession" of the coupled $\mathbf{I}$ and $\mathbf{J}$ vectors around $\mathbf{F}$ (see, e.g., Fig. 1 in Ref. [30]) and changes in the relative orientation of the individual nuclear spin vectors (which we denote "spin flipping"). Previous experiments on hyperfine-induced depolarization of single rotational states have shown that this effect (hereafter referred to as "precession-type depolarization") leads to a general time-dependent decrease in the molecular alignment [19,20,22–31]. Figure 2(a) shows $\langle\cos^2\theta_{2D}\rangle_{coh}$ superposed with the sum of $J \neq J'$ trace elements calculated without quadrupole coupling (denoted $\langle\cos^2\theta_{2D}\rangle_{coh}^{eqQ=0}$) for comparison. It is seen that the quadrupole coupling also strongly affects the revival structures.

To understand the cause of the amplitude loss and substructure modification in $\langle\cos^2\theta_{2D}\rangle_{coh}$, the effects of precession-type depolarization were artificially suppressed in the model by changing all M_J's in Eq. (3) to the M_i from

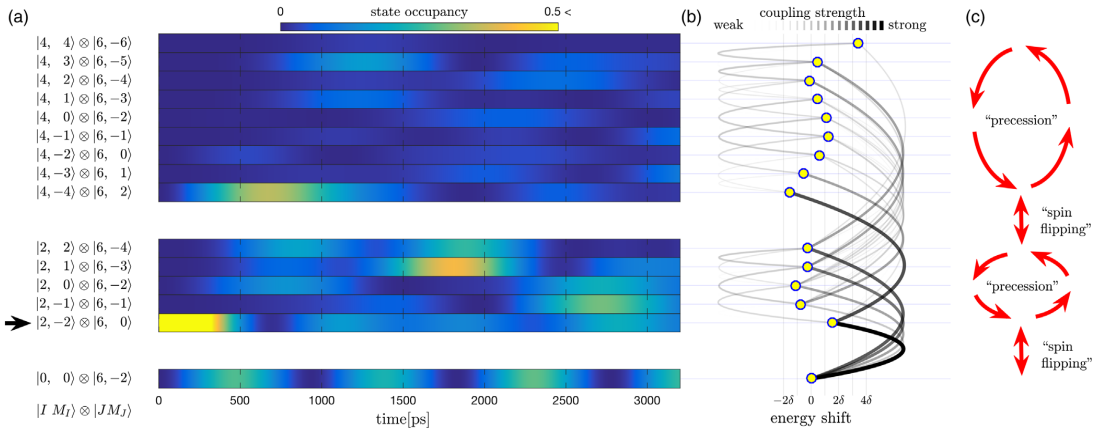

FIG. 3. (a) Occupancy of initial state $|2,-2\rangle \otimes |6,0\rangle$ and the $|IM_I\rangle \otimes |JM_J\rangle$ states it couples to evolving over the timescale of the experiment. (b) Sketch of the state energy splittings and relative coupling strengths ($\delta = 57$ MHz). (c) Schematic classical interpretation of the system dynamics.

the initial $\sum_J a_J|JM_i\rangle$ superposition when calculating the $\langle JM_J|\cos^2\theta_{2D}|J'M_J\rangle$ elements (while treating everything else as if the "actual" M_J's are still in place). Surprisingly, this has very little effect on the shape of $\langle\cos^2\theta_{2D}\rangle_{coh}$, indicating that some previously unexplored mechanisms associated with the quadrupole coupling are causing the modulations in the signal.

It is informative to show the quadrupole coupled dynamics of a molecule starting in a single spin isomer/J state combination. In Fig. 3(a), the time evolution of initial state $|2,-2\rangle \otimes |6,0\rangle$ is shown projected onto the $|IM_I\rangle \otimes |JM_J\rangle$ basis, where the (negligible) effect of inter-J coupling has been suppressed for clarity. The example in Fig. 3 illustrates how the quadrupole coupling will cause each $|JM_i\rangle$ from the initial $\sum_J a_J|JM_i\rangle$ superposition to spread out across a "J manifold" of coupled states. Also, Fig. 3 shows how all states in a given J manifold will have different $|IM_I\rangle$. Therefore, orthonormality of the $|IM_I\rangle$ spin states implies that each state in the J manifold will combine with at *most* one state in the J' manifold to yield a nonzero contribution to the alignment trace.

Given two or more superposed J states coupled to the same spin isomer at $t = 0$, the energy splitting, coupling strength, and number of states associated with each J manifold partially depend on J [attributable, e.g., to the appearance of $J^{a,b}$ in Eq. (2)]. Dissimilarities in the energy splitting between different J manifolds introduce multiple frequency shifts into the components of $\langle\cos^2\theta_{2D}\rangle_{coh}$. The beating caused by the introduction of these new frequencies modulates the alignment trace. We investigated the nature of this frequency beating by artificially suppressing its effect in the model. This was done by eliminating the quadrupole-coupling-induced frequency and phase shifts in the complex arguments of the coefficients governing the time evolution of all $|IM_I\rangle \otimes |JM_J\rangle$ states across all J manifolds. In this way, we calculate a modified trace $\langle\cos^2\theta_{2D}\rangle_{coh}^{\neg\delta\omega}$, where $\neg\delta\omega$ indicates that all frequency shifts introduced by the energy splitting have been removed while leaving the J-manifold population dynamics unchanged. A plot of $\langle\cos^2\theta_{2D}\rangle_{coh}^{\neg\delta\omega}$ is shown in Fig. 2(b). A comparison of the $\langle\cos^2\theta_{2D}\rangle_{coh}$ and $\langle\cos^2\theta_{2D}\rangle_{coh}^{\neg\delta\omega}$ traces shown in Fig. 2 reveals that the frequency beating plays a significant, but not singular, role in attenuating the peak amplitudes. It is also remarkable that the higher-order fractional revivals in $\langle\cos^2\theta_{2D}\rangle_{coh}^{\neg\delta\omega}$ do not exhibit the deviations and sign changes that are present in $\langle\cos^2\theta_{2D}\rangle_{coh}$. This demonstrates that the complex nonperiodic substructures observed in the experimental trace can be solely attributed to the new frequencies introduced into $\langle\cos^2\theta_{2D}\rangle_{coh}$ by the hyperfine coupling.

Note that the peak amplitudes in $\langle\cos^2\theta_{2D}\rangle_{coh}^{\neg\delta\omega}$ still decrease compared to $\langle\cos^2\theta_{2D}\rangle_{coh}^{eqQ=0}$. This is because, as stated earlier, the state population distributions of manifolds with different J will become increasingly dissimilar over time. These asynchronous distributional dynamics cause a net loss of amplitude due to the bijective or injective (one to at most one) way of combining different sets of states associated with different J manifolds when calculating nonzero contributions to the trace. Experimentally, some of the observed peak attenuation may, in principle, be caused by I_2 molecules in vibrationally excited states. Our analysis shows, however, that the potential impact is minor [34].

It has been remarked that precession-type depolarization in single J states is most significant when the coupled **I** and **J** vectors have similar magnitudes [29]. Conversely, our analysis suggests that the observed modulations in the revival structures of $\langle\cos^2\theta_{2D}\rangle_{coh}$ are not directly contingent on the magnitude of **I** or **J**. Therefore, we investigate

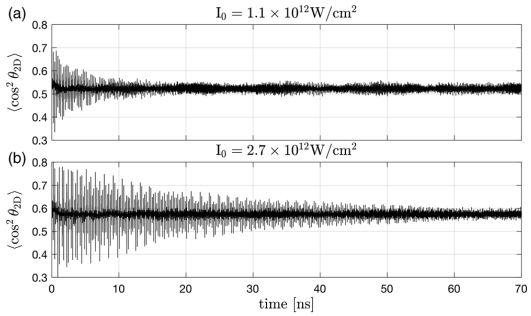

FIG. 4. Quadrupole-coupled alignment traces simulated to 70 ns, with alignment pulse intensities set to (a) the experimental and (b) 2.5× the experimental value.

what happens if rotational wave packets containing larger J are created. To this end, we simulated the effects of quadrupole coupling in I_2 molecules aligned with pulses up to 9× more intense than used in the current experiment.

Increasing the pulse intensity leads to initial revival peaks with larger amplitudes, as well as a higher level of mean alignment. The early decrease in the mean alignment observed in the experiment becomes less pronounced at higher intensities, and for all intensities the mean alignment is nearly constant when $t > 1$ ns. Additionally, it was found that for all intensities the revival structures *always* decay into what resembles low-amplitude unstructured "noise"; however, this decay takes longer for more intense pulses, as illustrated in Fig. 4 [34]. These observations agree qualitatively with our expectations; i.e., the classical model of precession predicts that $\langle\cos^2\theta_{2D}\rangle_{\text{perm}}$ will change less for wave packets with large J, whereas the scrambling or attenuating effects of the frequency beating and asynchronous dynamics will accumulate over time and eventually dominate the $\langle\cos^2\theta_{2D}\rangle_{\text{coh}}$ component of the trace regardless of the magnitude of the J values present in the wave packet.

In closing, we note that the alignment trace of any molecule containing heavy atoms (e.g., I or Br) with large quadrupole coupling constants is expected to show similar deviations from the rigid rotor approximation when excited into a coherent superposition of rotational eigenstates.

H. S. acknowledges support from the European Research Council-AdG (Project No. 320459, DropletControl).

[1] H. Stapelfeldt and T. Seideman, Colloquium: Aligning molecules with strong laser pulses, Rev. Mod. Phys. **75**, 543 (2003).
[2] T. Seideman and E. Hamilton, Nonadiabatic alignment by intense pulses. Concepts, theory, and directions, Adv. At. Mol. Opt. Phys. **52**, 289 (2005).
[3] Y. Ohshima and H. Hasegawa, Coherent rotational excitation by intense nonresonant laser fields, Int. Rev. Phys. Chem. **29**, 619 (2010).
[4] S. Fleischer, Y. Khodorkovsky, E. Gershnabel, Y. Prior, and I. Sh. Averbukh, Molecular alignment induced by ultrashort laser pulses and its impact on molecular motion, Isr. J. Chem. **52**, 414 (2012).
[5] T. Seideman, Revival Structure of Aligned Rotational Wave Packets, Phys. Rev. Lett. **83**, 4971 (1999).
[6] F. Rosca-Pruna and M. J. J. Vrakking, Experimental Observation of Revival Structures in Picosecond Laser-Induced Alignment of I_2, Phys. Rev. Lett. **87**, 153902 (2001).
[7] M. Machholm and N. E. Henriksen, Field-Free Orientation of Molecules, Phys. Rev. Lett. **87**, 193001 (2001).
[8] V. Renard, M. Renard, S. Guerin, Y. T. Pashayan, B. Lavorel, O. Faucher, and H. R. Jauslin, Postpulse Molecular Alignment Measured by a Weak Field Polarization Technique, Phys. Rev. Lett. **90**, 153601 (2003).
[9] P. W. Dooley, I. V. Litvinyuk, Kevin F. Lee, D. M. Rayner, M. Spanner, D. M. Villeneuve, and P. B. Corkum, Direct imaging of rotational wave-packet dynamics of diatomic molecules, Phys. Rev. A **68**, 023406 (2003).
[10] A. Przystawik, A. Kickermann, A. Al-Shemmary, S. Düsterer, A. M. Ellis, K. von Haeften, M. Harmand, S. Ramakrishna, H. Redlin, L. Schroedter, M. Schulz, T. Seideman, N. Stojanovic, J. Szekely, F. Tavella, S. Toleikis, and T. Laarmann, Generation of the simplest rotational wave packet in a diatomic molecule: Tracing a two-level superposition in the time domain, Phys. Rev. A **85**, 052503 (2012).
[11] S. Ramakrishna and T. Seideman, Intense Laser Alignment in Dissipative Media as a Route to Solvent Dynamics, Phys. Rev. Lett. **95**, 113001 (2005).
[12] T. Vieillard, F. Chaussard, D. Sugny, B. Lavorel, and O. Faucher, Field-free molecular alignment of CO_2 mixtures in presence of collisional relaxation, J. Raman Spectrosc. **39**, 694 (2008).
[13] N. Owschimikow, F. Knigsmann, J. Maurer, P. Giese, A. Ott, B. Schmidt, and N. Schwentner, Cross sections for rotational decoherence of perturbed nitrogen measured via decay of laser-induced alignment, J. Chem. Phys. **133**, 044311 (2010).
[14] J. M. Hartmann and C. Boulet, Quantum and classical approaches for rotational relaxation and nonresonant laser alignment of linear molecules: A comparison for CO_2 gas in the nonadiabatic regime, J. Chem. Phys. **136**, 184302 (2012).
[15] D. Pentlehner, J. H. Nielsen, A. Slenczka, K. Mølmer, and H. Stapelfeldt, Impulsive Laser Induced Alignment of Molecules Dissolved in Helium Nanodroplets, Phys. Rev. Lett. **110**, 093002 (2013).
[16] B. Shepperson, A. A. Søndergaard, L. Christiansen, J. Kaczmarczyk, R. E. Zillich, M. Lemeshko, and H. Stapelfeldt, Laser-Induced Rotation of Iodine Molecules in Helium Nanodroplets: Revivals and Breaking Free, Phys. Rev. Lett. **118**, 203203 (2017).
[17] W. Gordy and R. L. Cook, *Microwave Molecular Spectra*, 3rd ed. (Wiley, New York, 1984).
[18] R. N. Zare, *Angular Momentum* (Wiley, New York, 1988).
[19] R. F. Code and N. F. Ramsey, Molecular-beam magnetic resonance studies of HD and D_2, Phys. Rev. A **4**, 1945 (1971).
[20] U. Fano and J. H. Macek, Impact excitation and polarization of the emitted light, Rev. Mod. Phys. **45**, 553 (1973).

[21] R. Altkorn, R. N. Zare, and C. H. Greene, Depolarization of optically prepared molecules by two randomly oriented spins, Mol. Phys. **55**, 1 (1985).

[22] C. Yan and A. C. Kummel, Effect of hyperfine depolarization upon creation and detection of alignment in free-jet expansions via selective photodissociation, J. Chem. Phys. **98**, 6869 (1993).

[23] S. F. Gough and A. Crowe, The effect of hyperfine depolarization on electron-photon angular correlation measurements in krypton, J. Phys. B **26**, 2403 (1993).

[24] T. A. Cool and N. Hemmi, Hyperfine polarization quantum beats in cyanogen, J. Chem. Phys. **103**, 3357 (1995).

[25] J. Zhang, C. W. Riehn, M. Dulligan, and C. Wittig, An experimental study of HF photodissociation: Spin-orbit branching ratio and infrared alignment, J. Chem. Phys. **104**, 7027 (1996).

[26] E. R. Wouters, L. D. A. Siebbeles, K. L. Reid, B. Buijsse, and W. J. van der Zande, Observation of fine structure and hyperfine structure depolarization in the photofragment anisotropy in triplet H_2, Chem. Phys. **218**, 309 (1997).

[27] A. D. Rudert, J. Martin, W.-B. Gao, J. B. Halpern, and H. Zacharias, Collisional effects on angular momentum orientation in acetylene $\tilde{X}^1\Sigma_g^+(\nu_2'' = 1, j'')$. I. Preparation, detection and conservation in single collisions, J. Chem. Phys. **111**, 9549 (1999).

[28] D. Sofikitis, L. Rubio-Lago, M. R. Martin, D. J. Ankeny Brown, N. C.-M. Bartlett, A. J. Alexander, R. N. Zare, and T. P. Rakitzis, Optical control of ground-state atomic orbital alignment:$Cl(^2P_{3/2})$ from $HCl(v = 2, j = 1)$ photodissociation, J. Chem. Phys. **127**, 144307 (2007).

[29] N. C.-M. Bartlett, D. J. Miller, R. N. Zare, A. J. Alexander, D. Sofikitis, and T. P. Rakitzis, Time-dependent depolarization of aligned HD molecules, Phys. Chem. Chem. Phys. **11**, 142 (2009).

[30] N. C.-M. Bartlett, J. Jankunas, R. N. Zare, and J. A. Harrison, Time-dependent depolarization of aligned D_2 caused by hyperfine coupling, Phys. Chem. Chem. Phys. **12**, 15689 (2010).

[31] K. Grygoryeva, J. Rakovský, O. Votava, and M. Fárník, Imaging of rotational wave-function in photodissociation of rovibrationally excited HCl molecules, J. Chem. Phys. **147**, 013901 (2017).

[32] B. Shepperson, A. S. Chatterley, A. A. Søndergaard, L. Christiansen, M. Lemeshko, and H. Stapelfeldt, Strongly aligned molecules inside helium droplets in the near-adiabatic regime, J. Chem. Phys. **147**, 013946 (2017).

[33] A. A. Søndergaard, B. Shepperson, and H. Stapelfeldt, Nonadiabatic laser-induced alignment of molecules: Reconstructing $\langle\cos^2\theta\rangle$ directly from $\langle\cos^2\theta_{2d}\rangle$ by Fourier analysis, J. Chem. Phys. **147**, 013905 (2017).

[34] See Supplemental Material at http://link.aps.org/supplemental/10.1103/PhysRevLett.120.163202 for extended simulations and analyses.

[35] *NIST Chemistry WebBook, NIST Standard Reference Database Number 69*, edited by P. J. Linstrom and W. G. Mallard (National Institute of Standards and Technology, Gaithersburg, MD, 2017), http://webbook.nist.gov.

[36] R. Bacis, M. Broyer, S. Churassy, J. Vergès, and J. Vigué, eQq measurements in the X, 1g, O_g^+ and B state of I_2: A test of the electronic molecular eigenfunctions, J. Chem. Phys. **73**, 2641 (1980).

[37] D. M. Lubman, C. T. Rettner, and R. N. Zare, How isolated are molecules in a molecular beam?, J. Phys. Chem. **86**, 1129 (1982).

[38] G. Maroulis, Accurate dipole polarizability for $Cl_2(X^1\Sigma_g^+)$, Mol. Phys. **77**, 1085 (1992).

[39] G. Maroulis, C. Makris, U. Hohm, and D. Goebel, Electro-optical properties and molecular polarization of iodine, I_2, J. Phys. Chem. A **101**, 953 (1997).

[40] U. Even, J. Jortner, D. Noy, N. Lavie, and C. Cossart-Magos, Cooling of large molecules below 1 K and He clusters formation, J. Chem. Phys. **112**, 8068 (2000).

[41] F. Filsinger, J. Küpper, G. Meijer, L. Holmegaard, J. H. Nielsen, I. Nevo, J. L. Hansen, and H. Stapelfeldt, Quantum-state selection, alignment, and orientation of large molecules using static electric and laser fields, J. Chem. Phys. **131**, 064309 (2009); https://aip.scitation.org/doi/full/10.1063/1.3194287.

[42] C.-C. Shu, E. F. Thomas, and N. E. Henriksen, Femtochemistry in the electronic ground state: Dynamic stark control of vibrational dynamics, Chem. Phys. Lett. **683**, 234 (2017).

[43] A. Yokozeki and J. S. Muenter, Laser fluorescence state selected and detected molecular beam magnetic resonance in I_2, J. Chem. Phys. **72**, 3796 (1980).

[44] D. A. McQuarrie, *Statistical Mechanics* (Harper & Row, New York, 1976).

[45] R. L. Cook and F. C. De Lucia, Application of the theory of irreducible tensor operators to molecular hyperfine structure, Am. J. Phys. **39**, 1433 (1971).

[46] C. Z. Bisgaard, Ph.D. thesis, Aarhus University, 2006.

[47] A. A. Søndergaard, Ph.D. thesis, Aarhus University, 2016.

Supplemental Material

Hyperfine-structure-induced depolarization of impulsively aligned I_2 molecules

Esben F. Thomas,[1] Anders A. Søndergaard,[2] Benjamin Shepperson,[2] Niels E. Henriksen,[1] and Henrik Stapelfeldt[2]

[1]*Department of Chemistry, Technical University of Denmark, Building 206, DK-2800 Kongens Lyngby, Denmark*

[2]*Department of Chemistry, Aarhus University, Langelandsgade 140, DK-8000 Aarhus C, Denmark*

(Dated: March 15, 2018)

CONTENTS

ARE EXPERIMENTAL FACTORS INFLUENCING THE OBSERVED ALIGNMENT DYNAMICS?

Firstly, the conditions of the molecular beam used were such that there was absolutely no collisions between the I_2 molecules and other molecules or atoms on the nanosecond observation time of the experiment [1].

Secondly, the maximum delay of the probe pulse with respect to the kick pulse was 3.2 ns (see Fig. 1 in the main text). With a speed of about 1700 m/s (determined by the helium carrier gas in the supersonic expansion) the I_2 molecules moved a maximum of 3.2 ns $\times$ 1700 m/s = 5.4 μm between the kick pulse and the probe pulse. The probe laser beam and the kick laser beam were spatially overlapped in the experiment and their Gaussian spotsizes were $\omega_0(\text{kick}) = 25$ μm and $\omega_0(\text{kick}) = 35$ μm. This ensured that the probe pulse actually probed molecules that had been aligned by the kick pulse. If the delay had been increased to e.g. 10 ns or more it would have been necessary to spatially offset the focus of the probe beam downstream of the molecular beam.

Thirdly, the extraction field in the VMI spectrometer is about 500 V/cm. Since I_2 is nonpolar there were no interaction with a possible dipole moment. In addition, the interaction between the extraction field and the polarizability of the molecules is negligible.

We conclude that none of the three experimental factors influence the observed alignment dynamics.

SIMULATION WITH CENTRIFUGAL DISTORTION

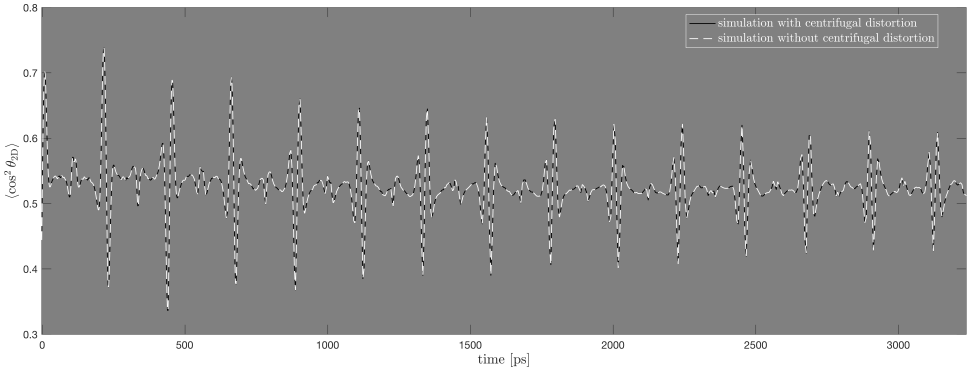

Figure 1. Overlaid simulated quadrupole coupled traces with (black solid line) and without (white dashed line) the effects of centrifugal distortion included. The background color has been darkened to enhance the contrast between the two traces since they are nearly identical.

Centrifugal distortion leads to a decrease in the energy spacing of the rotational energy levels as a function of J. It is one of the well-known ways that the behaviour of a real molecule will deviate from the rigid rotor approximation, and its effect on our quantum mechanical model is therefore worth investigating. The effects of centrifugal distortion can be included in our model by modifying the rotational energy as a function of J in the following way:

$$E_J = B_0 J(J+1) - D_0 J^2 (J+1)^2, \tag{1}$$

where $B_0 = 1.11863$ GHz and $D_0 = 67.7531$ Hz are, respectively, the molecular rotational constant and centrifugal distortion constant of I_2 in the vibrational ground state [2]. A rough calculation shows that the size of the centrifugal correction term will be comparable to that of the B_0 constant when $J \approx 50$. In a sense this means that we should not expect centrifugal distortion to play a significant role when $J < 50$.

The average J value in the rotational wave packets generated by our experimental pulse is about 5, so based on our rough analysis we are very far from the threshold where centrifugal distortion will play a role. Nevertheless, a simulation was performed where the centrifugal correction term was added to $\mathcal{H}_B$ in Eq. (2) of the main article text. The result of this

simulation is overlaid with the simulation performed without centrifugal distortion in Fig. 1, and as expected the two traces are almost completely identical. This underlines that the deviations from the rigid rotor model observed in the experimental trace are in no meaningful way associated with the effect of centrifugal distortion.

SIMULATION WITH FITTED TEMPERATURE

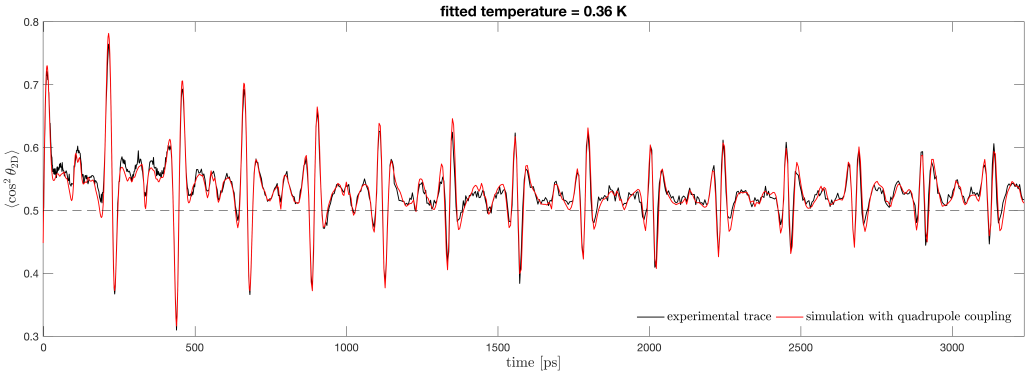

Figure 2. Experimental results (black) and the model calculations (red) calculated using a fitted initial rotational temperature of $T = 0.36$ K.

As stated in the main article text, fitting the simulated initial rotational temperature to minimize the RMSE will lead to a simulated trace that agrees better with the experimental data during the initial 600 ps. This result can be seen in Fig. 2, where the fitted temperature was found to be 0.36 K. Note that the agreement at times after 600 ps is roughly the same as in the 0.8 K case shown in Fig. 1 of the main article.

Generally, it was found that using simulated temperatures in the range of $\sim 0.3 - 1$ K would lead to good agreement between the theoretical and experimental traces at times after 600 ps. This gives credence to the conclusion that the observed deviations from the rigid rotor approximation are specifically due to quadrupole coupling, and not a result of parametric overfitting.

ANALYSIS OF THE IMPACT OF THE VIBRATIONAL TEMPERATURE

The molecular beam in our experiments is created by expanding ~ 1 mbar iodine gas in 80 bar of He gas into vacuum through an Even Lavie valve. As mentioned in the main text this leads to a rotational temperature of about 1 K. Such low rotational temperatures have been reported for several other molecules [3, 4] and it has also been shown that the high pressure expansion leads to strong vibrational cooling [3]. As such we expected that most of the I_2 molecules reside in the vibrational ground state prior to the kick pulse. Nevertheless, since we do not have a precise estimate for the vibrational temperature in the experiment, in this section we investigate how molecules in the first excited vibrational state influence the alignment dynamics.

At temperatures from $0-300$ K, only the first two vibrational states, ν_0 and ν_1, have the potential to be significantly populated. I_2 in the ν_1 vibrational state (hereby denoted $I_2^{\nu_1}$) has a rotational constant that is slightly smaller ($\sim 0.3\%$) than the rotational constant of I_2 in the vibrational ground state ($I_2^{\nu_0}$). This means that in general the alignment trace of $I_2^{\nu_1}$ will be slightly "stretched" compared to that of $I_2^{\nu_0}$. Therefore, an incoherent superposition of $I_2^{\nu_1}$ and $I_2^{\nu_0}$ traces will initially start to destructively (and later constructively) interfere over time as they move out of (and back into) phase with each other. Qualitatively, the initial destructive interference will manifest itself as an attenuation of the peak height in the $\langle\cos^2\theta_{2\mathrm{D}}\rangle_{\mathrm{coh}}$ component of the alignment trace.

Effectively, the introduction of higher vibrational states will have some of the same qualitative effects on the alignment trace as that of the quadrupole coupling (decreasing the peak amplitude over time). The question that must be answered is therefore how much of the observed peak attenuation is due to quadrupole coupling, and how much is potentially due to I_2 molecules in higher vibrational states?

To this end, we performed simulations of the quadrupole and non-quadrupole coupled systems, where all parameters were the same except the rotational constant was modified to that of $I_2^{\nu_1}$ (the eqQ quadrupole coupling constant for $I_2^{\nu_1}$ can safely be assumed to be identical to that of $I_2^{\nu_0}$ [5]). We then incoherently added the $I_2^{\nu_1}$ traces to the $I_2^{\nu_0}$ traces to reflect thermal vibrational distributions from $0-300$ K. Results for vibrational temperatures of 1, 100, 200 and 300 K are shown with and without quadrupole coupling and compared to the experimental results in Fig. 3 for trace structures appearing between 2600 and 3200 ps

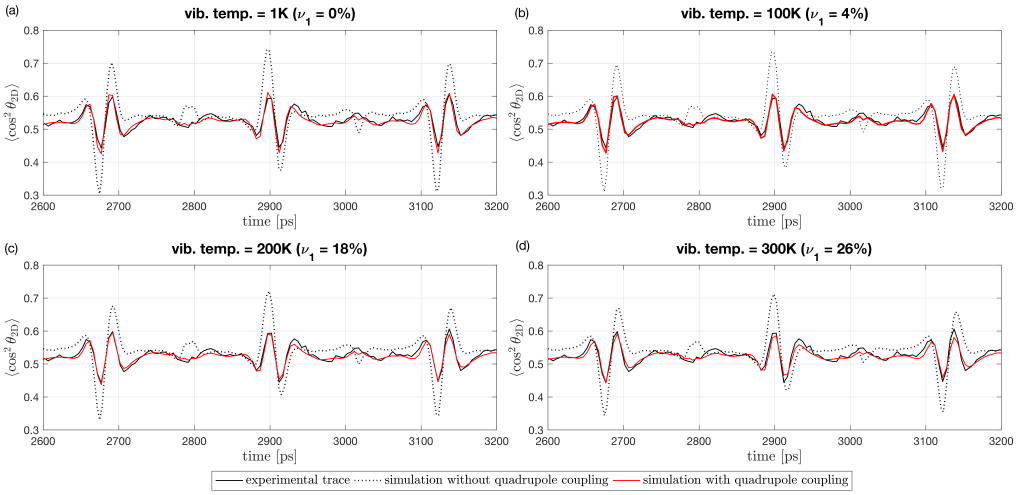

Figure 3. Close-up view of the $n = 6 - 7$ revival peaks appearing between 2600 and 3200 ps. calculated at various vibrational temperatures with (red line) and without (dotted line) quadrupole coupling, compared to the experimental trace (black line). In (a) we assume that the vibrational temperature is roughly the same as the rotational temperature, i.e. only the ground vibrational state ν_0 is populated and the trace is identical to the one appearing in Fig. 1 of the main article. In (b), (c) and (d) we incoherently sum traces calculated for I_2 molecules in ν_0 and ν_1 vibrational states with proportions corresponding to Boltzmann distributions at 100, 200 and 300 K, respectively.

(we focus on this region of the trace because the attenuating effect of the higher vibrational states only becomes significant at longer time scales).

While close inspection of Fig. 3 indicates that vibrational temperatures from $100 - 300$ K will have a small impact on the peak amplitudes of both the quadrupole coupled and non-quadrupole coupled traces, it is clear that the quadrupole coupling plays the dominant role in modulating the overall amplitude and/or structure of the trace. In particular, the pronounced changes of the shape of the quarter revivals can only be accounted for by the quadrupole coupling.

It is also in principle possible that the kick pulse causes some excitation from the vibrational ground state to the first excited vibrational state through a stimulated Raman transition. In Ref. [6], the authors simulate hitting Cl_2 molecules in the vibrational ground state with transform limited pulses where the widths have been optimized to induce vibra-

tional transitions. Even though the simulated intensities are about 10× higher than our experimental pulse, this only leads to a ν_1 population of about 0.1%. The derivative of the polarizability function at the equilibrium bond distance (and therefore the Raman transition probability) of I_2 is similar to that of Cl_2 [7, 8], so the results from Ref. [6] strongly indicate that it is unlikely that any significant vibrational excitation is caused by our experimental pulse.

SIMULATION OF HIGH-J WAVEPACKET TO 1 μS

As stated in the main article text, it is already well understood from, e.g., the classical illustration in Ref. [9], that if $|J|$ is much larger than $|I|$ then the relative change in the projection M_J along the z axis as **I** and **J** precess around **F** will be insignificant, putting an absolute limit on how much depolarization will occur in $\langle\cos^2\theta_{2D}\rangle_{\rm perm}$. As we uncover in our analysis, this is not the case for $\langle\cos^2\theta_{2D}\rangle_{\rm coh}$, where it is posited that peak structures will eventually decay to the same "background" level regardless of the magnitude of the J values present in the rotational wave packet (although the size of the J's is associated with how long the decay takes).

In the main text we test this claim by creating wave packets with larger J, by increasing the simulated pulse intensity. In this supporting section, we go further by upping the intensity to 10 TW/cm^2, over 9 times the experimental value, creating a rotational wave packet with an average J value of 39, almost 8 times larger than the biggest I value (5) present in the system.

The decay of the peak structures in $\langle\cos^2\theta_{2D}\rangle_{\rm coh}$ will happen very slowly in this case, so it is computationally unfeasible to simulate the entire alignment trace until the peaks disappear. Fortunately, the properties of our simulation allow us to jump forward to any time interval without having to calculate the preceding dynamics. Fig. 4 shows the simulated alignment trace in 500 ps segments beginning at 0, 200, 500, and 1000 ns. It can be clearly seen that the revival peak structures are almost completely gone by 1000 ns, whereas the change in the permanent (average) alignment from the initial level is very small.

This result further serves to underline one of the aforementioned main qualitative differences between how the quadrupole coupling affects the $\langle\cos^2\theta_{2D}\rangle_{\rm coh}$ and $\langle\cos^2\theta_{2D}\rangle_{\rm perm}$ components of the alignment trace for rotational wave packets in the high J limit; the effect on $\langle\cos^2\theta_{2D}\rangle_{\rm perm}$ becomes negligible whereas the effect on $\langle\cos^2\theta_{2D}\rangle_{\rm coh}$ always eventually becomes significant (as a side note, it is clear the time scales where this happens can potentially become so long that they are not feasible to measure in a given experimental setup).

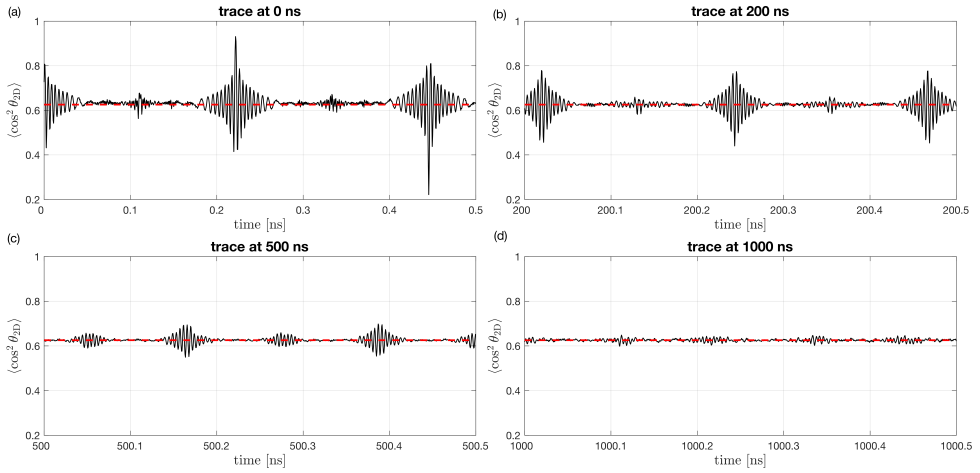

Figure 4. Quadrupole-coupled alignment trace simulated in 500 ps intervals starting at 0, 200, 500, and 1000 ns, using an alignment pulse intensity of 10 TW/cm^2. A pulse of this intensity yields a system of rotational wave packets where the average J value is 39, significantly larger than the I values present in the system. The horizontal red dashed lines are set to the mean of the trace values calculated at 500 and 1000 ns, and are meant to serve as visual aids to illustrate how little the average level of alignment deviates from its initial value over time. Note that because of the large J states present here, we have included centrifugal distortion in our simulation.

[1] D. M. Lubman, C. T. Rettner, and R. N. Zare. How isolated are molecules in a molecular beam? *J. Phys. Chem.*, 86:1129, 1982.

[2] P.J. Linstrom and W.G. Mallard Eds. *NIST Chemistry WebBook, NIST Standard Reference Database Number 69*. National Institute of Standards and Technology, Gaithersburg MD, 20899, http://webbook.nist.gov, 2017.

[3] U. Even, J. Jortner, D. Noy, N. Lavie, and C. Cossart-Magos. Cooling of large molecules below 1 K and He clusters formation. *J. Chem. Phys.*, 112(18):8068, May 2000.

[4] F. Filsinger, J. Küpper, G. Meijer, L. Holmegaard, J. H. Nielsen, I. Nevo, J. L. Hansen, and H. Stapelfeldt. Quantum-state selection, alignment, and orientation of large molecules using static electric and laser fields. *J. Chem. Phys.*, 131(6):064309, 2009.

[5] R. Bacis, M. Broyer, S. Churassy, J. Vergès, and J. Vigué. eQq measurements in the X, 1g, O_g^+ and B state of I_2: A test of the electronic molecular eigenfunctions. *J. Chem. Phys.*, 73:2641, 1980.

[6] Chuan-Cun Shu, Esben F. Thomas, and Niels E. Henriksen. Femtochemistry in the electronic ground state: Dynamic stark control of vibrational dynamics. *Chem. Phys. Lett.*, 683:234–239, 2017.

[7] G. Maroulis. Accurate dipole polarizability for $Cl_2(X^1\Sigma_g^+)$. *Mol. Phys.*, 77:1085, 1992.

[8] G. Maroulis, C. Makris, U. Hohm, and D. Goebel. Electrooptical properties and molecular polarization of iodine, I_2. *J. Phys. Chem. A*, 101:953, 1997.

[9] N. C.-M. Bartlett, J. Jankunas, R. N. Zare, and J. A. Harrison. Time-dependent depolarization of aligned D_2 caused by hyperfine coupling. *Phys. Chem. Chem. Phys.*, 12:15689–15694, 2010.

Appendix D

Phase-Modulated Nonresonant Laser Pulses Can Selectively Convert Enantiomers in a Racemic Mixture

THE JOURNAL OF PHYSICAL CHEMISTRY Letters

Letter

pubs.acs.org/JPCL

Phase-Modulated Nonresonant Laser Pulses Can Selectively Convert Enantiomers in a Racemic Mixture

Esben F. Thomas and Niels E. Henriksen*

Department of Chemistry, Technical University of Denmark, Building 206, DK-2800 Kongens Lyngby, Denmark

Supporting Information

ABSTRACT: Deracemization occurs when a racemic molecular mixture is transformed into a mixture containing an excess of a single enantiomer. Recent advances in ultrafast laser technology hint at the possibility of using shaped pulses to generate deracemization via selective enantiomeric conversion; however, experimental implementation remains a challenge and has not yet been achieved. Here we suggest a simple, yet novel approach to laser-induced enantiomeric conversion based on dynamic Stark control. We demonstrate theoretically that current laser and optical technology can be used to generate a pair of phase-modulated, nonresonant, linearly polarized Gaussian laser pulses that can selectively deracemize a racemic mixture of 3D-oriented, 3,5-difluoro-3′,5′-dibromobiphenyl ($F_2H_3C_6-C_6H_3Br_2$) molecules, the laser-induced dynamics of which are well studied experimentally. These results strongly suggest that designing a closed-loop coherent control scheme based on this methodology may lead to the first-ever achievement of enantiomeric conversion via coherent laser light in a laboratory setting.

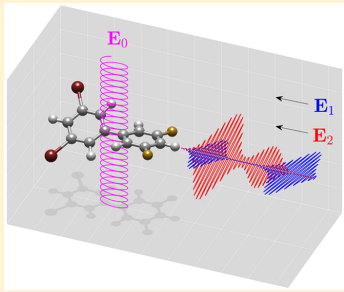

Save for possible tiny energy differences due to parity violating forces,[1] the inherent symmetries of the physical laws mean that enantiomeric pairs possess identical energies. Because of this, synthesizing molecules with chiral structures will generally result in a 50%:50% mixture of left- and right-handed forms (i.e., a racemic mixture) unless a chiralic precursor is applied at some point to target molecules of a certain configuration. Deracemization occurs when a racemic mixture of molecules is transformed into a mixture containing an excess of a single enantiomer. The majority of the work done on deracemization at present time has been concerned with the use of chemical reagents to separate or transform enantiomers (see, e.g., refs 2 and 3).

Here we explore a fundamentally different approach to deracemization where coherent laser light is used to selectively transform the structure of a specific enantiomer in a racemic mixture into its mirrored form while leaving the opposite enantiomer unchanged. A number of theoretical studies have shown that this may be possible (see, e.g., refs 4−14); however, laser-induced deracemization via enantiomeric conversion has not yet been demonstrated in a laboratory, presumably because experimental implementations of the theoretical principles remain unfeasible for a variety of reasons (e.g., the theoretically optimal laser pulse waveforms cannot easily be generated by existing laser and optical technology).

In general, the concept of applying ultrashort laser pulses to control the dynamics of molecular systems has been a topic of interest for some time. A large body of theoretical (see, e.g., refs 15−19) and experimental (see, e.g., refs 20−26) work has been produced in which the feasibility of applying custom-tailored laser pulses to drive various systems into specific target states has been demonstrated. Experimentally, so-called "closed-loop" optimization schemes have proven to be particularly successful. Essentially, the closed-loop approach is based around the application of an adaptive algorithm[27] to the inputs of a spectral pulse shaper[28,29] in a feedback loop, where the pulse-shaper inputs are updated and optimized "on the fly" based on experimental data generated by the interaction of the molecular system with preceding pulses.

We will demonstrate a robust method of controlling the very delicate process of deracemization based on a computational closed-loop scheme that manipulates the same inputs to the optimization problem that an experimentalist would have access to. In addition to this, we have ensured that the various control parameters lie within the bounds of what is demonstrably achievable in a laboratory. For these reasons, our approach marks a departure from previous theoretical studies of laser-induced deracemization. Our model system is the 3,5-difluoro-3′,5′-dibromobiphenyl molecule shown in Charts 1 and 2 (which we will henceforth refer to as $F_2H_3C_6-C_6H_3Br_2$). $F_2H_3C_6-C_6H_3Br_2$ is an advantageous choice for at least two reasons: It has an axially chiral structure where simple torsional rotation around the stereogenic axis leads to transformations between left- and right-handed enantiomeric forms and its laser-induced dynamics are well studied experimentally. The motivation for the latter statement is primarily based on an impressive series of experiments conducted by Madsen et al.,[30−32] in which it was demonstrated that one or two nonresonant femtosecond pulses can induce torsional vibration

Received: March 20, 2017
Accepted: May 3, 2017
Published: May 3, 2017

DOI: 10.1021/acs.jpclett.7b00662
J. Phys. Chem. Lett. 2017, 8, 2212−2219

Chart 1. Molecular Structure of 3,5-Difluoro-3′,5′-dibromobiphenyl ($F_2H_3C_6-C_6H_3Br_2$)[a]

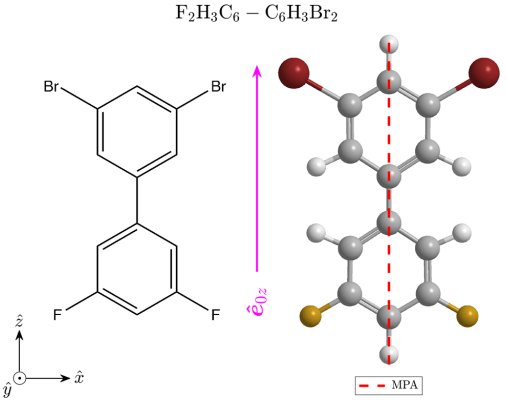

[a]The most polarizable axis (MPA) is also shown (dashed red line). In the simulations performed throughout this article, the MPA is always oriented along the $\hat{z}$ axis with the Br-substituted ring pointing in the positive direction as shown. The magenta arrow shows the direction of the major polarization axis of the elliptical orientation pulse $\mathbf{E}_0$, denoted by $\hat{\boldsymbol{\epsilon}}_{0z}$.

Chart 2. Top-Down View of the 3D-Oriented S_a and R_a Enantiomers When Their Second Most Polarizable Axes (SMPA, dashed blue line) Are Aligned with the Minor Polarization Axis of the Alignment Pulse E_0, Denoted by $\hat{\boldsymbol{\epsilon}}_{0x}$ (Magenta Arrow)[a]

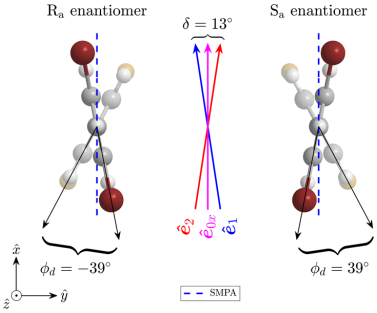

[a]The dihedral angle in this coordinate system is defined as $\phi_d = \phi_{Br} - \phi_F$, where ϕ_{Br} and ϕ_F are the rotational angles of the Br- and F-substituted rings around the stereogenic ($\hat{z}$) axis with respect to $\hat{x}$, respectively. For reference, the polarization axes of the kick pulses $\mathbf{E}_1$ and $\mathbf{E}_2$, denoted, respectively, by $\hat{\boldsymbol{\epsilon}}_1$ (blue arrow) and $\hat{\boldsymbol{\epsilon}}_2$ (red arrow) are pictured as well.

around the stereogenic axes of a Boltzmann population of aligned or oriented $F_2H_3C_6-C_6H_3Br_2$ molecules in the gas phase.

We use a genetic algorithm[27,33] (GA) to optimize the peak intensity and phase modulation of a pair of superposed, linearly polarized, nonresonant Gaussian laser pulses in a manner that leads to an increase in the amplitude of the aforementioned torsional oscillations and a transfer of the molecular wave packet over the potential energy barrier separating two enantiomeric forms. Moreover, we show how to limit this transfer so it occurs in only one type of enantiomer, leading to deracemization. The laser pulses couple to the molecular polarizability functions by way of the dynamic Stark effect,[34−36] which is proportional to the square of the field envelope $|\mathcal{E}(t)|^2$ times the molecular polarizability term α. Therefore, an advantage of this method over previous work is that we are not limited by the carrier frequency of the laser because it can be shown that the molecules will only respond to changes in the electric field envelope in the dynamic Stark regime.

At high temperatures, the two substituted phenyl rings of the molecule rotate freely around the axial C−C bond that connects them; however, in the work by Madsen et al. it is demonstrated that cooling a gas-phase population to a few Kelvin will hinder the internal rotation, and the dihedral angle ϕ_d between the ring planes will become fixed at $\phi_d = 39°$ or $\phi_d = -39°$. As Chart 2 demonstrates, these angular configurations correspond to two different stable structures that are each other's mirror image, that is, an enantiomeric pair. Here we adopt the notation of labeling the 39° and −39° configurations as S_a and R_a enantiomers, respectively. The most polarizable axis (MPA) of the molecule lies along the stereogenic axis, as shown in Chart 1. The second most polarizable axis (SMPA) of both enantiomers is orthogonal to the MPA and oriented at a relative angle of 11 and 28° with relation to the Br- and F-substituted ring, respectively, as shown in Chart 2.

The initial 3D orientation of the molecules is critical to the approach described here. Note that we adopt the standard nomenclature where the term "orientation" differs from the term "alignment" in the sense that molecular orientation imposes the additional requirement that all molecules point in the same direction, a stricter condition than that of molecular alignment, which does not differentiate between parallel and antiparallel configurations. Orientation of the S_a and R_a enantiomers, for example, so the Br ring of every molecule points in the positive $\hat{z}$ direction as illustrated by Chart 1, can be achieved by combining an adiabatic (ns) alignment pulse with a static field.[37] Experiments have shown[38] that elliptically polarizing the alignment pulse will extend this 1D orientation to 3D by confining the MPA and SMPA along the major and minor axes of the pulse, respectively,[30] effectively causing the S_a and R_a SMPAs to lie parallel to each other, as shown in Chart 2. The 3D orientation in our suggested setup is achieved by combining a static field with an elliptically polarized alignment/orientation pulse $\mathbf{E}_0$ (see Abstract graphic), where the form of this pulse can be expressed in lab frame coordinates as

$$\mathbf{E}_0(t) = \mathcal{E}_{0z}(t)\hat{\boldsymbol{\epsilon}}_{0z} + \mathcal{E}_{0x}(t)\hat{\boldsymbol{\epsilon}}_{0x} \quad (1)$$

where $\hat{\boldsymbol{\epsilon}}_{0z}$ and $\hat{\boldsymbol{\epsilon}}_{0x}$ are unit vectors aligned with the respective $\hat{z}$ and $\hat{x}$ axes and where $\mathcal{E}_{0z}(t)$ and $\mathcal{E}_{0x}(t)$ are the respective time-dependent amplitudes of the major and minor pulse axes. The suggested peak intensities of the major/minor axes of the theoretical alignment pulse are, respectively, 3 and 1 TW/cm^2, and the suggested wavelength is 1064 nm, as these parameters are comparable to experimental pulse parameters used in ref 32 to align a similar molecule.

The lowest frequency normal mode of the ground-state $F_2H_3C_6-C_6H_3Br_2$ system corresponds primarily to the torsional motion between the phenyl rings. Neglecting all higher frequency modes, we can simplify the internal potential energy surface of the molecule to a 2D representation of the torsional energy as a function of the rotational angle of each ring, that is, $V_{tor}(\phi_{Br}, \phi_F)$,[9,31] where ϕ_{Br} and ϕ_F are the respective angles of

DOI: 10.1021/acs.jpclett.7b00662
J. Phys. Chem. Lett. 2017, 8, 2212−2219

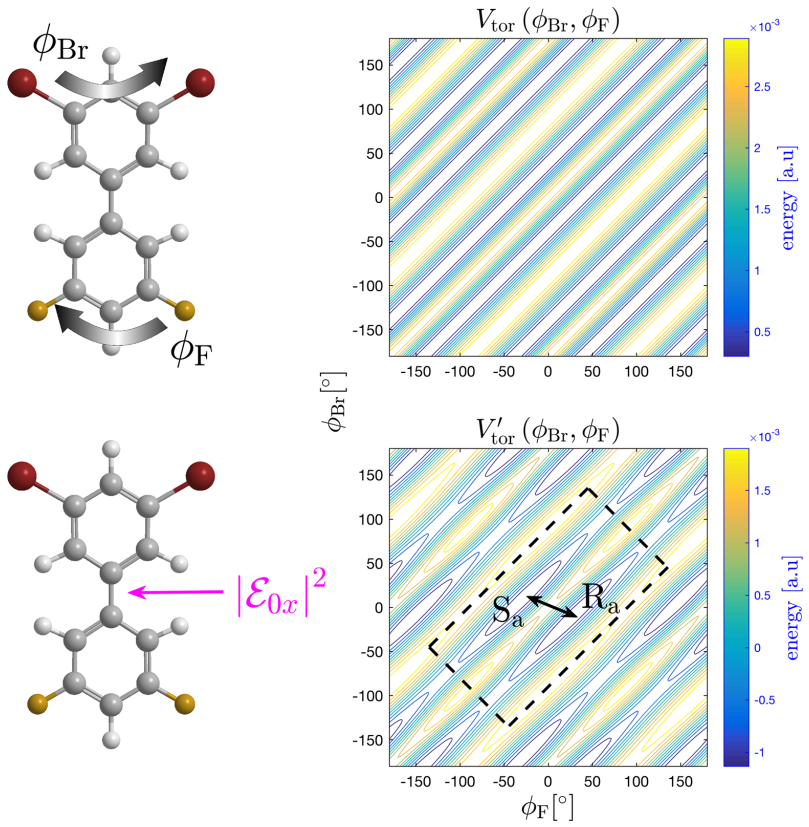

Figure 1. Upper diagram shows the field free torsional potential V_{tor} as a function of the rotational angles of the Br- and F-substituted rings, that is, moving in the positive diagonal direction corresponds to rotating the entire molecule while keeping the dihedral angle fixed, and moving in the negative diagonal direction corresponds to changes in the dihedral angle ϕ_d. The lower diagram shows how the field free potential is perturbed by an alignment field applied along the laboratory frame $\hat{x}$ axis (see Chart 2 and eq 2), where in this case $|\mathcal{E}_{0,x}|^2/c\mu_0 = 1$ TW/cm^2. The area bounded by the dashed black lines on the lower potential surface shows the domain where we choose to simulate the dynamics, as transferring a wave packet between the two minima located here is equivalent to switching from one enantiomeric form to the other.

the Br- and F-substituted rings with regard to the lab frame $\hat{x}$ axis, as illustrated in the top part of Figure 1. In a comparison with experimental data in figure 4 of ref 32, it is demonstrated that this 2D model will provide a very good approximation of the system dynamics in ϕ_d as long as we limit the duration of the simulated dynamics to $\lesssim$20 ps time scales.

The nonresonance and relatively large (ns) temporal width of the adiabatic alignment pulse means we can model its effects on the system by simply adding a time-independent perturbation to the field-free potential $V_{tor}(\phi_{Br}, \phi_F)$, that is

$$V'_{tor}(\phi_{Br}, \phi_F) = V_{tor}(\phi_{Br}, \phi_F) - \frac{1}{4}|\mathcal{E}_{0x}|^2 \alpha_0 \quad (2)$$

where $|\mathcal{E}_{0x}|^2$ is assumed to be constant over the simulated time scales. (See Supporting Section Is for the derivation of the polarizability term α_0.) The inclusion of the alignment field introduces local minima in the $V'_{tor}(\phi_{Br}, \phi_F)$ potential surface. (See Figure 1.) This means that the first few solutions to the time-independent Schrödinger equation will be bound states located in these minima, which translates into angular confinement of the SMPA at low temperatures. Note that the potential surface in the bottom right panel of Figure 1 contains eight minima, corresponding to four physically identical enantiomeric pairs. It is assumed that the optimized transformation will involve a coherent trajectory along the minimum energy path separating any two of these pairs. For this reason, we reduce the simulation domain to the region bounded by the black dashed lines. Boundary conditions are handled by assuming that any portion of the wave packets that cross the edge of the reduced simulation space are essentially "lost", a condition that is enforced by adding an absorbing negative imaginary potential (NIP)[39] to the simulation boundaries. (See Supporting Section IIs.)

The first two bound eigenstates (ψ_0, ψ_1) of this reduced domain potential were calculated using the relaxation method.[40] In general, the eigenstates of the system are odd and even functions around $\phi_d = 0$. These states may be combined to construct localized superpositions confined to the R_a or S_a well, that is, $\chi_{R_a} = (\psi_0 + \psi_1)/\sqrt{2}$ and $\chi_{S_a} = (\psi_0 - \psi_1)/\sqrt{2}$. The energy spacing of the solutions suggest that we can

DOI: 10.1021/acs.jpclett.7b00662
J. Phys. Chem. Lett. 2017, 8, 2212−2219

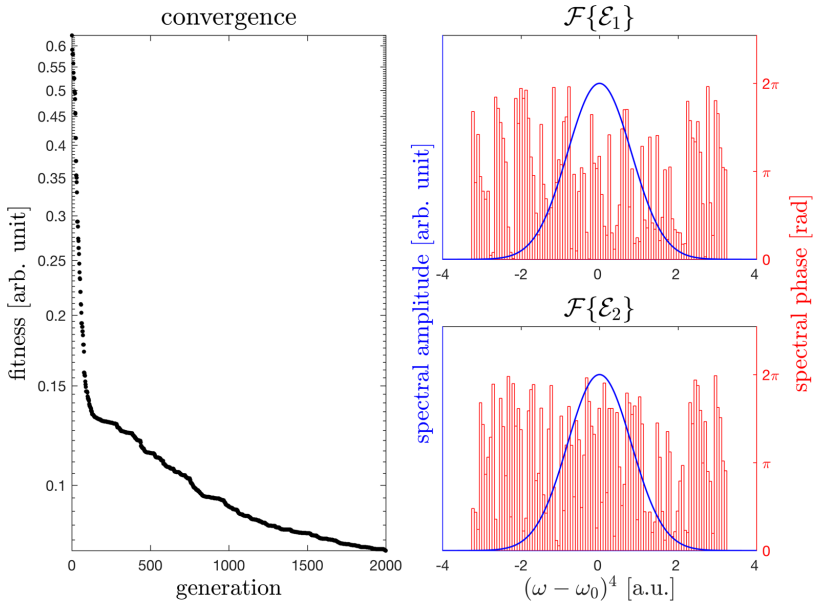

Figure 2. Left panel shows the fitness of the best performing individual from each generation of the GA optimization. (Note that in the GA we use higher fitness corresponds to lower values.) The two right panels show the spectral phase (red) and amplitude (blue) of the optimized pulse envelopes $\mathcal{E}_1$ and $\mathcal{E}_2$ with a fixed Gaussian spectral distribution, where $(\omega - \omega_0)^4$ on the frequency axes indicates that the values have been shifted and scaled to enhance readability.

assume, to a very good approximation, that the first two eigenstates of the system will be equally occupied, and at temperatures below 10 K all higher states will be empty. (Note that the eigenenergy spacing of the unreduced domain potential will be slightly different, but qualitatively the argument is the same.) As such, the initial thermal distribution can be rewritten as the (incoherent) sum of densities associated with χ_{R_a} and χ_{S_a};[6] that is, the wave packet in the R_a or S_a well at simulation time $t = 0$ can be expressed as $\Psi_{R_a}(0) = \chi_{R_a}$ or $\Psi_{S_a}(0) = \chi_{S_a}$, respectively. The energies of ψ_0 and ψ_1 are nearly degenerate, so their superposition leads to relatively long-lived (on the order of tens of milliseconds) states that are confined to the left or right well.[30]

As shown in the experimental setup sketched in the Abstract graphic, the two deracemizing kick pulses $\mathbf{E}_1$ and $\mathbf{E}_2$ propagate in the same direction, and their polarization axes are rotated away from the minor alignment pulse axis by equal and opposite angles $\pm\delta/2$, as shown in Chart 2. Dealigning the kick pulse axes in this manner ensures that the optimized pulses can break the inversion symmetry of the time-dependent dynamics between the two enantiomers, a critical prerequisite to successfully achieving deracemization. To gain an intuitive understanding of how this symmetry breaking is made possible by the dealignment of the kick pulses, we refer again to Chart 2, which shows the orientation of the R_a/S_a SMPAs in the presence of the alignment field $\mathbf{E}_0$. It is illustrative to construct a metaphor where applying a linearly polarized kick pulse to the R_a/S_a system is loosely analogous to hitting the molecules with a hammer moving in the same direction as the polarization axis of the laser. We must ensure that when we swing the "hammer" it will hit R_a and S_a from different angles because hitting them in the same place (e.g., if the kick pulses were aligned with $\hat{x}$) will only lead to mirrored (inversion symmetric) time-dependent dynamics. Within this framework, it is clear from inspection of Chart 2 that hitting the oriented molecules from the direction of $\hat{\mathbf{e}}_1$ or $\hat{\mathbf{e}}_2$ will (initially) lead to the desired asymmetrical interaction. Note that the above argumentation does not suffice to explain the reason for using two driving fields with different polarization axes. To understand this, consider that applying a single field, polarized, for example, along $\hat{\mathbf{e}}_1$, will cause the SMPAs of both enantiomers to rotate toward and, on average, become more aligned with the $\hat{\mathbf{e}}_1$ axis over time, once again leading to issues with inversion symmetry. Using two dealigned kick pulses makes it possible to continually disrupt this type of unwanted molecular alignment by changing the direction of the driving field. The total field induced by the kick pulses, expressed in lab-frame coordinates, is given by

$$\begin{aligned}\mathbf{E}_{tot}(t) &= \mathbf{E}_1(t) + \mathbf{E}_2(t) \\ &= \mathcal{E}_1(t)\hat{\mathbf{e}}_1 + \mathcal{E}_2(t)\hat{\mathbf{e}}_2\end{aligned} \tag{3}$$

where

$$\hat{\mathbf{e}}_1 = \begin{bmatrix}\cos(\delta/2)\\ \sin(\delta/2)\\ 0\end{bmatrix} \quad \text{and} \quad \hat{\mathbf{e}}_2 = \begin{bmatrix}\cos(-\delta/2)\\ \sin(-\delta/2)\\ 0\end{bmatrix} \tag{4}$$

where $\mathcal{E}_1(t)$ and $\mathcal{E}_2(t)$ are the (complex) time-dependent field amplitudes of each kick pulse. Including the interaction with $\mathbf{E}_{tot}$, the full lab-frame system Hamiltonian becomes

DOI: 10.1021/acs.jpclett.7b00662
J. Phys. Chem. Lett. 2017, 8, 2212−2219

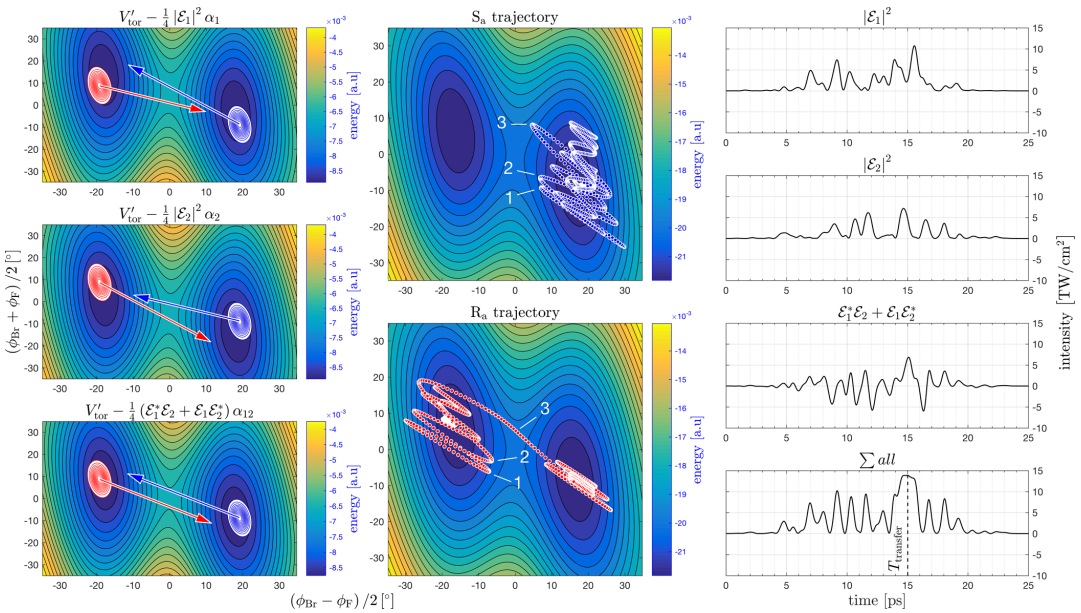

Figure 3. Right column shows the intensity envelopes of the two optimized kick pulses (first and second panels) as well as the cross term (third panel) and the sum of all three terms (fourth panel). The three panels on the left show a sketch of how the potential surface V'_{tor} is modified by each of the three field components, assuming $|\mathcal{E}_1|^2/c\mu_0 = |\mathcal{E}_2|^2/c\mu_0 = (\mathcal{E}_1^*\mathcal{E}_2 + \mathcal{E}_1\mathcal{E}_2^*)/c\mu_0 = 5$ TW/cm^2. The red and blue ovals show the R_a and S_a wave packets at $t = 0$, respectively, and the arrows indicate the direction and magnitude of the wave packet acceleration in the fields. The two center panels illustrate the trajectories of the mean wave packet positions when the system is driven by the optimized pulses, where the potential surface is shown at $t = T_{transfer}$, where $T_{transfer}$ is when the R_a wave packet crosses the central saddle point. The annotations on the middle panels are discussed in the article text.

$$H_{mol} = -\frac{1}{2I_{Br}}\frac{\partial^2}{\partial\phi_{Br}^2} - \frac{1}{2I_F}\frac{\partial^2}{\partial\phi_F^2} + V'_{tor} - \frac{1}{4}[|\mathcal{E}_1|^2\alpha_1 + |\mathcal{E}_2|^2\alpha_2 + (\mathcal{E}_1^*\mathcal{E}_2 + \mathcal{E}_1\mathcal{E}_2^*)\alpha_{12}] \quad (5)$$

where we have omitted the time dependence of the field amplitudes for clarity, I_{Br} and I_F are the respective inertial moments of the Br- and F-substituted rings, and the polarizabilities α_1, α_2, and α_{12} are functions of ϕ_{Br}, ϕ_F, and δ. (See Supporting Section Is.) Note that the molecular polarizability tensor couples to $\mathbf{E}_{tot}$ to second order, which explains the $\mathcal{E}_1^*\mathcal{E}_2$ and $\mathcal{E}_1^*\mathcal{E}_2$ cross terms appearing in the second line of eq 5.

Choosing realistic pulse parameters is clearly important if we wish to maintain experimental feasibility. The intensity envelopes of the initial, unshaped kick pulses are modeled as Gaussian functions with fixed fwhm widths of 495 fs. For reference, we assume that the central wavelengths of the unshaped pulses are 800 nm, although this choice has no impact on our simulated model because the field interaction in the nonresonant limit is independent of the carrier frequency. The GA was allowed to manipulate the peak intensities of the unshaped pulses as free parameters in a range from 25 to 150 TW/cm^2, leading to optimized peak intensities of 142.3 and 143.7 TW/cm^2. This corresponds to a pulse energy of roughly 1 mJ, assuming the beam diameter is focused to 43 μm when interacting with the molecules, as in ref 30. Energies in this range can be handled by modern pulse shapers. It is also possible to generate the shaped pulses at lower energies and boost the intensity using a pulse amplifier.[41]

Experimental spectral pulse shapers typically use an adjustable mask consisting of, for example, a pixel array of nematic liquid crystals that independently modify the optical path of discrete regions of the pulse spectrum by changing their orientation when voltage is applied.[28,29] The details of how we chose to model the pulse shaping can be found in Supporting Section IIIs. In short, we start by taking the numerical Fourier transform of the unshaped Gaussian temporal pulse. The pixels of the spectral mask are modeled by dividing a region around the center of the spectral pulse distribution into 101 discrete bins, as shown in the right side of Figure 2. The GA modifies the spectral phase shift produced by each bin as a boundless parameter, which is then wrapped to a range between 0 and 2π. Including the peak intensity of the unshaped pulses, this leads to a total of 204 optimization parameters. These phase-chirped pulses are reverse Fourier-transformed back into the temporal domain, and the effects of spatiotemporal coupling[42−45] are included by multiplying the center of the shaped pulse envelopes by a 10 ps fwhm Gaussian function of height 1. The result is a model of a pair of shaped and spatially filtered pulses, each generated by an unshaped laser with a 1.5 mm beam spot diameter being run through a pulse shaper with a spatiotemporal coupling speed of 150 μm/ps, representing typical experimental values.[29,46]

The shaped pulses are simulated interacting with the system using split-operator propagation[39] to solve the time-dependent

DOI: 10.1021/acs.jpclett.7b00662
J. Phys. Chem. Lett. 2017, 8, 2212−2219

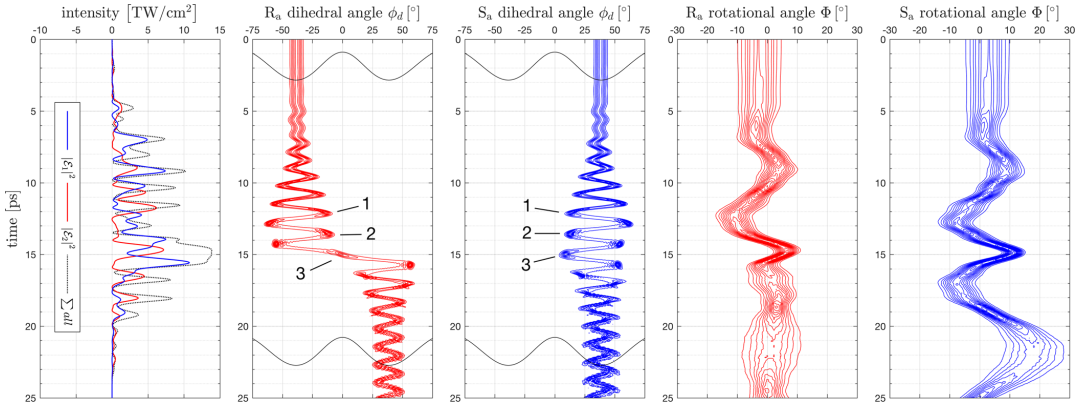

Figure 4. First panel from the left shows an overlay of the optimized field components. The second and third panels show the 1D marginal probability distribution of the 2D wave packet in the ϕ_d coordinate for the R_a (red) and S_a (blue) wave packets. The fourth and fifth panels show the marginal probability distribution in the weighted rotational angle Φ. The second and third panels also include a sketch of the field free potential in ϕ_d (black solid line) to illustrate the localization of the wave packets before and after the interaction with the optimized pulses. The annotations on panels 2 and 3 are discussed in the article text.

Schrödinger equation. (See Supporting Section IIs for simulation details.) When the simulation is finished, the fitness of the trial solution is evaluated and fed back into the GA. (Fitness function details can be found in Supporting Section IVs.) In short, the function evaluates how close the final R_a and S_a wave packets are to the location of the target well as well as imposing penalties on the summed intensity envelope of the combined pulses (see the bottom left panel of Figure 3) when the peak intensity is close to or higher than a user-defined threshold. The left side of Figure 2 shows the optimization convergence of a population of 600 individuals iterated for 2000 generations, and the right side shows the resulting phase functions of the optimal spectral pulses. The fitness curve shown in Figure 2 is typical of the type of convergence we observed across multiple optimizations; that is, there was generally a very rapid initial improvement in performance, followed by a long period of slow convergence. This rapid initial improvement indicates that in an actual experiment it is probably not necessary to iterate as many generations as we have here to get decent results.

The optimized temporal intensity envelopes $|\mathcal{E}_1|^2$ and $|\mathcal{E}_2|^2$ as well as the cross term $\mathcal{E}_1^*\mathcal{E}_2 + \mathcal{E}_1\mathcal{E}_2^*$ of the two pulses corresponding to the spectral distributions in Figure 2 are shown in the top three panels on the right side of Figure 3. The direct sum of all three field components, $\sum all$, is shown in the bottom right panel to illustrate that the total intensity never exceeds 15 TW/cm², which experimental data[47] suggests is well within a safe limit to avoid unwanted ionization effects. The two middle panels in Figure 3 show the trajectories of the expectation value of the R_a and S_a wave-packet positions when the molecules are driven by the optimized pulse envelopes. These trajectories clearly demonstrate how the mean position of the R_a wave packet transfers from the left to the right well while the S_a wave packet remains in its original position. By integration of the numerical wave packets at t = 25 ps, we find that 98% of the molecules are now S_a enantiomers. The three panels on the left side of Figure 3 show sketches of the initial R_a and S_a wave packets (i.e., $\Psi_{R_a}(0)$ in red and $\Psi_{S_a}(0)$ in blue), as well as illustrations of how the potential surface is modified when the α_1, α_2, or α_{12} terms are independently applied to the system when $|\mathcal{E}_1|^2$, $|\mathcal{E}_2|^2$, and $\mathcal{E}_1^*\mathcal{E}_2 + \mathcal{E}_1\mathcal{E}_2^*$ are set to a "typical" intensity of 5 TW/cm². The red and blue arrows in each panel illustrate the direction and (arbitrarily scaled) magnitude of the initial wave packet acceleration in the presence of the field terms. Note that the directions of the R_a/S_a acceleration vectors associated with the α_1 or α_2 terms do not align (unlike the vectors associated with the α_{12} term, which are antiparallel). This indicates that modifying the potential surface with $\mathbf{E}_1$ or $\mathbf{E}_2$ will propel $\Psi_{R_a}(0)$ and $\Psi_{S_a}(0)$ along divergent trajectories, again demonstrating how the dealigned pulses can break the inversion symmetry of the system.

To better illustrate the optimized dynamics, we can transform the 2D time-dependent wave packets into 1D time-dependent marginal probability distributions by integrating Ψ_{R_a} and Ψ_{S_a} along coordinates that are transverse to the dihedral angle $\phi_d = \phi_{Br} - \phi_F$, and the weighted rotational angle $\Phi = (I_{Br}\phi_{Br} + I_F\phi_F)/(I_{Br} + I_F)$. Like ϕ_{Br} and ϕ_F, ϕ_d and Φ do not couple in the kinetic energy operator of the Hamiltonian.[9] (There are couplings expressed in terms of the boundary conditions that depend on the ratio of the moments of inertia,[9] but this issue is avoided because the interplay of the fitness function with the NIP boundary leads to optimized wave-packet trajectories that never reach the edge of the simulation domain.) The advantage of using the ϕ_d and Φ coordinates is that they allow us to separately view the "internal" and "external" dynamics of the system; that is, dynamics in ϕ_d represent relative changes in the (internal) molecular coordinates and dynamics in Φ represent changes in the overall molecular rotation with regard to the (external) lab frame coordinates.

Because of mutual association with the overall molecular rotation, changes in Φ are concomitant with changes in the orientation of the molecular SMPAs. Combined with information shown in Figure 4, this can help explain how the optimized pulses work. As discussed, alignment of the SMPA with $\hat{\mathbf{e}}_1$ (or $\hat{\mathbf{e}}_2$) leads to unwanted inversion symmetry in the dynamics generated by $\mathbf{E}_1$ (or $\mathbf{E}_2$). This is dealt with by

DOI: 10.1021/acs.jpclett.7b00662
J. Phys. Chem. Lett. 2017, 8, 2212−2219

gradually alternating between using $\mathbf{E}_1$ and $\mathbf{E}_2$ to pump the amplitude of the dihedral oscillations. As panels 4 and 5 in Figure 4 show, this causes the Φ/SMPA angle to sweep back and forth between $\hat{e}_1$ and $\hat{e}_2$, maintaining the broken inversion symmetry of the interaction. This "switching" dynamic between $\mathbf{E}_1$ and $\mathbf{E}_2$ can be observed in the changing $\mathcal{E}_1/\mathcal{E}_2$ contribution to the train of five moderately intense pulses visible in the plot of $\sum all$ between 6 and 12 ps in panel 1 of Figure 4. Panels 2 and 3 in the same Figure show how this pulse train significantly increases the amplitude of the dihedral oscillations via "pseudo-resonant"[36] driving, as the pulse spacing is approximately equivalent to the vibrational period in ϕ_d. The preceding mechanisms effectively "prime" the system for the asymmetric transfer that occurs at 15 ps, when the fields combine to generate a broad, intense pulse that propels the R_a wave packet over the potential barrier, whereas the slightly dissimilar trajectory of the S_a wave packet causes it to rebound instead. To clarify the relationship between the dynamics plotted in Figures 3 and 4, we identify the location of three turning points in the ϕ_d oscillations leading up to the transfer, labeled by 1, 2, and 3, on both Figures. (Note that for R_a label 3 denotes the transfer point and not a turning point.) Using these reference points, the 2D trajectories pictured in Figure 3 clearly show how the R_a and S_a wave packets hit the barrier in places with different heights, which explains the asymmetric transfer.

Note that the symmetry of the two kick pulses with regard to the initial alignment of the system (see, e.g., Chart 2) means that if we wanted to deracemize the system into the R_a configuration instead of S_a as done here, we need only swap the polarization directions of the optimized $\mathbf{E}_1$ and $\mathbf{E}_2$ pulses. This leads to identical-but-mirrored dynamics across the system; that is, the S_a enantiomers will now become R_a instead of vice versa. The upshot of this is that once we have found a pulse optimized for one type of deracemization, we can freely select which enantiomer we want to generate with our laser.

The fitness function we have used to optimize the pulses is based on the norm of the quantum wave packet. (See eq 29s in Supporting Section IVs.) In principle, it is possible to extract this type of statistical information from the system in an experiment, for example, by using Coulomb explosion to map the positions of the Br and F rings (see, e.g., refs 30−32); however, this approach may be time-consuming because it is likely to require many repeated measurements. A simpler technique could be to use a linear field to measure the polarization rotation produced by the molecular ensemble because this quantity is related to the overall chirality of the sample.[48] While this would certainly be faster, it yields less specific information about the position of the quantum wave packets.

It is also likely that the effect of intramolecular vibrational energy redistribution[49] will become more pronounced at higher vibrational amplitudes. While our model does not capture this type of coupling to other degrees of freedom, an experimental closed-loop optimization scheme should be able to correct for this type of discrepancy.

■ ASSOCIATED CONTENT

Supporting Information

The Supporting Information is available free of charge on the ACS Publications website at DOI: 10.1021/acs.jpclett.7b00662.

Model and computational details (PDF)

■ AUTHOR INFORMATION

Corresponding Author

*E-mail: neh@kemi.dtu.dk.

ORCID

Niels E. Henriksen: 0000-0001-7036-2670

Notes

The authors declare no competing financial interest.

■ ACKNOWLEDGMENTS

We thank Henrik Stapelfeldt for his correspondence and providing supplemental information pertaining to the experiments performed by his group and Peter Uhd Jepsen for helping with questions about laser optics.

■ REFERENCES

(1) Quack, M.; Stohner, J.; Willeke, M. High-Resolution Spectroscopic Studies and Theory of Parity Violation in Chiral Molecules. *Annu. Rev. Phys. Chem.* **2008**, *59*, 741−769.

(2) McKendry, R.; Theoclitou, M.-E.; Rayment, T.; Abell, C. Chiral Discrimination by Chemical Force Microscopy. *Nature* **1998**, *391*, 566−568.

(3) Noyori, R. Asymmetric Catalysis: Science and Opportunities (Nobel Lecture). *Angew. Chem., Int. Ed.* **2002**, *41*, 2008−2022.

(4) Salam, A.; Meath, W. On Enantiomeric Excesses Obtained from Racemic Mixtures by Using Circularly Polarized Pulsed Lasers of Varying Durations. *Chem. Phys.* **1998**, *228*, 115−129.

(5) Fujimura, Y.; González, L.; Hoki, K.; Manz, J.; Ohtsuki, Y. Selective Preperation of Enantiomers by Laser Pulses: Quantum Model Simulation for H_2POSH. *Chem. Phys. Lett.* **1999**, *306*, 1−8.

(6) Fujimura, Y.; González, L.; Hoki, K.; Kröner, D.; Manz, J.; Ohtsuki, Y. From a Racemate to a Pure Enantiomer by Laser Pulses: Quantum Model Simulations for H_2POSH. *Angew. Chem., Int. Ed.* **2000**, *39*, 4586−4588.

(7) Shapiro, M.; Frishman, E.; Brumer, P. Coherently Controlled Asymmetric Synthesis with Achiral Light. *Phys. Rev. Lett.* **2000**, *84*, 1669−1672.

(8) Umeda, H.; Takagi, M.; Yamada, S.; Koseki, S.; Fujimura, Y. Quantum Control of Molecular Chirality: Optical Isomerization of Difluorobenzo[c]phenanthrene. *J. Am. Chem. Soc.* **2002**, *124*, 9265−9271.

(9) Hoki, K.; Kröner, D.; Manz, J. Selective Preparation of Enantiomers from a Racemate by Laser Pulses: Model Simulations for Oriented Atropisomers with Coupled Rotations and Torsions. *Chem. Phys.* **2001**, *267*, 59−79.

(10) Hoki, K.; González, L.; Fujimura, Y. Control of Molecular Handedness Using Pump-Dump Laser Pulses. *J. Chem. Phys.* **2002**, *116*, 2433−2438.

(11) Bychkov, S. S.; Grishanin, B. A.; Zadkov, V. N.; Takahashi, H. Laser Coherent Control of Molecular Chiral States via Entanglement of the Rotational and Torsional Degrees of Freedom. *J. Raman Spectrosc.* **2002**, *33*, 962−973.

(12) Král, P.; Thanopulos, I.; Shapiro, M.; Cohen, D. Two-Step Enantio-Selective Optical Switch. *Phys. Rev. Lett.* **2003**, *90*, 03001−4.

(13) Gerbasi, D.; Shapiro, M.; Brumer, P. Theory of "Laser Distillation" of Enantiomers: Purification of a Racemic Mixture of Randomly Oriented Dimethylallene in a Collisional Environment. *J. Chem. Phys.* **2006**, *124*, 074315−9.

(14) Parker, S. M.; Ratner, M. A.; Seideman, T. Simulating Strong Field Control of Axial Chirality Using Optimal Control Theory. *Mol. Phys.* **2012**, *110*, 1941−1952.

(15) Judson, R. S.; Rabitz, H. Teaching Lasers to Control Molecules. *Phys. Rev. Lett.* **1992**, *68*, 1500−1503.

(16) Rice, S. A.; Zhao, M. *Optical Control of Molecular Dynamics*; Wiley: New York, 2000.

(17) Tiwari, A. K.; Møller, K. B.; Henriksen, N. E. Selective Bond Breakage Within the HOD Molecule Using Optimized Femtosecond

DOI: 10.1021/acs.jpclett.7b00662
J. Phys. Chem. Lett. 2017, 8, 2212−2219

Ultraviolet Laser Pulses. *Phys. Rev. A: At., Mol., Opt. Phys.* **2008**, *78*, 065402−4.
(18) Brif, C.; Chakrabarti, R.; Rabitz, H. Control of Quantum Phenomena: Past, Present and Future. *New J. Phys.* **2010**, *12*, 075008−68.
(19) Sharma, S.; Singh, H.; Balint-Kurti, G. G. Genetic Algorithm Optimization of Laser Pulses for Molecular Quantum State Excitation. *J. Chem. Phys.* **2010**, *132*, 064108−10.
(20) Assion, A.; Baumbert, T.; Bergt, M.; Brixner, T.; Kiefer, B.; Seyfried, V.; Strehle, M.; Gerber, G. Control of Chemical Reactions by Feedback-Optimized Phase-Shaped Femtosecond Laser Pulses. *Science* **1998**, *282*, 919−922.
(21) Weinacht, T. C.; Ahn, J.; Bucksbaum, P. H. Controlling the Shape of a Quantum Wavefunction. *Nature* **1999**, *397*, 233−235.
(22) Levis, R. J.; Menkir, G. M.; Rabitz, H. Selective Bond Dissociation and Rearrangement with Optimally Tailored, Strong-Field Laser Pulses. *Science* **2001**, *292*, 709−713.
(23) Pearson, B. J.; White, J. L.; Weinacht, T. C.; Bucksbaum, P. H. Coherent Control Using Adaptive Learning Algorithms. *Phys. Rev. A: At., Mol., Opt. Phys.* **2001**, *63*, 063412−12.
(24) Vogt, G.; Krampert, G.; Niklaus, P.; Nuernberger, P.; Gerber, G. Optimal Control of Photoisomerization. *Phys. Rev. Lett.* **2005**, *94*, 068305−4.
(25) Savolainen, J.; Fanciulli, R.; Dijkhuizen, N.; Moore, A. L.; Hauer, J.; Buckup, T.; Motzkus, M.; Herek, J. L. Controlling the Efficiency of an Artificial Light-Harvesting Complex. *Proc. Natl. Acad. Sci. U. S. A.* **2008**, *105*, 7641−7646.
(26) Florean, A. C.; Cardoza, D.; White, J. L.; Lanyi, J. K.; Sension, R. J.; Bucksbaum, P. H. Control of Retinal Isomerization in Bacteriorhodopsin in the High-Intensity Regime. *Proc. Natl. Acad. Sci. U. S. A.* **2009**, *106*, 10896−10900.
(27) Mitchell, M. *An Introduction to Genetic Algorithms*, 5th ed.; The MIT Press, 1999.
(28) Weiner, A. M. Femtosecond Pulse Shaping Using Spatial Light Modulators. *Rev. Sci. Instrum.* **2000**, *71*, 1929−1960.
(29) Monmayrant, A.; Weber, S.; Chatel, B. A Newcomer's Guide to Ultrashort Pulse Shaping and Characterization. *J. Phys. B: At., Mol. Opt. Phys.* **2010**, *43*, 103001−34.
(30) Madsen, C. B.; Madsen, L. B.; Viftrup, S. S.; Johansson, M. P.; Poulsen, T. B.; Holmegaard, L.; Kumarappan, V.; Jørgensen, K. A.; Stapelfeldt, H. A Combined Experimental and Theoretical Study on Realizing and Using Laser Controlled Torsion of Molecules. *J. Chem. Phys.* **2009**, *130*, 234310−9.
(31) Madsen, C. B.; Madsen, L. B.; Viftrup, S. S.; Johansson, M. P.; Poulsen, T. B.; Holmegaard, L.; Kumarappan, V.; Jørgensen, K. A.; Stapelfeldt, H. Manipulating the Torsion of Molecules by Strong Laser Pulses. *Phys. Rev. Lett.* **2009**, *102*, 073007−4.
(32) Christensen, L.; Nielsen, J. H.; Brandt, C. B.; Madsen, C. B.; Madsen, L. B.; Slater, C. S.; Lauer, A.; Brouard, M.; Johansson, M. P.; Shepperson, B.; et al. Dynamic Stark Control of Torsional Motion by a Pair of Laser Pulses. *Phys. Rev. Lett.* **2014**, *113*, 073005−5.
(33) *MATLAB*, version 9.0.0.341360 (R2016a); The MathWorks, Inc.: Natick, MA, 2016.
(34) Townsend, D.; Sussman, B. J.; Stolow, A. A Stark Future for Quantum Control. *J. Phys. Chem. A* **2011**, *115*, 357−373.
(35) Sussman, B. J. Five Ways to the Nonresonant Dynamic Stark Effect. *Am. J. Phys.* **2011**, *79*, 477−484.
(36) Thomas, E. F.; Henriksen, N. E. Non-Resonant Dynamic Stark Control of Vibrational Motion with Optimized Laser Pulses. *J. Chem. Phys.* **2016**, *144*, 244307−10.
(37) Friedrich, B.; Herschbach, D. Manipulating Molecules via Combined Static and Laser Fields. *J. Phys. Chem. A* **1999**, *103*, 10280−10288.
(38) Tanji, H.; Minemoto, S.; Sakai, H. Three-Dimensional Molecular Orientation with Combined Electrostatic and Elliptically Polarized Laser Fields. *Phys. Rev. A: At., Mol., Opt. Phys.* **2005**, *72*, 063401−4.
(39) Kosloff, R. Time-Dependent Quantum-Mechanical Methods for Molecular Dynamics. *J. Phys. Chem.* **1988**, *92*, 2087−2100.
(40) Kosloff, R.; Tal-Ezer, H. A Direct Relaxation Method for Calculating Eigenfunctions and Eigenvalues of the Schrödinger Equation on a Grid. *Chem. Phys. Lett.* **1986**, *127*, 223−230.
(41) Strickland, D.; Mourou, G. Compression of Amplified Chirped Optical Pulses. *Opt. Commun.* **1985**, *55*, 447−449.
(42) Wefers, M. M.; Nelson, K. A. Analysis of Programmable Ultrashort Waveform Generation Using Liquid-Crystal Spatial Light Modulators. *J. Opt. Soc. Am. B* **1995**, *12*, 1343−1362.
(43) Wefers, M. M.; Nelson, K. A. Space-time Profiles of Shaped Ultrafast Optical Waveforms. *IEEE J. Quantum Electron.* **1996**, *32*, 161−172.
(44) Dorrer, C.; Salin, F. Phase Amplitude Coupling in Spectral Phase Modulation. *IEEE J. Sel. Top. Quantum Electron.* **1998**, *4*, 342−345.
(45) Frei, F.; Galler, A.; Feurer, T. Space-Time Coupling in Femtosecond Pulse Shaping and its Effects on Coherent Control. *J. Chem. Phys.* **2009**, *130*, 034302−14.
(46) Monmayrant, A.; Chatel, B. New Phase and Amplitude High Resolution Pulse Shaper. *Rev. Sci. Instrum.* **2004**, *75*, 2668−2671.
(47) Hankin, S. M.; Villeneuve, D. M.; Corkum, P. B.; Rayner, D. M. Nonlinear Ionization of Organic Molecules in High Intensity Laser Fields. *Phys. Rev. Lett.* **2000**, *84*, 5082−5085.
(48) Atkins, P.; Friedman, R. *Molecular Quantum Mechanics*, 4th ed.; Oxford University Press, 2005.
(49) Nesbitt, D. J.; Field, R. W. Vibrational Energy Flow in Highly Excited Molecules: Role of Intramolecular Vibrational Redistribution. *J. Phys. Chem.* **1996**, *100*, 12735−12756.

DOI: 10.1021/acs.jpclett.7b00662
J. Phys. Chem. Lett. 2017, 8, 2212−2219

Supporting Information: Phase-Modulated Non-Resonant Laser Pulses can Selectively Convert Enantiomers in a Racemic Mixture

Esben F. Thomas and Niels E. Henriksen (neh@kemi.dtu.dk)
Department of Chemistry, Technical University of Denmark, Building 206, DK-2800 Kongens Lyngby, Denmark

Is. MODELING THE FIELD INTERACTION

Combining equations 2 and 3 from the main text, the Hamiltonian of the system can be written as

$$H_{\mathrm{mol}} = -\frac{1}{2I_{\mathrm{Br}}}\frac{\partial^2}{\partial\phi_{\mathrm{Br}}^2} - \frac{1}{2I_{\mathrm{F}}}\frac{\partial^2}{\partial\phi_{\mathrm{F}}^2} + V'_{\mathrm{tor}}\cdots \\ \cdots - \frac{1}{4}\mathbf{E}^*_{\mathrm{tot}}(t)\cdot\boldsymbol{\alpha}\cdot\mathbf{E}_{\mathrm{tot}}(t), \quad (1s)$$

where $I_{\mathrm{Br}} = 8911925$ a.u., $I_{\mathrm{F}} = 1864705$ a.u., and $\boldsymbol{\alpha}$ is the polarizability tensor in the molecular frame:

$$\boldsymbol{\alpha} = \begin{bmatrix} \alpha_{xx} & \alpha_{xy} & \alpha_{xz} \\ \alpha_{yx} & \alpha_{yy} & \alpha_{yz} \\ \alpha_{zx} & \alpha_{zy} & \alpha_{zz} \end{bmatrix}, \quad (2s)$$

where $\alpha_{ij} = \alpha_{ji}$, and where $\alpha_{xx,yy,xy}$ are functions of ϕ_d. The $\alpha_{xx,yy}(\phi_d)$ functions are of the form $A_{xx,yy}\cos(\phi_d) + B_{xx,yy}$, and $\alpha_{xy}(\phi_d)$ is of the form $A_{xy}\sin(\phi_d) + B_{xy}$, where the coefficients $A_{xx,yy,xy}$ and $B_{xx,yy,xy}$ are determined by fitting to the data in table I of ref [30], and found to be $A_{xx} = 16.832$, $B_{xx} = 200.871$, $A_{yy} = -20.1435$, $B_{yy} = 112.4955$, $A_{xy} = -18.81$, and $B_{xy} = 0$ (expressed in atomic units). Note that the $\alpha_{zz,zx,zy}$ components are not required, since the kick pulses are assumed to be orthogonal to the molecular MPA, which is defined to be parallel to the molecular frame (and lab frame) $\hat{z}$ axis. As stated in the article text, $\mathbf{E}_{\mathrm{tot}}(t)$ is the vector sum of kick pulse 1 and 2:

$$\mathbf{E}_{\mathrm{tot}}(t) = \mathbf{E}_1(t) + \mathbf{E}_2(t), \quad (3s)$$

and the first kick pulse $\mathbf{E}_1(t)$ is rotated away from the laboratory $\hat{x}$ axis in the xy plane by angle $\delta/2$:

$$\mathbf{E}_1(t) = \mathcal{E}_1(t)\begin{bmatrix}\cos(\delta/2)\\ \sin(\delta/2)\\ 0\end{bmatrix}, \quad (4s)$$

where $\mathbf{E}_1(t)$ is the complex time-dependent field amplitude. Similarly, the second kick pulse $\mathbf{E}_2(t)$ is rotated away from the laboratory $\hat{x}$ axis in the xy plane by angle $-\delta/2$:

$$\mathbf{E}_2(t) = \mathcal{E}_2(t)\begin{bmatrix}\cos(-\delta/2)\\ \sin(-\delta/2)\\ 0\end{bmatrix}. \quad (5s)$$

Neglecting the implicit time-dependence for clarity of notation, we expand the $\mathbf{E}^*_{\mathrm{tot}}\cdot\boldsymbol{\alpha}\cdot\mathbf{E}_{\mathrm{tot}}$ term in eq 1s by combining it with eq 3s:

$$\mathbf{E}^*_{\mathrm{tot}}\cdot\boldsymbol{\alpha}\cdot\mathbf{E}_{\mathrm{tot}} = \mathbf{E}^*_1\cdot\boldsymbol{\alpha}\cdot\mathbf{E}_1 + \mathbf{E}^*_2\cdot\boldsymbol{\alpha}\cdot\mathbf{E}_2 + \mathbf{E}^*_1\cdot\boldsymbol{\alpha}\cdot\mathbf{E}_2 + \mathbf{E}^*_2\cdot\boldsymbol{\alpha}\cdot\mathbf{E}_1. \quad (6s)$$

To proceed we need to re-express $\boldsymbol{\alpha}$ in the laboratory frame. This is achieved using rotational cosine matrices:

$$\boldsymbol{\alpha}_{\mathrm{lab}} = \mathbf{R}^T\boldsymbol{\alpha}\mathbf{R}, \quad (7s)$$

where $\mathbf{R}$ is the rotational cosine matrix:

$$\mathbf{R} = \begin{bmatrix} \cos(\psi)\cos(\phi) - \cos(\theta)\sin(\phi)\sin(\psi) & \cos(\psi)\sin(\phi) + \cos(\theta)\cos(\phi)\sin(\psi) & \sin(\psi)\sin(\theta) \\ -\sin(\psi)\cos(\phi) - \cos(\theta)\sin(\phi)\cos(\psi) & -\sin(\psi)\sin(\phi) + \cos(\theta)\cos(\phi)\cos(\psi) & \cos(\psi)\sin(\theta) \\ \sin(\theta)\sin(\phi) & -\sin(\theta)\cos(\phi) & \cos(\theta) \end{bmatrix}. \quad (8s)$$

The Euler angles ψ, θ and ϕ are represented in figure 1s, and due to the molecular orientation, in our case we let $\psi = 0$, $\theta = 0$ and $\phi = \phi_{\mathrm{Br}}$. We can now rewrite the expressions for the interaction term by simply performing the matrix multiplications. For the first term in eq 6s, we get

$$\mathbf{E}^*_1\cdot\mathbf{R}^T\boldsymbol{\alpha}\mathbf{R}\cdot\mathbf{E}_1 \quad (9s)$$

The matrix multiplication yields an expression that can be collected into three terms based on the relation to the α_{ij} elements of $\boldsymbol{\alpha}$ (eq 2s). After applying some straightforward trigonometric identities, we arrive at

$$\mathbf{E}^*_1\cdot\boldsymbol{\alpha}_{\mathrm{lab}}\cdot\mathbf{E}_1 = |\mathcal{E}_1|^2\alpha_1, \quad (10s)$$

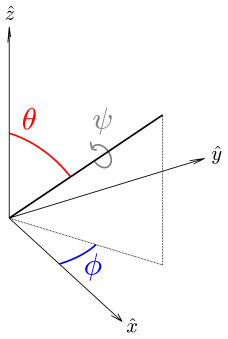

Figure 1s. *Molecular rotational angles in the laboratory frame.*

where

$$\alpha_1 = \alpha_{xx}\cos^2(\phi_{\rm Br}-\delta/2)\ldots + \alpha_{yy}\sin^2(\phi_{\rm Br}-\delta/2)\ldots - 2\alpha_{xy}\sin(\phi_{\rm Br}-\delta/2)\cos(\phi_{\rm Br}-\delta/2). \quad (11s)$$

The result for $\mathbf{E}_2^* \cdot \boldsymbol{\alpha}_{\rm lab} \cdot \mathbf{E}_2$ will be the same except we replace $\delta/2$ with $-\delta/2$ in the final expression:

$$\mathbf{E}_2^* \cdot \boldsymbol{\alpha}_{\rm lab} \cdot \mathbf{E}_2 = |\mathcal{E}_2|^2\alpha_2, \quad (12s)$$

where

$$\alpha_2 = \alpha_{xx}\cos^2(\phi_{\rm Br}+\delta/2)\ldots + \alpha_{yy}\sin^2(\phi_{\rm Br}+\delta/2)\ldots - 2\alpha_{xy}\sin(\phi_{\rm Br}+\delta/2)\cos(\phi_{\rm Br}+\delta/2). \quad (13s)$$

Now, treating the first cross-term from equation 6s, i.e. $\mathbf{E}_1^* \cdot \mathbf{R}^T\boldsymbol{\alpha}\mathbf{R} \cdot \mathbf{E}_2$. Here the outer product of the field direction vectors does not disappear:

$$\mathcal{E}_1{}^*\mathcal{E}_2\begin{bmatrix}\cos(\delta/2) & \sin(\delta/2) & 0\end{bmatrix}\cdot\mathbf{R}^T\boldsymbol{\alpha}\mathbf{R}\cdot\begin{bmatrix}\cos(-\delta/2)\\ \sin(-\delta/2)\\ 0\end{bmatrix} \quad (14s)$$

Performing the matrix multiplication and simplifying as before yields

$$\mathbf{E}_1^* \cdot \boldsymbol{\alpha}_{\rm lab} \cdot \mathbf{E}_2 = \mathcal{E}_1{}^*\mathcal{E}_2\alpha_{12}, \quad (15s)$$

where

$$\alpha_{12} = \alpha_{xx}\cos(\phi_{\rm Br}+\delta/2)\cos(\phi_{\rm Br}-\delta/2)\ldots + \alpha_{yy}\sin(\phi_{\rm Br}+\delta/2)\sin(\phi_{\rm Br}-\delta/2)\ldots - 2\alpha_{xy}\cos(\phi_{\rm Br})\sin(\phi_{\rm Br}) \quad (16s)$$

The form of this solution implies that the other cross term $\mathbf{E}_1^* \cdot \mathbf{R}^T\boldsymbol{\alpha}\mathbf{R} \cdot \mathbf{E}_2$ will yield an identical expression save for the complex amplitudes of the fields, which will be conjugated. Therefore, $\mathbf{E}_1^* \cdot \boldsymbol{\alpha}_{\rm lab} \cdot \mathbf{E}_2 + \mathbf{E}_2^* \cdot \boldsymbol{\alpha}_{\rm lab} \cdot \mathbf{E}_1$ can be written as

$$\mathbf{E}_1^* \cdot \boldsymbol{\alpha}_{\rm lab} \cdot \mathbf{E}_2 + \mathbf{E}_2^* \cdot \boldsymbol{\alpha}_{\rm lab} \cdot \mathbf{E}_1 = (\mathcal{E}_1{}^*\mathcal{E}_2 + \mathcal{E}_1\mathcal{E}_2{}^*)\alpha_{12}. \quad (17s)$$

Combining eqs 10s, 12s and 17s with eqs 6s and 1s, we arrive at the expression for the Hamiltonian given in lab-frame coordinates shown in eq 5 of the main text.

A. Alignment Field

The expression for the polarizability term of the orientating field α_0 is identical to the expressions for α_1 or α_2 (eq 11s or 13s) if we set $\delta = 0$. The observant reader will note that there should in principle also exist a cross term between the alignment field and the two kick pulses, however because the wavelength of the alignment field is 1064 nm and the wavelengths of the two kick pulses are 800 nm, this cross term will only contribute a "beating" oscillation to the field with a frequency that is much faster than the response time of the system (i.e. it is non-resonant). Because the mean contribution of this beating term to the total field is 0 in the non-resonant regime, it can be ignored just as the central carrier frequencies of the pulses can be ignored in the dynamic Stark regime.

IIs. MODELING THE MOLECULE

As shown in section Is, the Hamiltonian of the system can be written as

$$H_{\rm mol} = -\frac{1}{2I_{\rm Br}}\frac{\partial^2}{\partial\phi_{\rm Br}^2} - \frac{1}{2I_{\rm F}}\frac{\partial^2}{\partial\phi_{\rm F}^2} + V'_{\rm tor}\ldots - \frac{1}{4}\Big[|\mathcal{E}_1|^2\alpha_1 + |\mathcal{E}_2|^2\alpha_2 + (\mathcal{E}_1^*\mathcal{E}_2 + \mathcal{E}_1\mathcal{E}_2^*)\alpha_{12}\Big], \quad (18s)$$

where

$$V'_{\rm tor} = V_{\rm tor} - \frac{1}{4}|\mathcal{E}_{0x}|^2\alpha_0. \quad (19s)$$

Note that the torsional potential energy function $V_{\rm tor}$ varies as a function of the dihedral angle $\phi_d = \phi_{\rm Br} - \phi_{\rm F}$, and that the symmetry of the molecule implies that $V_{\rm tor}(\phi_d)$ is π periodic and $V_{\rm tor}(\phi_d) = V_{\rm tor}(-\phi_d)$. In our model, the form of $V_{\rm tor}(\phi_d)$ is determined by fitting a series of 7 functions that satisfy the same periodicity and symmetry requirements to the numerical data extracted from the curve in figure 1(b) from ref [31], i.e.

$$V_{\rm tor}(\phi_d) = \sum_{n=0}^{6} C_n\cos(2n\phi_d), \quad (20s)$$

where the coefficients of eq 20s are found to be $C_0 = 41.4478$, $C_1 = -13.5702$, $C_2 = 38.1985$, $C_3 = 7.3650$, $C_4 = 0.9870$, $C_5 = 0.3590$, and $C_6 = 0.0813$ (expressed

in eV). In practice, we reduce the size of the simulation space by using a different coordinate system:

$$\phi_x = \frac{1}{2}(\phi_{\rm Br} - \phi_{\rm F}), \tag{21s}$$

$$\phi_y = \frac{1}{2}(\phi_{\rm Br} + \phi_{\rm F}). \tag{22s}$$

Expressed in these coordinates, the Hamiltonian becomes

$$H_{\rm mol} = -\frac{1}{2M_1}\left(\frac{\partial^2}{\partial\phi_x^2} + \frac{\partial^2}{\partial\phi_y^2}\right) - \frac{1}{2M_2}\frac{\partial}{\partial\phi_x}\frac{\partial}{\partial\phi_y} + V'_{\rm tor} \ldots$$
$$\ldots - \frac{1}{4}\Big[|\mathcal{E}_1|^2\alpha_1 + |\mathcal{E}_2|^2\alpha_2 + (\mathcal{E}_1^*\mathcal{E}_2 + \mathcal{E}_1\mathcal{E}_2^*)\alpha_{12}\Big], \tag{23s}$$

where $M_1 = 4I_{\rm F}I_{\rm Br}/(I_{\rm F}+I_{\rm Br})$ and $M_2 = 2I_{\rm F}I_{\rm Br}/(I_{\rm F}-I_{\rm Br})$ (Note the cross term in the kinetic energy operator). Due to symmetry considerations discussed in the main text, we can reduce the simulation domain to the area bounded by the black dashed lines in the bottom part of article figure 3. As stated, it is assumed that the optimal transfer will involve a coherent trajectory along a minimum energy path between the two adjacent minima located within this region, as denoted by the double arrow in the figure. It is therefore assumed that any portion of the wave packets that cross the boundaries of the reduced simulation space are essentially "lost". In practice, this condition is implemented by adding an absorbing negative imaginary potential[39] (NIP) to the simulation boundaries. Using the ϕ_x and ϕ_y coordinates, the simulation domain is set to $-\pi/4 \le \phi_x \le \pi/4$ and $-\pi/2 \le \phi_y \le \pi/2$. When a negative imaginary potential function $\mathrm{NIP}(\phi_x, \phi_y)$ is included, we extend the simulation domain by adding a border of width $\pi/32$ and $\pi/16$ to the domain edges in the ϕ_x and ϕ_y directions, respectively. By trial and error, a good form of the $\mathrm{NIP}(\phi_x, \phi_y)$ function was found to be:

$$\mathrm{NIP}(\phi_x,\phi_y) = -0.04i\Theta\Big(\phi_x - \frac{\pi}{4}\Big)\Big(\phi_x - \frac{\pi}{4}\Big)^2 \ldots$$
$$\ldots - 0.04i\Theta\Big(-\phi_x - \frac{\pi}{4}\Big)\Big(-\phi_x - \frac{\pi}{4}\Big)^2 \ldots$$
$$\ldots - 0.01i\Theta\Big(\phi_y - \frac{\pi}{2}\Big)\Big(\phi_y - \frac{\pi}{2}\Big)^2 \ldots$$
$$\ldots - 0.01i\Theta\Big(-\phi_y - \frac{\pi}{2}\Big)\Big(-\phi_y - \frac{\pi}{2}\Big)^2, \tag{24s}$$

where generally $\Theta(r)$ is the Heaviside step function applied in the r direction. As stated, the solution to the time-dependent Schödinger equation (TDSE) was found numerically using split operator propagation[39]. Because the full genetic algorithm optimization requires solving the TDSE over one million times, the simulation step size was set as large as possible to 1000 a.u., and the number of grid points in the ϕ_x and ϕ_y directions was set as low as possible to 128, in order to minimize the computational costs. Once the optimization was finished, we decreased the simulation time step to 100 a.u., and increased the number of grid points in the ϕ_x and ϕ_y directions to 256, and simulated the system interacting with the optimal pulse in order to generate the plots and data shown in the article (it was found that further increasing the number of time steps and/or grid points did not impact the results). Generally, adjusting the time step spacing of the numerically shaped pulses for simulation purposes was achieved using linear interpolation.

IIIs. MODELING THE PULSE SHAPING

In a computer, the temporal pulse data of the unshaped pulse is represented by complex function $\mathcal{E}(t_n)$, where t_n are a discrete series of N equally spaced time steps with total length T and spacing $\Delta t = T/(N-1)$. An easy way to approximate the effect of a phase-only spectral pulse shaper on $\mathcal{E}(t_n)$ is to simply apply the discrete Fourier transform (DFT) to the data. This results in spectral distribution $\widetilde{\mathcal{E}}(\omega_n) = \mathcal{F}\{\mathcal{E}_0(t_n)\}$, where ω_n are a series of equally spaced frequencies with spacing $\Delta\omega = 2\pi/T$, and $\mathcal{F}\{\}$ represents the application of the DFT transformation matrix. The N phases of the spectral signal are then modulated by multiplying the elements of $\widetilde{\mathcal{E}}(\omega_n)$ by a complex exponential argument:

$$\widetilde{\mathcal{E}}(\omega_n)\exp[i\Omega(\omega_n)], \tag{25s}$$

where $\Omega(\omega_n)$ represents the change in phase angle of the signal at frequencies ω_{0-N}. The shaped temporal pulse $\mathcal{E}_S(t_n)$ is then generated by applying the inverse DFT matrix:

$$\mathcal{E}_S(t_n) = \mathcal{F}^{-1}\Big\{\widetilde{\mathcal{E}}_0(\omega_n)\exp[i\Omega(\omega_n)]\Big\}. \tag{26s}$$

This simplistic approach is able to roughly demonstrate the general principle of spectral pulse shaper operation, however there are numerous extra factors that come into play in an experimental situation that complicate the picture. The details of experimental pulse shaper operation have been the subject of numerous theoretical analyses (see e.g. refs [42–45]), and it is in principle possible to construct a very complete and/or accurate model of the pulse shaping process that includes e.g. the effect of gaps between pixels in the spectral mask[45]. In spite of this, we assume that omitting some of these effects will not significantly impact our results, since the genetic algorithm doesn't particularly "care" about all the minutiae involved in the relationship between the phase modulation and the shaped pulse, i.e. it will automatically correct for small discrepancies between our numerical model of pulse shaping and an actual experimental setup.

A. Spectral Width of the Mask Pixels

For this reason, we have chosen to only include factors that we have deemed play fundamentally significant

roles in the spectral pulse shaping process. The first is related to the maximum width of the shaped pulse. In general, the maximum temporal width of the time window in which the pulse shaper can control the shape of the pulse is inversely related to spectral width of the phase mask pixels. The impact that this property has on a numerical approach using the DFT will now be discussed.

As stated, if we take the DFT of a Gaussian pulse located within a time window of total length T and constant time step size Δt, the pulse spectrum will be represented on a grid of equally spaced frequencies with spacing $\Delta\omega = 2\pi/T$. Let $\delta\Omega$ be the spectral width of the pixels in the phase-adjustable liquid crystal mask (LCM) of the experimental pulse shaper. If $\delta\Omega = \Delta\omega = 2\pi/T$, it is clear that the pulse shaper will be able to modify every frequency in the pulse spectrum independently, leading to the maximum possible controllability of the pulse shape within the time window T. Now, using the same pulse parameters and time step size, we increase the size of the pulse time window to $3T$, letting $\Delta\omega'$ be the new frequency spacing in the spectral domain, i.e. $\Delta\omega' = 2\pi/3T$. Clearly, the general shape of the spectral distribution will be unchanged, however the size of the frequency grid spacing is now reduced by a factor of three, i.e. $\Delta\omega = 3 \times \Delta\omega'$. If the mask pixel width $\delta\Omega$ remains unchanged, each pixel in the spectral mask will now contain three frequencies. The first column of figure 2s illustrates this concept, where the same randomly generated phase mask with fixed pixel width $\delta\Omega = 2\pi/T$ is applied to the spectral distributions of a Gaussian pulse, centered at time $t = 0$, calculated using time windows of length T, $3T$ and $11T$ (note that it is always assumed that $\Delta t = const.$).

The second column of figure 2s shows the temporal amplitudes of the shaped pulses that correspond to the three phase-modulated spectra in the first column. Here it can be seen that the shapes of all three pulses are similar within the central region of width T (bounded by the blue lines). It can also be seen that the effect of including more frequencies per pixel leads to a general spreading of the pulse shape beyond this central region. The temporal pulse with the $11T$ time window shows that the pulse spreading is characterized by repeating identical subsequences, or "replicas", of diminishing amplitude. These replicas also appear in experimentally shaped pulses due to the finite spectral width of the spectral mask pixels[46].

The plots in the second column of figure 2s indicate that in the region demarcated by the blue lines (i.e. from $-T/2 < t < T/2$), there is a limit where further increase in the total duration of the pulse time window (and therefore the number of frequencies per mask pixel) will cease to significantly impact the pulse shape. This limit is visualized in the right panel of figure 2s using a plot of the integrated pulse area from $-T/2$ to $T/2$, as a function of the number of frequencies per phase element. Here, it is seen that when the number of frequencies per pixel is > 7, the integrated area converges to a nearly constant value, i.e. there are negligible changes in the pulse shape in the region $-T/2$ to $T/2$ as a function of the frequency/pixel ratio beyond this limit. In an experimental situation, the finite width of the pixels in the phase mask means that each pixel will modulate a large number of adjacent frequencies. Here, we have shown that given a phase mask pixel width of $\delta\Omega = 2\pi/T$, the numerically shaped pulse will closely resemble the experimentally shaped pulse from $-T/2$ to $T/2$ as long as the total size of the numerically shaped pulse time window is $> 7T$.

What follows is a description of how we make use of the principles we have just outlined to generate the numerically shaped pulses. Given a spectral amplitude distribution of form $\exp\left(-(\omega-\omega_0)^2/2\sigma^2\right)$, we define the phase modulated region to lie within a frequency window centered at ω_0 and of width $W_\omega = 8\sigma$, where the phase is set to 0 everywhere outside of this region. The amplitude functions of the unshaped pulses are 700 fs FWHM Gaussians, which means that the frequency window will span $W_\omega = 2.69 \times 10^{13}$ rad. Now, we once again let $\delta\Omega$ represent the spectral width of a single phase mask pixel, and T the size of the time window where there is maximum possible controllability of the pulse shape (i.e. there will be no pulse replicas within a window of size $T = 2\pi/\delta\Omega$). In the simulations performed in our paper, we chose a time window of size $T = 23.6$ ps, yielding a pixel width of $\delta\Omega = 2.66 \times 10^{11}$ rad, which means that within the phase modulated frequency window there will be $\lfloor W_\omega/\delta\Omega \rfloor = 101$ equally spaced discrete phases that can be controlled by the algorithm. To ensure that the numerically shaped pulse will accurately resemble its experimental counterpart, the total size of the time domain was set to $T_{\text{tot}} = 256$ ps, leading to at least 10 frequencies per pixel in the numerical representation of the phase mask. In order to ensure that the representation of the shaped pulse is not under sampled in the temporal domain, the full pulse in the time window T_{tot} is represented on a grid of $N = 2^{17}$ points, yielding a time step size of $\Delta t = 1.9$ fs.

B. Spatiotemporal Coupling

A property inherent to all spectral pulse shapers known as spatiotemporal coupling[42–45] presents us with a convenient way to disregard the parts of our numerical pulse where $|t| \gg 0$, i.e. the outer regions that contain the replicated structures. In short, spatiotemporal coupling is a result of the finite spot size of the experimental laser, which leads to a convolution of the spectral pulse with its spatial intensity profile. The consequence of this is that temporal shifts of size Δt in the shaped pulse are associated with spatial shifts in the transverse spatial coordinate of size $\Delta x = v\Delta t$. The variable v is the so-called spatiotemporal coupling speed, the value of which typically ranges from ~ 85 to ~ 145 μm/ps, depending on the experimental configuration of the pulse shaper[29,46].

Effectively, inclusion of spatiotemporal coupling effects

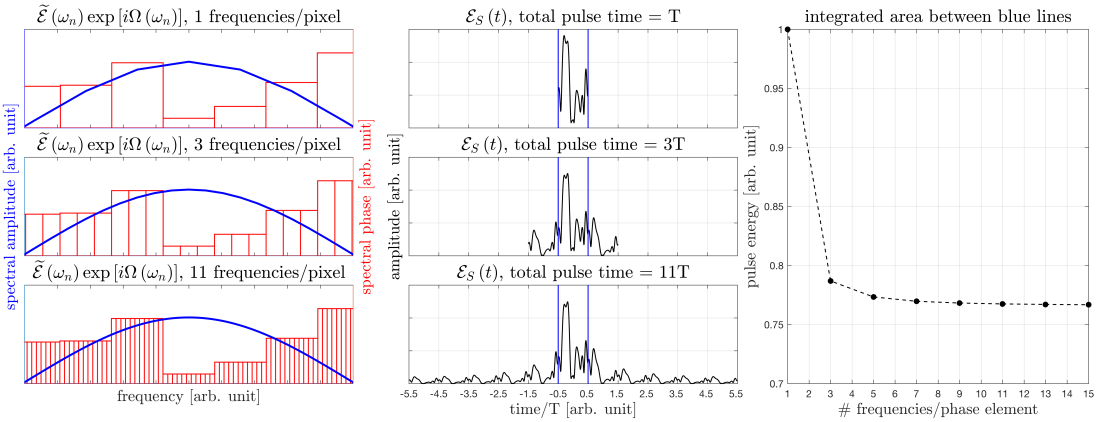

Figure 2s. *Given a series of random discrete phase shifts in the spectral domain with fixed pixel width $\delta\Omega = 2\pi/T$, the left columns show how increasing the size of the numerical time window for the shaped (Gaussian) pulse from T to $3T$ to $11T$ will increase the number of frequencies per pixel from 1 to 3 to 11. The middle column shows how increasing the time window in this manner leads to the shaped pulse becoming spread out with repeating "replicas" appearing outside of the central time window of width T (blue lines). The middle and right panels also illustrate how the pulse within the central time window converges to a constant shape as the number of frequencies per pixel increases.*

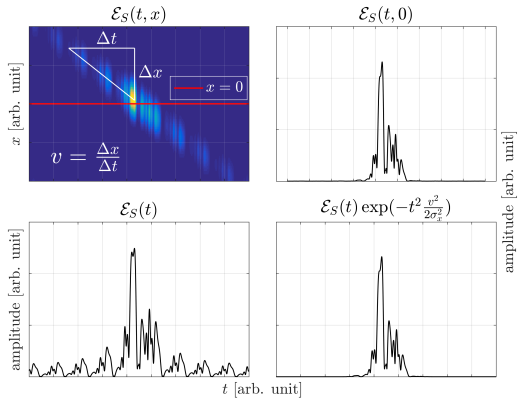

Figure 3s. *The bottom left panel shows the shaped pulse from figure 2s, and the panel above shows how this pulse will look in 2D when the spatiotemporal coupling effects are included. The two right panels illustrate how plotting $\mathcal{E}(t,x)$ along the central transverse coordinate at $x = 0$ (top right panel) is equivalent to multiplying the 1D representation of the pulse $\mathcal{E}(t)$ by a simple Gaussian function in the temporal domain (bottom right panel) .*

in our model means that the shaped pulse is now a function of t and x, i.e. $\mathcal{E}_S(t,x)$ as illustrated in the top left panel of figure 3s. Note that if we set $v = 0$ and confine the description of the pulse to the central transverse coordinate (i.e. $x = 0$), we revert to the 1D description of the pulse from subsection IIIs A, i.e. $\mathcal{E}_S(t,x)|_{v=0,x=0} = \mathcal{E}_S(t)$ as shown in the bottom left panel of figure 3s. Assuming the temporal and spatial intensity profiles of the unshaped pulse in the t and x coordinates are well represented using Gaussian functions, i.e.

$$\mathcal{E}_S(t,x) = \exp\left(-\frac{t^2}{2\sigma_t^2}\right)\exp\left(-\frac{x^2}{2\sigma_x^2}\right). \tag{27s}$$

It can be shown[28] that if $v > 0$ and $\sigma_t \ll v/\sigma_x$, the following relation will hold:

$$\mathcal{E}_S(t,0) \approx \mathcal{E}_S(t)\exp\left(-t^2\frac{v^2}{2\sigma_x^2}\right), \tag{28s}$$

i.e. we can approximate $\mathcal{E}_S(t,x)$ in the central transverse coordinate at $x = 0$ (the red line in the top left panel of figure 3s) by simply multiplying the 1D transform $\mathcal{E}_S(t)$ by a Gaussian "masking" function of height 1. As the top and bottom panels on the right side of figure 3s show, this leads to a truncation of the shaped pulse time window that is related to the spot size of the unshaped pulse σ_x, and spatiotemporal coupling speed v. Experimentally, this type of truncation can be achieved via spatial filtering, e.g. by placing an iris after the pulse shaping setup[28]. For the purposes of our model, this type of filtering has the nice effect of eliminating the replicating structures that appear outside of the center of the numerically shaped pulse, provided we select a masking function with an appropriate width.

The effects of spatiotemporal coupling where incorporated in the numerically shaped pulses by truncating them to a 24 ps time window by multiplying them by a 10

ps FWHM Gaussian function of height 1. Assuming that the FWHM diameter of the Gaussian beam spot is 1.5 mm, this translates into a spatiotemporal coupling speed in the pulse shaper of $v = 150$ μm/ps, which is fairly typical of what one would encounter in an experimental situation.

C. The Nonimpact of the Carrier Frequency

In the main article text we state that the two kick pulses have 800 nm wavelengths, which places them far into the non-resonant regime and allows us to disregard the impact of the carrier frequency on the molecular dynamics. While this is clearly important from an experimental point of view, our model of the field interaction implicitly disregards the carrier frequency by construction, regardless of what we choose it to be. This is because our system couples to the pulse envelopes $|\mathcal{E}_1(t)|^2$ and $|\mathcal{E}_2(t)|^2$, i.e. the complex field oscillations are removed (note also that the ${\mathcal{E}_1}^*(t)\mathcal{E}_2(t)$ and $\mathcal{E}_1(t){\mathcal{E}_2}^*(t)$ cross terms are independent of the absolute magnitude of the carrier frequency as well, since multiplication of the conjugated and unconjugated components will lead to complex arguments that are strictly a function of the relative frequency difference). As such, changing the central carrier frequency ω_0 of the unshaped pulses will have no impact on the shaped pulse envelopes, or the simulated dynamics. For this reason, we choose to simplify the numerical pulse shaping process by always letting $\omega_0 = 0$.

IVs. GENETIC ALGORITHM FITNESS FUNCTION

Let the full length of the pulse time window(s) be T, and the time-dependent wave packets starting in the R_a and S_a configurations be defined by $\Psi_{R_a}(t)$ and $\Psi_{S_a}(t)$, respectively (where we have omitted the spatial coordinates for clarity). Assuming the goal is deracemization into S_a enantiomers, the task of the optimization algorithm is to determine the phase mask inputs and initial pulse intensities that will lead to maximum localization of $\Psi_{R_a}(T)$ and $\Psi_{S_a}(T)$ in the S_a potential well. To do this, the genetic algorithm requires a way to measure the success or "fitness" of a given, arbitrary trial solution. Our approach is to monitor the temporal evolution of the wave packets over an "extra" time period of length T_e after the pulses are switched off. At a series of intermediate time steps between T and $T + T_e$, we analyze how close the wave packets are to the (in this example, S_a) target location using the expressions

$$\langle\Psi_{S_a}(t')|\Lambda_{S_a}|\Psi_{S_a}(t')\rangle \qquad \text{and} \qquad \langle\Psi_{R_a}(t')|\Lambda_{S_a}|\Psi_{R_a}(t')\rangle, \tag{29s}$$

where $T < t' < T + T_e$, and Λ_{S_a} is given by

$$\Lambda_{S_a} = \left[\frac{1}{2} - \frac{3}{2}\Theta(\phi_x)\right]\ldots \\ \ldots \times \left[1 - \frac{V'_{tor}(\phi_x,\phi_y) - \min[V'_{tor}(\phi_x,\phi_y)]}{\max[V'_{tor}(\phi_x,\phi_y)]}\right], \tag{30s}$$

where $\Theta(\phi_x)$ is the Heaviside step function applied along the ϕ_x coordinate. The second bracketed term on the right side of equation 30s normalizes and inverts the potential energy surface of $V'_{tor}(\phi_x,\phi_y)$ so $\min(V'_{tor}) = 1$ and $\max(V'_{tor}) = 0$, and the first bracketed term is essentially a modified Heaviside step function that multiplies everything by -1 when $\phi_x > 0$ and 0.5 when $\phi_x < 0$. Multiplying Λ_{S_a} by the wave function norm and integrating over ϕ_x and ϕ_y will lead to positive values when the wave packet is near the "undesirable" (in this example, R_a) well and negative values when the wave packet is near the "desirable" (in this example, S_a) well.

The evaluated fitness for each enantiomer is calculated by applying eq 29s to the Ψ_{R_a} and Ψ_{S_a} wave packets N times with equal spacing over the time period T_e, i.e.

$$\Gamma_{R_a} = \frac{\sum_{n=0}^{N}\langle\Psi_{R_a}(T+n\Delta t)|\Lambda_{S_a}|\Psi_{R_a}(T+n\Delta t)\rangle}{2(N+1)} + 1, \tag{31s}$$

$$\Gamma_{S_a} = \frac{\sum_{n=0}^{N}\langle\Psi_{S_a}(T+n\Delta t)|\Lambda_{S_a}|\Psi_{S_a}(T+n\Delta t)\rangle}{2(N+1)} + 1, \tag{32s}$$

where $N\Delta t = T_e$, and dividing the summations by $2(N+1)$ and adding 1 normalizes the values of Γ_{R_a} and Γ_{S_a} to lie between 0 and 1. Generally T_e should be a long enough to get a good picture of the final state of the system, e.g. the length of a few oscillation periods in the ϕ_d coordinate. In our optimization, $T_e = 5$ ps and $N = 9$.

The final component of the fitness function is a term that penalizes pulses with peak intensities that are higher than a user-defined threshold limit I_{thresh}. The peak intensity of a candidate pulse is calculated by simply finding the maximum value of the the direct sum of the three field components discussed in section Is, i.e.

$$I_{peak} = \max\left[|\mathcal{E}_1|^2 + |\mathcal{E}_2|^2 + \mathcal{E}_1^*\mathcal{E}_2 + \mathcal{E}_1\mathcal{E}_2^*\right]/c\mu_0. \tag{33s}$$

Note that the fact that the two kick pulses do not share the same alignment axes means that the actual peak intensity will be slightly lower, so in effect I_{peak} represents an absolute upper bound. The intensity fitness is calculated by mapping I_{peak} to a value between 0 and 1 with a sigmoid function:

$$\Gamma_I = \{1 + \exp[-\beta(I_{peak} - I_{thresh})]\}^{-1}, \tag{34s}$$

where β is a factor that adjusts the steepness of the sigmoid function at I_{thresh}, allowing us to tune the "severity" of the cutoff limit. In our optimization, $I_{thresh} = 16$ TW/cm^2 and $\beta = 2$ cm^2/TW.

The final fitness of a given pulse is evaluated by taking the norm of $\Gamma_{\mathrm{R_a}}$, $\Gamma_{\mathrm{S_a}}$ and Γ_I:

$$\Gamma = \left(\Gamma_{\mathrm{R_a}}^2 + \Gamma_{\mathrm{S_a}}^2 + \Gamma_I^2\right)^{1/2}, \tag{35s}$$

where in practice, the GA tries to find parameters that minimize the value of Γ.

Vs. ALGORITHM IMPLEMENTATION

Our GA optimizations where performed using the MATLAB[33] implementation with adaptive mutation, a total population of 600, 2 "elite" individuals, and 2000 total generations (unless otherwise specified, all other settings where set to default). The calculations where run in parallel using 20 cpu cores. To avoid Hamming cliffs, the algorithm is allowed to modify the phases as boundless parameters. The peak intensity parameters for the unshaped pulses where restricted to a range between 25 and 150 TW/cm^2. Each kick pulse is characterized by 101 phase components, and 1 parameter that determines the peak intensity of the unshaped pulse, leading to a total of 204 parameters or "genes" characterizing each trial solution.

We will now outline how the GA optimizations where implemented. The initial population of 600 trial solutions, each with a "genome" consisting of 204 double precision floating point numbers, is randomly generated. For each trial solution the following steps are taken:

1. Within a time window running from $-128 \leq t \leq 128$ ps with temporal spacing $\Delta t = 1.9$ fs, a pair of unshaped 700 fs FWHM Gaussian pulses centered at $t = 0$ and with carrier frequency $\omega_0 = 0$ (see section IIIs C) are created with peak intensities defined by the first two genome parameters.

2. Two spectral phase mask functions consisting of 101 equally spaced "pixels" with values ranging from 0 to 2π are generated using the remaining 202 genome parameters. As described in section IIIs A, the full spectral width of each mask is $W_\omega = 2.69\times10^{13}$ rad, and they are centered around the peaks of the spectral pulse amplitude functions at $\omega = \omega_0 = 0$.

3. The phases of the two unshaped Gaussian pulses are modulated by their respective masks in the spectral domain and transformed back into the temporal domain to generate the shaped pulse amplitude functions $\mathcal{E}_1(t)$ and $\mathcal{E}_2(t)$.

4. The temporal functions $|\mathcal{E}_1(t)|^2$, $|\mathcal{E}_2(t)|^2$ and $\mathcal{E}_1{}^*(t)\mathcal{E}_2(t)+\mathcal{E}_1(t)\mathcal{E}_2{}^*(t)$ are multiplied by the Gaussian spatio-temporal coupling masking function as described in section IIIs B, and the pulse time windows are truncated to $-12 \leq t \leq 12$ ps.
5. Using linear interpolation, the shaped pulse data is resampled at the quantum simulation time step size of 1000 a.u..

6. Two simulations are performed by independently propagating the $\Psi_{\mathrm{R_a}}(t=0)$ and $\Psi_{\mathrm{S_a}}(t=0)$ wave packets interacting with the shaped pulses, as described in sections Is and IIs.

7. After propagating the interactions for the 24 ps pulse duration, the fitness parameters $\Gamma_{\mathrm{R_a}}$, $\Gamma_{\mathrm{S_a}}$ and Γ_I are evaluated and the total fitness of the trial solution is calculated as described in section IVs.

After the fitnesses of all 600 trial solutions have been evaluated, a new population is generated from the previous one using the GA selection and mutation procedures, and steps $1-7$ are repeated. This entire process is iterated 2000 times, and the best performing solution from the last generation is selected as the final converged result.

Appendix E

Breaking Dynamic Inversion Symmetry in Enantiomeric Mixtures using Trains of Laser Pulses

Breaking Dynamic Inversion Symmetry in a Racemic Mixture Using Simple Trains of Laser Pulses

Esben F. Thomas and Niels E. Henriksen
Department of Chemistry, Technical University of Denmark, Building 206, DK-2800 Kongens Lyngby, Denmark

Recent advances in ultrafast laser technology hint at the possibility of using shaped pulses to generate deracemization via selective enantiomeric conversion; however, experimental implementation remains a challenge and has not yet been achieved. Here, we describe an experiment that can be considered an accessible intermediate step on the road towards achieving laser induced deracemization in a laboratory. Our approach consists of driving a racemic mixture of 3D oriented 3,5-difluoro-3′,5′-dibromobiphenyl ($F_2H_3C_6 - C_6H_3Br_2$) molecules with a simple train of Gaussian pulses with alternating polarization axes. Using arguments related to the geometry of the field/molecule interaction, we illustrate why this will increase the amplitude of the torsional oscillations between the phenyl rings while simultaneously breaking the inversion symmetry of the dynamics between the left- and right-handed enantiomeric forms, two critical prerequisites to achieving the asymmetric wave packet transfer required for deracemization to occur. We verify our approach using numerical simulations, and show that it leads to significant and experimentally measurable differences in the internal enantiomeric structures when detected by Coulomb explosion imaging.

I. INTRODUCTION

Deracemization occurs when a racemic mixture of molecules is transformed into a mixture containing an excess of a single enantiomer. The majority of the work done on deracemization at present time has been concerned with the use of chemical reagents to separate or transform enantiomers (see, e.g., refs 1 and 2).

A number of theoretical studies have also demonstrated the feasibility of a fundamentally different approach, where deracemization is achieved using coherent laser light (see, e.g., refs 3–13). Many of these theoretical investigations have been based around determining the shape of the deracemizing laser pulse using some kind of optimization algorithm; for example in a previous study[14] done by our group we demonstrated theoretically that a genetic algorithm[15] can be used to optimize the spectral phase components[16] of two nonresonant, linearly polarized Gaussian laser pulses with polarization axes rotated 13° away from each other in a way that leads to selective enantiomeric conversion of a racemic mixture of 3D-oriented, 3,5-difluoro-3′,5′-dibromobiphenyl ($F_2H_3C_6 - C_6H_3Br_2$) molecules. However, achieving laser-induced deracemization in a laboratory has not yet been achieved. This is partly because experimentalists still consider it a "high risk" venture; the difficulty of performing the experiment means that it will require the allocation of significant resources.

Here, we therefore propose a more modest experiment that can be considered an intermediate step on the road towards fully achieving laser induced deracemization. Using an experimental setup similar to the one described in ref. 14, we theoretically demonstrate that applying a relatively simple series of driving laser pulses to a gas phase racemic mixture of 3D aligned/oriented $F_2H_3C_6 - C_6H_3Br_2$ molecules can lead to significant and measurable differences in the internal dynamics and structure between the left- and right-handed enantiomeric forms, effectively transforming a racemic 50/50 mixture into a 26/74 mixture that is skewed towards one of the enantiomeric species. The key difference between this work and that performed in ref. 14 is that the results presented here do not require significant optimization of the laser pulse shape; instead we exploit some of the general principles that we uncovered by analyzing the optimized fields in ref. 14 to "manually" construct the pulse train in a way designed to make experimental implementation more feasible.

II. BACKGROUND INFORMATION

The experimental and theoretical details pertaining to $F_2H_3C_6 - C_6H_3Br_2$ and similar molecular systems are covered in refs. 14, 17–19. To summarize, $F_2H_3C_6 - C_6H_3Br_2$ has an axially chiral structure where torsional rotation around the stereogenic axis leads to transformations between left- and right-handed enantiomeric forms. Gas-phase $F_2H_3C_6 - C_6H_3Br_2$ molecules can be oriented in 3D using an elliptical alignment pulse combined with a static electric field[20], where the alignment pulse is defined in lab frame coordinates $(\hat{x}, \hat{y}, \hat{z})$ as $\mathbf{E}_0(t) = E_{0z}\hat{z} + E_{0x}\hat{x}$, where the minor (major) polarization axis of the elliptical pulse lies along the $\hat{x}$ ($\hat{z}$) lab frame axis. It has been demonstrated experimentally[19] that the most polarizable axis (MPA) of the molecules will align along $\hat{z}$ with the major alignment pulse axis, and the second most polarizable axis (SMPA) of the molecules will align with the minor alignment axis along $\hat{x}$, as shown in figure 1.

As in our previous work in ref. 14, all laser pulses described in this paper couple to the molecular polarizability functions by way of the dynamic Stark effect[21–23], which is proportional to the square of the field envelope times the molecular polarizability term. An advantage of this method is therefore that we are not limited by the carrier frequency of the laser, as it can be shown that

the molecules will only respond to changes in the electric field envelope in the dynamic Stark regime.

As outlined in refs. 14 and 19, if we treat the F and Br substituted rings as two fixed rotors rotating in the $\hat{x}\hat{y}$ plane, we can represent the system in 2 dimensions using $\phi_{\rm F}$ and $\phi_{\rm Br}$ as coordinates describing, respectively, the angle of the F and Br substituted ring in relation to the $\hat{x}$ axis. As also shown in refs. 14 and 17, this 2D representation can be transformed into a coordinate system that decouples the kinetic energy of the "external" motion (i.e. changes in the weighted rotational angle Φ) of the molecules from their "internal" dynamics (i.e. changes in the relative dihedral angle $\phi_d = \phi_{\rm Br} - \phi_{\rm F}$ between the rings).

In the work performed in ref. 17 it is demonstrated that cooling a gas-phase population of $F_2H_3C_6{-}C_6H_3Br_2$ molecules to a few Kelvin will hinder the internal rotation, and the dihedral angle ϕ_d between the ring planes will become fixed at 39° and −39°. As figure 2 demonstrates, these angular configurations correspond to two different stable structures that are each other's mirror image, that is, an enantiomeric pair. Here we adopt the notation of labelling the 39° and −39° configurations as S_a and R_a enantiomers, respectively.

In a general sense, the deracemization process is characterized by selective changes in the internal structure of one of the enantiomers. For this reason, the process can be purely quantified by only following the internal dynamics of the R_a and S_a nuclear wave packets in the ϕ_d coordinate. However, as we shall soon demonstrate, the relative angle between the molecular orientations in Φ and the polarization axis of the driving pulse is also a critical factor to take into account for deracemization to be possible. We now introduce a concept that will be important in the following analyses; namely the structural symmetry axis of the system. Assuming that the dihedral angles of the enantiomers have equal and opposite signs, the structural symmetry axis is defined as the "mirror line" in the $\hat{x}\hat{y}$ plane that will perfectly reflect the structure and orientation of the R_a (S_a) enantiomer into its mirrored S_a (R_a) counterpart. Mathematically, this axis lies in the $\hat{x}\hat{y}$ plane where its angle in relation to the the $\hat{x}$ axis is defined by the mean value of the weighted rotational angles of both enantiomers, i.e.

$$\hat{\theta}_{\rm sym} = \cos\left(\frac{\Phi_{R_a} + \Phi_{S_a}}{2}\right)\hat{x} - \sin\left(\frac{\Phi_{R_a} + \Phi_{S_a}}{2}\right)\hat{y} \quad (1)$$

For example, the structural symmetry axis of the enantiomers will lie along the $\hat{x}$ axis when they are in their initial 3D aligned state, as can be seen in figure 2.

In ref. 14 it was discovered that the shaped pulses are able to achieve deracemization by concurrently satisfying at least two conditions; the dihedral oscillations in ϕ_d must become large enough for at least one of the enantiomeric wave packets to be able to move over the potential barrier separating the enantiomeric species, and the inversion symmetry of the dynamics in ϕ_d between the two enantiomers must be broken, i.e. the dynamics of the torsional oscillations in the R_a and S_a enantiomer must evolve in a way that leads to them becoming dissimilar.

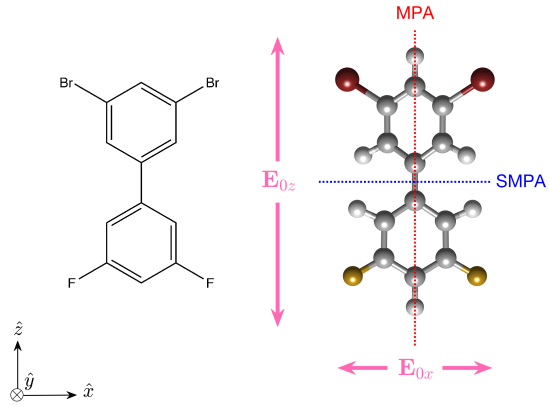

FIG. 1. Molecular structure of 3,5-Difluoro-3′,5′-dibromobiphenyl ($F_2H_3C_6 - C_6H_3Br_2$). The most polarizable axis (MPA) and second most polarizable axis (SMPA) are represented by respective red and blue dotted lines in the $\hat{x}\hat{z}$ plane. In the simulations performed throughout this article, the MPA is always oriented along the lab frame $\hat{z}$ axis with the Br-substituted ring pointing in the positive direction as shown. The elliptical orientation pulse $\mathbf{E}_0$ propagates along the $\hat{y}$ axis (see, e.g., figure 5), and the vertical (horizontal) pink arrows show the direction of its major (minor) polarization axes, denoted by $\mathbf{E}_{0z}$ ($\mathbf{E}_{0x}$).

III. SYMMETRY BREAKING PRINCIPLES

At this point, it is instructive to look at how the potential energy surfaces of the initial 3D-oriented enantiomers are modified in the presence of a nonadiabatically applied 10 TW/cm^2 field when the polarization axis of the field is rotated away from the $\hat{x}$ axis in the $\hat{x}\hat{y}$ plane by various angles. Panels (1a), (2a) and (3a) in figure 3 show the potential energy surfaces when the polarization axis of the applied field is respectively rotated 0°, 15°, and 30° away from the $\hat{x}$ axis, where the blue (red) dots show the initial S_a (R_a) wave packet expectation positions. Switching on the 10 TW/cm^2 field creates a potential gradient that causes the wave packets to accelerate. The solid blue (red) arrows in the same panels indicate the magnitude and direction of the initial S_a (R_a) wave packet acceleration vectors when projected onto the ϕ_d coordinate, and the blue (red) dotted lines show the equivalent acceleration in the Φ coordinate. Panels (1b), (2b), and (3b) in figure 3 show a sketch of the field polarization axes in relation to the oriented molecules in lab-frame coordinates, as well as illustrating how the acceleration vectors

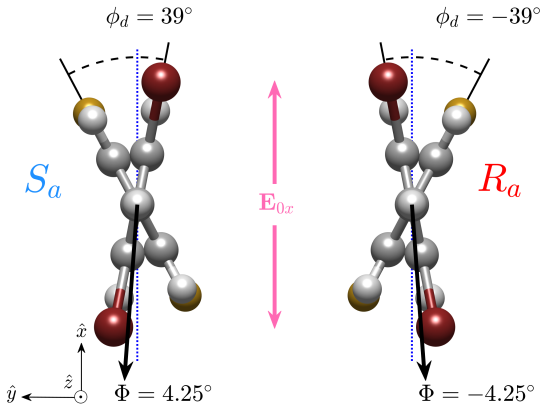

FIG. 2. Top-down view along the $\hat{z}$ axis of the 3D-oriented R_a and S_a enantiomers when their SMPA's (dotted blue lines) are aligned with the minor polarization axis of the alignment pulse $\mathbf{E}_{0x}$ (pink arrows). The dihedral angle (dashed black arcs) in this coordinate system is defined as $\phi_d = \phi_{\mathrm{Br}} - \phi_{\mathrm{F}}$, where ϕ_{Br} and ϕ_{F} are the respective rotational angles of the Br- and F- substituted rings around the stereogenic $\hat{z}$ axis with respect to $\hat{x}$. In this configuration, the weighted rotational angles Φ (black arrows) of the enantiomers have equal and opposite signs, i.e. the structural symmetry axis of the system $\hat{\theta}_{\mathrm{sym}}$ is aligned with the lab frame $\hat{x}$ axis (see equation 1). Note that the angular coordinate system used here and throughout the rest of this article is defined such that the positive direction corresponds to clockwise rotations.

depicted in panels (1a), (2a), and (3a) are represented in the "real" molecular geometry.

Panels (1a) and (1b) in figure 3 show that there will be no initial movement in the Φ coordinate when the polarization axis of the applied field is aligned with the $\hat{x}$ axis. Additionally, the ϕ_d component of the R_a and S_a acceleration vectors will have equal lengths and point in opposite directions. Panel (1b) illustrates that this corresponds to applying identical "pinching" forces to the rings of both enantiomers. The fact that the force vectors felt by each enantiomer are mirrored copies of each other can be understood geometrically by noting that the polarization axis of the driving field is parallel to the structural symmetry axis $\hat{\theta}_{\mathrm{sym}}$ shared by the enantiomers; in a sense the field is "seeing" two identical mirrored versions of the exact same molecule from this angle, so the dynamic response of the enantiomers to the field will necessarily also be mirrored across the $\hat{\theta}_{\mathrm{sym}}/\hat{x}$ axis at all subsequent times as long as the driving field remains polarized in this direction.

In a classical sense, evolving the system dynamics in time on the field-perturbed potential energy surface shown in panel (1a) of figure 3 will lead to torsional vibrations in ϕ_d as the wave packets oscillate in the potential wells created by the external field. Furthermore, applying the $\hat{x}$-aligned field dynamically using, e.g., a train of pulses with spacings approximately equal to the torsional vibrational period will result in resonant driving that increases the amplitude of this torsional motion, a phenomenon that is well understood[23,24] and has been demonstrated experimentally on similar molecules[19]. This satisfies the first criteria that must be met for deracemization to occur; namely that the amplitude of the torsional vibrations must become large enough to facilitate wave packet transfer over the saddle point located at $\phi_d = 0$ that separates the enantiomeric forms. Note, however, that the structure of the R_a and S_a enantiomers will remain symmetrical across the polarization axis of the driving field as we propagate the dynamics forward in time, i.e. the molecules will remain mirror images of each other as long as the driving field is polarized along $\hat{\theta}_{\mathrm{sym}}/\hat{x}$. This means that any transformation that takes place in one enantiomer will always take place in its mirrored counterpart as well, effectively making deracemization impossible.

Breaking the dynamic inversion symmetry while simultaneously increasing the amplitude of the torsional vibrations requires a slightly different approach. As stated, the center and right columns in figure 3 show what happens when the polarization axis of the driving field is de-aligned from the structural symmetry axis by, respectively, 15° and 30° in the $\hat{x}\hat{y}$ plane. There are a number of things to note here. First of all, both enantiomer wave packets will start to accelerate in the positive direction of the Φ coordinate as the molecules rotate around the $\hat{z}$ axis towards the polarization axis of the driving field. Secondly, the magnitude of the acceleration vectors in ϕ_d generally become smaller and, most importantly, *dissimilar* as the de-alignment angle is increased.

These differences in the accelerations that the R_a and S_a torsional wave packets will experience as the polarization axis of the driving field is rotated away from the structural symmetry axis of the enantiomers can be understood if we once again consider the geometry of the overall field/molecular configuration. Unlike the previously discussed case where the polarization axis was aligned with the $\hat{\theta}_{\mathrm{sym}}/\hat{x}$ axis, the field is now effectively "seeing" the R_a and S_a molecules from two different angles. For example, in panel (3a) of figure 3 it can be seen that the polarization axis of the 30° rotated field is now nearly parallel with the F-ring of the R_a enantiomer, and rotated roughly 60° away from the F-ring of the S_a enantiomer. These geometrical differences lead to subtle changes in the way the field interacts with each enantiomer, a result that manifests itself in the form of dissimilar forces being applied to the torsional wave packets. This is critically important because it can potentially lead to dissimilar torsional dynamics, which is the second criteria that must be met for deracemization to be possible.

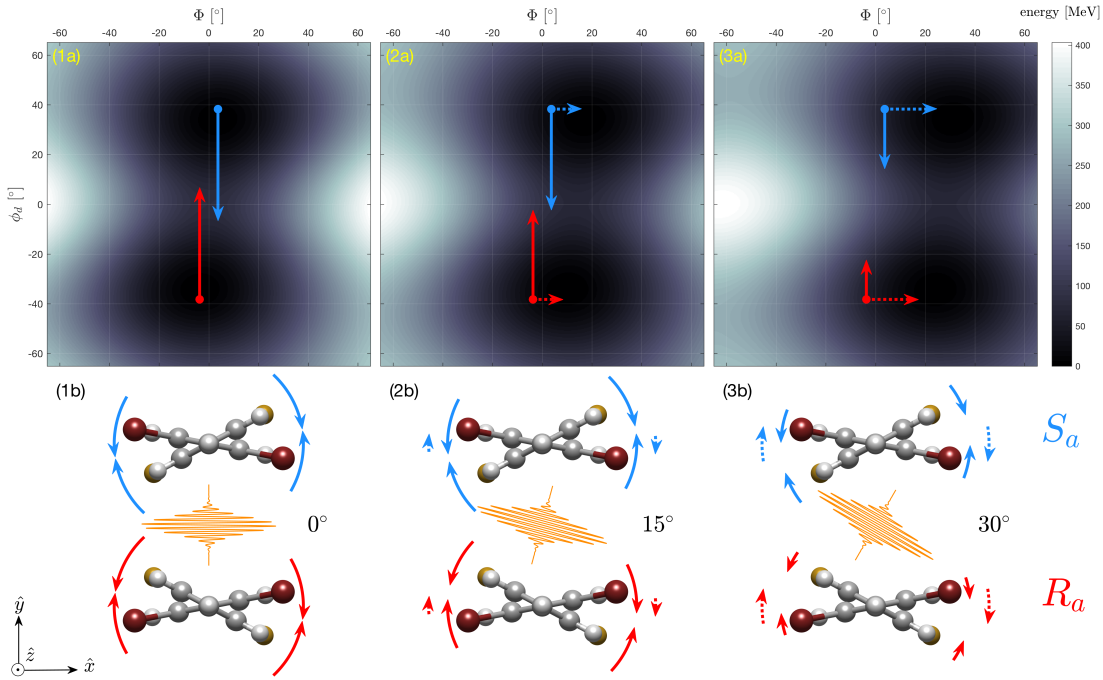

FIG. 3. As discussed in the article text, when the molecules are in their initial 3D oriented state, the application of a kick pulse polarized in the $\hat{x}\hat{y}$ plane will exert a force on the molecular wave packets. Panels (1a), (2a), and (3a) show the field perturbed potential energy surfaces in the (Φ, ϕ_d) coordinate system when the polarization axis of the applied field is rotated 0°, 15° and 30° away from the alignment field axis, where the solid and dotted arrows show the ϕ_d and Φ components of the respective initial wave packet acceleration vectors of the R_a (red) and S_a (blue) enantiomers. Panels (1b), (2b), and (3b) show a sketch of the molecular orientations in space compared to the changing polarization direction of the applied field, where the solid curved arrows illustrate the "pinching" forces that the field will apply to the torsional motion, and the dotted arrows show the direction and magnitude of the field induced rotation in the Φ coordinate.

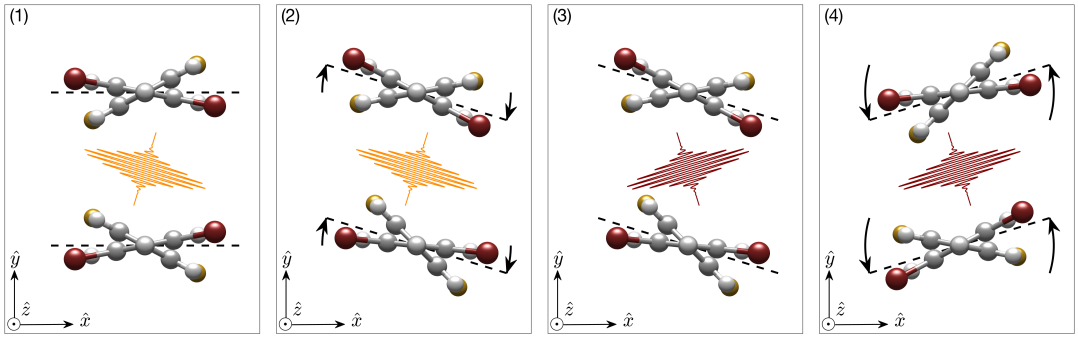

FIG. 4. The four panels illustrate how the amplitude of the dihedral oscillations can be driven while maintaining the asymmetrical nature of the enantiomer/field interaction by continually alternating the polarization axes of the driving pulses (see article text for full explanation). The dashed black lines represent the angle structural symmetry axis shared by the enantiomers $\hat{\theta}_{\text{sym}}$.

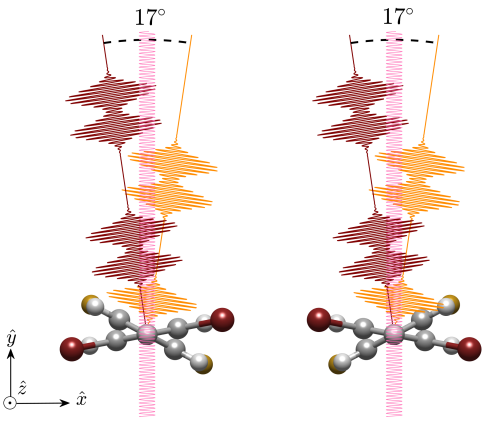

FIG. 5. A sketch of the initial 3D oriented R_a/S_a system, and two pulse trains with field polarization axes rotated $\pm 8.5°$ away from the $\hat{x}$ axis in the $\hat{x}\hat{y}$ plane. As sketched in figure 4, driving the molecules with these pulse trains will increase the torsional oscillations and simultaneously break the dynamic inversion symmetry of the torsional motion between the enantiomers (see figure 6 for the simulated results). For reference the alignment pulse is also shown in pink.

IV. DESIGNING THE PULSE TRAIN

Based on the present information, it would be reasonable to assume that driving the oriented system with a train of pulses with a polarization axis that is de-aligned from the initial structural symmetry axis along the $\hat{x}$ coordinate will allow us increase the amplitude of the dihedral oscillations while simultaneously breaking the inversion symmetry of the enantiomeric dynamics in ϕ_d. However, there is a problem with this idea; the rotation of both enantiomers in Φ will eventually cause $\hat{\theta}_{\text{sym}}$ to align (or nearly align) with the polarization axis of the pulse train, which will once again make it difficult to apply the dissimilar forces to the torsional motion that are required to further break the inversion symmetry of the structural dynamics.

In ref. 14 it was discovered that this problem can be addressed by driving the system with two different fields $\mathbf{E}_1$ and $\mathbf{E}_2$, where the polarization axis of $\mathbf{E}_1$ ($\mathbf{E}_2$) is rotated away from the minor alignment pulse axis ($\hat{x}$) by $-6.5°$ ($6.5°$) in the $\hat{x}\hat{y}$ plane (see, e.g., chart 2 from the same paper). This allowed the optimization algorithm to generate a combined field that changes its polarization axis over time, effectively maintaining large differences between the structural symmetry axis of the molecules and the polarization axis of the driving field. In this way, the amplitude of the torsional oscillations could be increased while maintaining the asymmetrical interaction forces that are required for the wave packet trajectories in ϕ_d to become sufficiently dissimilar over time to facilitate deracemization.

Our approach here is to once again apply the aforementioned principles by driving the system with two different fields with polarization axes that are rotated away from the lab frame $\hat{x}$ axis by equal and opposite angles in the $\hat{x}\hat{y}$ plane. However, instead of optimizing the pulse shapes, we now take a more rudimentary approach by combining the fields to make a simple train of equally spaced pulses with alternating polarization axes. Sketches illustrating this general idea are shown in figures 4 and 5. Panel 1 in figure 4 shows how the aligned system is initially driven by a pulse with a polarization axis that is rotated away from the structural symmetry axis by a positive angle. Referring back to panels (3a) and (3b) in figure 3, it can be seen that this will induce (asymmetric) torsional vibrations in the enantiomers, as well as causing both enantiomers to rotate around the lab frame $\hat{z}$ axis towards the angle of the current field polarization axis. Panel 2 of figure 4 shows how this rotation will cause the structural symmetry axis of the molecules to become aligned with the current polarization axis of the driving field, effectively leaving the system in a configuration similar to the one shown in panels (1a) and (1b) of figure 3, i.e. the forces applied to the enantiomeric wave packets in the ϕ_d coordinate will now be nearly symmetrical. To remedy this, we change the polarization axis of the next pulse in the train to the opposite angle as shown in panel 3 of figure 4. This restores the asymmetrical nature of the enantiomer/field interaction, as well as causing both enantiomers to rotate in the opposite direction around $\hat{z}$ as they move to align with the new polarization axis. When this alignment eventually occurs, as shown in panel 4 of figure 4, the polarization direction of the driving field is changed again, and the process is repeated.

Based on this operating principle, we constructed a train of 7 Gaussian pulses where the polarization axes of the first, fourth and fifth pulses where rotated away from the $\hat{x}$ axis by $8.5°$, and the axes of the second, third, sixth, and seventh pulses where rotated away from $\hat{x}$ by $-8.5°$ (see the sketch in figure 5). As the forthcoming simulated results (figure 6) will show, our strategy for choosing the polarization axis of each pulse in the combined pulse train was to simply alternate the polarization angle of the subsequent pulse any time the angle of the structural symmetry axis $\hat{\theta}_{\text{sym}}$ crosses the angle of the current pulse polarization axis. As a side note to experimentalists, figure 5 also illustrates how the suggested field polarization geometry can be achieved in a laboratory by propagating the two driving pulses along axes that are rotated away from the alignment pulse propagation ($\hat{y}$) axis by $\pm 8.5°$. While there are other directions the driving laser pulses could be applied from to achieve the same results (see, e.g., the abstract figure in ref. 14), this particular setup is advantageous because it will maximize the volume of the effective region where all three lasers overlap and interact with the molecules, which should lead to better measurement statistics.

Besides being polarized at different angles, all 7 pulses

shown in figure 5 have identical shapes with peak intensities of 10 TW/cm^2 and FWHM widths of 0.67 ps, and the pulses were equally spaced at an interval of 1.26 ps. In general, the pulse parameters where chosen based on prior knowledge the system. The peak pulse intensity was selected to approximate the intensity of the optimized pulse envelope in ref. 14, as is expected to be well below the ionization limit[25] of the molecules. The choice of pulse spacing was based on the estimated wave packet oscillation period of $T = 1.2$ ps found in ref. 17, and the FWHM pulse widths were also defined in relation to the oscillation period based on an analysis performed in ref. 23, where it is estimated that optimal excitation with a Gaussian pulse at a fixed intensity is achieved when the relationship between the FWHM pulse width and the oscillation period T is given by $\text{FWHM}/T = 2\sqrt{\ln 2}/\pi$. Note that through trial and error we found that slightly increasing the pulse spacing from 1.2 ps to 1.26 ps (while also appropriately increasing the pulse widths) yielded marginally better results in terms of induced wave packet asymmetries. Finally, while using an angle of 17° between the polarization axes of the two pulse trains gave the best results in our simulations, dealignment angles between 13° and 20° were also able to generate significant wave packet asymmetries. The message to experimentalists here is that although we have tuned our pulse parameters to a certain extent there is a relatively large range of pulse parameters that will yield good results.

V. RESULTS AND DISCUSSION

The pulse trains were simulated interacting with the 3D oriented racemic mixture using split-operator propagation[26] to solve the time-dependent Schrödinger equation, and the initial wave packets at $t = 0$ were calculated using the relaxation method[27]. The simulation results are shown in panels (1a), (1b), and (1c) in figure 6. Panel (1a) shows the intensity profiles of the pulses, panel (1b) shows the expectation value of the weighted rotational angle $\langle\Phi\rangle$ of each enantiomer, and the angle of the structural symmetry axis $\hat{\theta}_{\text{sym}}$, as a function of time. For reference, the polarization angle of the current pulse is also shown, since this is the angle that $\hat{\theta}_{\text{sym}}$ will generally rotate towards to as the dynamics evolve in time. Panel (1c) shows the corresponding evolution of the expectation value of the dihedral angle $\langle\phi_d\rangle$ of each enantiomer. Note that in panel (1c) the curve corresponding to the ϕ_d trajectory of the R_a enantiomer has been multiplied by -1 to facilitate better comparison between the dynamics; i.e. when the enantiomeric dynamics in $\langle\phi_d\rangle$ are mirrored, the curves on the bottom panel will lie exactly on top of each other, and conversely, any asymmetries in the torsional dynamics will be characterized by divergence between the two curves.

Panel (1b) of figure 6 shows how alternating the polarization axis of the field as the system interacts with the pulse train shown in panel (1a) causes the rotational angles (and symmetry axis angle) of the enantiomers to oscillate back and forth around $\Phi = 0$ with steadily increasing amplitudes. This happens because the time scale of the alternations of the field polarization axis are similar to the time scale of the pendular oscillations of the molecules in the potential wells generated by the same fields. These "driven" oscillations in Φ lead to increasing dealignment angles between the structural symmetry axis of the enantiomers and the polarization axis of the driving field. As discussed (and shown in figure 3), this leads to larger asymmetries in the forces driving the torsional oscillations. The impact of these asymmetrical forces on the dihedral trajectories in $\langle\phi_d\rangle$ can clearly be seen in panel (1c), where the expected positions of the R_a and S_a wave packets in ϕ_d begin to significantly diverge at around 7 ps; in fact some degree of deracemization ends up occuring since the mean position of the R_a wave packet eventually moves over the potential barrier located at $\phi_d = 0$, while the S_a wave packet remains fairly well localized on the same side of the barrier that it started out on.

For comparison, we also drove the racemic mixture with a train of 7 pulses using the same parameters as before, except this time the polarization axes of all the pulses were dealigned from $\hat{x}$ by 8.5° (i.e. we did not alternate the polarization axes of the pulses in the driving field to ensure the asymmetrical nature of the interaction was maintained/increased). The $\langle\Phi\rangle$ and $\langle\phi_d\rangle$ dynamics generated by this pulse train are respectively shown in panels (2b) and (2c) of figure 6. In panel (2b) it can be seen that now the structural symmetry axis of the enantiomers spends most of its time aligned, or nearly aligned (within about 8°) of the polarization axis of the driving field. While the small amount of dealignment between the polarization axis and $\hat{\theta}_{\text{sym}}$ leads to minor asymmetries in the forces applied to the dihedral oscillations, it is far less than when we used the pulse train with alternating polarization axes to drive the enantiomers. This is also apparent in panel (2c), where only minor divergences between the blue and red curves are observed, i.e. the inversion symmetry in the torsional dynamics of the enantiomers becomes broken, but not to a significant degree.

As a final test, we once again drove the enantiomers using a train of pulses with the same parameters as before, except this time the polarization axes of all the pulses were aligned with $\hat{x}$. The rotational and torsional dynamics generated by this pulse train are respectively shown in panels (3b) and (3c) of figure 6, and it is apparent that they are perfectly symmetrical at all times. This is because, as stated, the field/molecule interaction in this case will always apply symmetrical forces to both enantiomeric wave packets, since the polarization axis of the driving field always remains parallel to the structural symmetry axis of the system. Note that the R_a and S_a dynamics in Φ are also symmetrical for this reason, although they appear to exchange positions at around 7 ps. This can be explained by considering the fact that the

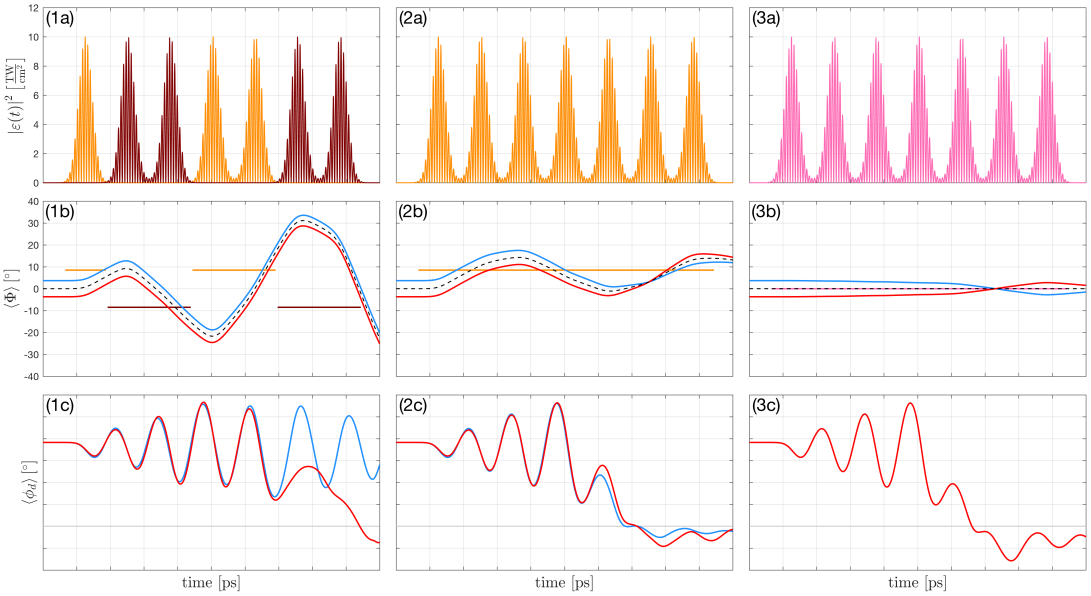

FIG. 6. The three columns show the rotational dynamics (middle row) and dihedral dynamics (bottom row) when three different types pulse trains are applied to the 3D oriented racemic mixture of R_a (red curves) and S_a (blue curves) molecules. The pulse train in the first column corresponds to the one shown in figure 5, i.e. the polarization axes are alternated in a way that ensures that the interaction between the field and the molecules remains asymmetrical. The pulse train in the middle column corresponds to applying 7 pulses with polarization axes that are all de-aligned from the initial molecular symmetry axis by 8.5°, and the pulse train in the right hand column corresponds to applying 7 pulses with polarization axes that are all aligned with the initial molecular symmetry axis $\hat{x}$. Note that the evolution of the $\langle\phi_d\rangle$ value for the R_a enantiomer in the bottom row of plots has been multiplied by -1 to better facilitate comparison (see article text).

mean positions of both enantiomeric wave packets in ϕ_d transfer into their respective opposite wells at around 7 ps, i.e. each enantiomer has effectively been transformed into its own mirror image.

In order to better illustrate the critical elements of the evolution in the torsional states in panel (1c) from figure 6, the wave packets dynamics in the interval between 6 and 10 ps were projected onto the ϕ_d coordinate axis, resulting in the marginal probability distributions of the dihedral wave packet shown in figure 7. Here we see that the R_a wave packet becomes bifurcated on the potential barrier at $\phi_d = 0$ at around 7.5 ps, i.e. part of it is transferred into the right hand well and part of it remains in its original position in the left well. This is a similar, albeit more crude, example of what happens to the enantiomeric wave packets when the system interacts with the optimized pulse in ref. 14, where the R_a wave packet was propelled over the potential barrier separating the enantiomeric forms and the slightly dissimilar trajectory of the S_a wave packet caused it to rebound entirely back into its own well instead, leading to a deracemized mixture where 98% of the molecules were S_a enantiomers. In the present case, the simplified pulse train leads to a final S_a population of 74%. While this is certainly a result that can be improved on, achieving this in a laboratory would still be a significant and important accomplishment.

VI. FUTURE PERSPECTIVES

As stated at the article outset, one of the primary goals of this paper has been to suggest a relatively simple experiment that will bring experimentalists a step closer to achieving laser induced deracemization in a laboratory. For this reason, it is relevant to discuss what the measurement data generated by the pulse train in panel (1a) of figure 6 can be expected to look like.

In previous experiments, Coulomb explosion imaging has been used to determine the angular configurations of the Br- and F-substituted phenyl rings in $F_2H_3C_6 - C_6H_3Br_2$ and similar molecules[17–19,28]. This technique is based around the application of a very brief and intense probe pulse to ionize the molecules at an instant in time. The fragmented Br^+ and F^+ ions are ejected axially from the phenyl rings and accelerated along the lab-frame $\hat{z}$ axis by a static electric field un-

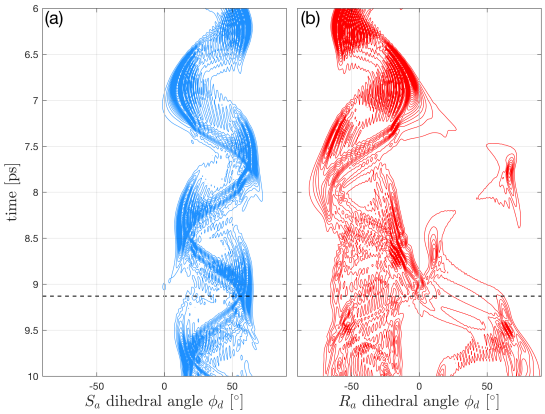

FIG. 7. Marginal probability distribution of the S_a and R_a enantiomeric wave packets projected onto the ϕ_d axis. Quantitative analysis reveals that the R_a/S_a enantiomeric fraction has now become 26/74, i.e. some deracemization has taken place. The horizontal dashed line shows the point where the difference in $\langle\phi_d\rangle$ between the R_a and S_a enantiomer is the largest, i.e. the point where the structures of the each enantiomer have, in a sense, become the most dissimilar. A sketch of how this configuration will look on the experimental detector plate is shown in figure 8.

til they collide with a circular detection plate oriented in the $\hat{x}\hat{y}$ plane at one end of the experimental chamber (see, e.g. figure 1 in ref. 28). Because the Br^+ and F^+ ions have different weights, they will experience different accelerations in the static field, and subsequently they will arrive at the detection plate at different times. This makes it possible to differentiate between a Br^+ and a F^+ ion hit on the detector by keeping track of the delay between the arrival of the probe pulse and the detection event. By performing repeated measurements and recording the angular distributions of the ejected Br^+ and F^+ fragments, experimentalists can construct a picture of the wave packet probability distributions corresponding to the angular configurations of the Br- and F-substituted phenyl rings at various instances in time (see, e.g. figure 3 in ref. 28).

We will now describe how we calculated simulated angular distributions of the ejected Br and F fragments as they are expected to appear on the detector plate. Let $\Psi_{R_a}(\phi_{\mathrm{Br}},\phi_{\mathrm{F}})$ and $\Psi_{S_a}(\phi_{\mathrm{Br}},\phi_{\mathrm{F}})$ represent the simulated 2D wave packets of the respective R_a and S_a enantiomers, now represented in the $(\phi_{\mathrm{Br}},\phi_{\mathrm{F}})$ coordinate system. Each enantiomeric wave packet can be used to create two 1D marginal probability distributions by integrating out either ϕ_{Br} or ϕ_{F}, i.e.

$$P_{S_a}(\phi_{\mathrm{Br}}) = \int |\Psi_{S_a}(\phi_{\mathrm{Br}},\phi_{\mathrm{F}})|^2 d\phi_{\mathrm{F}} \tag{2}$$

$$P_{S_a}(\phi_{\mathrm{F}}) = \int |\Psi_{S_a}(\phi_{\mathrm{Br}},\phi_{\mathrm{F}})|^2 d\phi_{\mathrm{Br}} \tag{3}$$

$$P_{R_a}(\phi_{\mathrm{Br}}) = \int |\Psi_{R_a}(\phi_{\mathrm{Br}},\phi_{\mathrm{F}})|^2 d\phi_{\mathrm{F}} \tag{4}$$

$$P_{R_a}(\phi_{\mathrm{F}}) = \int |\Psi_{R_a}(\phi_{\mathrm{Br}},\phi_{\mathrm{F}})|^2 d\phi_{\mathrm{Br}}, \tag{5}$$

$P_{S_a}(\phi_{\mathrm{Br}})$ and $P_{S_a}(\phi_{\mathrm{F}})$ represent the angular probability distributions of the respective Br- and F-substituted ring for the S_a enantiomer, and $P_{R_a}(\phi_{\mathrm{Br}})$ and $P_{R_a}(\phi_{\mathrm{F}})$ represent the angular probability distributions of the respective Br- and F-substituted rings for the R_a enantiomer.

At this point it is important to note that in an experiment it isn't necessarily possible to tell which enantiomer a detected F^+ or Br^+ ion fragment has originated from. For this reason, $P_{S_a}(\phi_{\mathrm{Br}})$ and $P_{R_a}(\phi_{\mathrm{Br}})$ were incoherently summed to generate a distribution representing the total ion fragment signal intensity of the Br^+ ion fragments as a function of the detector plate angle:

$$P_{\mathrm{tot}}(\phi_{\mathrm{Br}}) = \frac{1}{2}[P_{S_a}(\phi_{\mathrm{Br}}) + P_{R_a}(\phi_{\mathrm{Br}})], \tag{6}$$

and $P_{S_a}(\phi_{\mathrm{F}})$ and $P_{R_a}(\phi_{\mathrm{F}})$ where combined in the same way to generate the corresponding distribution of F^+ fragments:

$$P_{\mathrm{tot}}(\phi_{\mathrm{F}}) = \frac{1}{2}[P_{S_a}(\phi_{\mathrm{F}}) + P_{R_a}(\phi_{\mathrm{F}})], \tag{7}$$

Note also that the symmetry of the phenyl rings means that whenever an ion is detected at ϕ° on the detector, another ion will appear at $(\phi + 180)^\circ$. This means that to get the angular distribution of ions as they will appear on the detector plate, the distributions $P_{\mathrm{tot}}(\phi_{\mathrm{Br}})$ and $P_{\mathrm{tot}}(\phi_{\mathrm{F}})$ have to be added to versions of themselves where the locations of the distributions have been shifted forward by 180°:

$$P^{\mathrm{det}}_{\mathrm{Br}}(\phi) = \frac{1}{2}\big[P^{\mathrm{tot}}(\phi_{\mathrm{Br}}) + P^{\mathrm{tot}}(\phi_{\mathrm{Br}} + 180)\big] \tag{8}$$

$$P^{\mathrm{det}}_{\mathrm{F}}(\phi) = \frac{1}{2}\big[P^{\mathrm{tot}}(\phi_{\mathrm{F}}) + P^{\mathrm{tot}}(\phi_{\mathrm{F}} + 180)\big], \tag{9}$$

where we introduce ϕ as a general coordinate representing the angle in the $\hat{x}\hat{y}$ plane with relation to the lab-frame $\hat{x}$ axis (i.e. the detector plate angle). $P^{\mathrm{det}}_{\mathrm{Br}}(\phi)$ and $P^{\mathrm{det}}_{\mathrm{F}}(\phi)$ were then projected onto radial surface plots in order to replicate the form of, e.g., the raw experimental data displayed in figure 3 in ref. 28. A plot of this result is shown in figure 8, where we have chosen to illustrate what the angular distributions of the ejected Br and F ions will look like on the detector plate at the moment in time when the difference between the expectation value of the R_a dihedral angle $\langle\phi_d\rangle_{\mathrm{R_a}}$ and the S_a dihedral angle $\langle\phi_d\rangle_{\mathrm{S_a}}$ is largest, which we determined would occur at

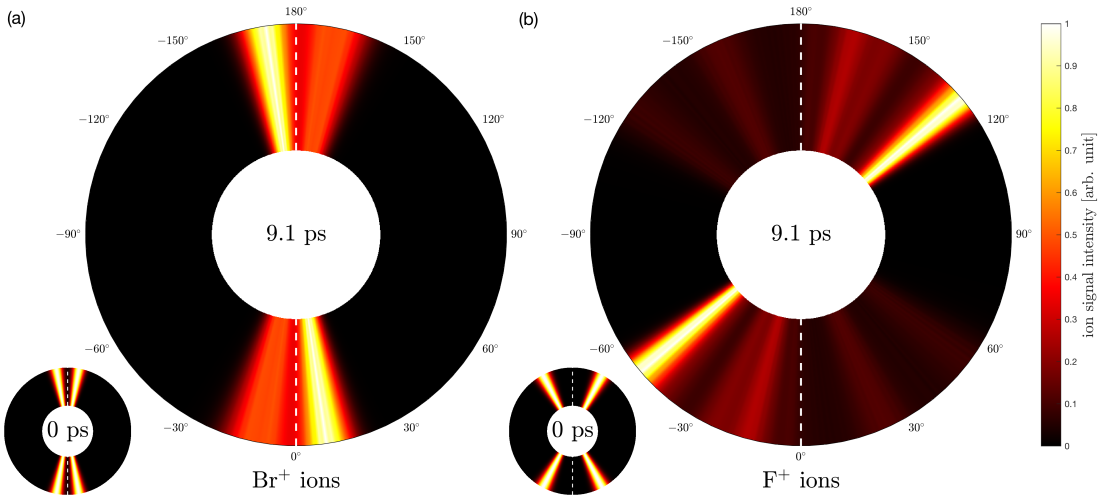

FIG. 8. Projecting $P_{\mathrm{Br}}^{\mathrm{det}}(\phi)$ and $P_{\mathrm{F}}^{\mathrm{det}}(\phi)$ onto radial surface plots illustrates the respective ion signal intensities of the ejected (a) Br and (b) F molecular fragments as they are expected to appear on the detection plates at $t = 9.1$ ps when the pulse train in figure 6(1a) is applied in an experimental situation. For comparison, the ion distributions at $t = 0$ are included as well. The details pertaining to the construction of these pictures can be found in the main article text, however the important feature to take note of is the highly asymmetrical nature of the distribution of F fragments across the vertical $0°/180°$ axis (dashed white line) at $t = 9.1$ ps in panel (b), as this demonstrates that the enantiomeric structures/wave packets have become very different from each other.

about 9.1 ps (as indicated by the black dashed horizontal lines in figure 7).

Note that we are only interested in the internal structure of the molecules, since their orientations in Φ do not directly relate to, or characterize, the process of deracemization. For this reason, the effect of external rotations of the molecules as they appear on the detector plate plots in figure 8 have been corrected (i.e. eliminated) by rotating the plotted distributions towards the $0°$ axis of the radial surface plots by an angle equivalent to the mean angular position of the Br rings. Effectively, this leads to a picture where the mean position of each Br ring will be mirrored across the vertical $0°/180°$ axis, as shown in figure 8(a). This makes it easier to see the asymmetries present in the internal structures of the enantiomers (i.e. ϕ_d), as they will be clearly visible as asymmetries across the $0°/180°$ axis in the distribution of F fragments shown in figure 8(b).

For comparison, the simulated Br^+ and F^+ ion fragment distributions at $t = 0$ are also included in the bottom left corner of panels (a) and (b) in figure 8, respectively. These initial distributions show the characteristic symmetrical "four-dot" geometry that has been experimentally observed before (see, e.g., figure 1 in ref. 28). Conversely, the illustration at $t = 9.1$ in figure 8(b) indicates that the angular distribution of the F^+ fragments has become highly asymmetrical, and the effect should be easy to see in a laboratory setting despite the presence of confounding factors such as experimental noise.

While the qualitative analyses of the general system dynamics and its response to a field discussed throughout this paper have been inspired by a classical picture (i.e. the molecular configurations in Φ and/or ϕ_d have generally not been described as probability distributions), figures 7 and 8 show that applying asymmetrical forces to the enantiomeric wave packets can also have a significant impact on the wave packet shapes and not just their expected positions. This is useful because it makes it even easier to see the asymmetries in an experimental situation, e.g. in figure 8(b) there is a strong peak in the distribution at about $130°/-50°$ that is caused by the relatively well-localized dihedral wave packet of the S_a enantiomer (see figure 7(a)), whereas the spread out areas of the distribution with lower signal intensity are cause by the bifurcation and subsequent delocalization of the R_a dihedral wave packet (see figure 7(b)).

VII. CONCLUSION

In this paper we have suggested, and theoretically verified, a relatively simple method of driving a racemic mixture of 3D oriented biphenyl $F_2H_3C_6 - C_6H_3Br_2$ molecules with a train of Gaussian pulses with alternating polarization axes in a way that will increase the amplitude of the torsional oscillations between the phenyl rings, as well as breaking the symmetry of the dynamics between the left- and right-handed enantiomeric forms.

We elucidate the fundamental principles behind our approach by describing the dynamic response of the enantiomers to the applied field in a coordinate system where the kinetic energy of the external/rotational and internal/conformational dynamics are decoupled.

Using the perturbed potential energy surfaces and arguments related to the geometry of the field/molecule interaction, we show how rotating the polarization axis of the driving field away from the shared structural symmetry axis of the enantiomers will break the dynamic inversion symmetry of the dihedral dynamics, a critical prerequisite to achieving the asymmetric wave packet transfer required for deracemization to occur.

Finally, we show how to maximize the broken dynamic inversion symmetry by properly alternating the polarization axis of the pulses in the driving field, and use numerical simulations to demonstrate that this approach will lead to significant, and most importantly, *experimentally measurable* structural differences between the enantiomers when detected by Coulomb explosion imaging.

ACKNOWLEDGMENTS

The authors wish to thank Professor Henrik Stapelfeldt and his group for providing us with invaluable information and the inspiration to write this paper.

[1] R. McKendry, M.-E. Theoclitou, T. Rayment, and C. Abell, Nature **391**, 566 (1998).
[2] R. Noyori, Angew. Chem. Int. Ed. **41**, 2008 (2002).
[3] A. Salam and W. Meath, Chem. Phys. **228**, 115 (1998).
[4] Y. Fujimura, L. González, K. Hoki, J. Manz, and Y. Ohtsuki, Chem. Phys. Lett. **306**, 1 (1999).
[5] Y. Fujimura, L. González, K. Hoki, D. Kröner, J. Manz, and Y. Ohtsuki, Angew. Chem. Int. Ed. **39**, 4586 (2000).
[6] M. Shapiro and E. Frishman, Phys. Rev. Lett. **84**, 1669 (2000).
[7] H. Umeda, M. Takagi, S. Yamada, S. Koseki, and Y. Fujimura, J. Am. Chem. Soc. **124**, 9265 (2001).
[8] K. Hoki, D. Kröner, and J. Manz, Chem. Phys. **267**, 59 (2001).
[9] K. Hoki, L. González, and Y. Fujimura, J. Chem. Phys. **116**, 2433 (2002).
[10] S. S. Bychkov, B. A. Grishanin, V. N. Zadkov, and H. Takahashi, J. Raman Spectrosc. **33**, 962 (2002).
[11] P. Král, I. Thanopulos, M. Shapiro, and D. Cohen, Phys. Rev. Lett. **90**, 03001 (2003).
[12] D. Gerbasi, M. Shapiro, and P. Brumer, J. Chem. Phys. **124**, 074315 (2006).
[13] S. M. Parker, M. A. Ratner, and T. Seideman, Mol. Phys. **110**, 1941 (2012).
[14] E. F. Thomas and N. E. Henriksen, J. Phys. Chem. Lett. **8**, 2212 (2017).
[15] M. Mitchell, *An Introduction to Genetic Algorithms*, 5th ed. (The MIT Press, 1999).
[16] A. Monmayrant, S. Weber, and B. Chatel, J. Phys. B **43**, 103001 (2010).
[17] C. B. Madsen, L. B. Madsen, S. S. Viftrup, M. P. Johansson, T. B. Poulsen, L. Holmegaard, V. Kumarappan, K. A. Jørgensen, and H. Stapelfeldt, J. Chem. Phys. **130**, 234310 (2009).
[18] C. B. Madsen, L. B. Madsen, S. S. Viftrup, M. P. Johansson, T. B. Poulsen, L. Holmegaard, V. Kumarappan, K. A. Jørgensen, and H. Stapelfeldt, Phys. Rev. Lett. **102**, 073007 (2009).
[19] L. Christensen, J. H. Nielsen, C. B. Brandt, C. B. Madsen, L. B. Madsen, C. S. Slater, A. Lauer, M. Brouard, M. P. Johansson, B. Shepperson, and H. Stapelfeldt, Phys. Rev. Lett. **113**, 073005 (2014).
[20] H. Tanji, S. Minemoto, and H. Sakai, Phys. Rev. A **72**, 063401 (2005).
[21] D. Townsend, B. J. Sussman, and A. Stolow, J. Phys. Chem. A **115**, 357 (2011).
[22] B. J. Sussman, Am. J. Phys **79**, 477 (2011).
[23] E. F. Thomas and N. E. Henriksen, J. Chem. Phys. **144**, 244307 (2016).
[24] A. M. Wiener, D. E. Leaird, G. P. Wiederrecht, and K. A. Nelson, J. Opt. Soc. Am. B **8**, 1264 (1991).
[25] S. M. Hankin, D. M. Villeneuve, P. B. Corkum, and D. M. Rayner, Phys. Rev. Lett. **84**, 5082 (2000).
[26] R. Kosloff, J. Phys. Chem. **92**, 2087 (1988).
[27] R. Kosloff and H. Tal-Ezer, Chem. Phys. Lett. **127**, 223 (1986).
[28] J. L. Hansen, J. H. Nielsen, C. B. Madsen, A. T. Lindhardt, M. P. Johansson, T. Skrydstrup, L. B. Madsen, and H. Stapelfeldt, J. Chem. Phys. **136**, 204310 (2012).

Appendix F

A Novel Pulse Optimization Scheme for use in Coherent Control Experiments

A Novel Pulse Optimization Scheme for use in Coherent Control Experiments

Esben F. Thomas and Niels E. Henriksen
Department of Chemistry, Technical University of Denmark, Building 206, DK-2800 Kongens Lyngby, Denmark

We propose a new method of experimental coherent control that exploits partial/prior knowledge of a molecular system to efficiently arrive at a solution. Our method is based on applying an artificial neural network (ANN) to generate a control field in consecutive temporal steps based on dynamic experimental feedback. We use a 1D double well potential model corresponding to the torsional motion of 3,5-difluoro-3′,5′-dibromobiphenyl ($F_2H_3C_6 - C_6H_3Br_2$) to outline and theoretically verify our approach. We demonstrate that an optimized ANN can achieve robust quantum control of nuclear wave packet transfer between wells despite the addition of random perturbations to the simulated molecular potential energy and polarizability surfaces. We argue that this robustness will potentially allow the ANN to achieve the same control objective in an experimental situation. We show that our method requires a number of measurements that is multiple orders of magnitude smaller than a standard closed-loop approach would typically require to achieve the same results.

I. INTRODUCTION

The concept of applying ultrashort laser pulses to control the dynamics of molecular systems has been a topic of interest for some time. A large body of theoretical (see, e.g., refs. 1–6) and experimental (see, e.g., refs. 7–13) work has been produced in which the feasibility of applying custom-tailored laser pulses to drive various molecular systems into specific target states has been demonstrated.

For simple molecules, where it is possible to make accurate theoretical predictions, a so called "open-loop" scheme may be employed, where the driving pulse shapes are designed based on knowledge of the system Hamiltonian. However, many molecular systems are too complicated for this approach to be of much use. Alternatively, a so called "closed-loop" scheme may be employed[1,14]. Essentially, the closed-loop approach is based on the application of an gradient-free optimization algorithm[15] to the inputs of a pulse shaper[14,16] in a feedback loop where the pulse shaper inputs are updated and optimized "on the fly" based on experimental data generated by the interaction of the molecular system with preceding pulses.

The efficacy of the closed-loop optimization scheme has been proven in a number of experiments, including ionization of gas phase diatomic sodium[10], photoisomerization of organic molecules[11], probing of chemical mechanisms via optimized pulse analysis[12], and manipulation of biological proteins[13]. One of the reasons that the closed-loop approach is so effective in experiments is that it requires little or no prior knowledge of the system it operates on; it is essentially a "black-box" approach to coherent control since the relationship between the problem inputs and outputs is unknown or does not need to be known.

The reality is, of course, that we generally have partial (but not complete) prior knowledge of any given molecular system and/or process that we wish to control. This naturally leads to the question of whether or not it is possible to devise a control scheme that makes use of this partial information in some way to arrive at a solution more quickly and/or efficiently. Such a scheme would be useful in a situation where, e.g., it takes a long time to gather the experimental data, since it would allow us to reduce the total number of measurements required to achieve a desired result.

The implementation of such a scheme can be accomplished in many different ways. One possibility is to simply use a closed-loop approach and construct the initial trial pulses using educated guesses based on theoretical knowledge of the system, in the hope the algorithm will be starting out "closer" to a valid solution in the parametric search space (in some sense, experimentalists already do this by default, since the choice of equipment and parameters used in an experiment will often be guided in some way by prior knowledge of the molecular system in question).

One problem with initializing the search algorithm with an educated guess in this manner is that the Hamming distance[17] between a guess and a solution within the parametric search space may still be very large even though the guess and the solution may "appear" similar; e.g. a small temporal shift in the spacing between two sub-pulses in a pulse train generated by a spectral pulse shaper will require the modification of a large number of pixels in the spectral mask. One way around this issue is to reparameterize the relationship between the problem inputs and outputs in a way that makes it easier for the required adjustments to be made, but this isn't always possible as we don't necessarily know how a guess and a solution are going to differ beforehand.

Our approach to implementing a control scheme that makes use of previously known information about a given system is based on the fundamental assumption that any discrepancies between the theoretical description of an experiment and what happens in reality can, in principle, be rectified by adding some kind of perturbative term(s) to the theoretical model. Based on this premise, we demonstrate theoretically how an artificial neural network[18] (ANN) can be "taught" to achieve a desired control objective when applied to a theoretical molecular model with randomly perturbed potential and laser-

molecule interaction functions. Furthermore, we suggest that an ANN that has been trained in this manner will be able to achieve the same control objective in a real experimental situation.

While the results in this paper are purely theoretical, we substantiate the general experimental feasibility of our approach by demonstrating that the ANN only requires the measurements of experimentally observable quantities to be able to generate an optimized field that achieves the desired control objective. This is accomplished by training the ANN to construct the field directly in the temporal domain in consecutive steps, where the amplitude at each time step is based on measurements of the system at previous time steps. We also demonstrate that the number of required measurements is equal to the dimensionality of the optimization problem (i.e. the number of discrete temporal components that characterize the shape of the field), which is far fewer measurements than would typically be needed if we applied a closed-loop optimization scheme to the same problem.

At this point it is relevant to mention local control theory (LCT)[19,20], a qualitatively similar approach that allows for on-the-fly calculation of an electric field based on the dynamics of a theoretical model system at each time step in a way that leads to a monotonic increase (or decrease) in some predefined expectation value. A key difference between our method and LCT is that ours is intended for use on experimental, real-world systems as an alternative to the standard closed-loop approach, whereas LCT is generally used as a more efficient alternative to optimal control theory[21] (OCT) when working, e.g., with theoretical models that are very computationally expensive to simulate.

II. MODEL SYSTEM

To illustrate our concept with an example, we consider a model system with parameters based on the torsional potential energy surface of 3,5-difluoro-3′,5′-dibromobiphenyl (which we will henceforth refer to as $F_2H_3C_6 - C_6H_3Br_2$) in the electronic ground state (see figure 1). In ref. 22 it is shown that the lowest vibrational mode of this molecule corresponds primarily to the torsional motion of the phenyl rings. Furthermore, it is shown that by aligning the most polarizable axis of the molecule along the lab-frame $\hat{z}$ axis (see figure 1) and neglecting all higher frequency modes, the Hamiltonian of the system interacting with a non-resonant laser pulse polarized in the $\hat{x}\hat{y}$ plane can be approximated by (using atomic units):

$$\hat{H}_{\Phi,\phi_d} = -\frac{1}{2I}\frac{\partial^2}{\partial\Phi^2} - \frac{1}{2I_{\rm rel}}\frac{\partial^2}{\partial\phi_d^2} + V_{\rm tor}(\phi_d) - \frac{1}{4}\varepsilon^2(t)\alpha(\Phi,\phi_d), \tag{1}$$

where $\Phi = (\phi_{\rm Br}I_{\rm Br} + \phi_{\rm F}I_{\rm F})/(I_{\rm Br} + I_{\rm F})$ is the weighted azimuthal angle, $\phi_{\rm Br}$ ($\phi_{\rm F}$) and $I_{\rm Br}$ ($I_{\rm F}$) are, respectively,

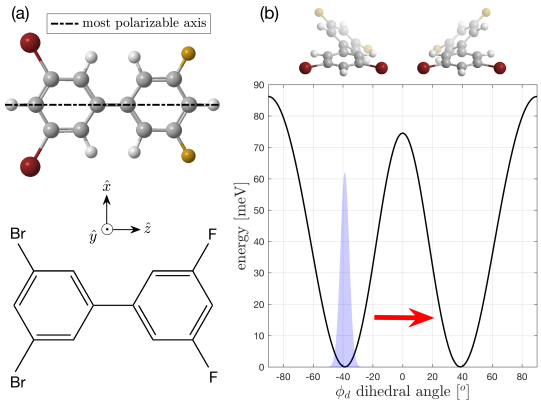

FIG. 1. (a) Molecular structure of the $F_2H_3C_6 - C_6H_3Br_2$ molecule. The most polarizable axis (MPA) is also shown (dashed black line). In the simulations performed throughout this article, the MPA is always oriented along the lab frame $\hat{z}$ axis (b) potential energy surface as a function of the torsional angle ϕ_d between the Br and F substituted rings. The minimum energy nuclear wave packet localized in the left well is shown in light blue, and the red arrow illustrates the desired control objective; wave packet transfer from the left to the right well using a shaped laser pulse.

the rotational angle and inertial moment of the Br (F) substituted ring, $I = I_{\rm Br} + I_{\rm F}$ is the total moment of inertia for rotation around the stereogenic axis, $I_{\rm rel} = I_{\rm Br}I_{\rm F}/(I_{\rm Br} + I_{\rm F})$ is the relative moment of inertia, $\phi_d = \phi_{\rm Br} - \phi_{\rm F}$ is the relative torsional angle between the rings, $V_{\rm tor}(\phi_d)$ is the torsional potential energy, $\varepsilon(t)$ is the time dependent electric field of the laser, and $\alpha(\Phi,\phi_d)$ is the molecular polarizability function (the exact forms of the $V_{\rm tor}(\phi_d)$ and $\alpha(\Phi,\phi_d)$ functions we use, as well as other model details, can be found in ref. 23).

Note that the first term on the right side of equation 1 describes the overall rotational kinetic energy of the molecule, and the second term describes the "internal" energy of the torsional oscillations. In addition to inducing torsional vibrations in the ϕ_d coordinate, driving the system with a time-dependent field will generally lead to rotation in the Φ coordinate as the second most polarizable axis (SMPA, see, e.g., fig. 2 in ref. 22) rotates to align with the field polarization axis. In ref. 22 it is argued that this rotation will occur on nanosecond timescales, whereas the dihedral oscillations and the laser pulses driving the system will generally operate on picosecond timescales. Furthermore, if we assume that the SMPA of the molecule is pre-aligned with the polarization direction of the driving field, there will be very little induced rotation in the Φ coordinate. In such a case, the Hamiltonian can be reduced to 1D by considering the dihedral motion at a fixed Φ coordinate, i.e.

$$\hat{H}_{\phi_d} = -\frac{1}{2I_{\rm rel}}\frac{\partial^2}{\partial\phi_d^2} + V_{\rm tor}(\phi_d) - \frac{1}{4}\varepsilon^2(t)\alpha(\Phi;\phi_d), \quad (2)$$

where the $\Phi;\phi_d$ notation in $\alpha(\Phi;\phi_d)$ indicates that Φ is held fixed over the duration of the pulse. Note that we will henceforth always assume that $\Phi = -4.25°$ (which corresponds to alignment of the SMPA with the field polarization direction), and for clarity of notation Φ will therefore be dropped from subsequent equations.

Having defined our model, the control task will be to generate a field that can transfer the minimum energy wave packet localized in the left well of the system over the energy barrier located at $\phi_d = 0$, and into the right well (see the right side of figure 1).

In ref. 22 it is demonstrated that the description of the $F_2H_3C_6 - C_6H_3Br_2$ system given by equation 2 will yield provisionally accurate results based on comparisons with experimental data. However, it is clear that such a drastic simplification will generally not be able to accurately reproduce the real behaviour of the system, particularly if the torsional oscillations become very large.

III. CORRECTING FOR DISCREPANCIES

The potential energy $V_{\rm tor}(\phi_d)$ and polarizability $\alpha(\phi_d)$ functions used in equation 2 are derived from a series of quantum-chemical calculations performed in ref. 22 where the torsional angle of the central $C - C$ bond was held fixed at various angles and the remaining structure was allowed to relax into the minimum energy configuration before calculating the energy and polarizability.

We can identify at least two sources of error that are likely to cause discrepancies in the dynamic behaviour of the experimental system compared to the simulated system; the first is simply due to unavoidable inaccuracies associated with the chosen method of quantum-chemical calculation, and the second is due to the fact that it is likely that other modes will become activated as the amplitude of the torsional oscillations become large, which will in turn lead to time-dependent distortions in the potential energy and polarizability surfaces that the simplified Hamiltonian in equation 2 does not account for.

As stated in section I, the central idea behind our approach is that any discrepancies between the model and the real dynamics can be rectified via the addition of one or more perturbing functions to the model Hamiltonian. To illustrate this concept, we now modify the Hamiltonian in equation 2 by respectively adding perturbing functions $\eta_V(\phi_d,t)$ and $\eta_\alpha(\phi_d,t)$ to the torsional energy function $V_{\rm tor}(\phi_d)$ and the polarizability function $\alpha(\phi_d)$:

$$\hat{H}'_{\phi_d} = -\frac{1}{2I_{\rm rel}}\frac{\partial^2}{\partial\phi_d^2} + [V_{\rm tor}(\phi_d) + \eta_V(\phi_d,t)] - \frac{1}{4}\varepsilon^2(t)[\alpha(\phi_d) + \eta_\alpha(\phi_d,t)]. \quad (3)$$

In a sense, $\eta_V(\phi_d,t)$ and $\eta_\alpha(\phi_d,t)$ effectively represent the "difference" between the simulated and experimental systems. The implicit assumption is, therefore, that for a given field $\varepsilon(t)$, some set of $\eta_V(\phi_d,t)$ and $\eta_\alpha(\phi_d,t)$ functions exist that will reproduce the behaviour of the experimental wave packet with perfect accuracy if we insert them into the Hamiltonian in equation 3 and simulate the dynamics.

The problem is still, of course, that we do not know the "correct" form of $\eta_V(\phi_d,t)$ and $\eta_\alpha(\phi_d,t)$. However, if the aforementioned assumption is valid, then there is a non-zero probability that a randomly generated set of $\eta_V(\phi_d,t)$ and $\eta_\alpha(\phi_d,t)$ functions will accurately reproduce the behaviour of the experimental wave packet. Furthermore, if we can teach a computer to generate a field that accomplishes the simulated control task on the Hamiltonian in equation 3 given *any* set of $\eta_V(\phi_d,t)$ and $\eta_\alpha(\phi_d,t)$ functions, then it should, in principle, be able to accomplish the same control task in an experimental situation with no further optimization required. While this may seem like a tall order, if we assume that the method(s) used to calculate $V_{\rm tor}(\phi_d)$ and $\alpha(\phi_d)$ are moderately accurate, we can simplify the task somewhat by making the following assumptions:

- Structural distortions that occur as the dihedral oscillations become large will primarily be caused by the activation of the other low-frequency modes present in the system. As a result, the temporal variation of the features in $\eta_V(\phi_d,t)$ and $\eta_\alpha(\phi_d,t)$ will occur on a time-scale that is comparable to the time-scales of these modes.

- As the system interacts with the driving pulse the configuration of the structural distortions will not dramatically fluctuate as the dihedral angle between the rings changes by a small amount. Consequently, the features in $\eta_V(\phi_d,t)$ and $\eta_\alpha(\phi_d,t)$ will vary relatively smoothly as a function of ϕ_d.

- The amplitudes of the features appearing in $\eta_V(\phi_d,t)$ and $\eta_\alpha(\phi_d,t)$ are relatively small compared to the characteristic energies (e.g., the potential barrier heights) and polarizabilities of the calculated $V_{\rm tor}(\phi_d)$ and $\alpha(\phi_d)$ surfaces.

Based on these assumptions/simplifications, we will now outline how we generated random $\eta_V(\phi_d,t)$ and $\eta_\alpha(\phi_d,t)$ perturbing functions. While there are countless ways we can attempt to model these functions depending on how realistic/plausible we want them to be, an in-depth analysis of this topic is beyond the scope of this

paper, as the intention here is to merely provide a basic proof of concept. For this reason, we have chosen a relatively simple approach based around the application of a Gaussian lowpass filter to a 2D white noise signal, the details of which can be found in appendix A.

Applying this method allowed us to generate random $\eta_V(\phi_d, t)$ perturbation functions consisting of features with an amplitude variance of 11.9 meV, a mean angular coherence length of 12.2° in the ϕ_d dimension, and a mean temporal coherence length of 0.27 ps in the temporal dimension (see appendix A for an explanation of how the coherence lengths are defined). Figure 2 shows 2D plots of $V(\phi_d)$ combined with an example of a randomly generated $\eta_V(\phi_d, t)$ function to demonstrate how these perturbations will modify the potential energy surface. The parameters we used to generate the $\eta_\alpha(\phi_d, t)$ perturbation functions were identical to the ones we used to generate the $\eta_V(\phi_d, t)$ functions, where the variance was scaled so the mean amplitude variance of the $\eta_\alpha(\phi_d, t)$ features was also equal to 11.9 meV when the field strength was at its maximum value.

The choice of coherence length for the temporal features in $\eta_V(\phi_d, t)$ and $\eta_\alpha(\phi_d, t)$ is roughly based on a normal mode analysis performed in ref. 22, and the coherence length in the angular dimension is roughly based on a potential energy surface calculation performed in ref. 24. Note that, as stated, these parameters are not intended to be any more than rough estimates.

On a final note, it is reasonable to assume that the relative moment of inertia I_{rel} will also vary over time since the moments of inertia of the two phenyl rings will change slightly when the structure of the molecule becomes distorted. While including this effect in the perturbed Hamiltonian in equation 3 is in principle not difficult, we do not expect it to significantly impact the qualitative conclusions that will be presented in this paper. For this reason, we have decided to forgo the inclusion of this effect in our model for simplicity.

IV. NEUROEVOLUTION OVERVIEW

The task is now to develop an algorithm that can achieve the control task outlined in section II on the system described by equation 3, for any given set of $\eta_V(\phi_d, t)$ and $\eta_\alpha(\phi_d, t)$ functions generated using the process and parameters outlined in section III. In the subsequent sections we will demonstrate how this can be accomplished using an ANN combined with a genetic algorithm (GA)[15] using a technique called neuroevolution[25].

ANNs and similar machine learning techniques are currently a hot topic in a variety of fields. Because the literature related to this topic is already quite extensive (see, e.g., refs. 18, 25–27), we will here only provide a brief general description of ANNs and their operating principles.

An ANN is essentially a mathematical function that can be characterized by a network of directionally linked nodes connected to a set of network input and output vectors. Each node in the ANN consists of a so-called "activation function" that receives a series of node inputs and generates a node output based on their weighted sum, i.e.

$$f = K\left(\sum_i w_i p_i\right), \tag{4}$$

where p_i represents the "raw" value from the i^{th} incoming connection, w_i is the corresponding connection weight, and K is the activation function that maps $\sum_i w_i p_i$ to scalar node output f. Each node input p_i comes either from other nodes within the network, or from "outside" the network as part of the network input vector. Likewise, each node output can connect to other nodes within the network and/or to the network output vector. Evaluation of a given network input by the ANN is achieved by propagating the "signal" from the network input vector through the network nodes until it reaches the network output vector.

An ANN can "learn" generalized relationships between the inputs and outputs associated with a given problem and/or task. This is accomplished by optimizing all the internal connection weights until the ANN consistently produces the "correct" output for a given input. In many cases, the connection weights can be optimized by gradient descent using backpropagation[27]. However, this method can only be used if we have access to a training set of valid input-output pairs. For example, if we want teach an ANN to find the mathematically optimal move on a chess board in an arbitrary configuration, we need an extensive list of configurations where the mathematically optimal move is already known. Because determining the mathematically optimal move in chess is often an extremely difficult (if not impossible) task, we have no way of generating a comprehensive training set of input-output pairs we can use to train the ANN.

Neuroevolution avoids the aforementioned issue by using a GA to optimize the network connection weights, where each candidate set of network weights is evaluated based on how well it allows the network to perform a desired behaviour. Referring back to the chess example, this means that instead of trying to teach the network to make the mathematically optimal move given every possible board configuration it might encounter, the fitness of a candidate network would be characterized by how often it wins against an opponent when allowed to play out an entire game. This makes neuroevolution useful for reinforcement learning tasks where the correct network outputs for any given set of network inputs may not be known.

In section V we will describe our operational approach to using an ANN to generate a field based on dynamic feedback from an arbitrarily perturbed $F_2H_3C_6 - C_6H_3Br_2$ system, and we will demonstrate why our approach requires that we use neuroevolution to optimize the ANN connection weights.

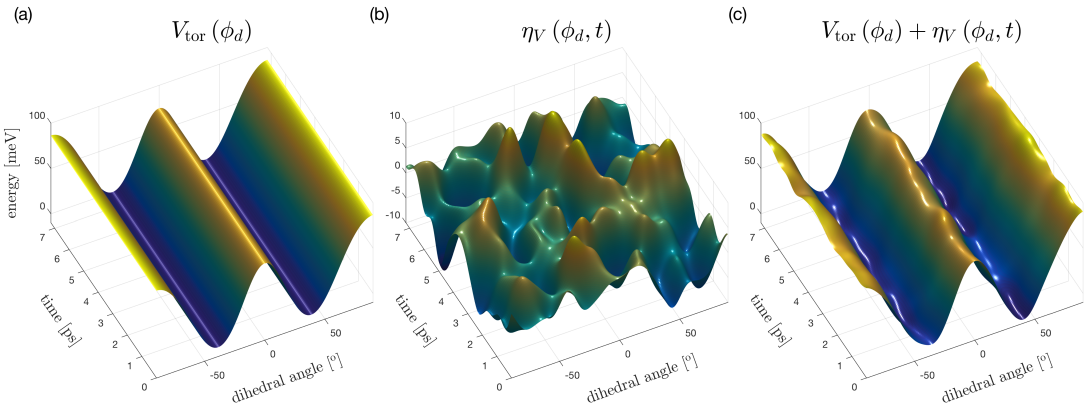

FIG. 2. (a) the theoretical torsional potential energy function $V_{\mathrm{tor}}(\phi_d)$. (b) Example of the perturbing $\eta_V(\phi_d, t)$ function displaying the characteristic size scale of the perturbations in the temporal and spatial domains. (c) When $\eta_V(\phi_d, t)$ is added to $V_{\mathrm{tor}}(\phi_d)$, the torsional potential is perturbed in time and space. $\eta_\alpha(\phi_d, t)$ perturbs $\alpha(\phi_d)$ in a similar fashion (not shown).

V. IMPLEMENTING THE ANN

As stated in section I, the ANN is used to construct the field directly in the temporal domain in consecutive steps. The temporal pulse envelope is characterized by a series of N discrete, equally spaced regions or "bins" with width δt and total length $N \times \delta t = T$. The ANN assigns the amplitude of the bin at time step $n+1$ with a constant value based on information about the system behaviour from time steps 0 to n.

We will now outline the general procedure. First, let ε_n and $\langle\phi_d\rangle_n$ denote the respective field amplitude and position expectation value at the n^{th} time step, and let $\mathbf{M}_n$ denote the list of positions between time step 0 and n, i.e.

$$\mathbf{M}_n = \{\langle\phi_d\rangle_0, \langle\phi_d\rangle_1, \ldots, \langle\phi_d\rangle_{n-1}, \langle\phi_d\rangle_n\}. \tag{5}$$

Now, let $F(\subseteq \mathbf{M}_n)$ denote the evaluation of the ANN when it receives a subset of the information in $\mathbf{M}_n$ as input(s). At each general time step n, the amplitude of the subsequent field component (ε_{n+1}) is constructed as follows:

$$\varepsilon_{n+1} = F(\subseteq \mathbf{M}_n). \tag{6}$$

Next, ε_{n+1} is appended to the total field shape, the system wave packet is propagated forward from time step n to time step $n+1$ using split-operator propagation[28], and the expectation value of the new wave packet position $\langle\phi_d\rangle_{n+1}$ is calculated. Note that in the corresponding experimental situation the overall pulse shape would be updated to include the appended component, the new pulse would be applied to the molecules, and a new measurement of the system would be performed at the appropriately updated time step, as shown in figure 3. The new positional information is added to $\mathbf{M}_n$ (which now becomes $\mathbf{M}_{n+1}$), and the ANN is reapplied to determine the field amplitude at time step $n+2$, i.e.

$$\varepsilon_{n+2} = F(\subseteq \mathbf{M}_{n+1}). \tag{7}$$

Iterating this procedure for all N time steps allows the ANN to construct the entire field envelope in consecutive steps based on dynamic feedback from the system. Note that in practice we also "seeded" the dynamics by uniformly setting the field amplitude at the first 10 time steps to the maximum value, as it was found that this led to performance improvements in the forthcoming optimizations.

To further clarify, an illustration demonstrating how the ANN uses the measurements from previous time steps as inputs to determine the amplitude of the next portion of the field is shown in figure 4, the steps involved in an experimental implementation of the process are shown in figure 3, and a sketch of the topology and connection weights of an optimized ANN is shown in figure 5. Here it can be seen that in practice the ANN only takes $\langle\phi_d\rangle_n$, $\langle\phi_d\rangle_{n-3}$ and $\langle\phi_d\rangle_{n-6}$ as inputs, as it was discovered through trial and error that this led to the best performance. Note that we also use the numerical value of the current time step (n) as an input, as shown in figure 5.

The choice of ANN topology (i.e. the number of nodes in the network and their connectivity) and the type of activation function(s) used in the network nodes (see, e.g., equation 4) can significantly impact the quality of the results. We found that a simple feedforward configuration[26] with a single hidden layer with 20 nodes containing tanh activation functions yielded good results (see figure 5).

Having summarized our general approach to constructing the field envelope with an ANN, the task is now

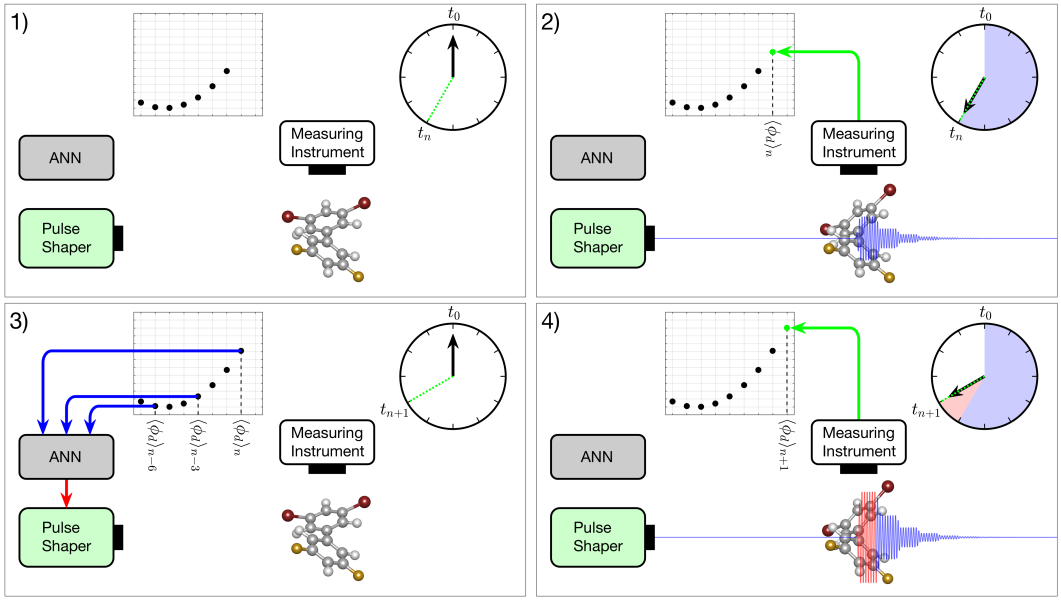

FIG. 3. Illustration of how the trained ANN can be implemented to construct an optimized field in an experimental situation. Note that this figure is meant to show a single intermediate iteration at the n^{th} step of a process that has already been repeated $n-1$ times beforehand. 1) At time step n the measurement acquisition time is set to t_n (where $t_n = n \times \delta t$), as represented by the dotted green line on the clock. 2) The current form of the shaped pulse is applied to the experimental system, a measurement of the system is performed when $t = t_n$, and the new measurement data is added to the full set of information about the system from time steps 0 to n. 3) The measurement acquisition time is updated to t_{n+1}, and a subset of the list of measurement data is used as inputs to the ANN, which in turn informs the pulse shaper what the field amplitude at time step $n+1$ should be. 4) The pulse shaper generates a new pulse identical to the former albeit with the newly appended field component appearing between t_n and t_{n+1} (shown in red), and a new measurement is performed when $t = t_{n+1}$. At this point the value of the current time step is increased by 1 and steps $3-4$ are repeated until N time steps have passed.

to build an ANN that is capable of achieving the control objective defined in section II, i.e. generating a field that transfers a wave packet from the left well of the $F_2H_3C_6 - C_6H_3Br_2$ system into the right well (see, e.g., the right side of figure 1). As stated in section IV, this is achieved via optimization of the ANN connection weights.

Note that we do not know what the optimized field will look like beforehand, so we do not know what the correct network output should be at any given time step (i.e. we do not have access to a training set of valid input-output pairs). For this reason, we cannot optimize the ANN weights using backpropagation/gradient descent. As explained in section IV, neuroevolution of the network weights using a GA is an alternative method that sidesteps this issue, and consequently is the method that we will use to optimize the ANN.

We will now explain how we used a GA to optimize the network connection weights in order to achieve the stated control objective. Note that the feedforward network we wish to train contains a total of 121 connection weights (see figure 5). This means that we will essentially be using the GA to solve a 121 parameter optimization problem, i.e. each candidate GA solution is represented by a "genome" consisting of 121 double-precision floating point numbers. Each number in a given genome defines a unique network connection weight within the predefined network topology. For this reason, a given genome can be used to generate its corresponding "phenotype" by mapping its values to the weights of a network, and conversely the "genotype" of a given network can be extracted by mapping its connection weights to the corresponding genome positions. In the following outlined steps it should therefore be understood that the terms "genome" and "network" essentially mean the same thing, and will be used interchangeably depending on context.

1. Generate S random "training" systems consisting of perturbed potential functions $V_s(\phi_d, t) = V_{\text{tor}}(\phi_d) + \eta_V(\phi_d, t)$ and the corresponding perturbed polarizabilities $\alpha_s(\phi_d, t) = \alpha(\phi_d) + \eta_\alpha(\phi_d, t)$.

2. Define the initial wave packet configuration of each training system, $\Psi_s(\phi_d, t = 0)$, by calculating the

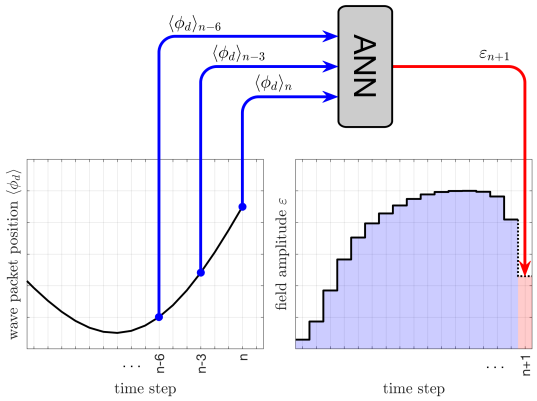

FIG. 4. Schematic showing how information about the system from time steps 0 to n is used by the ANN to determine the field amplitude at time step $n+1$. The left and right panels respectively show the wave packet position $\langle\phi_d\rangle$ and the field amplitude ε at an (arbitrary) interval between time steps $n-15$ and $n+1$. As stated in the article text, once the ANN determines the amplitude of ε_{n+1}, the new component is added to the total field and the system is propagated forward from time step n to $n+1$. Finally, a new measurement of the wave packet position at time step $n+1$ is made, and the process is repeated.

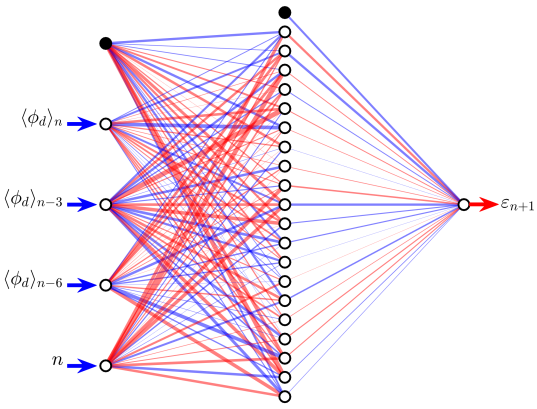

FIG. 5. Sketch of the optimized feedforward network with 4 inputs and a single hidden layer with 20 nodes. The blue (red) lines indicate positive (negative) connection weights, and the line thicknesses correspond to the absolute weight magnitude (for reference, the mean absolute weight magnitude is 3.6, and the maximum absolute weight magnitude is 11.1). All hidden and output nodes contain tanh activation functions, and the black nodes at the top of the structure are bias nodes set to constant output 1. The bottom input, labelled n, inputs the current time step. All inputs are pre-processed by scaling them to a range between approximately -1 and 1, and the network output is scaled to a value between 0 and the (user-defined) laser intensity cutoff limit.

minimum energy state localized in the left well of $V_s(\phi_d, t=0)$ using the Fourier grid Hamiltonian[29] (FGH) method.

3. For each training system, define a set of 10 target states, $\overline{\chi_s} = [\chi_{s,0}, \chi_{s,1}, \ldots, \chi_{s,9}]$, by using the FGH method to calculate the 10 lowest energy states localized in the right well of $V_s(\phi_d, t=T)$.

4. Create a random initial "population" of M networks where, as stated, the genome of each network is characterized by a list of values that each define a unique connection weight in the network.

5. Apply the m^{th} network to all S training sets in the manner outlined previously in this section, resulting in S different wave packets propagated to time T by the network generated fields, $\Psi_{m,s}(\phi_d, t=T)$.

6. Assign the m^{th} network a fitness score F_m, defined as the mean overlap of all $\Psi_{m,s}(\phi_d, t=T)$ from step 5 with the target states in $\overline{\chi_s}$, i.e.

$$F_m = \frac{1}{S}\sum_{s=1}^{S}\sum_{k=0}^{9}|\langle\Psi_{m,s}(\phi_d, t=T)|\,\chi_{s,k}\rangle|^2 \qquad (8)$$

7. Repeat steps $5-6$ for all M networks, and use the GA to create a population of new networks/genomes by mutating and cross breeding networks/genomes from the current generation with higher fitness scores (see appendix B for details about our GA implementation).

8. Repeat steps $5-7$ until the maximum fitness level of the population converges and/or ceases to significantly improve.

By evaluating the performance of the networks on the same S training systems every generation, we ensure that the convergence is monotonic (this would not be the case if we, e.g., created a new set of training systems for each new generation). The caveat of this approach is that we must include a set of training systems that is large enough to prevent overfitting; i.e. if we use too few training systems, then it is unlikely that a network will be able to learn the general rules it needs to know to be able to successfully tackle a system that isn't part of the training set. In practice, the appropriate number of training systems was determined through trial and error, by cross validating the network performance on a series of new systems not included in the training set. If the training fitness is similar to the cross validation fitness, then it is reasonable to assume that the training set is of a sufficient size.

It is important that the range of the initial guesses provided by the GA, as well as the size of the GA mutations, are scaled to reflect the range where the tanh activation function changes from -1 to 1. In our optimization, the

range of the initial weights was between −6 and 6, and the weights were mutated by adding a random Gaussian variable with 0 mean and a standard deviation that did not exceed 0.6.

VI. RESULTS AND DISCUSSION

Using the methodology outlined in section V we optimized a network using a population of $M = 300$ networks, where each network was applied to a training set containing $S = 100$ different test systems that were generated using the noise parameters described in section III. The pulse time window was set to $T = 7.25$ ps, and the number of field components (and measurements) was $N = 300$. The network outputs were scaled to a value between 0 and a peak pulse intensity of 20 TW/cm^2

Figure 5 shows a sketch of the optimized ANN. We tested this ANN by applying it to 10^5 new systems created using the same noise parameters as the training sets, and calculated the resulting overlap of the propagated wave packets with the target wave functions. The red histogram in figure 6 shows the distribution of the target occupation levels for all 10^5 measurements. It is clear that the fields generated by the network are quite effective at achieving the control objective, as the distribution is strongly peaked with a mean value of 0.95.

Note also that these results are achieved after performing a total of 300 measurements on each system, which, as stated in section I, is equal to the number of free parameters used to characterize the shape of the field. A naive closed-loop approach to the same problem would be, e.g., to use a GA to optimize the 300 temporal components of the field instead, as described in ref. 30. As a rule of thumb, the population of a GA (and therefore the number of measurements performed per iteration/generation) should generally be larger than the dimensionality of the search space. Furthermore, the GA will generally require multiple iterations before finding a good solution (e.g. the 400 parameter optimization performed in ref. 30 required 346 iterations of a population containing 2000 individuals, meaning a total of 692000 theoretical "measurements" had to be performed before a converged solution was found). This demonstrates that optimizing the field shape using a closed-loop scheme in the aforementioned manner will likely require a number of measurements that is multiple orders of magnitude larger than our method requires.

It is possible that the optimization process may have created a network that simply produces a generalized pulse shape that works well across all perturbations, i.e. the ANN may not actually be making "intelligent" decisions based on the immediate behaviour of the wave packet in a particular system. To test this hypothesis, we took the 10^5 pulses that the network generated in the previous analysis and applied each one to a different system than the one it was intended to work for.

The blue histogram in figure 6 shows the distribution of target occupation levels when we tested the pulses in the aforementioned manner. If the shapes of the pulses generated by the network are not contingent on the specific perturbed system that the network is operating on, we would expect that a given pulse shape will work equally well on any perturbed system we apply it to (assuming all perturbations are created using the same noise parameters). The fact that the blue distribution in figure 6 is relatively flat compared to the red distribution indicates that this is not the case; the significant difference between the red and blue distributions demonstrates that the network is creating pulses that are specifically tailored to the unique set of perturbing functions associated with each test system.

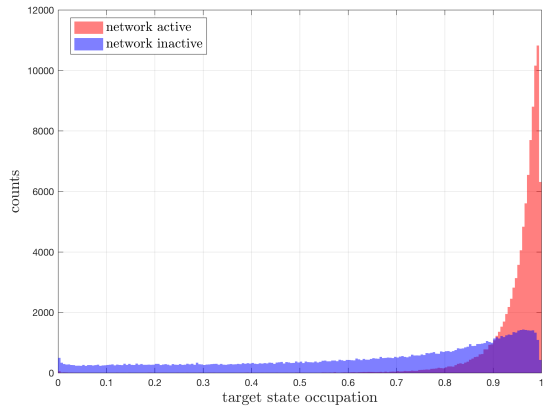

FIG. 6. The red histogram shows the distribution of target state occupations when the optimized network is applied to 10^5 random test systems (note that these systems are not included in the set that was used to train the network). The blue histogram shows the corresponding distribution when the 10^5 pulses generated by the network in the aforementioned analysis are used to drive different systems than the ones they were intended for. (Note that the red and blue histograms have been visually overlaid, i.e. the darker area in the lower right corner is where the shapes of the two distributions overlap.)

Figure 7 shows a comparison of 40 pulse envelopes generated by the network when applied to a series of systems perturbed by different $\eta_V(\phi_d, t)$ and $\eta_\alpha(\phi_d, t)$ functions. By comparing the similarities and differences between various pulses, we can gain some insight into the general principles of network operation. The right side of figure 7 shows a "top down" view of the pulses, and the left side shows the 40 overlaid trajectories of the corresponding wave packet expectation values.

Here it can be seen that each optimized field broadly consists of a number of pulses appearing at similar times, and the wave packet trajectories all follow similar paths. In general, the initial "seed" pulse at $t = 0$ and the following pulse are responsible for pumping the amplitude of the dihedral oscillations for two periods in the left well,

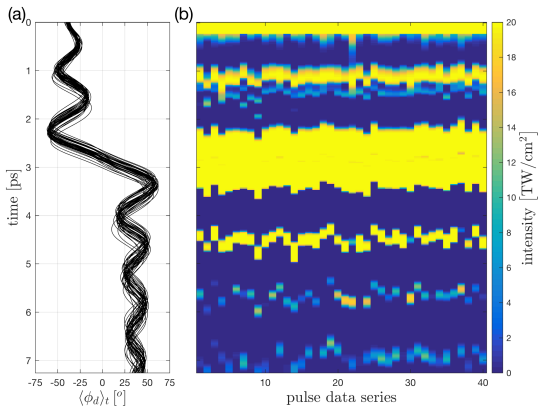

FIG. 7. (a) Overlaid time-dependent position expectation values of wave packet trajectories generated by applying the optimized ANN from figure 5 to 40 different test systems being perturbed by different $\eta_V(\phi_d, t)$ and $\eta_\alpha(\phi_d, t)$ functions created using the parameters outlined in section III. (b) top-down view of the corresponding 40 optimized pulse envelopes generated by the ANN.

the large third pulse is responsible for transferring the wave packet over the central energy barrier at $\phi_d = 0$, and the last $2 - 3$ pulses are used to dampen the amplitude of the oscillations in the right well. Despite these overarching similarities, figure 7 also illustrates that there are differences between the separate systems. Specifically, there are noticeable variations in the temporal and spatial locations of the turning points of the oscillations, as well as the temporal locations of the rising and falling edges of the pulses.

While the complexity of the connections in figure 5 make it difficult to ascertain exactly how the network uses the inputs to make decisions, we can make a few educated guesses based on the input data characteristics. As stated in section V, it was discovered through trial and error that the ANN performs best when it receives the wave packet positions at $\langle\phi_d\rangle_{n-6}$, $\langle\phi_d\rangle_{n-3}$ and $\langle\phi_d\rangle_n$. The shape of the wave packet trajectory on the left side of figure 4 shows that the temporal spacing between these three measurements is similar to the time scale of changes in the wave packet trajectory, which indicates that the ANN may be combining the inputs to numerically estimate the velocity and acceleration of the wave packet at a given time step.

Intuitively, it makes sense that information about the velocity of the wave packet is useful for the ANN, as this can help identify the oscillation turning points as they occur. However, it was found that removing $\langle\phi_d\rangle_{n-3}$ or $\langle\phi_d\rangle_{n-6}$ from the inputs resulted in a marked decrease in performance, which suggests that the wave packet acceleration is also a significant factor in the decision making process (conversely, it was found that increasing the number of inputs by including measurements from earlier time steps did not improve the results).

Another aspect worth considering is how well the ANN performs when noise is added to its inputs and outputs. This is important because these types of effects are essentially unavoidable in a laboratory situation where, e.g., experimental measurements of the wave packet position will generally not reflect the actual position with 100% accuracy. To investigate, we modified the process outlined in section V by adding a random uniformly distributed variable within a range of $\pm 6°$ to each $\langle\phi_d\rangle_n$ "measurement", and a similar random variable within a range of $\pm 10\%$ of the peak field amplitude to each ε_n being output by the ANN. This modified model was then applied to 10^5 randomly perturbed test systems exactly as before, which yielded a mean target state occupation of 87%. This suggests that the ANN is able to robustly contend with moderate experimental noise.

As stated in section III, finding a way to model realistic perturbations is another aspect of our proposed scheme that is at least as important as the implementation and optimization of the ANN. For this reason, we decided to test the performance of the optimized ANN from figure 5 when it encounters perturbations that are outside of the parameter space of the training data. We did this by applying it to 10^5 new test sets generated with perturbation amplitudes that were on average 50% larger than the original training set. This yielded a mean target state occupation of 0.82, meaning that the ANN is generally about 13% less successful at achieving the control objective when faced with the larger perturbations. Next, we tried to improve on this result by retraining the network on systems containing the larger amplitude perturbations. Despite repeated attempts using modified network topologies, GA parameters, and pulse time window lengths, we were not able to create a new network that could exceed the performance of the original network on the new test sets.

It is encouraging to see that the original ANN is able to "handle" the larger amplitude perturbations moderately well, as this suggests a degree of flexibility with respect to how realistically the perturbations need to be constructed. However, the fact that an increase in perturbation amplitude leads to a seemingly uncorrectable decrease in performance despite repeated optimization attempts suggests that there are some fundamental limitations associated with our current approach. Inspection of the systems where the network fails to perform well indicate that the problem arises when the wave packet does not make it over the central barrier in one piece, i.e. part of it is transferred and part remains in the left well. The resulting delocalization means that the position expectation value $\langle\phi_d\rangle$ is no longer a good indicator of the actual position of the wave packet, which has a deleterious effect on the ANNs ability to move it into the right well.

While our current setup may not be able to provide the ANN with the information it requires to successfully avoid delocalization in strongly perturbed systems, there

are countless other ways an ANN could be used to generate an optimized field based on feedback from a given molecular system, some of which may lead to increased robustness against large perturbations. For example, the problem with delocalization might be mitigated by including information about the wave packet variance in the ANN inputs, or by modifying the procedure in a way that allows the ANN to also look "ahead" a few time steps as it constructs the field.

As stated earlier, our motivation for suggesting this scheme is the possibility of developing an experimental alternative to the standard closed-loop approach to coherent control that is more efficient. While the preliminary results outlined here indicate that our approach may be feasible, there are a number of issues and/or limitations that may need to be addressed before an experimental implementation is possible. For example, for our current method to work properly it is a requirement that we have access to some kind of information about the intermediate states of the system before the end of the pulse (whereas in a typical closed-loop approach the algorithm only "cares" about the terminal state). Depending on the experimental setup, these type of intermediate measurements may be difficult or impossible to obtain.

Another concern is how to properly implement the temporal step-by-step construction of the field in an experimental situation; ultrafast pulse shapers generally operate in the Fourier domain by manipulating the frequency components of the pulse spectrum, so constructing a field by precisely controlling the amplitude of the temporal features as outlined in this paper may pose a challenge. Nevertheless, arbitrary pulse shape generation in the temporal domain has been demonstrated using pulse shapers that combine phase and amplitude manipulation in the spectral domain[31]. Another way around this problem could be to characterize the field as a train of Gaussian pulses generated with a beam splitter[32], where the ANN could be used to determine the optimal intensity of each pulse.

VII. CONCLUDING REMARKS

In this paper, we have proposed a new method of experimental coherent control that is designed to make use of partial prior knowledge of a molecular system to arrive at a solution more quickly and/or efficiently than a standard closed-loop approach by reducing the required number of measurements. Our method is based on the application of a trained ANN in a manner that allows it to generate a controlling field in consecutive temporal steps based on dynamic experimental feedback from the molecular system.

Using a 1D model of the torsional motion in $F_2H_3C_6 - C_6H_3Br_2$, we have outlined an approach to modelling discrepancies between simulation and experiment by adding perturbing functions to the theoretical model Hamiltonian. We rationalized this treatment by discussing the likely sources of error that will cause differences between the simulated and experimental dynamics, and we suggested a method of generating random perturbing functions that we argue will have a finite probability of reproducing the experimental dynamics when included in the model Hamiltonian.

Using neuroevolution, we optimized an ANN in a way that allows it to achieve robust quantum control of a simulated molecular system, despite the addition of the aforementioned random perturbations to the molecular potential energy and polarizability surfaces. We argued that this robustness will potentially allow the optimized ANN to achieve the same control objective in an experimental situation. We also demonstrated that the ANN can achieve the control objective using a number of measurements that is potentially multiple orders of magnitude smaller than a closed-loop approach would typically require to produce the same results.

In closing, the purpose of this paper is not to provide a definitive answer regarding the best way to implement a coherent control algorithm based on an ANN. Instead, it is to provide a tentative proof of concept for this novel idea that hopefully leads to lines of further inquiry.

Appendix A: Modelling Realistic Perturbations

For clarity we will use a 1D example in the following description, however the results can easily be generalized to 2 or more dimensions. The goal is to generate a "noisy" signal where it is possible to control the amplitude of the noise fluctuations as well as the "smoothness" of the noise features (i.e. how correlated a given part of the signal is with its adjacent values).

We start by creating a discrete ordered sequence $\nu(x)$ (where $x = \mathbb{N}$), with statistically independent random values. Each value in the sequence is selected from a Gaussian probability distribution function (PDF):

$$P\{\nu(x) = z\} = \frac{1}{\sqrt{2\pi\sigma_\nu^2}} \exp\left(-\frac{z^2}{2\sigma_\nu^2}\right), \qquad \text{(A1)}$$

i.e. for long sequences the mean value of $\nu(x)$ will be ~ 0. This type of uncorrelated sequence or signal is often called "white" Gaussian noise because its power spectral density is constant at all frequencies. Next, $\nu(x)$ is convoluted with a Gaussian low pass filter and multiplied by constant β to create the filtered and scaled sequence $\eta(x)$, i.e.:

$$\eta(x) = \frac{\beta}{\sqrt{2\pi\sigma_G^2}} \sum_{m=-\infty}^{\infty} \exp\left(-\frac{m^2}{2\sigma_G^2}\right)\nu(x-m). \qquad \text{(A2)}$$

Varying the width of the Gaussian kernel σ_G allows us to control the smoothness of $\eta(x)$. The autocorrelation function can be used to obtain a quantifiable measure of this smoothness in terms of the characteristic size of

the features in $\eta(x)$. For a signal generated using equations A1 and A2, it can be shown that the mean autocorrelation function of $\eta(x)$ can be approximated by the following analytical expression:

$$\overline{R_\eta(l)} \approx \exp\left(-\frac{l^2}{4\sigma_G^2}\right). \tag{A3}$$

Using equation A3, we can borrow a measure of the mean signal coherence length from turbulence theory in the form of the Eulerian integral macro-time scale, which is given by

$$L_\eta = \int_0^\infty \overline{R_\eta(l)} dl = \sigma_G\sqrt{\pi}. \tag{A4}$$

Furthermore, it can be shown that the variance of the values in $\eta(x)$ can be approximated by

$$\sigma_\eta^2 \approx \frac{\beta^2\sigma_\nu^2}{2\sigma_G\sqrt{\pi}}. \tag{A5}$$

Using equations A5 and A4, we can control the mean coherence length and/or amplitude of the features in $\eta(x)$ by modifying σ_G and/or β.

Appendix B: Genetic Algorithm Details

We wrote our own custom GA implementation, although the selection and cross breeding functions are identical to those used in the MATLAB[33] GA. As stated, we used a population of 300 individuals where the genomes were initialized with uniformly distributed values between -6 and 6.

When constructing a new generation, the two best performing individuals in the previous generation where included in the new generation unchanged. Of the remaining new individuals to be constructed, 80% were "children" created by selecting two "parents" from the current generation and cross breeding their genomes, and the remaining 20% were "mutants" created by selecting an individual from the current generation and mutating its genome.

Selection of P parents/mutants from a population containing N individuals is accomplished as follows:

1. Rank all N individuals according to their raw fitness scores.
2. Assign each individual a scaled fitness value proportional to its rank. The scaled fitness function employed here is $F(R_n) = 1/\sqrt{R_n}$, where R_n is the rank of the n^{th} individual.
3. Create a line of length L with N segments, where the length of the n^{th} segment is proportional to the scaled fitness of the n^{th} individual.
4. Starting from the beginning of the line, take a step of random length l_0 along the line, where $0 \le l_0 \le L/P$. Select the individual that corresponds to this position on the line as the first selection of the P individuals that are to be selected.
5. Select the remaining $P-1$ individuals by moving along the line with equally spaced steps of length l, where $l = L/P$.

Cross breeding between parent A and B is accomplished by generating random binary vectors with lengths equal to the number of genes in the genome. The n^{th} gene in the child is then assigned the n^{th} gene from parent A (B) when the n^{th} value in the vector is 0 (1).

Mutation is accomplished by adding a random Gaussian variable with a mean value of 0 and a standard deviation of σ to each gene. The size of σ used to construct the mutants in the n^{th} generation is adaptable (albeit with a maximum value of 0.6), and determined by the maximum fitness at generation $n-1$ and $n-2$. If the maximum fitness has not improved between generation $n-2$ and $n-1$, the current value of σ is updated by multiplying the previous value by 20. If the fitness between generation $n-2$ and $n-1$ has increased, the current value of σ is updated by dividing the previous value by 20. Finally, there is also a 1% chance that any gene in a genome that has been selected for mutation will be completely replaced with a new uniformly distributed random value between -6 and 6.

[1] R. S. Judson and H. Rabitz, Phys. Rev. Lett. **68**, 1500 (1992).
[2] S. A. Rice and M. Zhao, *Optical Control of Molecular Dynamics* (Wiley, New York, 2000).
[3] M. Shapiro and P. Brumer, *Quantum Control of Molecular Processes* (Wiley, New York, 2012).
[4] C. Brif, R. Chakrabarti, and H. Rabitz, New J. Phys. **12**, 075008 (2010).
[5] A. K. Tiwari, K. B. Møller, and N. E. Henriksen, Phys. Rev. A **78**, 065402 (2008).
[6] S. Sharma, H. Singh, and G. G. Balint-Kurti, J. Chem. Phys. **132**, 064108 (2010).
[7] A. Assion, T. Baumbert, M. Bergt, T. Brixner, B. Kiefer, V. Seyfried, M. Strehle, and G. Gerber, Science **282**, 919 (1998).
[8] T. C. Weinacht, J. Ahn, and P. H. Bucksbaum, Nature **397**, 233 (1999).
[9] R. J. Levis, G. M. Menkir, and H. Rabitz, Science **292**, 709 (2001).
[10] B. J. Pearson, J. L. White, T. C. Weinacht, and P. H. Bucksbaum, Phys. Rev. A **63**, 063412 (2001).
[11] G. Vogt, G. Krampert, P. Nikaus, P. Nuernberger, and G. Gerber, Phys. Rev. Lett. **94**, 068305 (2005).
[12] J. Savolainen, R. Fanciulli, N. Dijkhuizen, A. L. Moore, J. Hauer, T. Buckup, M. Motzkus, and J. L. Herek, Proc. Natl. Acad. Sci. USA **105**, 7641 (2008).
[13] A. C. Florean, D. Cardoza, J. L. White, J. K. Lanyi, R. J. Sension, and P. H. Bucksbaum, Proc. Natl. Acad. Sci. USA **106**, 10896 (2009).
[14] A. Monmayrant, S. Weber, and B. Chatel, J. Phys. B **43**, 103001 (2010).
[15] M. Mitchell, *An Introduction to Genetic Algorithms*, 5th ed. (The MIT Press, 1999).
[16] A. M. Weiner, Rev. Sci. Instrum. **71**, 1929 (2000).
[17] R. W. Hamming, Bell Labs Tech J. **29**, 147 (1950).
[18] J. Schmidhuber, Neural Networks **61**, 85 (2015).

[19]R. Kosloff, S. A. Rice, P. Gaspard, S. Tersigni, and D. J. Tannor, Chem. Phys. **139**, 201 (1989).
[20]V. Engel, C. Meier, and D. J. Tannor, "Local control theory: Recent applications to energy and particle transfer processes in molecules," in *Advances in Chemical Physics*, Vol. 141 (Wiley-Blackwell).
[21]A. P. Peirce, M. A. Dahleh, and H. Rabitz, Phys. Rev. A **37**, 4950 (1988).
[22]C. B. Madsen, L. B. Madsen, S. S. Viftrup, M. P. Johansson, T. B. Poulsen, L. Holmegaard, V. Kumarappan, K. A. Jørgensen, and H. Stapelfeldt, J. Chem. Phys. **130**, 234310 (2009).
[23]E. F. Thomas and N. E. Henriksen, J. Phys. Chem. Lett. **8**, 2212 (2017).
[24]J. Haruyama, C. Hu, and K. Watanabe, Phys. Rev. A **85**, 062511 (2012).
[25]X. Yao, Int. J. Intell. Syst. Tech. Appl. **4**, 539 (1993).
[26]D. E. Rumelhart, G. E. Hinton, and R. J. Williams, *Parallel Distributed Processing: Explorations in the Microstructure of Cognition, Vol. 1*, edited by D. E. Rumelhart, J. L. McClelland, and C. PDP Research Group (MIT Press, 1986) pp. 318–362.
[27]I. Goodfellow, Y. Bengio, and A. Courville, *Deep Learning* (MIT Press, 2016).
[28]R. Kosloff, J. Phys. Chem. **92**, 2087 (1988).
[29]C. C. Marston and G. G. BalintKurti, J. Chem. Phys. **91**, 3571 (1989).
[30]E. F. Thomas and N. E. Henriksen, J. Chem. Phys. **144**, 244307 (2016).
[31]A. M. Wiener, J. P. Heritage, and E. M. Kirschner, J. Opt. Soc. Am. B **5**, 1563 (1988).
[32]C. W. Siders, J. L. W. Siders, A. J. Taylor, S.-G. Park, and A. M. Weiner, Appl. Opt. **37**, 5302 (1998).
[33]MATLAB, *version 9.0.0.341360 (R2016a)* (The MathWorks Inc., Natick, Massachusetts, 2016).

Bibliography

[1] Ahmed H. Zewail. Femtochemistry. past, present and future. *Pure Appl. Chem.*, 72(12):2219–2231, 2000.

[2] A. D. McNaught and A. Wilkinson. *IUPAC Compendium of Chemical Terminology.* Wiley-Blackwell, 1997.

[3] H. Hartridge and F. J. W. Roughton. A method of measuring the velocity of very rapid chemical reactions. *Proc. Royal Soc. Lond*, 104:376–394, 1923.

[4] M. Eigen. Methods for investigation of ionic reactions in aqueous solutions with half-times as short as 10^{-9} sec. *Faraday Discuss.*, 17:194–205, 1954.

[5] Antoine Monmayrant, Sébastian Weber, and Béatrice Chatel. A newcomer's guide to ultrashort pulse shaping and characterization. *J. Phys. B*, 43:103001–34, 2010.

[6] F. Krausz and M. Ivanov. Attosecond physics. *Rev. Mod. Phys.*, 81:163–234, 2009.

[7] Ahmed H. Zewail. Laser selective chemistry - is it possible? *Phys. Today*, 33(11):27–33, 1980.

[8] Richard S. Judson and Herschel Rabitz. Teaching lasers to control molecules. *Phys. Rev. Lett.*, 68:1500–1503, 1992.

[9] Stuart A. Rice and Meishan Zhao. *Optical Control of Molecular Dynamics.* Wiley, New York, 2000.

[10] Ashwani Kumar Tiwari, Klaus B. Møller, and Niels E. Henriksen. Selective bond breakage within the HOD molecule using optimized femtosecond ultraviolet laser pulses. *Phys. Rev. A*, 78:065402–4, 2008.

[11] Constantin Brif, Raj Chakrabarti, and Herschel Rabitz. Control of quantum phenomena: Past, present and future. *New J. Phys.*, 12:075008–68, 2010.

[12] Sitansh Sharma, Harjinder Singh, and Gabriel G. Balint-Kurti. Genetic algorithm optimization of laser pulses for molecular quantum state excitation. *J. Chem. Phys.*, 132:064108–10, 2010.

[13] A. Assion, T. Baumbert, M. Bergt, T. Brixner, B. Kiefer, V. Seyfried, M. Strehle, and G. Gerber. Control of chemical reactions by feedback-optimized phase-shaped femtosecond laser pulses. *Science*, 282:919–922, 1998.

[14] T. C. Weinacht, J. Ahn, and P. H. Bucksbaum. Controlling the shape of a quantum wavefunction. *Nature*, 397:233–235, 1999.

[15] Robert J. Levis, Getahun M. Menkir, and Herschel Rabitz. Selective bond dissociation and rearrangement with optimally tailored, strong-field laser pulses. *Science*, 292:709–713, 2001.

[16] B. J. Pearson, J. L. White, T. C. Weinacht, and P. H. Bucksbaum. Coherent control using adaptive learning algorithms. *Phys. Rev. A*, 63:063412–12, 2001.

[17] G. Vogt, G. Krampert, P. Nikaus, P. Nuernberger, and G. Gerber. Optimal control of photoisomerization. *Phys. Rev. Lett.*, 94:068305–4, 2005.

[18] Janne Savolainen, Riccardo Fanciulli, Niels Dijkhuizen, Ana L. Moore, Jürgen Hauer, Tiago Buckup, Marcus Motzkus, and Jennifer L. Herek. Controlling the efficiency of an artificial light-harvesting complex. *Proc. Natl. Acad. Sci. USA*, 105(22):7641–7646, 2008.

[19] Andrei C. Florean, David Cardoza, James L. White, J. K. Lanyi, Roseanne J. Sension, and Philip H. Bucksbaum. Control of retinal isomerization in bacteriorhodopsin in the high-intensity regime. *Proc. Natl. Acad. Sci. USA*, 106(27):10896–10900, 2009.

[20] Anthony P. Peirce, Mohammed A. Dahleh, and Herschel Rabitz. Optimal control of quantum-mechanical systems: Existence, numerical approximation, and applications. *Phys. Rev. A*, 37:4950–4964, 1988.

[21] D.C. Champeney. *Fourier Transforms and Their Physical Applications.* International Geophysics. Academic Press, 1973.

[22] Ronnie Kosloff. Time-dependent quantum-mechanical methods for molecular dynamics. *J. Phys. Chem.*, 92(8):2087–2100, 1988.

[23] William H. Press, Saul A. Teukolsky, William T. Vetterling, and Brian P. Flannery. *Numerical Recipes 3rd Edition: The Art of Scientific Computing*. Cambridge University Press, New York, NY, USA, 3 edition, 2007.

[24] Niels E. Henriksen and Flemming Y. Hansen. *Theories of Molecular Reaction Dynamics*. Oxford University Press, 2008.

[25] R. P. Feynman. Forces in molecules. *Phys. Rev.*, 56:340–343, 1939.

[26] David J. Tannor. *Introduction to Quantum Mechanics, a Time-Dependent Perspective*. University Science Books, 2007.

[27] Walter Rudin. *Real and Complex Analysis*. McGraw Hill, 3rd edition, 1987.

[28] Esben. F. Thomas and Niels. E. Henriksen. Non-resonant dynamic stark control of vibrational motion with optimized laser pulses. *J. Chem. Phys.*, 144:244307–10, 2016.

[29] Rida T. Farouki. The bernstein polynomial basis: A centennial retrospective. *Comput. Aided Geom. Des.*, 29(6):379 – 419, 2012.

[30] Benjamin J. Sussman. Five ways to the nonresonant dynamic stark effect. *Am. J. Phys*, 79(5):477–484, 2011.

[31] Doron Meshulach and Yaron Silberberg. Coherent quantum control of multiphoton transitions by shaped ultrashort optical pulses. *Phys. Rev. A*, 60(2):1287–1292, 1999.

[32] A. M. Wiener, D. E. Leaird, Gary P. Wiederrecht, and Keith A. Nelson. Femtosecond multiple-pulse impulsive stimulated raman scattering spectroscopy. *J. Opt. Soc. Am. B*, 8(6):1264–1275, 1991.

[33] Paul Brumer and Moshe Shapiro. One photon mode selective control of reactions by rapid or shaped laser pulses: An emperor without clothes? *Chem. Phys.*, 139(1):221 – 228, 1989.

[34] Moshe Shapiro and Paul Brumer. On the origin of pulse shaping control of molecular dynamics. *J. Phys. Chem. A*, 105(12):2897–2902, 2001.

[35] Anders Aspegren Søndergaard. *Understanding Laser-Induced Alignment and Rotation of Molecules Embedded in Helium Nanodroplets*. PhD thesis, Aarhus University, 2016.

[36] David J Griffiths. *Introduction to electrodynamics; 4th ed.* Pearson, Boston, MA, 2013. Re-published by Cambridge University Press in 2017.

[37] Jun John Sakurai. *Modern quantum mechanics; rev. ed.* Addison-Wesley, Reading, MA, 1994.

[38] Robert L. Cook and Frank C. De Lucia. Application of the theory of irreducible tensor operators to molecular hyperfine structure. *Am. J. Phys.*, 39:1433–1454, 1971.

[39] J. W. Cederberg. Application of racah algebra to molecular point groups. *Am. J. Phys.*, 40(1):159–172, 1972.

[40] C. Z. Bisgaard. *Laser Induced Alignment.* PhD thesis, Aarhus University, 2006.

[41] C. Froehly, B. Colombeau, and M. Vampouille. Shaping and analysis of picosecond light pulses. *Progress in Optics*, 20:63–153, 1983.

[42] Melanie Mitchell. *An Introduction to Genetic Algorithms.* The MIT Press, 5th edition, 1999.

[43] Christopher J. Bardeen, Vladislav V. Yakovlev, Kent R. Wilson, Scott D. Carpenter, Peter M. Weber, and Warren S. Warren. Feedback quantum control of molecular electronic population transfer. *Chem. Phys. Lett.*, 280(1):151 – 158, 1997.

[44] MATLAB. *version 9.0.0.341360 (R2016a).* The MathWorks Inc., Natick, Massachusetts, 2016.

[45] C. B. Madsen, L. B. Madsen, S. S. Viftrup, M. P. Johansson, T. B. Poulsen, L. Holmegaard, V. Kumarappan, K. A. Jørgensen, and H. Stapelfeldt. A combined experimental and theoretical study on realizing and using laser controlled torsion of molecules. *J. Chem. Phys.*, 130:234310–9, 2009.

[46] C. B. Madsen, L. B. Madsen, S. S. Viftrup, M. P. Johansson, T. B. Poulsen, L. Holmegaard, V. Kumarappan, K. A. Jørgensen, and H. Stapelfeldt. Manipulating the torsion of molecules by strong laser pulses. *Phys. Rev. Lett.*, 102:073007–4, 2009.

[47] Lauge Christensen, Jens H. Nielsen, Christian B. Brandt, Christian B. Madsen, Lars Bojer Madsen, Craig S. Slater, Alexandra Lauer, Mark Brouard, Mikael P. Johansson, Benjamin Shepperson, and Henrik Stapelfeldt. Dynamic stark control of torsional motion by a pair of laser pulses. *Phys. Rev. Lett.*, 113:073005–5, 2014.

[48] A. Salam and W.J. Meath. On enantiomeric excesses obtained from racemic mixtures by using circularly polarized pulsed lasers of varying durations. *Chem. Phys.*, 228:115–129, 1998.

[49] Y. Fujimura, L. González, K. Hoki, J. Manz, and Y. Ohtsuki. Selective preparation of enantiomers by laser pulses: Quantum model simulation for H_2 POSH. *Chem. Phys. Lett.*, 306:1–8, 1999.

[50] Yuichi Fujimura, Leticia González, Kunihito Hoki, Dominik Kröner, Jörn Manz, and Yukiyoshi Ohtsuki. From a racemate to a pure enantiomer by laser pulses: Quantum model simulations for $h_2$posh. *Angew. Chem. Int. Ed.*, 39(24):4586–4588, 2000.

[51] Moshe Shapiro and Einat Frishman. Coherently controlled asymmetric synthesis with achiral light. *Phys. Rev. Lett.*, 84(8):1669–1672, 2000.

[52] Hiroaki Umeda, Masato Takagi, Saburou Yamada, Shiro Koseki, and Yuichi Fujimura. Quantum control of molecular chirality: Optical isomerization of difluorobenzo[c]phenanthrene. *J. Am. Chem. Soc.*, 124:9265–9271, 2001.

[53] K. Hoki, D. Kröner, and J. Manz. Selective preparation of enantiomers from a racemate by laser pulses: Model simulations for oriented atropisomers with coupled rotations and torsions. *Chem. Phys.*, 267:59–79, 2001.

[54] Kunihito Hoki, Leticia González, and Yuichi Fujimura. Control of molecular handedness using pump-dump laser pulses. *J. Chem. Phys.*, 116(6):2433–2438, 2002.

[55] Stanislalv S. Bychkov, Boris A. Grishanin, Victor N. Zadkov, and Hiroaki Takahashi. Laser coherent control of molecular chiral states via entanglement of the rotational and torsional degrees of freedom. *J. Raman Spectrosc.*, 33:962–973, 2002.

[56] Petr Král, Ioannis Thanopulos, Moshe Shapiro, and Doron Cohen. Two-step enantio-selective optical switch. *Phys. Rev. Lett.*, 90(3):03001–4, 2003.

[57] David Gerbasi, Moshe Shapiro, and Paul Brumer. Theory of "laser distillation" of enantiomers: Purification of a racemic mixture of randomly oriented dimethylallene in a collisional environment. *J. Chem. Phys.*, 124:074315–9, 2006.

[58] Shane M. Parker, Mark A. Ratner, and Tamar Seideman. Simulating strong field control of axial chirality using optimal control theory. *Mol. Phys.*, 110:1941–1952, 2012.